EPID Dosimetry in Intensity Modulated Radiation Therapy Applications

Mohammad Mohammadi, M.Sc.

ADELAIDE
UNIVERSITY
AUSTRALIA
SUB CRUCE LUMEN

Thesis submitted for the degree of
Doctor of Philosophy
In the School of Chemistry and Physics
University of Adelaide

Supervisors:

Dr. Eva Bezak
Dr. Lotte Fog

September 2006

Preface

Contents

CHAPTER 7. VERIFICATION OF DOSE DELIVERY FOR SIMRT TREATMENT CASES USING A SLIC-EPID 143

CHAPTER 8. CONCLUSIONS AND POSSIBLE FUTURE RESEARCHES 177

APPENDIX A. COMPANION PAPER 181

APPENDIX B 191

REFERENCES 205

Abstract

Electronic Portal Imaging Devices (EPIDs) can be used for dosimetric purposes, provided that an appropriate dosimetric calibration is used. However, in most studies published so far, transmitted dose maps, measured using EPIDs, are used under limited conditions only and further investigation is required for more complex conditions.

In order to use a Scanning Liquid Ionization Chamber (SLIC)-EPID as a comprehensive two-dimensional dosimeter, a calibration method was developed in the current work. This includes investigation of the following issues: additional build-up layer on the EPID; relationship between Electronic Portal Images (EPIs) pixel values and dose on the beam central axis; variation in the measured dose with the radiation field size; SLIC-EPID response with gantry rotation; variation of EPIs with the acquisition time lag; and the reconstruction of the beam horns in off-axis areas using KODAK Extended Dose Range (EDR2) films.

In order to verify the calibration method, the radiation fluence maps measured using a SLIC-EPID were compared with EDR2 film measurements for open and wedged fields using the gamma function algorithm with Distance To Agreement (DTA) and Dose Difference (ΔD_{max}) of 2.54 mm and 1%, respectively. The SLIC-EPID relative dose measurements for a range of homogeneous and inhomogeneous phantoms were also compared to EDR2 film and *Pinnacle*^{3} Treatment Planning System (TPS) data sets.

Prior to using SLIC-EPID for complex treatment modalities, an investigation was carried out on the following: evaluating the SLIC-EPID to detect the minimum change in phantom/patient thickness; an evaluation of SLIC-EPID sensitivity to detect the phantom/patient positioning uncertainties and their effect on the transmitted dose maps; dosimetric characteristics of various radiation field set-ups such as the comparison of Multileaf Collimator (MLC) fields with conventional radiation fields; and evaluating MLC leaf positioning using a SLIC-EPID. Finally, SLIC-EPID response was assessed for segmented Intensity Modulated Radiation Therapy (sIMRT) applied to prostate, and head and neck cases. The results were compared to those that planned using Pinnacle^3

TPS calculation using the gamma function algorithm with DTA and ΔD_{max} of 2.54 mm and 3%, respectively.

For open and wedged fields (in air), the gamma scores for SLIC-EPID and EDR2 film measurements were found to be greater than 95% with 1%/2.54 mm (two pixels). For both homogenous and inhomogeneous phantoms, more than 90% agreement was achieved using gamma criteria of 2%/2.54 mm and 3%/2.54 mm, respectively.

The results showed that a 6 mm change in phantom/patient thickness of a homogeneous phantom can be detected using a transmitted dose measured by the SLIC-EPID. It was also found that SLIC-EPID can detect 1-2 mm patient positioning uncertainties. For radiation field set-up using conventional collimators and MLCs, a significant difference in the penumbra width and radiation field size was observed. A linear relationship was observed between relative dose difference and MLC leaf spatial displacement. The minimum detectable MLC leaf displacement was approximately 0.1 mm using standard edge detection algorithms.

For sIMRT prostate and head and neck cases, a good agreement ($\geq$ 92%) was found between measured and calculated transmitted dose maps for each subfield and the total field in the A-P direction. For non-zero gantry positions the discrepancies increase due to radiation beam absorption in the treatment couch. Several inconsistencies were also observed for small radiation fields.

It can be concluded that SLIC-EPID is a sensitive device for dose delivery verification in three-dimensional Conformal Radiation Therapy (CRT) and segmented Intensity Modulated radiation Therapy (sIMRT) as well as for Quality Assurance (QA) of the dosimetric characteristics of MLC fields. The radiation beam attenuation of the treatment couch for oblique beams and SLIC-EPID response for small radiation fields (less than 3 × 3 cm^2) should be considered as the main limitation in using SLIC-EPID for comprehensive dose delivery verification. In conclusion, SLIC-EPID can be used as a two dimensional dosimeter for complex treatment conditions when an appropriate dosimetric calibration is applied. It can also be used for regular QA of MLC fields.

Declaration

This work contains no material which has been accepted for the award of any other degree or diploma at any other university or other tertiary institution and to the best of my knowledge and belief, contains no material previously published or written by another person, except where due reference has been made in the text.

I give consent to this copy of my thesis, when deposited in the university Library, being available for loan and photocopying.

DATE: 22/12/06

Acknowledgments

First and foremost, I would like to thank my principle supervisor, **Eva Bezak** for her remarkable enthusiasm, guidance, support and encouragement. Her knowledge, ideas and experience in medical physics as well as her communication have enabled me to complete my thesis, to prepare papers for publishing in journals, and to attend conferences.

I would also like to acknowledge **Lotte Fog**, my co-supervisor, for her understanding, suggestion, proof-reading of the thesis, and guidance during my study.

Additionally, I would like to acknowledge **Tim van Doorn**, with whom I started my project, for his ideas and support especially during the early days of my project.

I also acknowledge **Judith Pollard**, as the postgraduate coordinator of Medical Physics for her guidance and her helping with financial support to attend conferences.

Many thanks to the members of the Medical Physics Department at the Royal Adelaide Hospital for their supports and help. Special thanks to **Madhava Bhat** and **Loredana Marcu** for lectures I participated in during my study, and their guidance. Also, **Christine Robinson** has been most helpful and patient. I also would like to thank **Ralph Nicholls** and **Kim Quach** for their assistance.

Many thanks to the IT officers in RAH for their support and my daily requests concerning my computers and, especially to **Margaret Sampson** and **Alan Baldock** for their kind support and friendly interactions.

I would like to acknowledge **Paul Reich** for his kind and thoughtful discussions during my study and for his in-house codes written in MATLAB used in this study to extract data from Treatment Planning System and his contribution to extended and rotated CT image code (see Appendix B3) used in Chapters 4 (Section 4.4.2) and 7 (Section 7.2.2.1).

I would also like to thank postgraduate students in the Department of Medical Physics, especially I never forget the support and friendship of **Setayesh Behin-Ain**. Thanks to other postgraduate students: **Wendy Tuckwell**, **Thuc Minh Pham**, **Rangdham Takam**, and **Saleh Ben Saleh** for their contributions in the weekly PhD meetings. I would also like to thank the Department of Radiation Oncology and the director **Eric Yeoh**, who helped me to receive travel assistance to attend the World Congress on Medical Physics and Bioengineering.

I also would like to appreciate all reviewers for papers and abstracts published and presented in journals and conferences. I have received a lot of useful feedback from them.

I am not able to express enough gratitude to my wife **Kiana** for her support and unconditional love during the preparation of this thesis. Also, my heart goes out towards my sons **Hamoun** and **Mahan**, because I have kept them alone many times when they needed me at home!

I finally would like to acknowledge gratefully the **Iranian ministry of health and medical education**, the **Hamadan University of Medical Sciences** and **Iranian scientific representative** in Canberra for awarding me with a scholarship to undertake my PhD and for their compassionate support.

Symbols and abbreviations

Symbols

$C(\mathrm{r})$	Composite algorithm
ΔD_{max}	Dose difference
$\gamma(\mathrm{r})$	The gamma function algorithm
ρ	Mass density
Γ	Gamma index

Abbreviations

3DCRT	Three-Dimensional Conformal Radiation Therapy
AAPM	American Association of Physicists in Medicine
A-P	Anterior-Posterior
a-Si EPID	amorphous Silicon (a-Si) Electronic Portal Imaging Device
BIS	Beam Imaging System
BUL	Build-Up Layer
CAX	Central Axis
CBCT	Cone Beam Computerised Tomography
CCD	Charge Coupled Device
CFM	Correction Factor Matrix
CRT	Conformal Radiation Therapy
CT	Computerised Tomography
DDF	Dose Difference
dIMRT	dynamic Intensity Modulated Radiation Therapy
DRR	Digitally Reconstructed Radiograph
DTA	Distance To Agreement
EDR2	Kodak Extended Dose Range
EPI	Electronic Portal Images
EPIDs	Electronic Portal Imaging Devices
FF	Flood Field
HV	High Voltage

ICRU	International Commission on Radiation Units and measurements
IMRT	Intensity Modulated Radiation Therapy
IMAT	Intensity Modulated Arc Therapy
KVCT	Kilovoltage Computerised Tomography
LiF	Lithium Fluoride
Linac	Linear accelerator
LoG	Laplacian of Gaussian
MC	Monte Carlo
MIT	Massachusetts Institute of Technology
MLCs	Multileaf Collimators
MOSFET	Metal Oxide Semiconductor Field Effect Transistor
MRI	Magnetic Resonance Imaging
MU	Monitor Unit
MVCBCT	Megavoltage Cone Beam Computerised Tomography
OAR	Organ At Risk
OAR	Off-Axis-Ratio
PCB	Printed Circuit Board
PDI	Portal Dose Images
POI	Point Of Interest
PTV	Planned Target Volume
QA	Quality Assurance
ROI	Region Of Interest
SED	Source to EPID Distance
SLIC	Scanning Liquid Ionization Chamber -EPID
SNR	Signal to Noise Ratio
SSDs	Source to Surface Distances
sIMRT	step-and-shoot Intensity Modulated Radiation Therapy
TPS	Treatment Planning System
TLD	Thermoluminescence Dosimeters

List of Figures

List of tables.

Publications and presentations:

The publications and presentations during the course of this thesis are:

Publications in refereed journals:

1. Mohammadi M, Bezak E, "**The Physical Characteristics of a SLIC-EPID for transmitted dosimetry**" Iran J Radiat Res, 2 (4), 175-183, 2005.

2. Mohammadi M, Bezak E, "**The evaluation of minimum detectable phantom thickness change using a scanning liquid filled ion chamber EPID dose response**" Iran J Radiat Res, 3 (1), 3-10, 2005.

3. Reich P, Bezak E, Mohammadi M, Fog L "**Portal dose prediction using Pinnacle^3 3D Treatment Planning System**" Australas Phys Eng Sci Med. 29 (1), 18-29, 2006.

4. Mohammadi M, Bezak E, "**Two dimensional transmitted dose measurements using a Scanning Liquid Ionization Chamber EPID**", Phys Med Biol, 51, 2971-2985, 2006.

5. Mohammadi M, Bezak E, and Reich P, "**Comparison of two-dimensional transmitted dose maps: evaluation of existing algorithms**" Australas Phys Eng Sci Med. 29 (2), 179-187, 2006.

Other Publications:

1. Mohammadi M, Bezak E, "***In vivo* dosimetry in Intensity Modulated Radiation Therapy; a review**" available at: http://www.iamp.ir/review%20articl/radiotherpy.htm

Submitted papers in refereed journals:

1. Mohammadi M, Bezak E, and Reich P, "**Verification of dose delivery for a prostate sIMRT treatment using a SLIC-EPID**" submitted in "*Physics in Medicine and Biology*"

2. Mohammadi M, Bezak E, and Reich P, "**The use of EDR2 film for dosimetric calibration of SLIC-EPID**" submitted in "*Journal of Applied Clinical Medical Physics*"

3. Mohammadi M, Bezak E, "**Evaluation of MLC leaf positioning using a SLIC-EPID**" submitted in "*Physics in Medicine and Biology*"

4. Reich P, Bezak E, Mohammadi M, "**Assessment and interpretation of transmitted dose maps for set-up errors in prostate CRT: A theoretical study**" submitted in "*Physics in Medicine and Biology*"

Conference presentation:

1. Mohammadi M, Bezak E "**The Evaluation of Electronic Portal Imaging Devices (EPIDs) Characteristics for transmitted dose measurements**" May 2004, 6th Iranian Medical Physics Congress, Mash-had, Iran.

2. Mohammadi M, Bezak E "***In vivo* Dosimetry in Intensity Modulated Radiation Therapy (IMRT).**" May 2004, 6th Iranian Medical Physics Congress, Mash-had, Iran.

3. Mohammadi M, Bezak E "**Dose and dose rate measurements using an Electronic Portal Imaging Device (EPID)**" The Annual Conference of Engineering and the Physical Sciences in Medicine (EPSM), Nov. 2004, Geelong, Victoria, Australia.

4. Mohammadi M, Bezak E "**The comparison of radiation field characteristics obtained by Electronic portal imaging Devices (EPIDs), EDR2 film and Ionization chamber.**" The Annual Conference of Engineering and the Physical Sciences in Medicine (EPSM), Nov. 2004, Geelong, Victoria, Australia.

5. Mohammadi M, Bezak E, Reich P "**Verification of two-dimensional dose measurement in the presence of homogenous/ inhomogeneous phantoms**" The Annual Conference of Engineering and the Physical Sciences in Medicine (EPSM), Oct. 2005, Adelaide, South Australia, Australia.

6. Mohammadi M, Bezak E "**The impact of patient/phantom positioning uncertainties on the transmitted dose**" The Annual Conference of Engineering and the Physical Sciences in Medicine (EPSM), Oct 2005, Adelaide, South Australia, Australia.

7. Mohammadi M, Bezak E "**The minimum detectable MLC leaf displacement using transmitted dose maps**" The Annual Conference of Engineering and the Physical Sciences in Medicine (EPSM), Oct 2005, Adelaide, South Australia, Australia.

8. Mohammadi M, Bezak E, Reich P **"Investigation of two-dimensional dose distribution evaluation tools"** The Annual Conference of Engineering and the Physical Sciences in Medicine (EPSM), Oct 2005, Adelaide, South Australia, Australia.

- Awarded IOP Publishing Student Poster Prize

9. Reich P, Bezak E, Mohammadi M **"The effect of simulated patient setup errors on transmitted dose in 3D prostate CRT"** The Annual Conference of Engineering and the Physical Sciences in Medicine (EPSM), Oct 2005, Adelaide, South Australia, Australia.

10. Reich P, Bezak E, Fog L, Mohammadi M **"Predicting 2D transmitted dose maps using a 3D treatment planning system"** The 8th biennale ESTRO meeting on physics and radiation technology for clinical radiotherapy, September 2005, Lisboa, Portugal.

11. Mohammadi M and Bezak E **"Evaluation of Dosimetric Characteristics of MLC Radiation Fields using SLIC-EPID"** 9th International Workshop on Electronic Portal Imaging. Apr. 2006, Melbourne, Australia.

12. Mohammadi M, Bezak E and Reich P. **"Verification of prostate sIMRT dose delivery using a SLIC-EPID"** 9th International Workshop on Electronic Portal Imaging. Apr. 2006, Melbourne, Australia.

13. Reich P, Bezak E and Mohammadi M **"Using a TPS to model the impact of 3D CRT patient treatment set up errors on predicted transmitted dose"** 9th International Workshop on Electronic Portal Imaging. Apr. 2006, Melbourne, Australia.

14. Bezak E, Mohammadi M, Liu G "**Assessment of Linac Flatness and Symmetry with EPIDs**" 9th International Workshop on Electronic Portal Imaging. Apr. 2006, Melbourne, Australia.

15. Mohammadi M, Bezak E **"The minimum detectable MLC leaf displacement using transmitted dose maps"** Radiation 2006, Apr. 2006, Sydney, New South Wales, Australia.

16. Mohammadi M, Bezak E and Reich P. **"IMRT Dose Verification Using a Scanning Liquid Ionization Chamber EPID for Prostate and Head and Neck Treatments"** World Congress on Medical Physics and Biomedical Engineering 2006, Aug- Sep. 2006, Seoul, Korea

Other Presentations:

1. Mohammadi M, Bezak E " **EPID as a two-dimensional in vivo dosimeter**" The 2004 student papers night, The Australian College of Physical Scientist and Engineers in Medicine- SA branch, Nov. 2004, Adelaide, South Australia, Australia.

2. Mohammadi M, Bezak E **"The impact of patient/phantom positioning uncertainties on the transmitted dose"** The 2005 student papers night, The Australian College of Physical Scientist and Engineers in Medicine- SA branch, Nov. 2005, Adelaide, South Australia, Australia.

3. Reich P, Bezak E, Mohammadi M **"The effect of simulated patient setup errors on transmitted dose in 3D prostate CRT"** The 2005 student papers night, The Australian College of Physical Scientist and Engineers in Medicine- SA branch, Nov. 2005, Adelaide, South Australia, Australia.

Papers in preparation

1. Mohammadi M, Bezak E **"The Evaluation of Electronic Portal Imaging Devices (EPIDs) Characteristics for transmitted dose measurements"**

2. Mohammadi M, Bezak E " **The Detection of Phantom/Patient set-up uncertainties for regular & irregular MLC fields using a SLIC-EPID"**

3. Mohammadi M, Bezak E " **Evaluation of gamma function uncertainties and the development as a three-dimensional dose assessment tool"**

4. Mohammadi M, Bezak E " **The Detection of Phantom/Patient set-up uncertainties for regular & irregular MLC fields using a SLIC-EPID"**

5. Mohammadi M, Bezak E **"Dose delivery verification using EPIDs: a Review"**

For My wonderful Family;

My wife **Kiana**, our sons **Hamoun** and **Mahan**

Chapter 1. Introduction

1.1. Background of the study

Radiation therapy is one of the three major modalities used to treat cancer individually or in combination with other two forms of treatment, surgery or chemotherapy. In cases when the radiation sensitivity of cancerous tissues is higher compared to surrounding healthy tissues, the radiation therapy aims to deliver a high dose of ionizing radiation to the tumour while minimizing radiation dose delivered to normal tissues.

Due to the harmful effects of radiation on healthy tissues, an inaccurate dose delivery leads to either a recurrence of the disease because of a lower dose to tumour or serious complications due to overdose of healthy tissues. As a result, verification of dose delivery is desirable. In order to verify the dose delivered to a patient, the radiation dose distributions should be measured and compared either with that prescribed by radiation oncologists or with planned dose calculated generally by Treatment Planning Systems (TPSs).

The delivered radiation dose can be measured using several types of dosimeters. The ionization chamber, the gold standard, is the most reliable dosimeter in radiation therapy. Another type of point dosimeter, for example Thermoluminescence Dosimeter (TLD), has also been used extensively (Kron 1994; 1995). Films have been used to measure dose distribution in two dimensions (Haus and Marks 1976; Williamson *et al* 1981; Dogan *et al* 2002; Ju *et al* 2002), however, they suffer several drawbacks such as beam energy dependency, processing, darkroom, storage, and scanning conditions. Gel as a three-dimensional dosimeter can also be considered but its application for routine clinical purposes is slow (Day and Stein 1950; Olsson *et al* 1992).

Today, one of the most persistent problems facing radiation therapy is the lack of a comprehensive on-line dosimeter. The aforementioned dosimeters are off-line dosimeters and dose delivered to the patient cannot be monitored during a treatment course. Although several point dosimeters such as silicon diode (Wright and Gager 1977) and Metal-Oxide-Semiconductor Field-Effect-Transistors (MOSFETs) can be used as on-line dosimeters (Sankaran *et al* 1981; Bharanidharan *et al* 2005), they are one dimensional in nature and their specific limitations should be taken into consideration.

Radiation therapy has developed significantly with the development of new complex techniques such as Conformal Radiation Therapy (CRT) and Intensity Modulated Radiation Therapy (IMRT), with the aim to decrease the Planned Target Volume (PTV), so that the dose to target can be safely increased. Consequently, the probability of error in dose delivery increases compared to the conventional radiotherapy. Therefore, a fast, comprehensive, and reliable dose delivery assessment is required.

Electronic Portal Imaging Devices (EPIDs) have originally been developed to provide on-line digital images to verify patient positioning during treatment (Leong 1986; van

Herk and Meertens 1988; Antonuk *et al* 1992; Boyer *et al* 1992a). Although a number of studies, over the last decade have shown that EPIDs can also be used for dosimetric purposes (Kirby and Williams 1993; Yin *et al* 1994; Essers *et al* 1995; Heijmen *et al* 1995). Due to the use of EPIDs under limited conditions, further investigation is required to show the reliability, accuracy, sensitivity and limitations of EPIDs' response, as comprehensive two-dimensional dosimeters.

In order to use EPIDs for dosimetric purposes, several empirical calibration methods have been proposed in the literature (Parsaei *et al* 1998; Chang *et al* 2001). However, the accuracy especially in off-axis areas of the radiation field is not sufficient. Several studies have evaluated EPID response as a two-dimensional dosimeter in the presence of complex phantoms, but have been performed either for conventional radiotherapy or for a single field. For more sophisticated treatment modalities, such as IMRT, the EPID response is mostly evaluated using primary fluence map only in the Anterior-Posterior (A-P) direction. As a result, more attention is required to verify the transmitted dose measured using EPIDs for this technique.

1.2. Aims of the current research

Among available dosimeters at the Medical Physics Department, Royal Adelaide Hospital, Scanning Liquid Ionization Chamber (SLIC)-EPID was found the best possible option for two-dimensional *in vivo* dosimetry. This work attempts to evaluate the abilities of a SLIC-EPID as an accurate and reliable two-dimensional transmitted dosimeter, defined as the dose at the build-up layer of a portal dosimeter located behind a patient. This is achieved through an investigation of a comprehensive dosimetric calibration procedure. The SLIC-EPID dose response is also investigated for primary radiation fluence map (in air), in the presence of homogenous and inhomogeneous phantoms as well as for more complex conditions, such as segmented IMRT for prostate and head and neck cases. The transmitted dose maps are measured using SLIC-EPID and the results are then compared with Extended Dose Range, EDR2, film measurements and those calculated using available TPS.

Several additional experiments, including the minimum detectable variation in the phantom thickness and the minimum detectable phantom/patient set-up uncertainties on the transmitted dose maps, are also performed to investigate the SLIC-EPID sensitivity as a two-dimensional dosimeter. Furthermore, several characteristics of MLC radiation fields including the dosimetric characteristics of MLC fields compared to conventional radiation fields, and the evaluation of MLC leaf positioning are evaluated.

1.3. Thesis outline and structure

The background to this study is outlined in Chapter 1, while the literature review regarding portal dosimetry focusing on EPID measurements is provided in Chapter 1 and Chapter 2. The corresponding experimental investigations are discussed in Chapters 3-7.

Chapter 1 introduces the background of the study and problems to be investigated.

Chapter 2 explains briefly the physics of SLIC-EPID and describes studies that have used EPIDs for dosimetric purposes, including calibration procedures, pre-treatment assessments, the use of EPIDs for Quality Assurance (QA) tests, and the verification of dose delivery.

Chapter 3 reports on the investigation of the general physical characteristics of a SLIC-EPID including reproducibility and noise level measurements of Electronic Portal Images (EPIs) acquired using SLIC-EPID. The chapter consists of a dosimetric calibration procedure defined for SLIC-EPID, an investigation of the extra build-up layer needed for maximum response, and an assessment of the beam field size effect on the acquired EPIs. In addition, the relationship between EPID pixel values and dose rate and dose values, the variation of EPI stability with acquisition time lag and the SLIC-EPID response for a range of gantry angles are investigated. This chapter concludes with an introduction of a Correction Factor Matrix (CFM) to reconstruct the radiation beam horns, removed during EPI generation, as a result of standard manufacturer designed EPID calibration procedure.

Chapter 4 presents the verification of dosimetric calibration, proposed in Chapter 3, in air using open and wedged fields for a range of Source to Surface Distances (SSDs). This also refers to the presence of homogeneous and inhomogeneous phantoms with the evaluation of an agreement between transmitted dose distributions measured using SLIC-EPID, EDR2 film pixel values, and those calculated using a *Pinnacle*^{3} TPS.

Chapter 5 focuses on a discussion of the minimum detectable change of phantom/patient thickness. In addition, this is an investigation of the relationship between transmitted dose distribution measured using SLIC-EPID with the uncertainty of phantom/patient positioning. These experiments are important for a reliable dosimeter.

Chapter 6 discusses the SLIC-EPID's ability to investigate the dosimetric characteristics of radiation fields formed using Multileaf Collimators (MLCs), and conventional jaws. It also evaluates the MLC leaf positioning using a SLIC-EPID. These experiments are essential before concentrating on the EPID response for complex modalities such as IMRT.

Chapter 7 investigates the SLIC-EPID response as a two-dimensional comprehensive dosimeter for step-and-shoot IMRT fields for A-P and non-zero angles directions. These are compared to those calculated using a *Pinnacle*^{3} TPS for prostate and head and neck cases in the presence of an anthropomorphic phantom.

This thesis is concluded in Chapter 8 and the main points are summarised. Several possible avenues for future research are outlined.

The flowchart of the work procedure starting from EPIs acquisition using a SLIC-EPID is shown in Figure 1.1.

In conjunction with the work presented in this thesis, an investigation was also undertaken into the evaluation of the existing algorithms used to compare two-dimensional transmitted dose maps. This work has been presented in Appendix A.

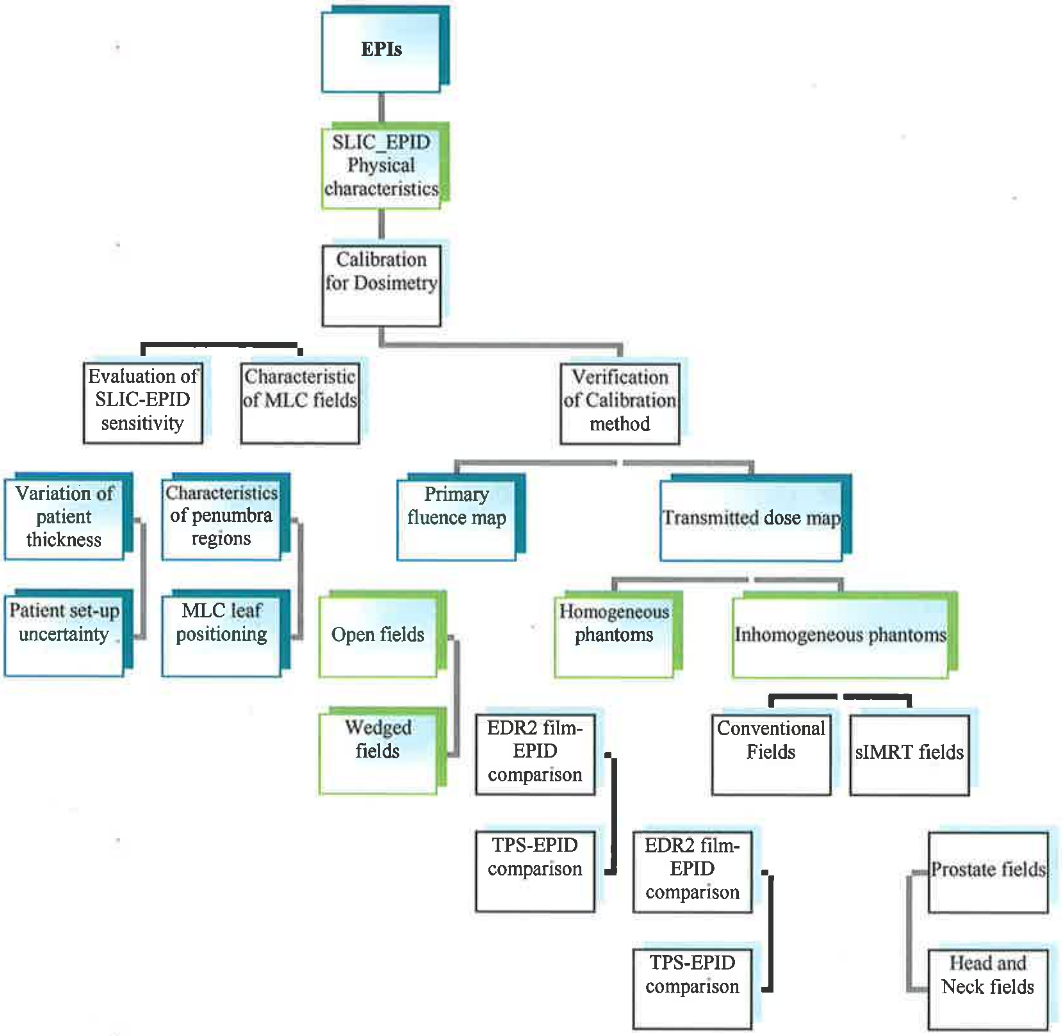

Figure 1.1. The flowchart of the work procedure.

Chapter 2. IMRT dose delivery verification using electronic portal imaging devices

2.1. Introduction

To verify the correct dose delivery to a patient as planned by a Treatment Planning System (TPS), two major considerations are required. Firstly, the patient set-up during planning, including medical linear accelerator (linac) gantry and radiation beam collimator settings, must be reproduced exactly. Secondly, an accurate amount of radiation with correct field shape, beam energy, and beam spectrum settings must be delivered. These are defined as geometric and dose delivery verification, respectively. This chapter provides a review of the literature published recently that concentrates on the patient dosimetry, mainly two-dimensional dose delivery verification. This chapter also briefly introduces new techniques developed for radiation therapy, devices used for dosimetric purposes, and some of the current relevant problems.

2.2. New techniques in radiation therapy

2.2.1. Conformal radiation therapy

Conformal Radiation Therapy (CRT) was designed to conform the shape of radiation fields as close as possible to the target volume shape. Moreover, firstly, the aim of CRT is to reduce the treatment volume without significant effects on the disease control and secondly, to decrease the complication rate (Tate *et al* 1986). This technique requires the use of more beams and smaller beam field sizes, compared to those used for conventional radiation therapy. In addition, due to the decrease of target volume, more accurate beam collimation and patient positioning is required.

Field shaping can generally be performed using either Cerrobend materials or Multileaf Collimators (MLCs). The Cerrobend materials are moulded and manually mounted in specific positions. In contrast, using computerized systems, MLCs remove the need for Cerrobend blocks and their manual positioning, thus saving machine time (Brewster *et al* 1995; Helyer and Heisig 1995), and providing a healthier environment for radiation therapy staff. However, the use of MLCs increases the penumbra region (the area within 20% - 80% of central dose at the radiation field edge), inter/intra leaf radiation leakages, and causes undulation of isodose curves (Boyer *et al* 1992b; Huq *et al* 1995).

2.2.2. Intensity modulated radiation therapy

Intensity Modulated Radiation Therapy (IMRT) uses the variation of radiation fluencies in different parts of the tumour using segmented radiation fields shaped by MLCs. In IMRT, the dose delivered to normal tissues, especially when they are highly sensitive to the radiation dose (Organ At Risk (OAR)), can be made small compared to conventional radiotherapy (Webb 2003), even with CRT (Alaei *et al* 2004).

The basic IMRT concept was presented several decades ago. Takahashi *et al* (Takahashi 1965) illustrated some important concepts of three dimensional CRT and IMRT. They planned a dynamic treatment and the first MLC was used in their experiment. In addition, some reports had been published by a group at the Massachusetts Institute of Technology (MIT) about field shaping of the target volume during radiation delivery (Wright *et al* 1959; Proimos 1960). The concept of the protection of an OAR located inside a target volume was also developed by Brahme *et al* (1982) using non-uniform intensity distributions to conform the dose distribution to the planning volume. By using inverse planning, both dose distributions to the PTV and the healthy surrounding tissues can be taken into account (Nutting *et al* 2000). IMRT has generally been divided into several delivery techniques, including segmented IMRT or step-and-shoot IMRT (sIMRT), dynamic or sliding window IMRT (dIMRT) and intensity modulated arc therapy (IMAT). These are discussed in the following sections.

2.2.2.1. Segmented IMRT

Segmented IMRT (sIMRT) is conceptually and technically the simplest type of IMRT. sIMRT is based on the sequential exposure of subfields that are formed by either MLCs or shaped blocks at a constant gantry angle. Using this technique, the radiation field is divided into several subfields or segments and different doses can be delivered to each segment. After irradiation of each subfield, the MLCs start to move to a new position for the next segment. Table 2.1 below shows the sequence of events used to deliver a modulated beam by a sIMRT system.

Several algorithms have been introduced for MLC leaf sequences such as “close in method” and “sliding window”. The former one is the simplest way to deliver the radiation dose desired to the widest segment first, then the second, and consequently to the smaller segments. The sliding window algorithm is a sequence of segments generated by defining the positions of the steps in the quantized distribution (Boyer *et al* 2001a).

The sIMRT is a popular form of IMRT (Boyer *et al* 2001a) and is currently used to treat cancer of the prostate, head and neck, lung, liver, brain and other sites (Nutting *et al* 2000; James *et al* 2004). However, there are many technical and practical challenges in designing segments to produce optimum modulation and in the application of MLCs in linacs as an irregular field restrictor.

Table 2.1. Sequence of dose delivery in a sIMRT adapted from Williams (2003).

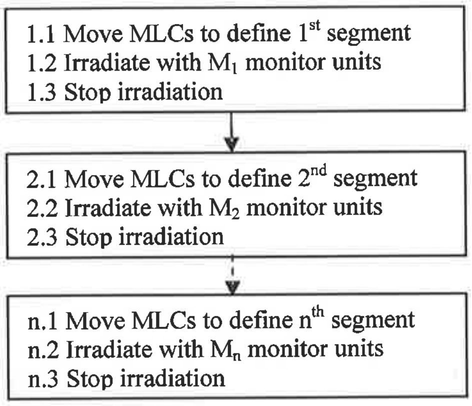

1.1 Move MLCs to define 1st segment
1.2 Irradiate with M_1 monitor units
1.3 Stop irradiation

2.1 Move MLCs to define 2nd segment
2.2 Irradiate with M_2 monitor units
2.3 Stop irradiation

n.1 Move MLCs to define nth segment
n.2 Irradiate with M_n monitor units
n.3 Stop irradiation

2.2.2.2. Dynamic IMRT

Dynamic IMRT (dIMRT), implemented for clinical use for the first time at the Memorial Sloan-Kettering Cancer Centre in New York (Boyer *et al* 2001a), is based on continuous irradiation during MLCs movement according to pre-calculated trajectories designed to deliver the required radiation dose modulation. Dynamic delivery is defined as an extension of segmented delivery where radiation dose delivery can be performed without interruption between segments. At the start point of irradiation the first point of the radiation field is positioned between the leaves and is exposed during the passage of left leaf. In this technique, both MLC leaf banks move in the same direction. The principle of dIMRT with a sliding window technique is outlined in Table 2.2.

Table 2.2. Sequence of dose delivery in dIMRT adapted from Williams (2003).

1. Movement of MLCs to the 1st control point
1.1. Irradiation with M_1 monitor units during movement of MLCs to 2nd control point

↓

2. Irradiation with M_2 monitor units during movement of MLCs to 3rd control point
⇓

↓

n. Irradiation with M_n monitor units during movement of MLCs to (n+1)th control point

2.2.2.3. Intensity modulated arc therapy

Intensity Modulated Arc Therapy (IMAT) is the combination of intensity modulation and rotational therapy. In this case, a dynamic beam modulation is used to accompany the gantry rotation around the patient during radiation delivery. In each treatment arc, the shape of the radiation field continuously changes during gantry rotation. This technique is well suited for concave tumours wrapped around a large organ at risk (OAR), especially when there is a narrow margin between the target and the OAR. IMAT deliveries require the conversion of the optimized beam intensities at all angles to the deliverable MLC segments. Figure 2.1 demonstrates a five-field IMAT treatment with the specified modulation for each field.

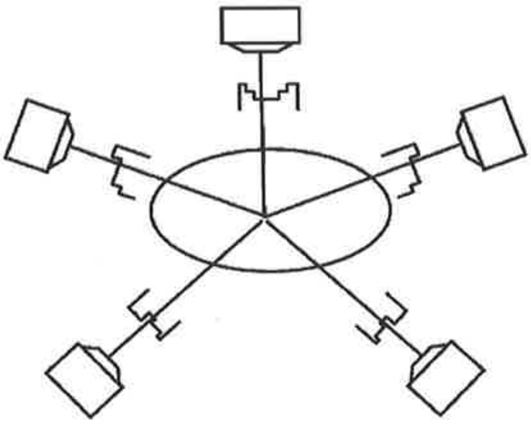

Figure 2.1. IMAT for a five-field plan adapted from Williams (2003).

A particular example of IMAT, called tomotherapy or slice therapy, is an IMRT technique using narrow slit beams (Williams 2003). In IMAT, the radiation beam is restricted to a narrow slit approximately 2 cm × 20 cm. Beamlets with various intensities are created during the gantry rotation. This technique was used for the first time at the Baylor College of Medicine (Boyer *et al* 2001a).

2.2.3. Summary

New radiation therapy techniques, like IMRT, allow higher dose delivery to target volume achieving improved treatment outcomes. In addition, compared to conventional and conformal radiotherapy, it provides better tumour response and normal tissue control (Teh *et al* 2002; Alaei *et al* 2004; Zietman *et al* 2005). However, an inadequate definition of treatment margins leads to higher risk of toxicity to normal tissues, or reduction in disease control.

2.3. Dosimetry in radiation therapy

An accuracy of ± 5% on the dose delivery to a target volume in a patient was recommended in the International Commission on Radiation Units and measurements (ICRU) report no. 24 (ICRU 1976). Several reports have emphasized that the overall precision in the target volume dose must not exceed ± 5% and 1.5 standard deviation (Goitein 1983; Dutreix 1984). In particular, based on the relative dose effects on tumour control and normal tissue damage, a requirement was proposed to combine random and systematic uncertainty in the absorbed dose delivery of 3.5% (1SD) (Mijnheer *et al* 1987). The contribution of dosimeter uncertainty is reported to be within 2% for shaped and blocked fields (Fraass *et al* 1998). In order to ensure that the prescribed dose is delivered precisely, accurate devices are required to measure the delivered radiation dose.

The dosimetry procedures used in radiation therapy can generally be categorized as follows: i) *in vivo* dosimetry, based on the absorbed dose measurements in the Region Of Interest (ROI) of the body, ii) *in vitro* dosimetry, which includes dose measurement in a condition simulated for the human body. The study of human tissues in Petri dish is the most popular technique utilized for *in vitro* dosimetry (Guy *et al* 1999). In contrast, *in vivo* dosimetry is the measurement of dose delivered to a patient during treatment. The first *in vivo* dosimetry was carried out by Rolf Maximilian Sievert, who measured the patients' dose using small ionization chambers in 1932. In another study, a patient, after receiving a therapeutic dose of Iodine-131, swallowed a single crystal of Lithium Fluoride (LiF). The crystal was recovered after passing through the digestive tract and measured to determine the energy absorbed from the radiation (Daniels and Rieman 1956). Because of the limitation of dose measurement inside the patient's body, *in vivo* dosimetry can be carried out either at the entrance, exit surface or in the patient's body cavities.

This section and following sub-sections briefly describe the following: point dosimeters including ionization chamber, TLDs, semiconductor diodes, two-dimensional dosimeters, such as films and Electronic Portal Imaging Devices (EPIDs), and three-dimensional gel dosimeter.

2.3.1. Dosimeters

2.3.1.1. Point dosimeters

Ionizing radiation produces ion pairs, charged molecular electrons and free electrons, when passing through materials by collisions with molecular electrons in its path. In the presence of an electric field, the ionized particles are collected by the opposing electrodes. This is the principle of ionization chamber operation, used widely for radiation dosimetry. Due to a high accuracy of ionization chamber dose measurements (within 1%), they are generally used as gold standard or reference dose measurement devices. However, due to the ion chambers' size, they have been reported as not being suitable detectors when high spatial resolution is required (Bucciolini *et al* 2003).

Although Thermoluminescence Dosimeters (TLDs) for *in vivo* dosimetry were first applied in the early 1950s, they were generally introduced to determine the absorbed dose in a routine manner, which occurred during the 1960s and 1970s. Radiation transmission as ionizing energy can be absorbed by TLD detectors. The absorbed energy in TLD materials is released as light when heated and this emitted light can be detected and analysed by a Photomultiplier (PMT) tube. The amount of emitted light is proportional to the radiation dose delivered to the TLD. The precision of an individual TLD reading has been reported to be within ± 2% (Ruden 1976; Kron 1994; 1995). Although TLDs are generally used for *in vivo* dosimetry, pre-calibration and post-treatment read-outs are very time-consuming. Another disadvantage is that of response fading with the time interval between irradiation and reading.

The use of semiconductor diodes has also been investigated for *in vivo* dosimetry (Gager *et al* 1977; Wright and Gager 1977). Diodes as semiconductors have active areas of 2-3 mm^2 and are usually packaged at the end of a coaxial cable. Ionizing radiation induces an electric current in the diode proportional to the dose rate (~10 pA/cGy/min). High sensitivity to radiation, small size, reasonable stability, absence of external voltage and real-time dose measurement are the main advantages of diodes. Several factors including source to surface distance (SSD), incident radiation angle, temperature, and beam energy should be taken into account when diodes are used for *in vivo* dosimetry (Jornet *et al* 2000). Using this type of dosimeter, like TLD, especially for an entrance dose measurement, also increases the skin dose due to their action as build-up layer (Ruden 1976; Nilsson *et al* 1988).

Other point dosimeters, including diamond (Planskoy 1980) and Metal Oxide Semiconductor Field Effect Transistor (MOSFET) (Sankaran *et al* 1981) detectors, have also been introduced for dosimetric purposes in radiation therapy. Their stability, high spatial resolution, nearly water-equivalent characteristics and linear response for a range of radiation dose delivered, are the main advantages of diamond detectors (Bucciolini *et al* 2003). The dose rate, beam energy and temperature dependency for diamond detectors have been reported to be smaller than that of semiconductor diode detectors. MOSFET detectors have been recently developed for *in vivo* dosimetry (Halvorsen 2005). They are designed to be suitable replacements for TLDs due to their smaller size and for diodes, as fewer correction factors need to be applied.

2.3.2.2. Two-dimensional dosimeters

Films or Electronic Portal Imaging Devices (EPIDs) can be used to determine two-dimensional dose distributions. Basically, two types of films have been mostly used for dosimetric purposes: firstly, radiographic films; X-OMAT V films (XV2 Film, Eastman Kodak Co., Rochester, NY), Agfa (Agfa Structurix D2, Structurix Film Systems, Ridgefield Park, NJ) and Kodak Extended Dose Range (EDR2, Eastman Kodak Co., Rochester, NY); and secondly, radiochromic films (Gafchromic TM). Although the use of Kodak XV2 films has been reported in the literature for verification of the dose distribution in conventional radiotherapy (Fiorino *et al* 1993; Bogaerts *et al* 2000; Bogaerts *et al* 2000) and IMRT (Tsai *et al* 1998; Xing *et al* 1999; Arnfield *et al* 2005), the use of Kodak XV2 film is limited due to response depending on the radiation beam energy. For instance, characteristic curves (Hurter and Driffield [H&D]) of Kodak XV2 film show that the linearity of their response is limited to 80 cGy (Williamson *et al* 1981; Burch *et al* 1997; Robar and Clark 1999; Sykes *et al* 1999; Danciu *et al* 2001; Bos *et al* 2002). In contrast, for EDR2 films the linear range of characteristic curves is extended to 500 cGy. Due to the extension of linearity in characteristic curves and near energy independence, EDR2 films are useful in IMRT dose verification (Dogan *et al* 2002). It has also been reported that EDR2 film is a useful tool for surface and build-up (Dogan and Glasgow 2003) and penumbra region dosimetry (Arnfield *et al* 2005).

Overall, radiographic films suffer from several drawbacks such as: chemical processing (Johnson and Khan 1994; Suchowerska *et al* 1999); scanning (Childress *et al* 2002); and the effect of time delay between irradiation and processing (Childress and Rosen 2004). In addition, the over-response of radiographic films for parallel film positioning relative to the beam axis (Williamson *et al* 1981) requires much effort to correct (Suchowerska *et al* 2001).

Radiochromic films have also been used to verify dose delivery. They do not need to be processed using chemicals and they also have excellent reproducibility and very low energy dependency (Klassen *et al* 1997; Niroomand Rad *et al* 1998; Butson *et al* 2003; Chiu-Tsao *et al* 2005). They are, however, too expensive and the measured data have to be analysed by a dedicated spectrophotometer.

EPIDs have many potential advantages over portal films used in radiation therapy, and these include: real-time image acquisition; ease of use; lack of chemical processing procedure; and consequently, no delay between image acquisition and reading out, and no space to store before and after irradiation. EPIDs are important in this study and therefore the types of EPIDs and their application in radiotherapy are discussed comprehensively in the following sections.

2.3.2.3. Three-dimensional dosimeters

Since the 1950s, Frick and polymer gels have been long considered the most promising development in three-dimensional dosimetry (Day and Stein 1950). Both gels are known to be tissue equivalent and their response has been reported to be independent of radiation quality and dose rate for typical clinical beams (Olsson *et al* 1992). The results of dose delivery to the gels is usually assessed either using Magnetic Resonance Imaging (MRI) or monochromatic light beam spectroscopy. Gel dosimetry is still being researched and its application for clinical purposes is currently slow.

2.4. Electronic Portal Imaging Devices (EPIDs)

Electronic Portal Imaging Devices (EPIDs) are two-dimensional imaging detectors mounted on a linac gantry. The number of EPIDs applied in modern linacs is growing quickly. The Electronic Portal Images (EPIs) acquired are immediately available and they can therefore be used interactively to correct patient set-up or field position during radiotherapy. In addition, the images are in digital format, which assists direct image processing, contrast improvement and image matching. Furthermore, digital archiving saves space and allows for rapid recall of images through a computerized network. The disadvantages of EPIDs are their cost, bulkiness and that they are not available in all radiotherapy departments. Furthermore the image quality still remains a contentious issue (Langmack 2001).

Although the main application of the EPIDs is to verify patient set-up during treatment, they can also be used to determine portal doses and in Quality Assurance (QA) procedures. The exit dose is "the dose measurement at the exit surface of the patient or in the last section of the patient's body with electronic equilibrium," while midplane dose is "the dose distribution delivered to the midline of target volume". They can both be calculated using backprojection from the transmitted dose distributions, measured using two-dimensional dosimeters.

2.4.1. EPID types

Several types of EPID have already been used for research in different institutions (Leong 1986; van Herk and Meertens 1988; Visser *et al* 1990; Morton *et al* 1991; Antonuk *et al* 1992; Evans *et al* 1992; Boyer *et al* 1992a; Heijmen *et al* 1995). This literature review focuses mainly on commercial EPIDs. According to the technology applied, they are classified into three major groups: fluoroscopic, Scanning Liquid Ionization Chamber (SLIC), and amorphous silicon (a-Si) EPIDs. The following sections concentrate on the EPIDs' structure and a brief review of their application in radiation therapy.

2.4.1.1. Fluoroscopic EPIDs

The digital megavoltage fluoroscopy technology, used in the first generation of EPIDs, was developed during the 1980s (Baily *et al* 1980; Leong 1986). The fluoroscopic EPIDs, also called mirror-based video systems, have been reported as the most common EPIDs used for megavoltage imaging until the 1990s (Boyer *et al* 1992a). They basically consist of a metal plate coated with a fluorescent phosphor screen and a video camera with a 45° mirror (see Figure 2.1). The interaction of photons with metal plate generates high-energy electrons and they, consequently, produce fluorescence in the phosphor layer. A small fraction (0.01%) of this light, emitted from the phosphor layer, is collected by the camera lens. The image acquired by the video camera is the raw EPI.

The advantages of fluoroscopic EPID are: firstly, the sensitive area of the EPID is quite large and therefore all photons that have passed through the patient can contribute to the acquired EPI; secondly, the spatial resolution is high due to small pixel size; and thirdly, image acquisition time is very short. Several disadvantages such as long optical path, the sensitivity of mirror set-up systems, and light scatter in the optical path have also been reported (Langmack 2001). In addition, quantum efficiency is low and therefore the produced EPI resolution is poor.

In order to enhance the fluoroscopic EPID response, several modifications to the metal plate (Bissonnette and Munro 1996; Mosleh-Shirazi *et al* 1998), different thickness of fluorescent layer and camera structures were reported (Leong 1986; Visser *et al* 1990; Boyer *et al* 1992a). In recent studies the mirror was replaced by a two-dimensional array of a fibre optic device (Boyer *et al* 1992a; Symonds-Tayler *et al* 1997) introduced as the second generation of fluoroscopic EPIDs, called a fibre optic system (Boyer *et al* 1992a). A 1.5 mm thick copper metal sheet for electron build-up is provided. In this type of fluoroscopic EPID, light produced by the interaction of beam photons with fluorescent layer is the camera input. The fibre optic channels consist of clear polystyrene columns with dimensions of 1.6×1.6 mm^2 and are coated with a thin acrylic cladding. The fibre optic efficiency is determined by input and output diameter, refraction indices, and fibre transmission. The main reported disadvantages are: fibre optic device sensitivity to the radiation, a decrease of light transmission and consequently decrease of device efficiency close to 5% for high dose values (10 kGy) (Boyer *et al* 1992a).

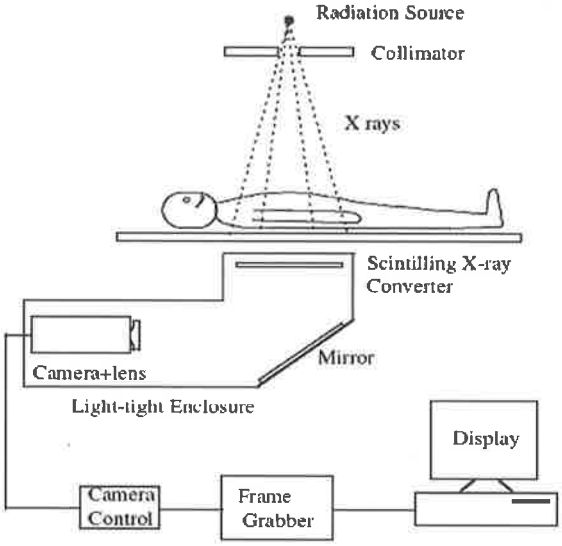

Figure 2.2. Structure of video camera based fluoroscopic EPID adapted from Antonuk (2002).

2.4.1.2. Scanning Liquid Ionization Chamber EPIDs

SLIC-EPIDs represent a special class of EPIDs. They were developed by van Herk and Meertens (1988). Liquid-filled ionization chambers are compact and efficient for high-energy X-ray beam detection. The first generation of this type of EPID consisted of a matrix of 128 × 128 liquid ionization chambers (van Herk and Meertens 1988). The commercial type of SLIC-EPID contains 256 × 256 liquid–filled ion chambers and each chamber is $1.27 \times 1.27 \times 1\ \mathrm{mm}^3$ in size.

The liquid used in the chamber is an organic fluid, Iso-Octane 2-2-4 trimethylpentane (Merck, spectroscopic quality), with a sufficient electron mobility (van Herk 1991). Two important factors in the selection of liquid, which is used as ionized medium, should be considered: integration of charge in the medium and collection of charge from the medium (Boyer *et al* 1992a). The matrix of ion chambers is formed by cross-points of 256 electrode strips on a front Printed Circuit Board (PCB) and 256 strips perpendicular to those on the back PCB. The signal and high-voltage electrodes cross each other perpendicularly and consequently, each crosspoint acts as a small ionization chamber. In matrix ion chambers, developed firstly by van Herk and Meertens (1988), a 1 mm liquid film serves as the ionization medium and a 1 mm thick stainless steel sheet acts as the build-up material. The free electrons are trapped for a few nanoseconds and they produce slow-moving ions.

The entire assembly is enclosed between two foam layers used for mechanical support and electrical shielding. A high voltage is applied to the electrodes of each chamber. One row of 256 ionization chambers is read out every ~20 ms. The polarizing voltage is applied to each row in turn. In order to acquire an EPI, the ionization matrix is scanned either one or two rows at a time (Varian-medical-system 2000; Chang *et al* 2003), using the switching of the high voltage electrodes and measuring ionization current in all 256 columns electrodes forming an image.

The Signal to Noise Ratio (SNR) of a SLIC-EPID has been determined through the modelling approach. The quantum efficiency was found to be about 1% (van Herk 1991). The spatial resolution was found to be either 2.3 mm × 2.9 mm, or 2.3 mm × 4.5 mm depending on the EPI acquisition mode. A variation of noise levels from 0.13% to 0.28% (Boyer *et al* 1992a) has been reported.

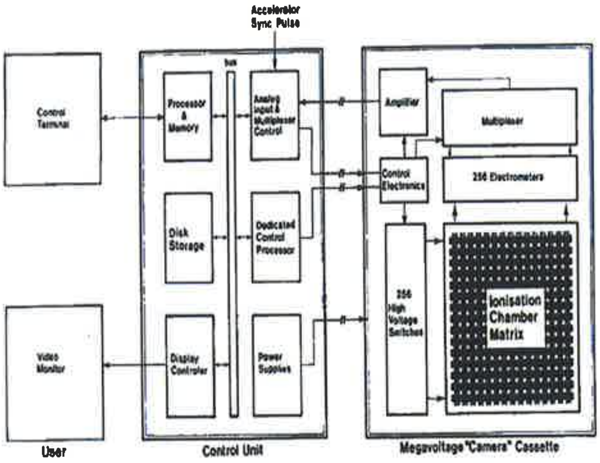

Figure 2.3. Schematic of the scanning liquid ionization chamber system adapted from van Herk and Meertens (1988).

2.4.1.3. Amorphous Silicon EPIDs

A non-optical EPID was developed at John Hopkins University using a scanning linear array of silicon diodes (Taborsky *et al* 1982). In this type of solid-state detector, hydrogenated amorphous silicon photodiodes (a-Si) (Antonuk *et al* 1992) and amorphous selenium photoconductors (Rowlands *et al* 1991), as a silicon alloy, were introduced. Large arrays of a-Si:H transistors, conjunct with the flat panel display and 14" diagonal displays including 1.5 million Field Effect Transistors (FETs) were developed. This type of EPID has a larger surface area and superior resolution compared to the SLIC-EPID. Its radiation sensitive layer consists of 1024 × 1024 pixels with a pitch of 400 μm, resulting in an active area of 40.96 × 40.96 cm^2. Like fluoroscopy camera systems, this imager is located under a metal plate and phosphor screen. This model is a suitable substitute for mirror, light box and light collection devices in mirror-based EPID. Emitted light from the phosphor layer is converted into electron–hole pairs in the silicon layer. Due to the proximity of phosphor layer in a-Si EPID detectors, a high percentage of light emitted (close to 50%) can be converted to the signal compared to the light generation efficiency (within 1%) in fluoroscopy camera and fibre optic systems (Boyer *et al* 1992a). It has been shown that a-Si EPID radiation resistivity is an important advantage for this type of portal imager.

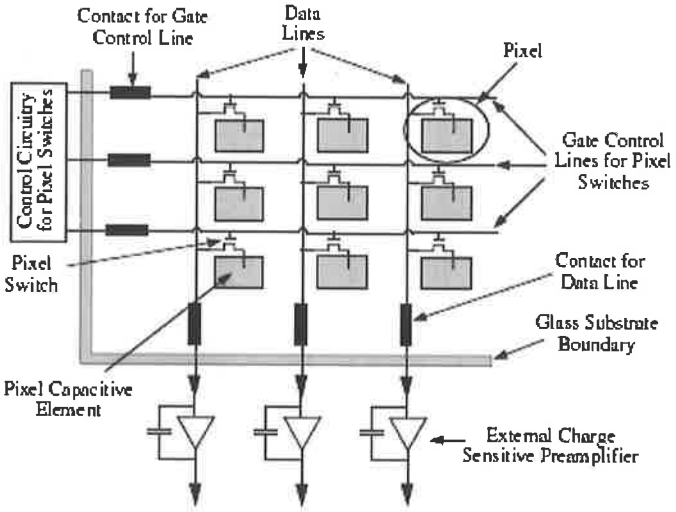

Figure 2.4. Schematic illustration of a corner of a flat panel imaging array used in a-Si EPID adapted from Antonuk (2002).

Compared to other type of EPIDs, although a-Si EPIDs have remarkable advantages such as good resolution and short acquisition time (Greer and Popescu 2003), they suffer significantly from ghosting (McDermott *et al* 2004; Van Esch *et al* 2004; Winkler *et al* 2005). Ghosting is the modification of detector response due to the foregoing irradiations, and the line artefacts in the frames due to the lack of synchronization between the accelerator and the imager.

2.4.2. The application of EPIDs in radiation therapy

EPIDs are generally used in three major areas: geometrical verification, dosimetric verification, and QA measurements. These tasks will be briefly followed in this section.

2.4.2.1. Geometrical verification by EPID

Geometrical verification is a general term including off-line and on-line patient positioning. Patient positioning, i.e. the target volume position with respect to surrounding tissues, during treatment planning and dose delivery, must be the same. However, due to errors in patient set-up, variation of patient anatomy during treatment compared to the corresponding position during planning, set-up verification should be the same. Several imaging devices, such as planar X-ray radiography and Computerised Tomography (CT) scan, are implemented in radiotherapy departments to identify target volume positioning for treatment planning.

The portal image acquired using either film or EPIDs are then used to verify patient positioning during treatment. Film measurements are time consuming due to their processing. In addition, the delay caused by film processing may lead to a change in patient positioning. Patient set-up errors can be reduced using EPID images. The patient positioning can be verified using EPIs and their alignment with those obtained during treatment planning procedure, named Digitally Reconstructed Radiographs (DRRs). However, due to the use of megavoltage beam, EPIs have inferior contrast compared to diagnostic radiographic images acquired using kilovoltage beams.

Several studies have been reported as aiming to increase the accuracy of image matching using EPIDs (Bijhold *et al* 1992; Pouliot and Lirette 1996; Hanley *et al* 1997; Hurkmans *et al* 2001). With online correction, using EPIs, the standard deviation of set-up errors can be reduced by 2 mm (1SD) if an automated image matching procedure is used to compare EPIs with reference images (Van den Heuvel *et al* 1995).

Inter or intra-fraction organ motion is another important factor which affects patient set-up. Several studies have shown that organ motion can be the major error source of dose delivery (Balter *et al* 1995; Kaatee *et al* 2002). Melian and colleagues (1997) showed that prostate can move by 3 cm during treatment course. Kroonwijk *et al* (1998) in a survey of 10 predicted Portal Dose Images (PDIs), for prostate cancer patients, showed that prostate movement is detectable without markers. Other studies have been done using on-line imaging during treatment for geometrical verification purposes. Cone beam (CB)-CT reconstruction using EPIDs, which is usually called megavoltage CBCT (MVCBCT), is a method for comparing diagnostic CT data, known as kilovoltage kVCT, in which treatment planning information is included (Ruchala *et al* 1999; Partridge 2000; Partridge *et al* 2002). The use of ultrasonic images in treatment position for geometrical verification has also been reported (Troccaz *et al* 1993), as has the use of EPID to verify patient positioning in IMRT. Introducing a novel method, Fielding *et al* showed that a fluoroscopic EPID can detect 1 mm of phantom shift, 2 mm of MLC leaf position error and 10% of dose delivery error (Fielding *et al* 2002; 2004).

2.4.2.2. Dosimetric verification by EPID

The use of EPIDs as dosimeters is based on converting the measured EPI pixel values to dose values. Measuring primary fluence and dose distribution, called the "transmitted dose map", can be performed directly using EPIDs by using an appropriate dosimetric calibration method (Parsaei *et al* 1998; Pasma *et al* 1998; Curtin-Savard and Podgorsak 1999; Chang *et al* 2001; Van Esch *et al* 2001; Warkentin *et al* 2003; Steciw *et al* 2005). Evaluation of exit and midplane dose distributions has also been reported using transmitted dose measurements (Hansen *et al* 1996; Boellaard *et al* 1997a; van Elmpt *et al* 2005; Wendling *et al* 2006). For instance, the exit dose distributions can be determined using backprojection of transmitted dose measurements. The phantom/patient midplane dose distributions can also be calculated using exit dose measurements.

The first studies that determined the transmitted dose using films were published in the early 1970s (Haus *et al* 1972; Haus and Marks 1976) while the first report using an EPID for dosimetric purposes occurred during the 1980s (Leong 1986; Boyer *et al* 1992a). Most studies that deal with portal dosimetry using EPIDs have generally been performed using three commercial EPID types: firstly the fluoroscopic, CCD camera-based Philips SRI-100 EPID, developed by Philips radiotherapy system and the Daniel den Hoed Cancer Centre (Heijmen *et al* 1995; Pasma *et al* 1998; Vieira *et al* 2003); secondly, SLIC-EPID, developed at the Antoni van Leeuwenhoek Hospital in Amsterdam (van Herk and Meertens 1988; van Herk 1991) accompanied by the Varian PortalVision; and thirdly a-Si EPID, developed by Antonuk and colleagues at the University of Michigan (1992; 2002).

The "dosimetric verification" term includes a number of different types of dose measurements such as: a) commissioning of new devices for dosimetric purposes (James *et al* 2004), b) evaluation of pre-treatment measurements (Van Esch *et al* 2001), c) comparing post-treatment measurements with other measurements or predictions (Nijsten *et al* 2004) and, d) evaluation of real-time dose delivery procedures. However, prior to dosimetric verification, the physical characteristics of EPIDs related to dose measurements must be considered. These will be described briefly in the following sub-sections.

2.4.2.2.1. EPID calibration methods for dosimetric purposes

In order to use an EPID as a two-dimensional dosimeter, several dosimetric calibration methods have been proposed. However, EPID physical characteristics such as reproducibility, satiability and noise level should originally be investigated first.

Camera-based EPIDs have been configured and used for dosimetric purposes. An excellent level of stability was reported for the SRI-100 EPID, which preceded the iView EPID. Pasma *et al* (1998) showed that the short-term reproducibility of a fluoroscopic EPID is less than 0.2% for a 6 MV photon beam. The long-term reproducibility was assessed as being better than 1% over a period of two years (Louwe *et al* 2004). Recently, a cooled CCD camera was incorporated in Theraview fluoroscopic EPID to improve SNR and image quality (Franken *et al* 2004). In order to reduce the high-energy electrons generated inside patient/phantoms, an additional 1 mm stainless steel sheet was placed on the EPID cover (Pasma *et al* 1998). However, due to the scattered photons the quality of acquired EPIs declined.

The response of this type of EPID depends on the manufacturer and supporting electronic systems. Heijmen *et al* (1995) showed that the relationship of measured grey scale values with transmitted dose is linear and independent of the thickness of flat, water-equivalent absorbers. However, a significant relationship between field size and EPID response was reported due to scattering in the optical system. Due to the non-linear electronic systems and difference between EPID and ionization chamber responses, the response of fluoroscopic EPID as a function of transmitted dose measured using an ionization chamber is not linear. However, a reasonably linear relationship between dose response of this EPID type using a software that supports an integrated dose mode and the corresponding transmitted dose measured using silicon diodes was reported (Kirby and Williams 1993; 1995). The characteristic curve, variation of dose response with field size and phantom thickness (energy response) of fluoroscopic EPID were also reported by He *et al* (1999). They showed that recorded pixel values, as grey values of less than 180 have a linear relationship with dose delivered to the EPID sensitive layer. They have an acceptable standard deviation and a decrease in the slope of the response curve was reported with pixel grey values of more than 180.

The crosstalk phenomenon has a major effect on the fluoroscopic EPID response. This originates from an increase in a signal due to light scatter from components of the EPID structure in the CCD chip. The impact of crosstalk effect on portal dosimetry has been noted in several studies (Pasma *et al* 1998; de Boer *et al* 2000). However, the crosstalk is inherently corrected by the field size correction. The non-uniformity of EPI, due to the 45° tilted mirror, is another factor which should be taken into account, if fluoroscopic EPID is used for accurate dosimetry purposes.

The SLIC-EPID was also used for dosimetric purposes. The construction and read-out characteristics of SLIC-EPIDs are more suitable to measure dose rate rather than delivered dose (Essers *et al* 1995; Roback and Gerbi 1995; Zhu *et al* 1995; Boellaard *et al* 1997a). The reproducibility of dose response characteristics for SLIC-EPIDs has also been reported in several studies. Short-term and long-term stabilities are better than 1% over two years for SLIC-EPIDs (Essers *et al* 1995; 1996; Louwe *et al* 2004). The acquired EPI pixel values were reported to be proportional to the square-root of the dose rate at low dose rates (van Herk 1991; Kirby and Williams 1993; Yin *et al* 1994; Essers *et al* 1995; Zhu *et al* 1995; Boellaard *et al* 1996; Parsaei *et al* 1998). An equation was then introduced to describe the relationship between the dose rate $\dot{D}$ and pixel value PV:

$$PV = f(\dot{D}) = a\sqrt{\dot{D}} + b\dot{D}\,, \qquad (2.1)$$

where "*a*" and "*b*" are parameters depending mainly on the linac repetition mode and acquisition time. This relationship can also be described by a power law (Van Esch *et al* 2001).

The variation on SLID-EPID response with the gantry rotation, called bulging effect, is one the most important factors that should be taken into account if the EPID is used for dosimetric purposes (van Herk and Meertens 1988; Van Esch *et al* 2001; Chin *et al* 2003). This variation is due to the gravity force applied to the dielectric liquid and the rigidity of the materials used to minimize flexing of the plates within the image detector (Varian-medical-system 2000).

Dosimetric characteristics of the flat-panel amorphous silicon detector (a-Si EPID) have also been investigated recently (McCurdy *et al* 2001; Grein *et al* 2002; Greer and Popescu 2003; Van Esch *et al* 2004; Winkler *et al* 2005). Good short-term and long-term reproducibilities are stated (Munro and Bouius 1998; Greer and Popescu 2003; Baker *et al* 2005; Winkler *et al* 2005) for different prototypes amorphous silicon EPIDs. The reproducibility for a-Si EPIDs was said to be less than 0.8% (1 SD) over a period of one month (Greer and Popescu 2003). Two prototype amorphous silicon EPIDs (Munro and Bouius 1998; El-Mohri *et al* 1999) as well as a commercial a-Si EPID (aS500) developed by Varian (Grein *et al* 2002; Greer and Popescu 2003) exhibit a highly linear relationship between EPID signal and the dose delivered. However, the variation of EPID response with pulse repetition frequency and dose per pulse is reported (McDermott *et al* 2004). Ghosting (McDermott *et al* 2004; Van Esch *et al* 2004; Winkler *et al* 2005), which arises from variation in the detector response due to foregoing delivered irradiation. Furthermore dead-time in frame acquisition (Greer and Popescu 2003) is reported as the main limitation of a-Si EPIDs for dosimetric tasks.

Several approaches have been reported for EPIDs' calibration for dosimetric purposes. They can be categorized as empirical and mathematical approaches. In an empirical approach, for instance, the relationship between EPI pixel values and ionization chamber dose reading on the central axis is determined. The use of a beam flattening material has been reported for calibration. This method enables removal of the radiation horns and the increased contribution of radiation in off-axis areas (Parsaei *et al* 1998). However, the discrepancy between corresponding dose values measured using a SLIC-EPID and an ion chamber increases with a radiation field size in the off-axis areas. Because of the existence of independent subfields in off-axis areas, the use of this approach is not also well suited for IMRT verification.

In the second practical approach, based on the measurement of equivalent EPID phantom-scatter factors, a SLIC-EPID was calibrated for dose measurements by using EPI pixel values and ionization chamber measurements for a range of field sizes (Chang *et al* 2001). However, the use of a single phantom scatter factor for all points in a radiation field decreases the accuracy of measurements. Although this method can be used for conventional radiotherapy techniques, due to the variation of EPID pixel values and ionization chamber ratio in off-axis areas, this decreases the accuracy for CRT and sIMRT techniques. In addition, due to the significant variation of SLIC-EPID pixel values with the change of linac repetition rate (Yin *et al* 1994), the calibration method cannot be used for dIMRT. A new dosimetry module in SLIC-EPID was also introduced to convert SLIC-EPID readings to two-dimensional maps of IMRT dose rate in real time. The image acquisition time linearity versus delivered dose was assessed and consequently the delivered dose was calculated using acquisition time and dose rate (Chang *et al* 2000; 2003).

The use of kernel-based convolution algorithm, as a mathematical approach, has been reported to calibrate EPID output for dosimetric purposes for different types of EPIDs. A kernel-based convolution was developed to convert the fluoroscopic EPID pixel values to absolute dose. The transmitted dose measured using camera-based EPIDs compared with ionization chamber measurements in water, was found to be in agreement within 1-2% (1SD) for open, wedged fields and intensity modulated radiation therapy (Pasma *et al* 1998; 1999). This accuracy is reported for the radiation field outside the penumbra region (Pasma *et al* 1999) and large deviations (approximately 10%) were observed in the penumbra region. The algorithm did not take into account the differences in lateral electron transports between water and the metal plate coated with fluorescent layer.

A calibration method for absolute dosimetry for SLIC-EPIDs was developed using a Monte Carlo model to detect a range of beam energies. A 3.8% absolute dose difference was reported between reference calculated and measured doses in the presence of homogeneous water equivalent phantom, concluding that the energy response of this type of EPID has to be taken into account for high precision dosimetry (Keller *et al* 1998). Due to the discrepancy, furthermore, observed in the measurement of dose rate, measured in air and that measured with EPID, a convolution of the EPIs was used to calibrate the SLIC-EPID for dosimetric purposes (Essers *et al* 1996). Results showed that the agreement between Off-Axis-Ratios (OARs) measured using a SLIC-EPID and ionization chamber decreases with the increase of Phantom-Detector Distances (PDD) in the presence of inhomogeneous phantoms.

A two-step kernel-based algorithm was applied, firstly, to predict the scattered energy fluence at the detector plane from portal dose images measured using an a-Si EPID, and secondly, to calculate the dose distribution at the portal detectors. A significant relationship was found between acquired EPI pixel values and optical photons, spread in the phosphor layer of detector, known as “glare phenomenon”. This effect was modelled as a “radially symmetric blurring kernel” and was used to calculate PDIs. In addition, a convolution-based calibration method was developed and then improved using an a-Si EPID for accurate dosimetry verification. The primary fluence map, measured using the a-Si EPID, was convolved using a Monte Carlo (MC)-based kernel to calculate the dose deposition in a homogeneous phantom. The discrepancies within 2.1% were reported for EPID and ion chamber dose measurements for a range of open radiation fields (Warkentin *et al* 2003; Steciw *et al* 2005).

2.4.2.2.2. Pre-treatment assessments

The term "pre-treatment dose verification" is defined as the verification of dose delivery in a phantom prior to the first patient radiotherapy session (Nijsten *et al* 2004). Several studies have been performed using EPIDs for pre-treatment work, especially for IMRT using fluoroscopic, SLIC- and a-Si EPIDs. For example, a pre-treatment verification measurement was performed using the Wellhöfer fast Beam Imaging System (BIS) to obtain a global correlation coefficient by comparing fluence maps (Ma *et al* 1997), concluded that the proposed method can be used for on-line IMRT QA. In addition, pre-treatment monitor unit verification with high accuracy and the verification of geometric parameters can be performed using the same EPI (Nijsten *et al* 2004). Curtin-Savarad and Podgorsak showed that the SLIC-EPID can be used to verify step-and-shoot IMRT fields, but, due to the EPI acquisition procedure, they are not well suited for verifying the dynamic IMRT fields (1999). In contrast, it has also been shown that the fluoroscopic EPIDs can be used to verify pre-treatment IMRT fields produced using dynamic MLCs (Pasma *et al* 1999). The results of absolute dosimetry for static and dynamic IMRT pre-treatment assessment (Cozzi *et al* 2004; Van Esch *et al* 2004), measured using EPIDs, have also been compared with film measurements and TPS calculations.

2.4.2.2.3. Dose delivery verifications

Verification of dose delivered to the patient can also be assessed using portal dose maps, measured using EPIDs. Basically, two methods have been developed to verify the dose delivered to the patient, using transmitted dose distributions. In the first approach, the transmitted dose maps, measured using EPIDs (Huyskens *et al* 1994; Hansen *et al* 1996; Boellaard *et al* 1997a; 1997b; 1998; 1998b), and other two-dimensional dosimeters (Noel *et al* 1995; Weltens *et al* 1998; Broggi *et al* 2002), are backprojected to obtain either the "exit dose" or "midplane dose" maps. The results can be compared with midplane dose distributions, calculated using TPSs. For instance, a method was introduced by Kirby and Williams (1993; 1995) to estimate the on-axis exit dose of a patient using EPIs acquired by a fluoroscopic SRI-100 EPID. However, this method imposes an inherent limitation on accuracy, especially for intensity modulated beams (Heijmen *et al* 1995).

A convolution model was developed to compute "exit dose" from transmitted dose measured using a SLIC-EPID. Due to the convolution of primary dose distribution with a kernel, a large air gap is required to estimate exit dose. The accuracy of this model for computation of the absolute exit dose for homogeneous and inhomogeneous phantoms was reported to be within 2% and 2.5%, respectively (Boellaard *et al* 1997a; 1997b). In addition, a backprojection algorithm was introduced to measure the midplane dose using exit dose values. The results were then compared with corresponding midplane dose measurements (Boellaard *et al* 1998). The method was used to verify midplane dose for larynx, breast, lung and prostate cases. Midplane dose distributions were compared with those calculated using TPS. The agreement between measured and calculated midplane doses were reported to be within 2.0% and 2.5% for larynx and prostate cases, respectively (Boellaard *et al* 1998b). In another related study, the backprojection of EPI pixel values through the planning CT was performed to yield a primary fluence distribution inside the patient for Anterior-Posterior (A-P) beams. The dose distribution was then convolved with dose deposition to measure midplane dose map. The results agreed with film and TLD measurements within 2% for the pelvic region of an anthropomorphic phantom (Hansen *et al* 1996).

With the second approach the transmitted dose maps were compared with those calculated using either TPSs or other similar approaches (Wong *et al* 1990; Ying *et al* 1990; McNutt *et al* 1996a; McNutt *et al* 1996b; Pasma *et al* 1998; Pasma *et al* 1998; Reich *et al* 2006). Several methods have been proposed to develop predicted calculated transmitted dose maps . Introducing a method called the "delta volume method", Wong *et al* (1990) and Ying *et al* (1990) calculated the PDIs using ^{60}Co beams for inhomogeneous phantoms and lung patients. The results were then compared with those measured using film and TLDs. Discarding the penumbra region, the agreement between calculated and measured data was found to be within 2.8% and 9.9% for anthropomorphic Rando phantoms and lung cancer cases, respectively. McNutt *et al* (1996a) argued that the "delta volume method" is not well suited for set ups with large air gaps between the phantom/patient and the portal imager. They then introduced a convolution/superposition method, based on the Monte Carlo data sets, to predict the transmitted dose distributions through an "extended phantom" including a phantom, an air gap between phantom and imager (up to 22 cm), and a modelled SLIC-EPID. The calculated transmitted dose maps generally agreed with EPID measurements within 4%. Pasma *et al* (1998) developed an algorithm which defined transmission functions for open fields and wedged fields (Pasma *et al* 2002) with the large air gaps (from 30 cm to 50 cm) (Pasma *et al* 1999). Based on the work by Pasma *et al*, a pencil beam scatter kernel was developed by van Elmpt *et al* (2005) to predict PDIs. This model enables the prediction of a PDI with an accuracy within 2% and 3% for symmetric situation situated around isocentre and homogeneous phantoms, respectively.

Several MC simulations have also been performed calculating portal dosimetry such as evaluation of scattered radiation beam contributions to EPIs (Jaffray *et al* 1994; Swindell and Evans 1996), generation of pencil beam kernels (Hansen *et al* 1997; McCurdy and Pistorius 2000), as well as evaluation of EPIDs for image construction and performance (Jaffray *et al* 1995; Kausch *et al* 1999). A Monte Carlo approach was used to simulate a SLIC-EPID for absolute dosimetry using dose spread kernels (Keller *et al* 1998). In other similar studies, a full EGS4-based Monte Carlo simulation of particle transport including a linac head and an a-Si EPID (Siebers *et al* 2004) and SLIC-EPID (Spezi and Lewis 2002) was also developed to predict PDIs. The PDIs, calculated using the Monte Carlo technique, were then compared with those measured by a calibrated EPID for dosimetric purposes. In addition, Chin *et al* (2003) developed a Monte Carlo simulation using BEAMnrc/DOSXYZnrc code to predict PDIs at oblique gantry angles with an accuracy within ± 1 °.

2.4.2.3. Application of EPID to quality assurance

Quality Assurance (QA) refers to a series of tests which must be carried out regularly to ensure that equipment and processes work within specified tolerances. Several studies have shown that some QA procedures performed conventionally using an ion chamber in a water-equivalent phantom, can be achieved using different type of EPIDs: fluoroscopic EPID (Evans *et al* 1995; Pasma *et al* 1999), SLIC-EPID (Roback and Gerbi 1995), and a-Si EPIDs (Menon and Sloboda 2003).

2.4.2.3.1. Radiation beam geometry assessment

Several studies have already shown that EPIs can be used to verify the radiation beam geometry. EPIDs were recognised as a quick and reliable alternative to film for congruence of radiation and light fields (Kirby 1995; Luchka *et al* 1996; Curtin-Savard and Podgorsak 1997; Dunscombe *et al* 1999; Prisciandaro *et al* 2003). Mechanical alignment (Liu *et al* 2000), flatness and symmetry of the radiation beam (Kirby 1995; Liu *et al* 2002), linac mechanical and radiation isocentre (Liu *et al* 2004) can also be assessed using EPIDs. They can also be used to evaluate image displacement and rotation with gantry angle (Kirby 1995). Curtin-Savard and Podgorsak (1997) showed that EPIs can be used to verify field junctions and the centre of collimator rotation, evaluation of the beam penumbra, collimator transmission determination, and compensator verification.

2.4.2.3.2. Evaluation of MLC leaf functioning

Multileaf collimators (MLCs) are the best substitution for lead and Cerrobend blocks due to the small margins (Curtin-Savard and Podgorsak 1999), shorter treatment time (Brewster *et al* 1995; Helyer and Heisig 1995), convenience of use, and a cleaner environment and computer-based control systems. MLC implementation is more complex and therefore a QA procedure is required. Several dosimetric characteristics of the output factors such as depth dose, isodose curves, field sizes effects, penumbra regions, and leaf positioning properties should be considered (Boyer *et al* 1992b; Galvin *et al* 1993; Huq *et al* 1995; Klein *et al* 1995; Palta *et al* 1996; Boyer and Li 1997; Stasi *et al* 1999; Pasquino *et al* 2001; Huq *et al* 2002; Cheng *et al* 2003). Geometric verification of MLC fields, including MLC leaf positioning, displacement, reproducibility of MLC leaf positioning evaluating the characteristics of penumbra region, and evaluation of MLC leaf motion during dynamic IMRT delivery, can also be assessed using EPIDs. This sub-section provides a brief overview of the literature concerning the assessment of MLC fields using EPIDs.

It has been shown that the radiation fields set up using MLCs have different properties compared to those set up using conventional jaws. Due to the EPID's standard calibration to produce flattened response, the radiation MLC fields measured using an amorphous silicon was reported to be slightly larger than those measured using radiographic films for the same conditions (Baker *et al* 2005). Increase in radiation field size causes an increase in undesired radiation dose delivered to the patient. Radiographic film studies showed that approximately 2%-2.5% of incident photons on the MLC leaves are transmitted and an additional 0.5% leakage occurs between the leaves (Galvin *et al* 1993; Huq *et al* 1995; Klein *et al* 1995). The characteristics of the penumbra region of a radiation field, defined as the area within 20%-80% of isodose lines, are reported in several studies using radiographic films (Boyer *et al* 1992b; Palta *et al* 1996; Boyer *et al* 2001b; Butson *et al* 2003). The penumbra region of a radiation field set up using MLCs is slightly wider (1-3 mm) than those set up using conventional collimator jaws (Boyer *et al* 1992b). In several circular, square, and irregular fields for patients with cancer of the head and neck, lung, and pelvis, the field penumbra width for all MLC conventions was found to be approximately 2 mm larger than that of the conventional block (Frazier *et al* 1995). The width of MLC field penumbra measurement using a SLIC-EPID has been reported for limited conditions (Curtin-Savard and Podgorsak 1997).

The correct dose delivery procedure depends on the MLC positioning's accuracy. Evaluation of MLC leaf positioning has been widely reported using radiographic films (Chui *et al* 1996; LoSasso *et al* 2001; Chang *et al* 2004; Sastre-Padro *et al* 2004) and ionization chambers (LoSasso *et al* 1998). A leaf positional error as small as ~ 0.2 mm can be detected using radiographic films. However, as mentioned before, the use of films involved labour-intensive procedures, such as processing, scanning and analysis of films to measure, interpret and quantify the MLC leaf positioning. Moreover, due to the film's misalignment problems (accuracy dependent on the radiation energy and darkroom conditions) it is concluded that it is practically difficult to detect any error less than 0.5 mm using film measurements (Yang and Xing 2004).

Several studies have been performed to evaluate the quantitative verification of MLC leaf positioning using different types of EPIDs including: fluoroscopic (James *et al* 2000; Partridge *et al* 2000; Vieira *et al* 2002), amorphous Silicon (a-Si) (Greer and Popescu 2003; Chang *et al* 2004; Yang and Xing 2004; Baker *et al* 2005) and SLIC-(Eilertsen 1997) EPIDs. The average and the best MLC detection precisions were reported to be 1 and 0.2 mm, respectively, for both fluoroscopic and a-Si EPIDs. For

SLIC-EPID, using single EPI and a one-dimensional Laplacian-of-Gaussian (LoG) edge detection algorithm, the leaf positioning was determined to be ~ 0.1 mm (Eilertsen 1997). Although this method enables the MLC leaf positioning to be detected accurately, its response is in the form of a binary data set.

2.5. Comparison of two-dimensional dose distributions

The QA of developed radiotherapy techniques, such as three-dimensional CRT and IMRT, is becoming more complex compared to conventional radiotherapy. For dosimetric evaluation, generally, a two-dimensional dose verification is required. In the other words, due to extensive use of CRT and IMRT instead of conventional radiotherapy, there is significant interest in verification of delivered dose distributions. The gamma function algorithm is becoming a popular tool to evaluate the agreement between two-dimensional dose distributions. This has been used in several studies that compared the agreement between reference and evaluated two-dimensional dose distributions (Sankaran *et al* 1981; Klassen *et al* 1997; Kausch *et al* 1999; Agazaryan *et al* 2003; Bucciolini *et al* 2004; Cozzi *et al* 2004; Siebers *et al* 2004; Van Esch *et al* 2004; Yudelev *et al* 2004; Sandilos *et al* 2004; Williams and Metcalfe 2006). The following section focuses briefly on the structure of gamma function algorithm and its current developments.

In the QA protocol for TPSs proposed by van Dyk *et al*, (1993) the radiation field is divided into two regions: high dose and low dose gradients. In the low dose gradient regions, the dose values of corresponding points can be compared directly. The difference between measured and calculated dose is then defined as the dose difference. In the high dose gradient regions, a small misalignment of two dose maps leads to large dose differences. In order to evaluate the agreement in the high dose gradient region, a criterion called "Distance To Agreement" (DTA), was introduced as "the distance between a measured data point and the nearest point in the calculated dose distribution with the dose within dose tolerances" (Harms *et al* 1998).

To evaluate the consistency between measured and calculated dose profiles based on van Dyk's idea, a composite analysis was introduced by Harms *et al* (1998). The analysis is based on a binary principle of a simple fail-pass assessment of both DTA and dose difference criteria. Each measured point is investigated to determine whether the dose difference (ΔD_{max}) or DTA (Δd_{max}) exceeds the suggested tolerance criteria of 3% and 3 mm, respectively. In the proposed algorithm, $\Delta\mathrm{D}(\mathbf{r}_m)$ and $\Delta\mathrm{d}(\mathbf{r}_m)$ are the dose difference and the distance of the investigated point $\mathbf{r}_m$ from the point of interest (POI), respectively (see figure 2.5). The Δd_{max} and the DTA were defined by the following functions $\Delta\mathrm{D}(\mathbf{r}_m)$ and $\Delta\mathrm{d}(\mathbf{r}_m)$:

$$\delta_f(\mathbf{r}_m) = 1 \text{ if } |\Delta\mathrm{D}(\mathbf{r}_m)| \le \Delta\mathrm{D}_{max} \text{ OR } \delta_f(\mathbf{r}_m) = 0 \text{ if } |\Delta\mathrm{D}(\mathbf{r}_m)| > \Delta\mathrm{D}_{max} \tag{2.2}$$

and

$$\mathrm{d}_f(\mathbf{r}_m) = 1 \text{ if } |\Delta\mathrm{d}(\mathbf{r}_m)| \le \Delta\mathrm{d}_{max} \text{ OR } \mathrm{d}_f(\mathbf{r}_m) = 0 \text{ if } |\Delta\mathrm{d}(\mathbf{r}_m)| > \Delta\mathrm{d}_{max} \tag{2.3}$$

where ($\mathbf{r}_m$) is the position of investigated dose point ($\mathbf{r}_m = (\mathrm{x}_m, \mathrm{y}_m)$). The composite binary distribution $c(\mathbf{r}_\mathrm{m})$ is then calculated as follows:

$$c(\mathbf{r}_m) = \Delta\mathrm{D}(\mathbf{r}_m) \times \Delta\mathrm{d}(\mathbf{r}_m) \tag{2.4}$$

The dose point that passes both agreement criteria will be attributed $c(\mathbf{r}_m)$ value of 1 and if one of the two criteria fails, the $c(\mathbf{r}_m)$ will be zero. Only the PASS/FAIL information can be obtained using the composite model. This method was further developed by Low *et al* (1998) for the comparison of measured and calculated dose distributions (see also (Low and Dempsey 2003)). Using this model, dose maps can be assessed using a gamma function defined by $\Gamma(\mathbf{r}_\mathrm{e}, \mathbf{r}_\mathrm{r})$ and $\gamma(\mathbf{r}_\mathrm{r})$ as follows:

$$\gamma(\mathbf{r}_\mathrm{r}) = \min[\Gamma(\mathbf{r}_\mathrm{e}, \mathbf{r}_\mathrm{r})]\forall[\mathbf{r}_\mathrm{e}] \tag{2.5}$$

and

$$\Gamma(\mathbf{r}_\mathrm{e}, \mathbf{r}_\mathrm{r}) = \sqrt{\frac{\Delta d^2}{\Delta d^2_{\max}} + \frac{\Delta D^2}{\Delta D^2_{\max}}} \tag{2.6}$$

where

$$\Delta\mathrm{d} = |\mathbf{r}_\mathrm{e} - \mathbf{r}_\mathrm{r}| = (x_e - x_r)^2 + (\vec{y}_e - y_r)^2$$

and,

$$\Delta\mathrm{D} = \mathrm{D}_\mathrm{e}(\mathbf{r}_\mathrm{e}) - \mathrm{D}_\mathrm{r}(\mathbf{r}_\mathrm{r}).$$

where $\mathbf{r}_\mathrm{e}$ and $\mathbf{r}_\mathrm{r}$ are the positions of evaluated and reference points, respectively. The PASS/FAIL criterion can also be extracted as:

$\gamma(\mathbf{r}_r) \leq 1$, two dose maps agree within ΔD_{max} and DTA criteria,
$\gamma(\mathbf{r}_r) > 1$, two dose maps disagree within ΔD_{max} and DTA criteria. (2.7)

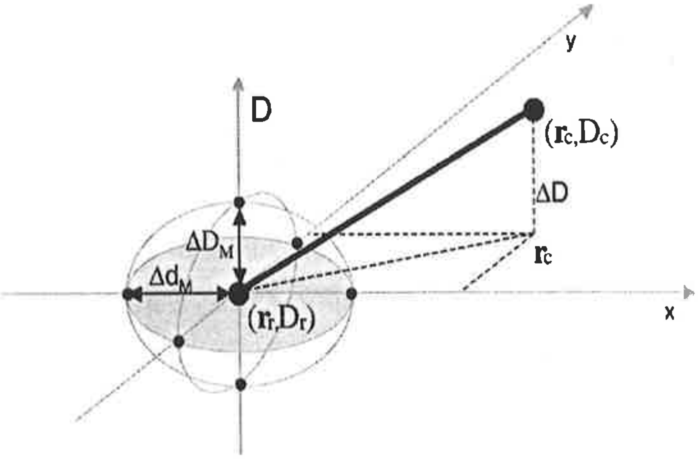

Figure 2.5. Schematic representation of the theoretical concept of the gamma function algorithm adapted from Depuydt *et al* (2002).

The concept of gamma function was developed further by Depuydt *et al* (2002). A filter cascade of multiple levels was introduced to obtain optimized comparison of two dose distributions. A clinically-based two-dimensional quantitative dose evaluation was introduced using new multidimensional dose comparison parameters: normalized agreement test (NAT) values and the NAT index (Childress and Rosen 2003). The original assumptions of the NAT values and NAT index lead to an acceptable level of evaluation, however they are not always valid. In addition, introducing the dose gradient dependent local acceptance thresholds, Bakai *et al* (2003) developed the concept of a gamma function. It takes into account the local dose gradients in a reference distribution for critical appraisal of misalignment in the z direction and collimation errors. Absolute dose differences can also be used in both methods.

2.6. Summary and conclusion

The need for precise determination of the dose delivered to the target is well documented, and high accuracy in the measurements is recommended (ICRU 1976; Brahme 1984; Mijnheer *et al* 1987). Although the accuracy recommended for dosimeters is less than 1.5% (ICRU 1976), the accuracy of two-dimensional dosimetry in previously published studies is within 3-4% for empirical calibration methods (McNutt *et al* 1996a; Parsaei *et al* 1998), and within 2.5% for kernel-based convolution methods (Boellaard *et al* 1997a; Vieira *et al* 2003; Warkentin *et al* 2003). In addition, convolution methods are labour intensive and generally unsuitable for clinical purposes, due to the kernel's reliance on the planning conditions and response of EPIDs (Pasma *et al* 1998). These observations motivated the author of this thesis to develop a simpler calibration procedure for two-dimensional dosimetry verification using a SLIC-EPID. This study investigated the feasibility of a two-dimensional portal dose determination that is accurate, non-labour intensive and suitable for clinical purposes. In order to verify the calibration method, the transmitted dose maps, measured using SLIC-EPID, were also compared with those measured using EDR2 films and those calculated by TPS for a range of homogeneous and inhomogeneous phantoms using the gamma function algorithm (Low *et al* 1998).

Several studies have been performed to evaluate the quantitative verification of MLC leaf positioning using different types of EPIDs: fluoroscopic (James *et al* 2000; Partridge *et al* 2000; Vieira *et al* 2002), amorphous Silicon (a-Si) (Greer and Popescu 2003; Chang *et al* 2004; Yang and Xing 2004; Baker *et al* 2005) and SLIC- (Eilertsen 1997) EPIDs. In addition, due to the use of geometric mode of EPIDs response (based on EPID raw pixel values) in most studies, the relationship between MLC leaf displacement and the variation of dose delivered to the patient must be investigated.

Although several studies have investigated either CRT or IMRT dose verification using EPIDs (Pasma *et al* 1999; Chang *et al* 2000; Depuydt *et al* 2002; Greer and Popescu 2003; Vieira *et al* 2003; Zeidan *et al* 2004; Steciw *et al* 2005; Winkler *et al* 2005), most studies have used either primary radiation fluence or homogeneous attenuators. In addition, most studies have been performed in A-P directions only. To reflect treatment delivery, measurements should be made in the presence of either phantoms or patients and for directions other than A-P. These observations also motivated an investigation of the transmitted dose distributions, measured using a SLIC-EPID, for a typical step-and-shoot prostate IMRT in the presence of an anthropomorphic phantom in A-P direction and oblique gantry angles.

Although the composite model enables identification of the agreeing and disagreeing regions in compared dose maps, the gamma function technique can be used to assess more quantitatively the agreement between two dose distributions. The gamma function does not identify which of the dose distributions has higher dose values, which would provide additional information in the comparison study. The overdosed/underdosed regions (the ratio of reference and evaluated doses at a given point) and the direction of the misalignment can be recognized with the enhanced gamma map convolved by a "Signed Matrix" (see Appendix A).

Chapter 3. Characteristics of a scanning liquid ionization chamber electronic portal imaging device

3.1. Introduction

An evaluation of the EPID's physical characteristics is important if it is to be used for dosimetric purposes. The physical and dosimetric characteristics of a Scanning Liquid Ionization Chamber (SLIC)-EPID were investigated. In the first stage, several experiments were performed to measure the physical characteristics of the Electronic Portal Images (EPIs), including an evaluation of: the additional build-up layer reaching the electronic equilibrium in the EPID detector layer; EPIs' short-term and medium-term reproducibilities; and EPIs noise level. In the second stage, the dosimetric characteristics of the SLIC-EPID including the relationship between EPI pixel values and dose and dose rate, were investigated, depending on the linear accelerator (linac) repetition rate. Variations in the dose measured using a SLIC-EPID with the radiation field size, the EPI dose values dependency on the gantry rotation and the variation of dose values extracted from EPIs with the lag of EPI acquisition time, were also studied.

3.2. Measurement of physical characteristics of SLIC-EPIDs

In this work all measurements were performed using a Varian 600CD linac equipped with the following: a standard 80-leaf Multileaf Collimator (MLC) (Varian Medical Systems, Palo Alto, CA, USA), Enhanced Dynamic Wedges (EDWs) and a SLIC-EPID

(LC250, Varian Oncology Systems, Palo Alto, CA, USA). The linac produces a 6 MV photon beam with repetition rates from 100 to 600 MU/min. Image acquisition was performed using all available repetition rates, with one monitor unit corresponding to a calibrated dose delivery of 1 cGy under reference conditions (Source to Surface Distance (SSD) = 100 cm, with a 10 × 10 cm^2 field at the depth of d_{max}).

The SLIC-EPID, used in this study, contains 256 × 256 detectors. The volume of each liquid ionization chamber and the sensitive area are 1.27 × 1.27 × 1.00 mm^3 and 32.5 × 32.5 cm^2, respectively. A polarizing voltage of 400 V is applied to each row of detectors (Boyer *et al* 1992a). EPI pixel acquisition time is 0.11105 second for a repetition rate of 300 MU/min and varies with linac repetition mode. EPIs were acquired in a fast read-out and full resolution mode (Chang *et al* 2003). Here, two EPIs acquired consecutively were averaged. The resultant image had pixel value standard deviation of less than 1%. The physical characteristics of the SLIC-EPID, used for this work, are shown in Table 3.1. More details are discussed in section 2.4.1.2.

The routine image acquisition and reconstruction process using a dark image (non-irradiated image) and a flood field image (uniform radiation image) was performed by PortalVision 6.1 software (PortalVision system, Varian Inc., Palo Alto, CA, USA) using equation 3.1. Measurements were carried out after the system had been switched on for more than 1 hour to ensure that the SLIC-EPID is in thermal equilibrium. All pixel value matrices, acquired from DICOM EPIs, were analysed using MATLAB software (MATLAB 7, MathWorks Inc, Natick, MA, USA). The EPID pixel values are determined as follows:

$$P_{(i,j)} = \frac{[P_a(i,j)-\varphi_a]-[P_0(i,j)-\varphi_0]}{[P_f(i,j)-\varphi_f]-[P_0(i,j)-\varphi_0]} \frac{\sum_{i=1}^{m}\sum_{j=1}^{n}\{[P_f(i,j)-\varphi_f]-[P_0(i,j)-\varphi_0]}{m\times n} \qquad (3.1)$$

where P_a, P_0 and P_f correspond to the measured, background (no-radiation image) and flood field (uniform irradiation image) pixel values, respectively. Φ_a, Φ_f and Φ_0 are electrometer offsets for each image acquired prior to the activation of High Voltage (HV) line. m and n are the numbers of rows and columns, respectively. i and j specify pixel location (i = 1, …… m and j = 1, …, n). The average background pixel value, when no radiation occurs on the EPID, was found to be 0.0078 for a 10 × 10 matrix on the central axis.

Table 3.1. The physical operating characteristics of the Varian 600CD linear accelerator and the SLIC-EPID used in this study.

Beam Energy	6 MV
Used repetition rates	100, 200, 300, 400, 500 and 600 MU/min
Source to EPID Distance (SED)	110, 115, 120, 125, 130, 135, 140, 150 and 160 cm
Matrix type	Full resolution
Frame averages	1
First Raw wait time	10 ms
Synchronization delay	2000 µs
Read-out mode	Fast
Start delay	500 ms
Acquisition mode	Standard

3.2.1. Investigation of the extra build-up layer

In order to achieve electronic equilibrium in the EPID sensitive layer, an additional build-up layer is required (Boellaard *et al* 1996; Essers *et al* 1996; Van Esch *et al* 2001; Greer and Popescu 2003; McDermott *et al* 2004). The thickness of extra build-up layer depends on the incident photon energy, EPID cover and physical protector, EPI acquisition settings, and supporting electronics. A significant deviation between measured and calculated dose values (up to 16%) in the absence of an extra build-up layer was reported (Boellaard *et al* 1996; Parsaei *et al* 1998). This was also investigated in the current work. In order to do this, RW3 sheets ($\rho = 1.045$ g/cm^3, PTW Freiburg, Germany) of thicknesses varying from 1 mm to 30 mm with a surface area of 30 × 30 cm^2 were placed on top of the EPID cover. A field size of 21.5 × 21.5 cm^2 at Source to EPID Distance (SED) = 140 cm was set up to cover the maximum surface of RW3 layer. A dose rate of 300 MU/min was used. Due to the dependency of build-up layer on the beam energy and the variation of beam profile in the off-axis areas, the thickness of extra build-up layer on the central axis and at 8 off-axis points was investigated. In order to do this, nine 10 × 10 pixel matrices were selected as shown in Figure 3.1 and the pixel values in each matrix were averaged. The area represented by this pixel matrix is 1.78 × 1.78 cm^2 at the EPID sensitive layer. This array size was chosen to minimize statistical fluctuations in pixel response with sufficient spatial resolution.

The variation of SLIC-EPID pixel values with the additional build-up layer for 9 points within a uniform radiation field is shown in Figure 3.2. The x and y axes represent the thickness of extra build-up layer and EPID pixel values, respectively. A small increase in pixel values was observed with an increase of build-up thickness from zero to 5 mm and a continuous decrease in pixel values was then observed for RW3 thicknesses greater than 5 mm. Five millimetres of RW3 material was found to increase the pixel values to the maximum possible value, thus producing the electronic equilibrium in the detector layer. No significant variation was observed between the optimal thickness of build-up layer required to reach the maximum pixel values for the central axis and other eight peripheral points.

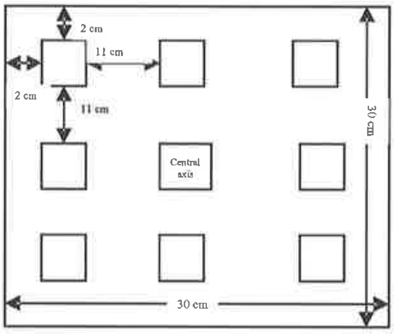

Figure 3.1. The position of the 9 matrices selected for investigating physical characteristics of the SLIC-EPID.

The electric current through the SLIC-EPID ion chambers (registered as pixel values) depends significantly on the number of free electrons reaching the EPID detector layer. When the electronic equilibrium is achieved, maximum pixel values are obtained. The thickness of the extra build-up layer, required to reach electronic equilibrium, depends on the energy of the incident photons, additional layers used in the SLIC-EPID structure and the supporting electronics. As the average energy of the radiation increases, the thickness of the build-up layer must be increased (Khan 1993). SLIC-EPIDs are produced with a thin build-up layer, made of stainless steel, approximately equivalent to 1 cm of solid water. To achieve electronic equilibrium in the sensitive layer for 6 MV or higher energies an additional build-up layer must be added. For instance, 8 and 28 mm polystyrene additional build-up layer is reported as reaching the electronic equilibrium for 6 MV and 25 MV photon beams, respectively (Boellaard *et al* 1996). However, as the extra build-up layer is required for dosimetric purposes, possible deterioration of the image quality must be tolerated. For a 6 MV photon beam, a 5 mm RW3 as additional build-up layer was found to be appropriate and used for all EPID measurements.

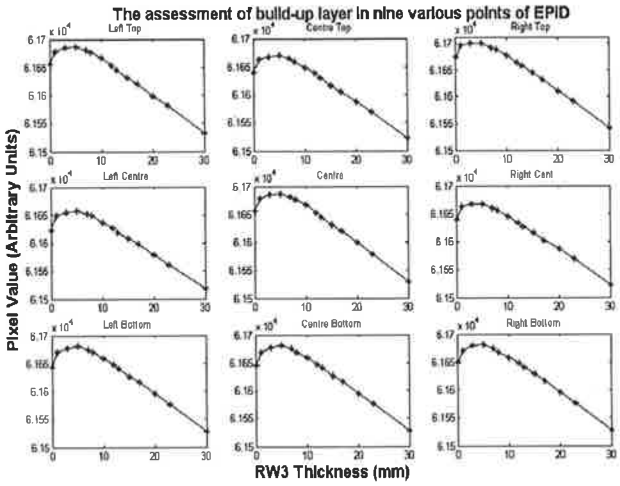

Figure 3.2. The variation of EPID pixel values with the extra build-up layer thickness.

3.2.2. Reproducibility of electronic portal images

Reproducibility is defined as the variation in average readings obtained from two or more measurements of the same parameters using the same technique at different times. The reproducibility of dose response characteristics must be well understood if EPIDs are to be used for dose verification purposes. The reproducibility of an EPID image can be affected by several factors such as detector type and ambient temperature, warm-up time, source to detector distance, and image acquisition settings (Varian-medical-system 2000; Louwe *et al* 2004). Despite the increase in the use of EPIDs for dosimetric purposes in recent years, only a few studies have investigated the short-term and long-term reproducibility (Essers *et al* 1995; Boellaard *et al* 1996; Louwe *et al* 2004).

SLIC-EPIDs are routinely calibrated to produce uniform EPIs using manufacturer designed calibrated procedure. As a result, several corrections such as data filtration, linear, and linear fix corrections are used in image acquisition processing, applied in the PortalVision software, to achieve an acceptably uniform image (Varian-medical-system 2000). Due to the variation in radiation beam spectrum in regards to distance from the central axis, these corrections affect the EPI pixel values.

In order to investigate the short-term reproducibility of EPIs, 10 consecutive images were acquired for a field size of 24 × 24 cm^2 and Source to EPID Distance (SED) = 130 cm, and repetition rate of 300 MU/min. For medium-term reproducibility, the experiment was then repeated every second day over a fortnight. The first image acquisition procedure was performed following a standard EPID calibration and no subsequent calibration was performed prior to the subsequent acquisitions. The acquired EPI pixel values were then evaluated in 9 points within the irradiated area by selecting and averaging a 10 × 10 pixel matrix at each point (see Figure 3.1). The EPIs were analysed to find the values of mean, median, maximum, minimum as well as standard deviation for each POI. The relative error was calculated as the ratio of maximum-minimum differences and mean pixel values in each selected POI multiplied by 100. The mean pixel values and the corresponding standard deviations are shown in Table 3.2.

Table 3.2. The mean pixel values and the corresponding standard deviations for 7 series of 10 consecutive acquired EPIs on the central axis.

Image No.	Date of Assessment						
	23 Feb	25 Feb	27 Feb	1 Mar	3 Mar	5 Mar	8 Mar
1	4198 ± 11	4156 ± 11	4134 ± 12	4150 ± 9	4136 ± 11	4141 ± 11	4154 ± 10
2	4200 ± 10	4154 ± 10	4137 ± 10	4149 ± 11	4138 ± 11	4140 ± 9	4159 ± 10
3	4199 ± 11	4169 ± 9	4149 ± 12	4152 ± 10	4152 ± 10	4144 ± 10	4160 ± 11
4	4212 ± 11	4171 ± 10	4152 ± 11	4166 ± 11	4154 ± 10	4144 ± 10	4176 ± 10
5	4214 ± 10	4172 ± 11	4152 ± 11	4165 ± 11	4153 ± 11	4154 ± 10	4175 ± 10
6	4211 ± 10	4172 ± 11	4149 ± 10	4162 ± 11	4153 ± 11	4153 ± 12	4178 ± 10
7	4217 ± 10	4173 ± 11	4150 ± 10	4162 ± 10	4168 ± 11	4157 ± 10	4177 ± 11
8	4209 ± 12	4172 ± 11	4152 ± 11	4164 ± 11	4170 ± 12	4155 ± 9	4177 ± 10
9	4213 ± 11	4172 ± 10	4152 ± 11	4164 ± 10	4168 ± 8	4155 ± 9	4178 ± 9
10	4213 ± 11	4183 ± 11	4150 ± 10	4134 ± 9	4169 ± 12	4157 ± 10	4178 ± 12
Mean	**4209 ± 11**	**4169 ± 11**	**4148 ± 11**	**4157 ± 10**	**4156 ± 11**	**4150 ± 11**	**4170 ± 10**

For assessing short-term and medium-term reproducibility the average pixel values in a 10 × 10 matrix on the central axis are shown in Figure 3.3 (a) and 3.3 (b), respectively. As Figure 3.3 shows, no systematic variations were observed between mean, maximum and minimum pixel values acquired during the study. The average pixel value was observed to be 4163. The maximum and minimum acquired pixel values were found to be 4213 and 4136, respectively. The relative error and average standard deviation were 0.8 % and 10.7, respectively.

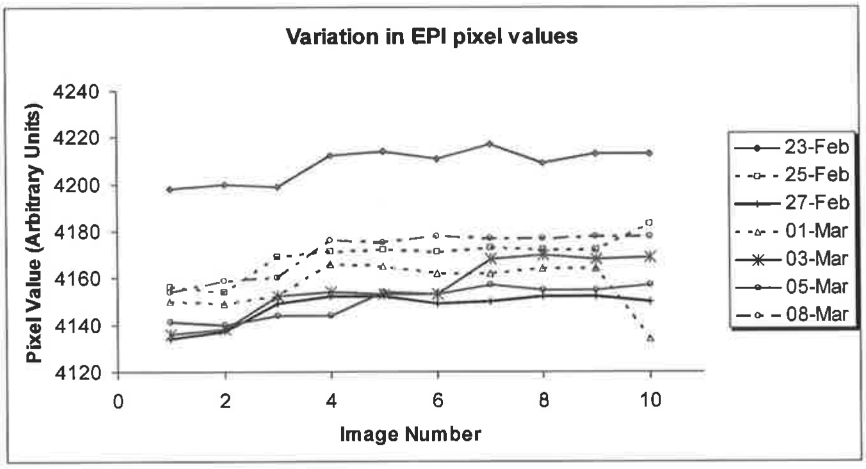

(a)

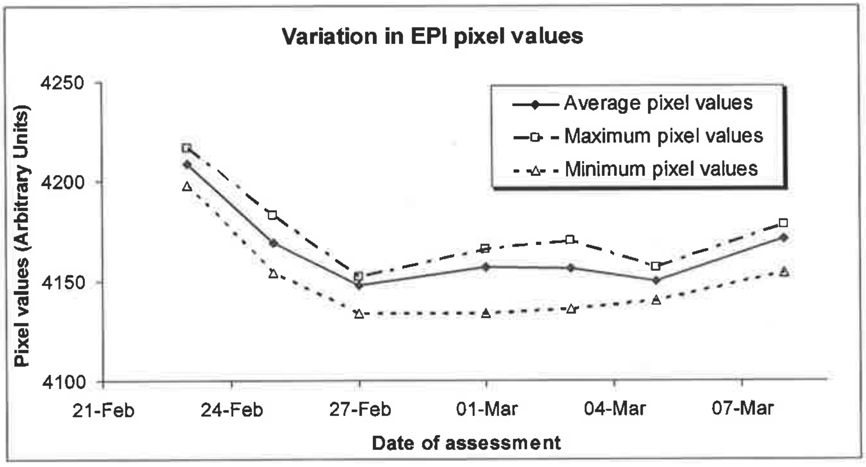

(b)

Figure 3.3. (a) The variation of EPI pixel values with time acquired in 7 series of 10 consecutive images. (b) The variation of average pixel values of 10 consecutive EPID images on the central axis with time that has elapsed from standard calibration of the EPID.

The mean pixel values for a 10 × 10 matrix, acquired during the study, are shown in Figure 3.3. The average relative error was found to be 0.3%, while the maximum relative error observed was 0.4% during the study. The results showed that both short-term and medium-term reproducibility is less than 1% and were found to be consistent with data reported in other studies (Essers *et al* 1995; Boellaard *et al* 1996; Louwe *et al* 2004). The consistency between reported reproducibility data and the findings here show that it is not necessary to perform daily calibration procedures of a SLIC-EPID for dosimetric purposes.

3.2.3. Noise level measurement

The quality of an image can be defined in terms of image noise, which limits low contrast resolution and spatial resolution. In conventional radiography, greater attenuation in thicker patients/absorbers and the increase of scattered photons mean that fewer primary photons are available to construct the image, resulting in an increase in the noise level.

In order to determine the noise level in EPID images, 10 consecutive EPIs were acquired for a nominal 24 × 24 cm^2 field size at SED = 130 cm (maximum achievable field size for a given SED). Five millimetres additional build-up layer was placed on the EPID cover for all measurements. The measurement was repeated every two days over a fortnight. The variation in EPI pixel values was obtained over a uniform image on the central axis for a 25 × 25 pixel matrix (3.17 × 3.17 cm^2). After finding the region of interest (ROI) in the acquired EPI, the noise level of pixel values was calculated as follows:

$$NL = \max\{100 \times \sum_{k=1}^{25} \sum_{l=1}^{25} \left[\sum_{i=-1}^{i=1} \sum_{j=-1}^{j=1} \sqrt{\frac{(PV_{k,l} - PV_{i,j})^2}{PV^2}} \right]\} \tag{3.2}$$

where NL and PV are the noise level and the EPI pixel value, respectively. k and l loop over the number of pixel values in the ROI. i and j loop over the pixels which are adjacent to the pixel under investigation. The measured noise levels and related standard deviations are shown in Figure 3.4.

As Figure 3.4. shows, no systematic variation was observed in noise level for the 7 data sets. The results also show that maximum and minimum noise levels are (1.10 ± 0.07)% and (0.68 ± 0.02)%, respectively. The average noise level and standard deviation obtained from 70 processed EPIs were 0.87% and 0.04, respectively. It can be concluded that the noise level in SLIC-EPID images generally is less than 1% and the data sets acquired can be used for dosimetric purposes.

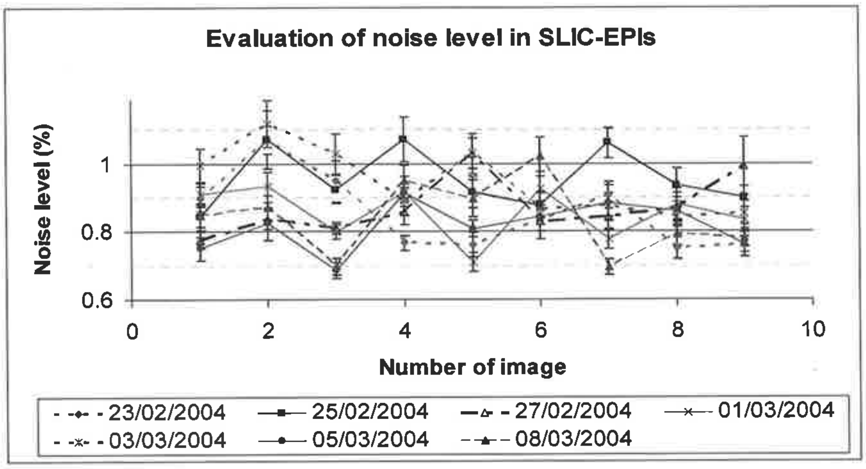

Figure 3.4. Noise variation level in 7 series of SLIC-EPIs.

3.3. Dosimetric characteristics of a SLIC-EPID

Several studies have evaluated the characteristics of the SLIC-EPID for dosimetric purposes, as these depend on the linac and EPI acquisition setting. In this current section, several dosimetric characteristics are investigated: SLIC-EPID response dependency on dose rate and dose, EPID field size response, impact of the gantry angle on EPID response, and the variation in EPID response with that of image acquisition lag.

The possibility of dose measurements using SLIC-EPIDs has been investigated in several studies. The acquired EPI pixel values were reported to be proportional to the square-root of the dose rate at low dose rates (Yin *et al* 1994; Essers *et al* 1995; Zhu *et al* 1995). Due to the many EPI acquisition software systems being used, the relationship between EPI pixel values and dose rate should also be found for each EPID if it is to be used for dosimetric purposes.

3.2.1. Dose rate and dose calculation using a SLIC-EPID

In this part of the study, the feasibility of dose determination using SLIC-EPIDs was investigated. The relationship between EPI pixel values, dose rate and dose was identified for various linac repetition modes. The calculated dose values on the central axis were then compared with data measured using a calibrated ionization chamber. The radiation intensity was varied by moving the EPID to distances of 10, 15, 20, 25, 30, 35, 40, 50 and 60 cm below the calibration point and using a range of possible repetition rate settings (100, 200, 300, 400, 500 and 600 MU/min) for a 10 × 10 cm^2 field size. Two consecutive EPIs were acquired and averaged for each measurement. The averaged EPIs were analysed to find the values of the mean and standard deviation of pixel values on the central axis for 10 × 10 pixels (1.27 × 1.27 cm^2 on the EPID sensitive layer) referred to as the POI. The relative error, defined as the ratio of the standard deviation per mean pixel values calculated from the pixel values in the irradiated field, was found to be less than 1%.

3.2.1.1. Dose rate measurement on the central axis

The relationship between SLIC-EPI pixel values and linac repetition rate rather than true dose rate was investigated. The pixel values of EPIs have arbitrary units. The nominal dose rate delivered to the EPID sensitive layer was calculated using the inverse square law and the nominal linac dose repetition rate. Figure 3.5 shows the variation of average EPI pixel values observed in a 10 × 10 pixel matrix in the centre of the radiation field versus the incident dose rate. A reasonable consistency was observed between data measured for the various repetition rates of 100, 300, 400 and 600 MU/min. A slight increase and a significant decrease were observed with repetition modes 200 and 500 MU/min, respectively.

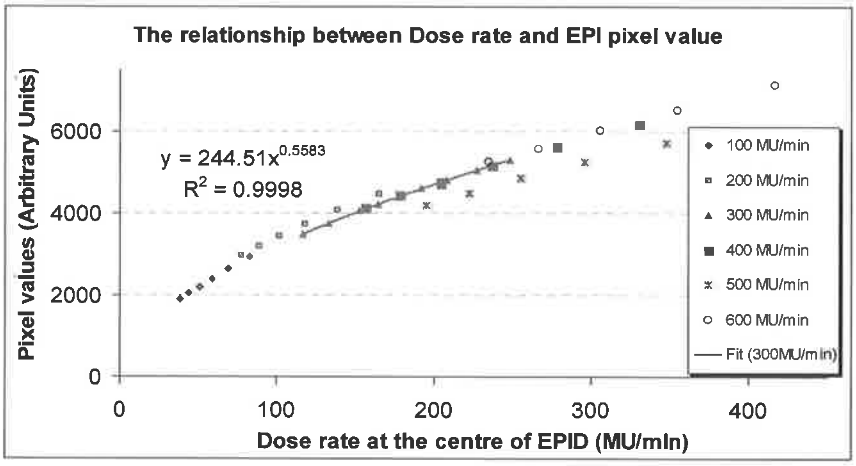

Figure 3.5. The relationship between incident dose rate and SLIC-EPI pixel values on the central axis for various linac repetition rates and SEDs.

Equation 3.3 was used to describe the EPI pixel value's dependence on the incident dose rate. All acquired data series from the EPIs were found to obey the following equation:

$$PV = a(\dot{D})^{b} \qquad (3.3)$$

where PV is the EPI pixel value determined using equation 3.3, $\dot{D}$ is the dose rate and a and b are parameters, determined using the fit function in Microsoft Excel. The values of a and b are shown in Table 3.3.

Table 3.3. The values of the parameters *a* and *b* in the equation 3.3 and the R-squared values for each linac repetition rate.

Repetition rate (MU/min)	*a*	*b*	R-squared value
100	221.06	0.5851	0.9999
200	268.22	0.5511	0.9999
300	244.51	0.5583	0.9998
400	270.49	0.5390	0.9998
500	241.43	0.5413	1.0000
600	287.29	0.5317	0.9992

Although several possible factors, such as image resolution, read-out mode, frame averaging, and image acquisition mode were kept constant during the image acquisition (Table 3.1), this part of work has shown that the response of SLIC-EPIDs depends very much on the particular linac settings. The acquired data (Tables 3.2 and 3.3) demonstrate significant differences between the EPI pixel values corresponding to different nominal repetition rate settings, i.e. 100 – 600 MU/min. Therefore, using a single dose calibration curve cannot be recommended. This variation is most likely caused by the synchronisation between EPI acquisition and linac pulse sequencing (Greer 1996; Varian-medical-system 2000). The scanning of the liquid ionization chamber rows is synchronised with the linac pulses, i.e. the radiation must be presented on the imager when a detector row is scanned. This synchronization varies with the repetition rate setting. For some repetition rate settings, e.g. 500 MU/min, not all linac pulses are used for image acquisition. As a result, if the SLIC-EPID is used for dosimetric purposes, serious attention should be given to the selection of the linac and

EPID image acquisition settings. The results of this study suggest that any change in these settings probably requires a new dose rate calibration of the EPID.

3.2.1.2. Dose calculation on the central axis

The relationship between dose delivered to the EPID and the acquired EPI pixel values was assessed. The monitor units delivered to the EPID were corrected for SED relative to the isocentre distance using the inverse square law. The dose delivered to the EPID sensitive layer was calculated by multiplying the acquisition time by the corresponding dose rate. The relationship between EPI mean pixel values on the central axis of the radiation beam and the average dose delivered to the EPID sensitive layer was determined (Figure 3.6). The following equation was then used to calculate dose values using the acquired EPI pixel values:

$$D=a'\,(PV)^{\,b'} \qquad (3.4)$$

where D and PV are the dose delivered to the EPID sensitive layer and the pixel values of the EPI acquired on the central axis, respectively. Table 3.4 shows the values of a' and b' were obtained for different linac repetition rates and corresponding acquisition times.

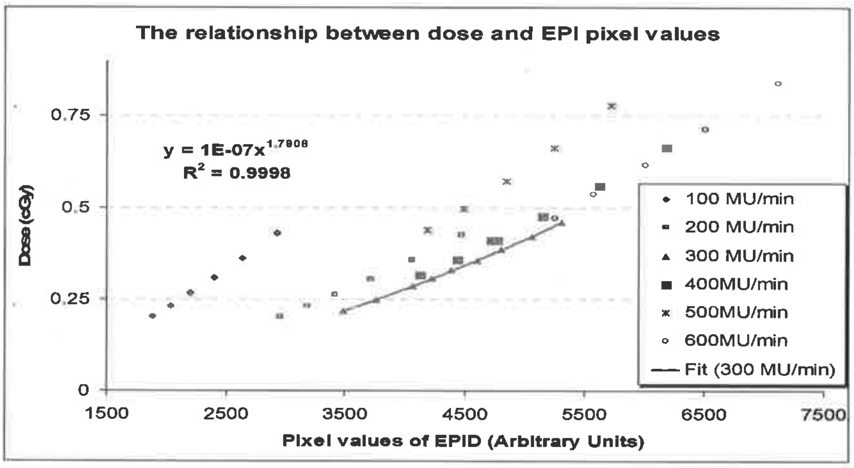

Figure 3.6. The variation of pixel values of SLIC-EPIs as a function of dose values delivered to the EPID.

The EPID dose values calculated on the central axis were verified using a calibrated ion chamber. A typical dose delivery setting, 200 monitor units at the isocentre, was delivered to the ionization chamber for a range of SSDs. The nominal exposure time for the ionization chamber was calculated using the ratio of total monitor units delivered (200 MU) to the linac repetition rate (300 MU/min). The ratio of EPI acquisition time and time of given dose delivered to the ion chamber was calculated. The fractional dose delivered to the ionization chamber for the EPI acquisition time was calculated (Figure 3.7, ion chamber 1).

In order to verify the SLIC-EPID calibration, a second data set was collected using an ionization chamber with different dose (100 MU) delivered at various distances (Figure 3.7, ion chamber 2). Due to the limitation on the EPID acquisition time (0.11105 sec for linac repetition rate of 300 MU/min), the measured and calculated dose values are shown on the central axis for low dose ranges, between 0.2 and 0.8 cGy in Figure 3.7. A good correlation was observed between dose values measured by the ionization chamber and calculated using the SLIC-EPI pixel values. The maximum difference between the measured using ionization chambers and calculated dose values using SLIC-EPID was found to be around 0.4%. Due to the limitation on EPI acquisition time, further investigations must be performed to confirm the results for large and absolute doses (greater than 1 cGy).

Table 3.4. The values of the constants *a'* and *b'* in the equation 3.4 and the R-squared values for each linac repetition rate.

Repetition rate (MU/min)	a'	b'	R-squared value
100	5×10^{-7}	1.709	0.9999
200	1×10^{-7}	1.814	0.9999
300	1×10^{-7}	1.791	0.9998
400	6×10^{-8}	1.853	0.9998
500	9×10^{-8}	1.847	1.0000
600	5×10^{-8}	1.879	0.9992

Although the current image acquisition modality can be used for relative dosimetry, due to the automatic image acquisition time, the integrated acquisition mode should be used, if available, (Kirby and Williams 1995; Chang *et al* 2000; 2003) for absolute dosimetry.

The relative dose can be measured using the software used in the current work (see Table 3.1) with a reasonable accuracy. However, due to the a' and b' dependency on linac repetition rate (equation 3.4), changing the linac repetition mode (especially in dIMRT where the repetition mode changes during treatment) must be taken into consideration.

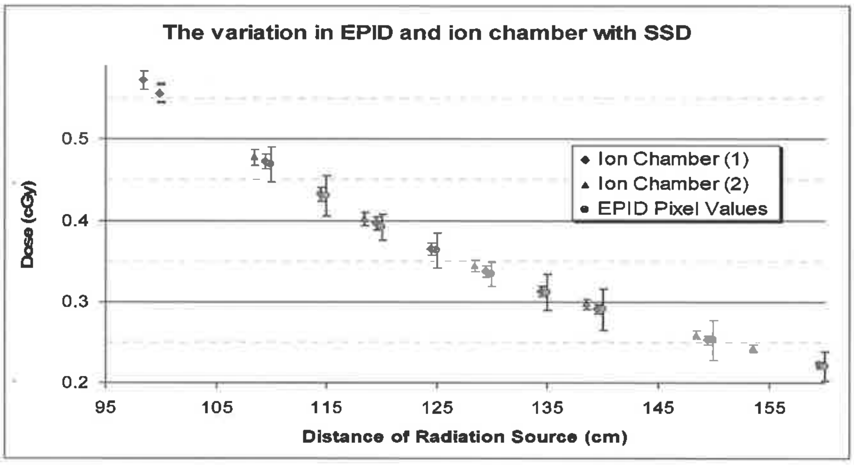

Figure 3.7. The variation in dose obtained by SLIC-EPIs and ionization chamber with SSD.

3.2.2. EPID field size response

When the radiation field is very small, the dose delivered to a point in the radiation field is mostly due to the primary radiation. As the radiation field size increases, the dose delivered to a point will increase because of the increased contribution for scattered radiation. Due to the different achievement to measure the dose delivered to the ionization chamber and EPID, the field size response should also be taken into account if EPID is to be used for dosimetric purposes.

An investigation was carried out on the variation of relative dose obtained from an SLIC-EPID and an ionization chamber versus the size of radiation field. The size of the radiation field varied from 3 × 3 to 24 × 24 cm^2 using square fields. The dose values were measured at the centre of radiation field averaged over 10 × 10 pixels using SLIC-EPID. After normalizing the measured dose values to the dose measured for the 10 × 10 cm^2 field size, the data set was compared with those measured using an ionization chamber acquired under the same conditions. The results are shown in Figure 3.8. The results show that the dose increases rapidly for the EPID and the ionization chamber with the increase of the radiation field size for up to 10 × 10 cm². It was also observed that the ionization chamber dose values increase more rapidly with field size than the EPID dose values for field sizes larger than 10 × 10 cm². The ratio of dose values measured using the SLIC-EPID and ionization chamber was defined for all measured data points. It varied from 1.0004 to 1.0126 for the smallest and largest measured field sizes, respectively.

As Figure 3.8 shows, the EPID output dependency on the radiation field size is different from the ionization chamber output under the same conditions. The difference between the basic performance characteristics of SLIC-EPID and ionization chamber data sets are responsible for the small differences shown in Figure 3.8. In addition, a 1 mm stainless steel, used in the EPID structure as an intrinsic build-up layer, attenuates low energy photons more compared to high energy photons. Therefore, the dose measured using SLIC-EPID is not increased by scattered X-ray radiation as much as the dose measured with the ionization chamber. In conclusion, For EPID absolute dosimetry in the large field sizes, a correction factor for scattering contribution is recommended.

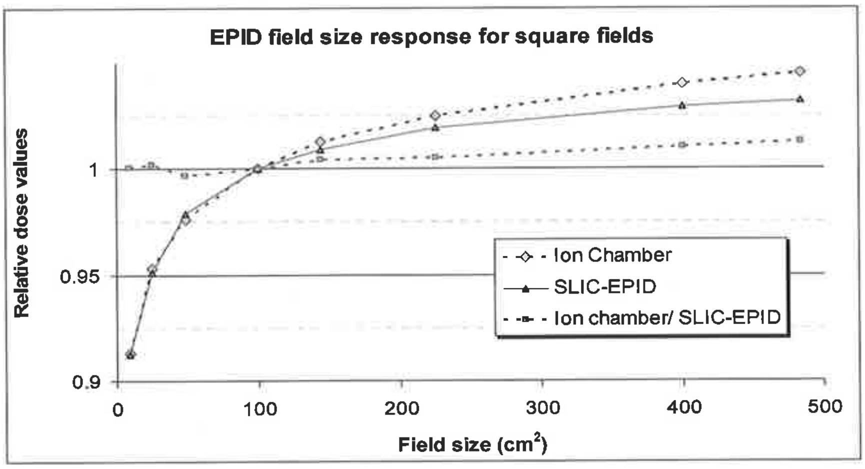

Figure 3.8. Ionization chamber and SLIC-EPID measured dose versus field size. The ratio of ionization chamber and EPID dose values is also shown.

3.2.3. SLIC-EPID response with gantry rotation

The EPIs, acquired using SLIC-EPID, varies with the linac gantry angle (Varian-medical-system 2000; Van Esch *et al* 2001; Chin *et al* 2004). Whereas most studies on portal EPID dosimetry have been performed at a gantry angle of 0°, there is a need for dose verification at non-zero gantry positions due to the use of oblique and lateral beams in radiation therapy.

The variation of EPI pixel values on the central axis and in off-axis regions was evaluated for gantry positions ranging from 0° to 345°. The variation in EPI pixel values on the central axis with gantry rotation is shown in Figure 3.9. A systematic variation of EPI pixel values was observed for a range of gantry positions. The maximum pixel value was observed at a gantry angle of 180°. The dose measured using the SLIC-EPID on the central axis is greater by 2.5% at gantry position of 180° than at 0°. For off-axis areas, the line profiles of EPIs acquired for non-zero degree gantry positions were compared with that acquired for a gantry angle of 0°.

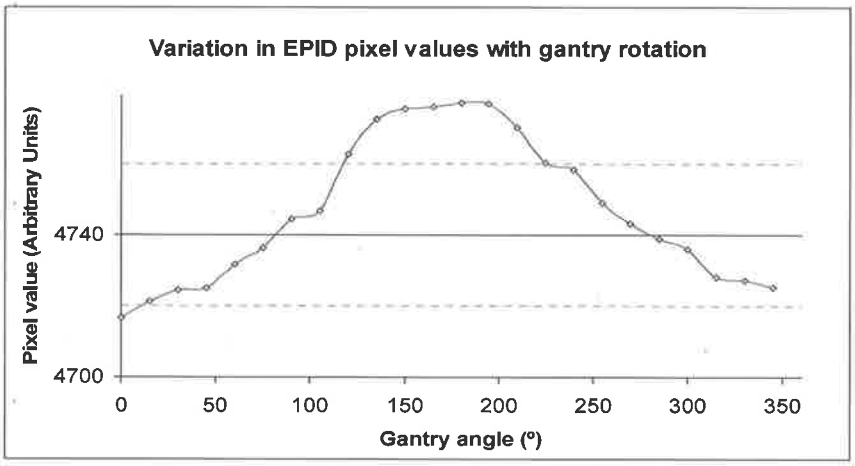

Figure 3.9. The variation in EPI pixel values, measured on the CAX, with the linac gantry rotation.

Due to a systematic variation in EPI pixel values with gantry angle observed for SLIC-EPID response, called “bulging effect”, the method introduced by Van Esch *et al* (2001) was used to remove this effect from the measured EPIs. In order to use this algorithm, several EPIs were acquired for the possible largest radiation field size for 0, 90, 180 and

270° gantry angles. Using the equation proposed, the averages that all EPIs acquired in non-zero degrees were then corrected.

$$FF_{\gamma(i,j)} = \frac{FF_{cal(i,j)}(0^\circ) + FF_{cal(i,j)}(90^\circ) + FF_{cal(i,j)}(180^\circ) + FF_{cal(i,j)}(270^\circ)}{4} + \sin(\gamma).\frac{FF_{cal(i,j)}(90^\circ) - FF_{cal(i,j)}(270^\circ)}{2} \quad (3.5)$$

Where *FF* is an averaged flood field EPI acquired in the given gantry angle and the γ is the gantry angle in which EPI for required to be corrected.

Typical line beam profiles of relative dose measured before and after the correction for the bulging effect and corresponding relative dose difference values are shown in Figure 3.10 (a). A comparison of relative dose difference profiles before and after the correction with a corresponding profile measured at 0° is also shown in Figure 3.10 (b). Although this method corrects well all EPIs acquired at all non-zero gantry angles, several inconsistencies in the penumbra region were observed between line profiles corrected and those measured at 0° gantry position.

For oblique and lateral beam deliveries, rotation of linac gantry is necessary. Ideally, the fluence incident on the EPID should be invariant with gantry angle if attenuation and scattering conditions are kept constant. In practice, however, the acquired SLIC-EPIs vary significantly with gantry angles. The variation of SLIC-EPID response with gantry angle depends on several factors. Firstly, it is caused by the variation in response of the EPID detector layer because the liquid sandwiching by the cassette is not completely rigid and the two plates of the ionization chamber flex as the gantry rotates. This can cause a non-uniform thickness of the liquid film across the EPID matrix. Secondly, to a lesser extent, the variation of linac output with the variation of gantry position (within 2%) may vary the incident fluence reaching the EPID (Varian-medical-system. 2000). Thirdly, imperfect mechanical rigidity of the support arm may cause vertical, longitudinal and lateral shifts of the SLIC-EPID with the respect to the isocentre of up to 1.3 cm. Finally, the variation of EPID position with floor/ceiling at the gantry angles of 0° to 180° varies the amount of scattered radiation reaching the EPID from surrounding materials (Chin *et al* 2004).

In conclusion, the method proposed by van Esch *et al* (2001) enables EPI uniformity to be restored within 2%. All EPIs acquired in this work for oblique and lateral beam deliveries were corrected with the above-mentioned technique.

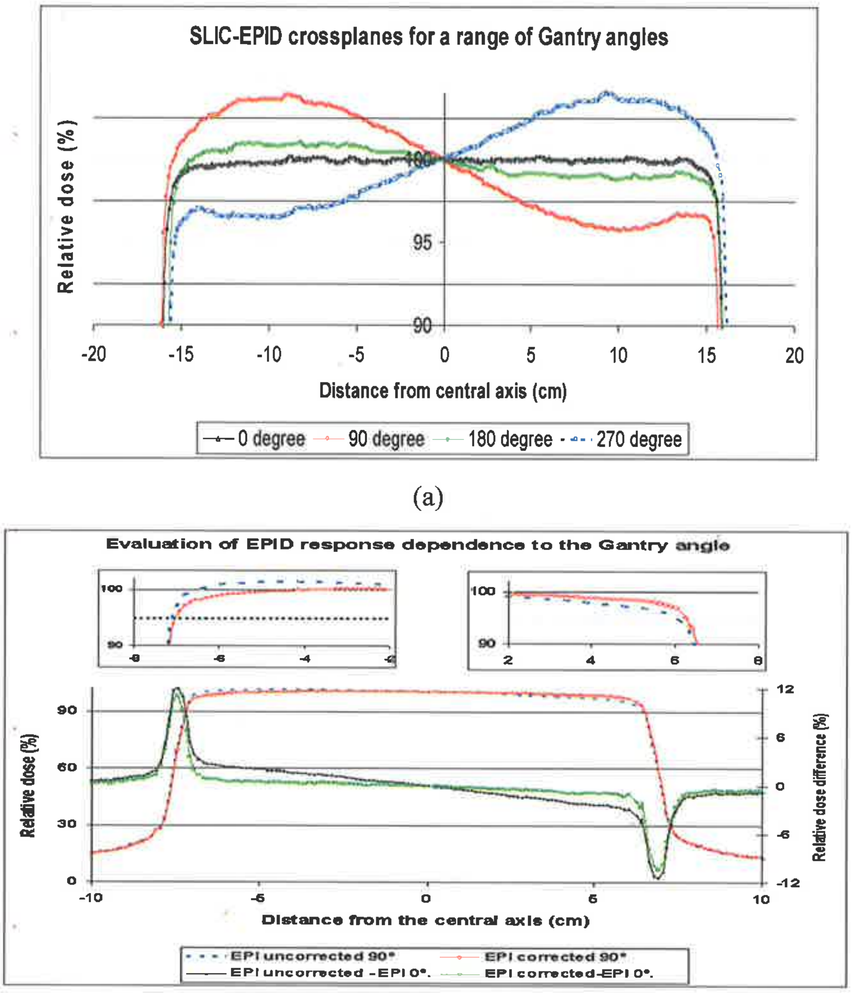

(a)

(b)

Figure 3.10. Crossplane profiles of (a) relative dose for a range of gantry angles. (b) Relative dose profiles for gantry angle of 90° before and after the correction, and the corresponding relative dose difference compared with that acquired at 0° of gantry rotation.

3.2.4. Variation of EPID response with the acquisition time lag

The lag of image acquisition time can be defined as the time interval between two consecutive EPIs. It has been reported as having an effect on dosimetric calibration of SLIC-EPIDs and should also be taken into consideration (Essers *et al* 1995; Curtin-Savard and Podgorsak 1999; Van Esch *et al* 2001). This is an important factor, especially when EPIDs are applied for absolute dosimetry purposes. This factor depends on the EPI acquisition settings.

The variation in portal dose values with the lag of EPI acquisition time was investigated here for a range of rest times between consecutive images from 1 second to 60 seconds. EPIs acquired were converted to dose values and 8 × 8 arrays were chosen as the transmitted dose delivered to the central axis. All EPIs were also normalized to the first image for each series.

The variation of EPI pixel values with the rest time between EPI acquisitions is shown in Figure 3.11. The mean of a 10 × 10 pixel matrix on the central axis was used as EPI pixel value. The first EPI of each series was used as a reference EPI and other EPIs were normalized to the first EPI pixel value. As more images were acquired, a slight increase in EPI pixel values was observed for images acquired with a 1s lag between image acquisitions. The maximum increase of pixel values (1.2%) was observed for the last few images acquired with a 1s gap. No systematic variation was observed for all other series of EPIs acquired for different time lags.

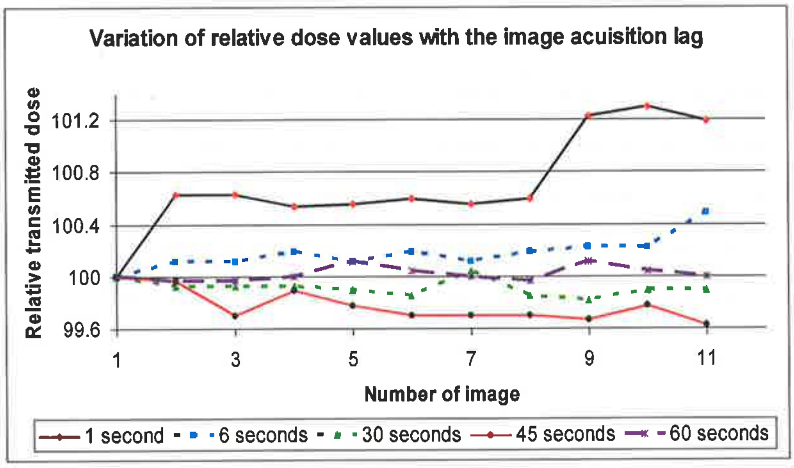

Figure 3.11. Variation of EPI pixel values for five series of 11 SLIC-EPIs acquired with different time lag.

Although in the current work an increase of 1.2 % of EPI pixel values was observed on the central axis of radiation field for a 1 s lag, due to the linac output tolerance (within 1%) and EPI noise level (within 1.0%, see section 3.2.3), it cannot be considered as a significant variation. When compared with the published results (Essers *et al* 1995; Curtin-Savard and Podgorsak 1999), measurements did not confirm previous findings and showed that the EPI reconstruction has been enhanced since then using either better supporting electronics or improved software. The low charge mobility in the iso-octane layer is the main reason for the variation in SLIC-EPID pixel values with variation in time lag between EPI acquisitions.

In this study, in order to control possible systematic errors during image acquisition time, lag times larger than 1 s were used for which no significant change in EPI pixel values was observed.

3.4. An SLIC-EPID as a two-dimensional dosimeter

Due to the standard manufacturer designed EPID calibration procedure aiming to produce uniform EPIs, correction must be made to measure dose in the entire radiation field. In order to do this, the EPID dose values have to be calibrated with another two-dimensional dosimeter. As described in the literature review, point dosimeters, for example ionization chamber, are difficult to use in two-dimensional dosimetry. Radiographic films can be used as two-dimensional dosimeters in radiation therapy. Due to the acceptable response for high dose values and near energy independency compared with other types of radiographic films, EDR2 films were used to calibrate the EPID for dosimetric purposes. However, the EDR2 film had to be calibrated initially.

3.4.1. Comparison of EPID dose values with other two-dimensional dosimeters

Due to the similar response of EDR2 film to the ionization chamber (Zhu *et al* 1995; Dogan *et al* 2002), EDR2 films were used to calibrate the SLIC-EPID as a two-dimensional dosimeter. The films were labelled for correct alignment corresponding to the positions on the EPIs and were then irradiated with a 3.0 Gy dose at d_{max} for a 10 × 10 cm^2 field size at SSD = 100 cm as well as for 20 × 20 cm^2 field sizes with SSDs of 110 and 130 cm. The irradiated films were then processed and scanned using an automatic Agfa Curix160 processor (Agfa-Gevaert NV, Mortsel, Belgium) and Vidar scanner (Vidar Systems Corporation, Herndon, VA, USA), respectively. Non-uniformity of the scanned films, especially in the horizontal axis, was found and corrected using a blank EDR2 film. The line profiles of the EDR2 film were compared with those corresponding to profiles measured with an ionization chamber at d_{max} for SSD = 100 cm. The experiment was repeated using a scanning ionization chamber situated in the water tank scanning system (Wellhöfer Dosimetrie, Scanditronix Medical, Schwarzenbruck, Germany), for the same conditions for SSDs of 110 and 130 cm.

An investigation of the non-irradiated scanned EDR2 film showed that there is a significant non-uniformity (~ 2%) between film pixel values in the horizontal axis of film scanner. The uncorrected and corrected pixel values of the blank EDR2 film are shown in Figure 3.12. No significant response was observed in the vertical axis.

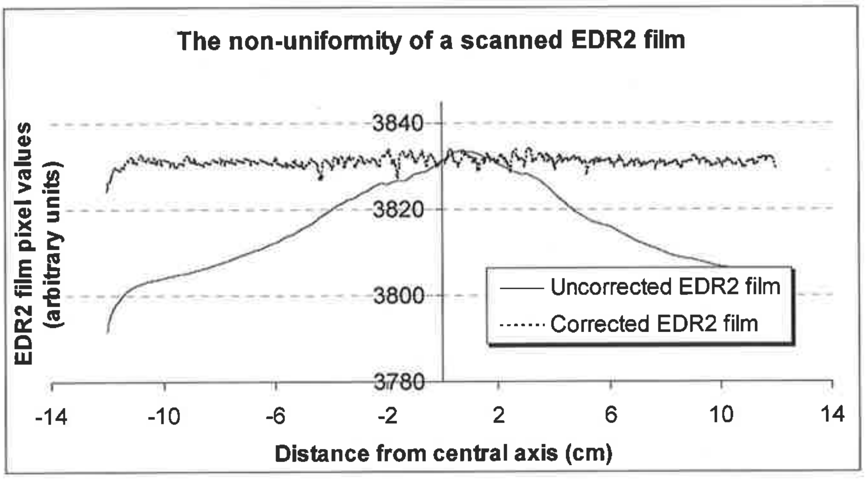

Figure 3.12. Variation in a scanned blank EDR2 film pixel values in the horizontal axis.

The relative inplane and crossplane profiles of the radiation beam were measured using EDR2 film (after correction for non-uniformity), SLIC-EPID and ionization chamber at SED = 110 cm and SED = 130 cm. The corresponding relative dose difference profiles are shown in Figure 3.13. As this figure shows, discarding the edge of the assessed ROIs, no significant differences were observed between the corresponding profiles measured with EDR2 film and ionization chamber at various SEDs (0.6 ± 0.5)% and (0.8 ± 0.5)% at SED = 110 cm and SED = 130 cm, respectively). On the other hand, significant differences of (4.0 ± 1.1)%, (4.0 ± 1.2)%, (4.2 ± 1.1)% and (4.8 ± 1.2)% were observed between EPID and ion chamber profiles and between EPID and EDR2 film profiles at SED = 110 cm and SED = 130 cm, respectively. Figure 3.13 also illustrates that SLIC-EPID dose profiles are significantly different from the ion chamber and EDR2 film profiles. As a result, the SLIC-EPID cannot be used as a reliable two-dimensional dosimeter directly in off-axis areas.

Despite the presence of a soft X-ray spectrum component in the off-axis areas for larger radiation fields, uniform profiles were observed for dose profiles measured using SLIC-EPID. The main reason for this is that the SLIC-EPID is calibrated for imaging purposes so that it produces an equal response for all the liquid ion chambers. In addition, to a lesser extent, the presence of 1 mm stainless steel in front of the EPID sensitive layer (van Herk 1991) acts as a filter that may attenuate the low energy X-rays more in the peripheral areas (due to angular distribution of the x-ray spectrum) than around the central axis, thus reducing the horns of the beam profiles. Due to the radiation beam divergence the path of photons, at the edge of the radiation field, passing through the thickness of 1 mm added filter, will be increased by approximately 3 % in large radiation fields. Consequently, the increase in 0.03 mm steel thickness can attenuate approximately ~ 3% of the intensity of photon for 6 MV (Johns and Cunningham 1983).

The discrepancy, observed in the penumbra region, could be caused by either the misalignment or the different size of pixels of scanned EDR2 film with those obtained from the ionization chamber readings. Due to the small average difference between

EDR2 film and ionization chamber data, it can be said that EDR2 film pixel values agree well with EPID pixel values in the ROI.

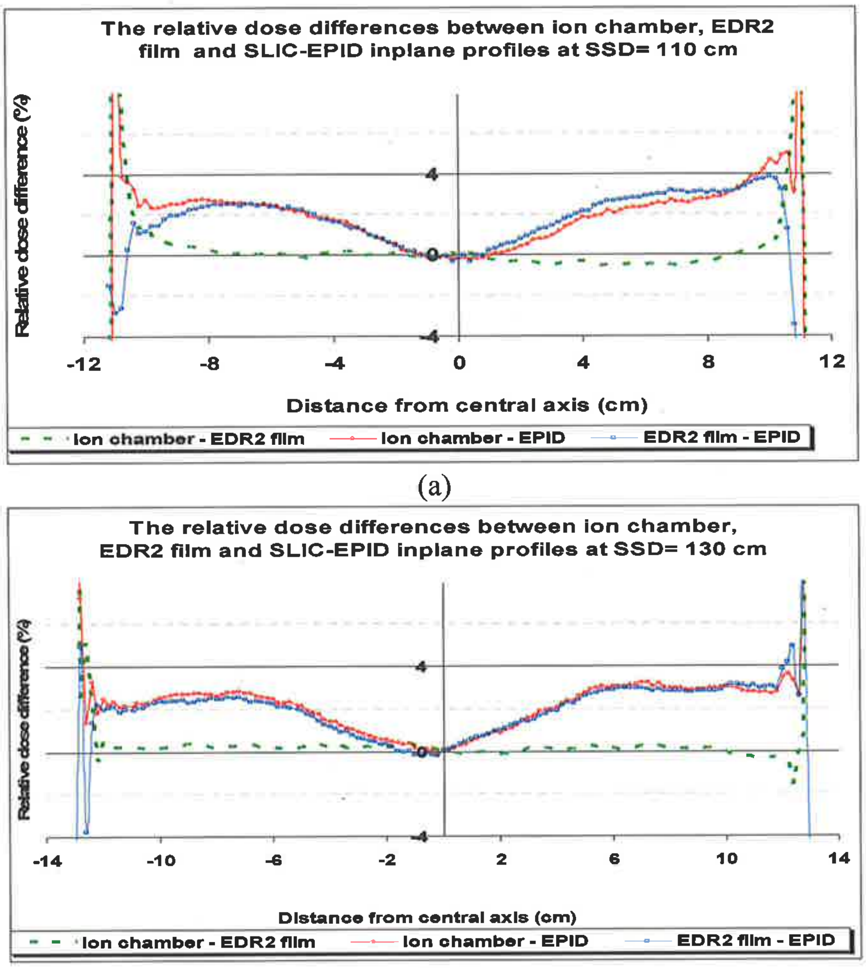

(a)

(b)

Figure 3.13. The relative dose differences between the radiation profiles obtained by ionization chamber, SLIC-EPID and EDR2 film measurements, (a) at SSD = 110 cm for a 20 × 20 cm^2 field size, (b) at SSD = 130 cm a 20 × 20 cm^2 field.

This study indicates that radiographic films are more effective than ionization chamber measurements for two-dimensional EPID calibration. The pixel size of film measurement for the optimum scanning condition (300 dpi) is routinely close to 0.3 mm and it can be improved to 0.05 mm. Although, in general, film dosimetry suffers from energy dependency, the EDR2 film has been found to be nearly energy independent and thus suitable for dosimetric calibration (Esthappan *et al* 2002; Olch 2002; Dogan and Glasgow 2003).

In conclusion, in off-axis areas a significant difference was observed between relative dose profiles measured using SLIC-EPID and other dosimeters. The difference between the dose measured by the EDR2 film and the EPID is a function of distance across the EPID from the central axis. This discrepancy suggests that in order to increase the accuracy of dose delivery measurements, a reliable correction factor for off-axis areas is required if EPID is used as a two-dimensional dosimeter.

3.4.2. Definition and determination of two-dimensional correction factors

SLIC-EPIDs are generally calibrated for imaging purposes so as to produce a uniform pixel response for an open field irradiation of the entire matrix. In order to reinstate the true dose profiles, when measured by a SLIC-EPID, a two-dimensional correction for off-axis areas was developed. Several EPIs were acquired at 10, 30, 40 and 60 cm below the isocentre for 20.2 × 24.7, 17.0 × 21.0, 15.8 × 19.5 and 13.9×17.0 cm^2 nominal radiation field sizes respectively (all have approximately the same area (approximately 22.1×27.2 cm^2) at the EPID detector layer covering the majority of the EPID detector), using linac repetition rate of 300 MU/min. Due to the correlation (within 1%) between EDR2 film and ionization chamber scans obtained with the water tank dosimetry system (Wellhöfer Dosimetrie, Scanditronix Medical, Schwarzenbruck, Germany), the experiment was repeated with EDR2 films in the same conditions using 3 Gy dose delivery at d_{max}. Several images were also acquired using both EPID and EDR2 films at SSD = 130, 140 and 160 using 15°, 30° and 60° wedges, positioned in the inplane direction. The details regarding irradiation in the presence of physical wedges are shown in Table 3.5.

The SLIC-EPID pixel values were converted to dose using a relationship measured as described in section 3.2.1. After the EDR2 film correction for inherent scanner non-uniformity, the Region Of Interest (ROI) for the EDR2 film and EPID dose maps was selected in the measured dose maps surrounded by a 50% isodose line using an in-house code (MATLAB 7, MathWorks Inc, Natick, MA, USA). The data sets of EDR2 films were rescaled to the same pixel size as the ROI for EPIs using bilinear interpolation. Both EPID and EDR2 film dose profiles were then normalized to the dose value on the central axis. A Correction Factor Matrix (CFM) was defined for each SSD in order to relate the two-dimensional EPID relative dose values to the corresponding EDR2 film relative dose values:

$$CFM_{i,j} = \frac{D_{i,j}(EDR2\ \ film)}{D_{i,j}(EPID)} \tag{3.6}$$

where, $D_{i,j}$ $(EDR2\ \ film)$ and $D_{i,j}$ $(EPID)$ are EDR2 film and EPID relative dose values in a pixel i,j respectively. By using CFM, the relative absorbed dose in water at all points of acquired EPIs can be calculated as follows:

$$D_{i,j}\ \ (Corrected\ \ EPID) = D_{i,j}\ \ (Measured\ \ EPID) \times CFM_{i,j} \tag{3.7}$$

The inplane and crossplane profiles of CFMs for different SEDs (110, 130, 140 and 160 cm) for open field and wedged fields are shown in Figures 3.14. The central point of CFMs is 1.00 by definition for all cases. Away from the central region of the ROIs, a significant increase of CFM values was observed in all inplane and crossplane profiles.

Table 3.5. Details of the measurements performed with wedges inserted in the radiation beam.

Physical wedge Angle	SED (cm)	Field size (cm^2)	Dose delivered to EDR2 films (MU)	Repetition mode (MU/min)
15°	130	(17×21)	550	300
	140	(15.8×19.5)	637	300
	160	(13.9×17)	833	300
30°	130	(17×21)	600	300
	140	(15.8×19.5)	695	300
	160	(13.9×17)	908	300
60°	130	(15×21)	800	300
	140	(15×19.5)	927	300
	160	(13.9×17)	1211	300

A symmetrical variation was observed for CFM values with the change of SSDs in the open fields. The inplane profiles of CFMs were found to be more consistent at the large SSDs, compared to those at the short SSDs. Discarding the CFM values in the ROI edges, no significant variation was observed in the shape of inplane profiles with variation in SSD for open fields. In contrast, away from the central axis, a significant difference was observed in the shape of crossplane profiles with the increase of SSD.

For the wedged fields the CFM values in the part of field that correspond to the thinner part of the wedge are smaller than those corresponding to the thicker. A significant variation was observed in the thinner part, compared to open fields at the same SSDs. While the shape of inplane profiles does not vary, in contrast, the shape of crossplane varies the change of SSD. A significant decrease in the CFM values was also observed for crossplane profiles in the penumbra regions of ROI for increasing SSD.

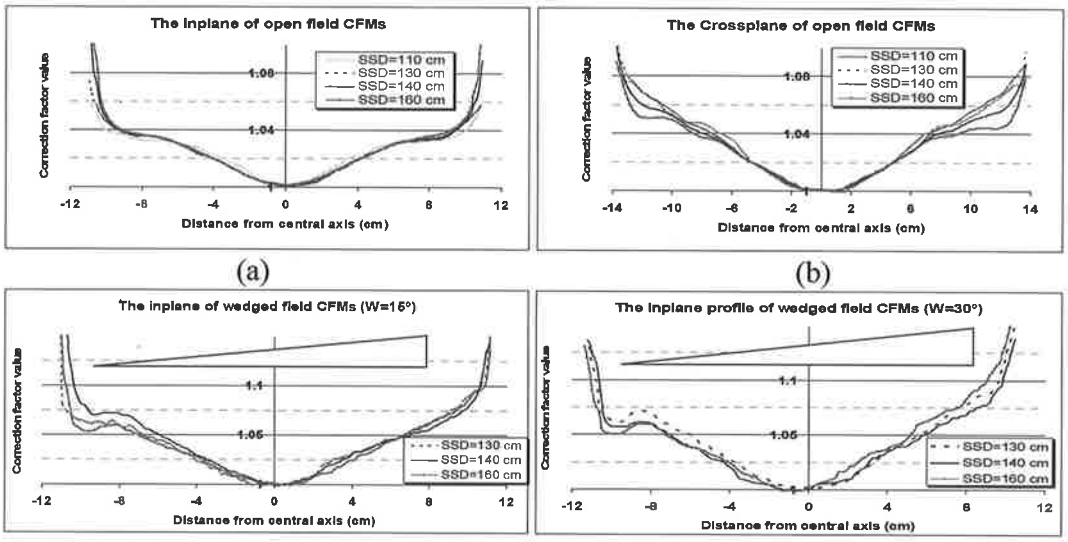

(a) (b)

(c) (d)

Figure 3.14. (a) The inplane and (b) crossplane profiles of the open field CFMs, (c & d) the crossplane profiles of the wedged field CFMs for different SSDs (130, 140 and 160 cm) for W=15° and W=30°, respectively. The position of wedged filters used in images acquisition is shown.

Several typical CFMs defined for open fields and wedged fields are shown in Figure 3.15. The x and y axes are the pixel coordinates. As described, due to the normalization to the central point of radiation fields, the central region of CFMs is around 1.00. For the wedged fields the CFM values in the part of the radiation field that correspond to the thinner part of the wedge are smaller than those corresponding to the thicker. A significant variation was observed in the thinner parts, compared to CFMs measured for open fields at the same SSDs.

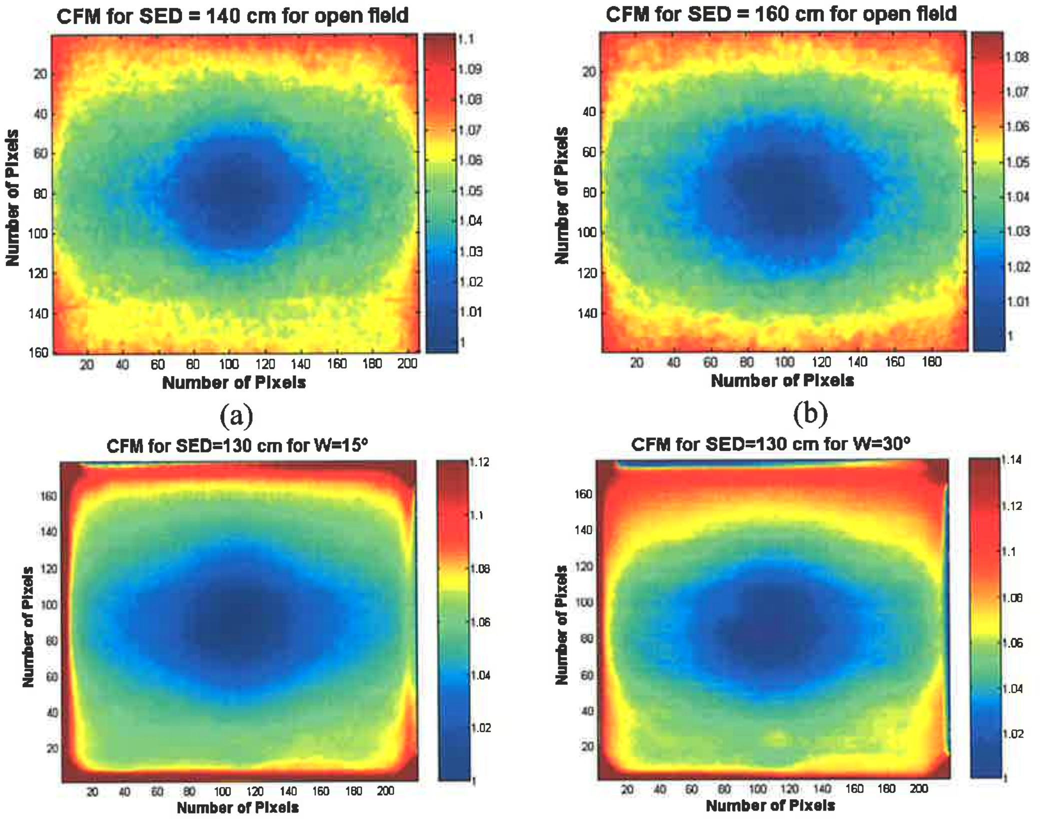

(c) (d)

Figure 3.15. Typical Correction Factor Matrix (CFM) for open fields at (a) SED = 140 cm for 15.8 × 19.5 cm^2 field size, (b) SED = 160 cm for 13.9 × 17.0 cm^2 field size, and for wedged fields at (c) SED = 130 cm for a 17.0 × 21.0 cm^2 field size, with a 15° wedge (d) SED = 130 cm for a 17.0 × 21 cm^2 field size with a 30° wedge. The upper part of the CFMs corresponds to the thinner part of wedged filters.

The two-dimensional dosimetric calibration procedure introduced in this part of the study does not require the EPID to be re-calibrated for each individual patient case for given linac settings. In addition, EDR2 film calibration is easy to set up and measure compared to ionization chamber scanning in a water tank. Here the radiation beam was not flattened as had been done in previous studies (Parsaei *et al* 1998) and EDR2 films were used to calibrate the EPID response for dosimetric purposes ("to unflatten" the profiles or to reconstruct beam horns). The method requires a simple set-up and can be performed quickly and accurately. It can also be performed in clinics more easily compared to using kernel-based convolution algorithms due to their dependence on EPID type and other settings (Warkentin *et al* 2003; Steciw *et al* 2005) and linac output (beam energy and the use of accessories) (Pasma *et al* 1998; 2002).

The radiation energy spectrum varies across the radiation field size due to beam divergence. This means that CFM values depend on SSDs significantly. In addition, in the presence of attenuators, such as physical wedges, the CFM values are different from those acquired in the open fields. In conclusion, because there is significant variation in CFMs values either for varying SSDs or wedge attenuators, the CFM acquired in the corresponding conditions has to be used to correct EPID dose values.

There are several sources of uncertainty in the EPID calibration procedure, including the uncertainty of a and b parameters in the calibration curve (equation 3.4), random fluctuation of EPID pixel values, the uncertainties of the ionization chamber dose measurements, and the variation in linac output. The uncertainty of the EPID calibration can be estimated using the standard deviations of the parameters CFM, a, b and PV as follows:

$$\sigma_{\dot{D}_{corr}} = \sqrt{\left(\frac{\partial \dot{D}_{corr}}{\partial (CFM)}\right)^2 \sigma^2{}_{CFM} + \left(\frac{\partial \dot{D}_{corr}}{\partial a}\right)^2 \sigma^2{}_{a} + \left(\frac{\partial \dot{D}_{corr}}{\partial b}\right)^2 \sigma^2{}_{b} + \left(\frac{\partial \dot{D}_{corr}}{\partial (PV)}\right)^2 \sigma^2{}_{PV}}\ , \tag{3.8}$$

where $\dot{D}_{corr} = (CFM)\dot{D}$, $CFM = \left(\frac{D_{film}}{D_{EPID}}\right)_{CAX}$, ($D_{film}$ are dose values obtained from film measurements), σ_{CFM}, σ_a, σ_b and σ_{PV} are the standard deviations in CFM, a, b and PV, respectively. The total relative uncertainty in the transmitted dose measured for the SLIC-EPID using equation 3.4 is approximately ± 2.3 %.

3.5. Summary and Conclusion

Investigating the reliability of using SLIC-EPID response for accurate dosimetric purposes is the main aim of this thesis. Several physical characteristics of a SLIC-EPID including thickness of extra build-up layer to reach the electronic equilibrium in the EPID detector layer, reproducibility, and noise level, were discussed. In addition, some dosimetric characteristics of SLIC-EPID such as the relationship between EPIs and incident dose rate and dose, field size response, the variation of portal dose map with the variation of gantry position and, the variation of dose values with the EPI time acquisition lag, were also investigated.

In order to evaluate physical characteristics, the amount of extra build-up layer required to increase the EPID pixel values to the highest values was found to be 5 mm RW3. No significant differences were found between the thickness of extra build-up layer at the central axis and off-axis points.

Regarding the reliability of SLIC-EPID response, both the short-term and medium-term reproducibility were investigated and were found to be less than 1%. Another physical characteristic of the SLIC-EPIs, the noise level, was evaluated. The noise level was generally found to be less than 1% and this will be referred to an acceptable dose level. The accuracy of portal dosimetry is dependent on the dose response characteristics. Without a comprehensive evaluation of dose response characteristics, EPIDs cannot be used for reliable dose measurements. In this chapter, the feasibility of relative transmitted dose determination using EPIs, acquired using SLIC-EPID, was investigated. The relationship between EPI pixel values, dose rate and dose was found for various linac repetition rate settings using calibrated ionization chamber measurements on the central axis. After calibration of the EPI pixel values with ionization chamber data, the calculated dose values on the central axis were compared with additional data measured using a calibrated ionization chamber for verification. The variation of relative dose values obtained from a SLIC-EPID and an ionization chamber versus the size of radiation field was investigated. The EPID data set was compared with the ionization chamber data set acquired under the same conditions.

The feasibility of using SLIC-EPID as a two-dimensional dosimeter was then assessed. Due to the standard manufacturer EPID calibration for imaging purposes, two-dimensional dose calibration using EDR2 film has been performed to restore radiation beam horns. In order to do this, a series of Correction Factor Matrices (CFMs) were defined as the ratio of EDR2 film pixel values and EPID dose values under various conditions.

Chapter 4. Verification of the dosimetric calibration for SLIC-EPID

4.1. Introduction

In this chapter, the dosimetric calibration method developed for SLIC-EPID, as described in Chapter 3, is verified for a range of conditions. In the first part of this chapter the verification of the calibration method for primary fluencies is evaluated for a range of open fields and wedged fields. This chapter also describes the verification of the calibration method developed for transmitted dose maps measured in the presence of homogeneous and inhomogeneous phantoms.

4.2. Verification of the calibration method for open fields

In order to verify the dosimetric calibration method for SLIC-EPIDs, several SLIC-EPID and EDR2 film images were acquired for a range of radiation field sizes. For each SSD (130 cm, 140 cm and 160 cm), two series of images were obtained for small (nominal field size: 7 × 10.5, 8 × 10, 7 × 8.5 cm^2) and medium field sizes (nominal field size: 10.5 × 15.8, 10 × 12, 10 × 12 cm^2). The acquired EDR2 films and the corresponding EPIs were processed (see section 3.4). EPIs, acquired using SLIC-EPID, were converted to dose using calibration method described in Chapter 3. The ROIs of EPIs were then compared with the corresponding ROIs obtained from EDR2 films acquired under the same conditions. The beam profiles were compared before and after the application of the corresponding CFMs measured in the same SSDs (see section 3.4.2). Due to the possible misalignment of EDR2 films with EPI dose maps, the percentage agreements for the whole ROI excluding areas 2.54 mm wide along the edges were assessed. The agreement between EDR2 film and corrected EPI was assessed based on the gamma function algorithm for Distance To Agreement (DTA) = 2.54 mm and the dose difference criterion (ΔD_{max}) = 1% (Low *et al* 1998) using a MATLAB in-house code (see Appendix B). Due to the SLIC-EPID pixel size, 1.27 × 1.27 mm^2, the distance criterion, DTA, was defined as 2.54 mm (two pixels) instead of 3 mm, which has been used in some studies (Van Dyk *et al* 1993; Low *et al* 1998).

Several typical line dose profiles measured using EDR2 films, SLIC-EPID (before and after the application of corresponding CFMs) for open fields at SSD = 130 and 160 cm are shown in Figure 4.1. The x and y axis values are distance from the central axis and relative dose, respectively. The corresponding gamma values are also shown on a secondary axis.

A good correlation was observed between EDR2 film and corrected EPID dose values, not including the edge of the ROI. Due to the normalization of the measured dose on the central axis, the gamma values are close to zero on the central axis. Gamma values were found to increase towards the edge of the ROI. Differences, however, were observed in the penumbra region. No significant variation in gamma values was found with the variation of SSD or field size. Although CFMs are symmetrical with respect to the central axis approximately, no symmetrical variation was observed for gamma values in all cases.

The relative dose differences between EDR2 and EPID data points for crossplane and inplane profiles are shown in Figure 4.2. The differences between relative dose values are less than 1% in the central part of inplane and crossplane profiles. Greater differences between EDR2 film and EPID data sets were observed in the penumbra region.

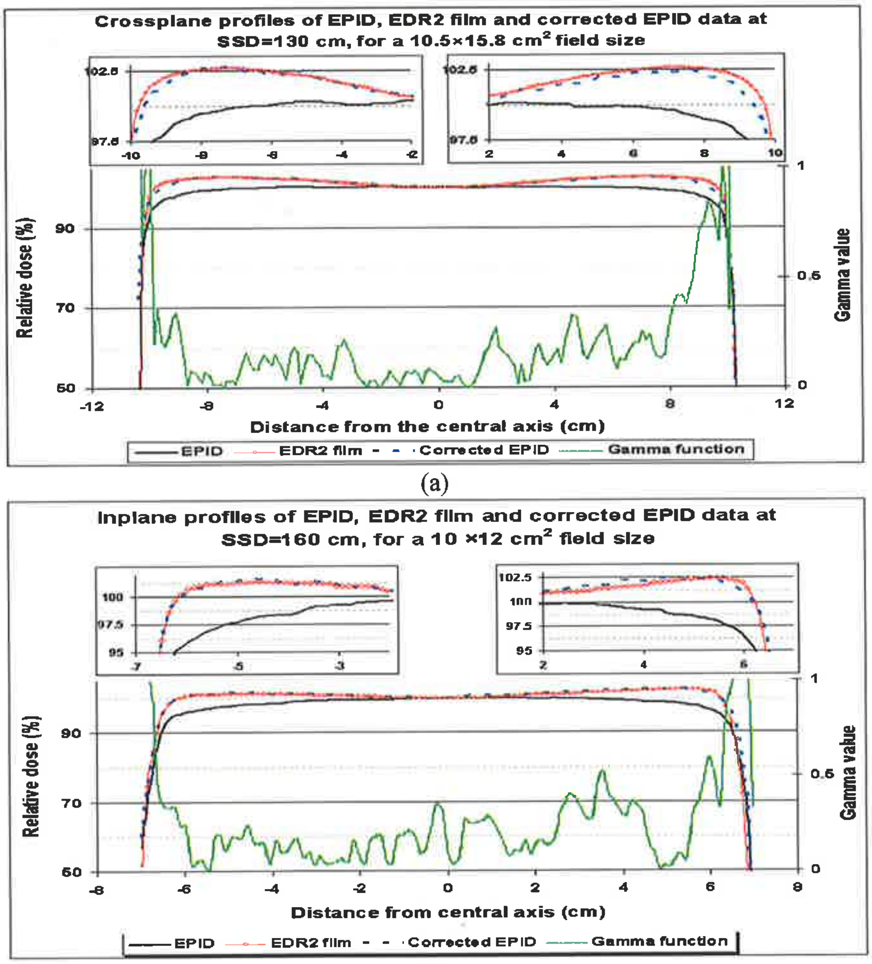

(a)

(b)

Figure 4.1. Typical line dose profiles measured using EDR2 film and EPID, corrected EPI profiles and the corresponding gamma values for open fields (a) at SSD = 130 cm for a 10.5 × 15.8 cm^2 field size, (b) at SSD = 160 cm for a 10 × 12 cm^2 field size. The DTA and ΔD_{max} criteria for gamma values were 2.54 mm and 1%, respectively.

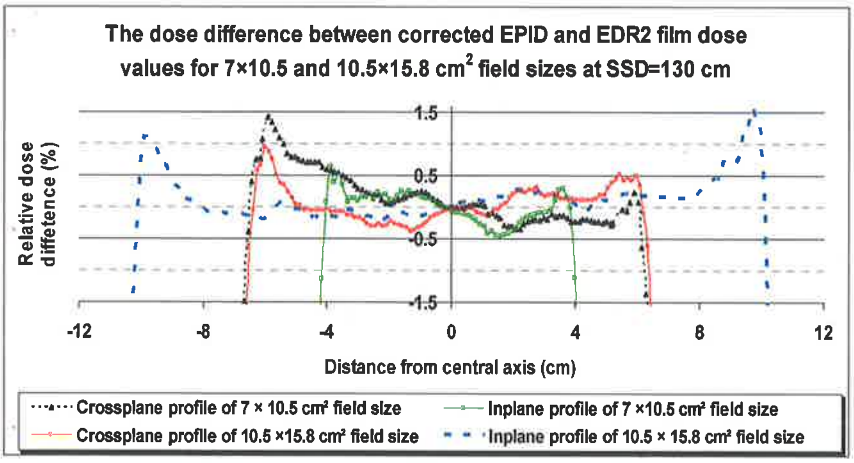

(a)

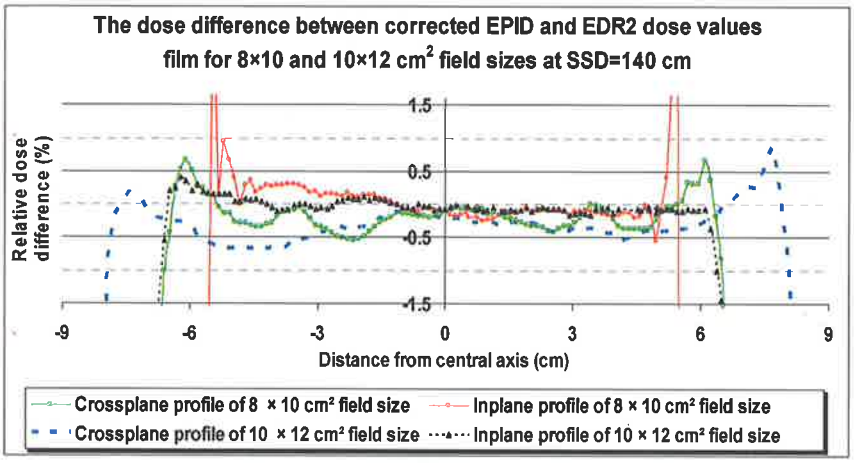

(b)

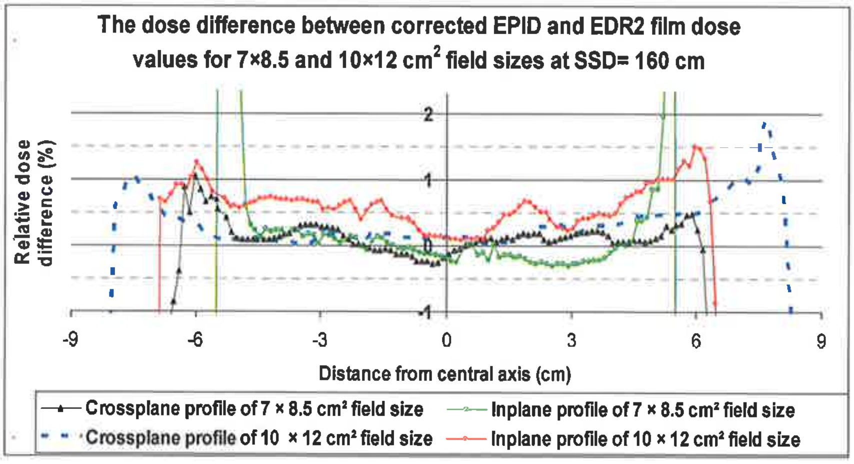

(c)

Figure 4.2. The relative dose differences in the crossplane and inplane profiles for (a) SED = 130 cm, (b) SED = 140 cm, and (c) SED = 160 cm for two field sizes.

Gamma maps before and after the application of CFMs for the ROIs in acquired images at SED = 130, 140 and 160 cm are shown in Figure 4.3. Dose values agreeing for the two compared dose maps within the specified criteria using the gamma function algorithm are shown in grey, while regions of disagreement are shown in colour. As Figure 4.3 (a & c series) show, due to the normalization to the central axis of radiation field, the central part of the ROI was observed to be in agreement before the use of the CFM. Also in Figure 4.3 (b & d series) it is shown that the application of CFMs decreases the gamma values to less than 1 for the ΔD_{max} = 1% and DTA = 2.5 mm criteria within most of the ROI. Several discrepancies were still observed near the edges of the ROIs.

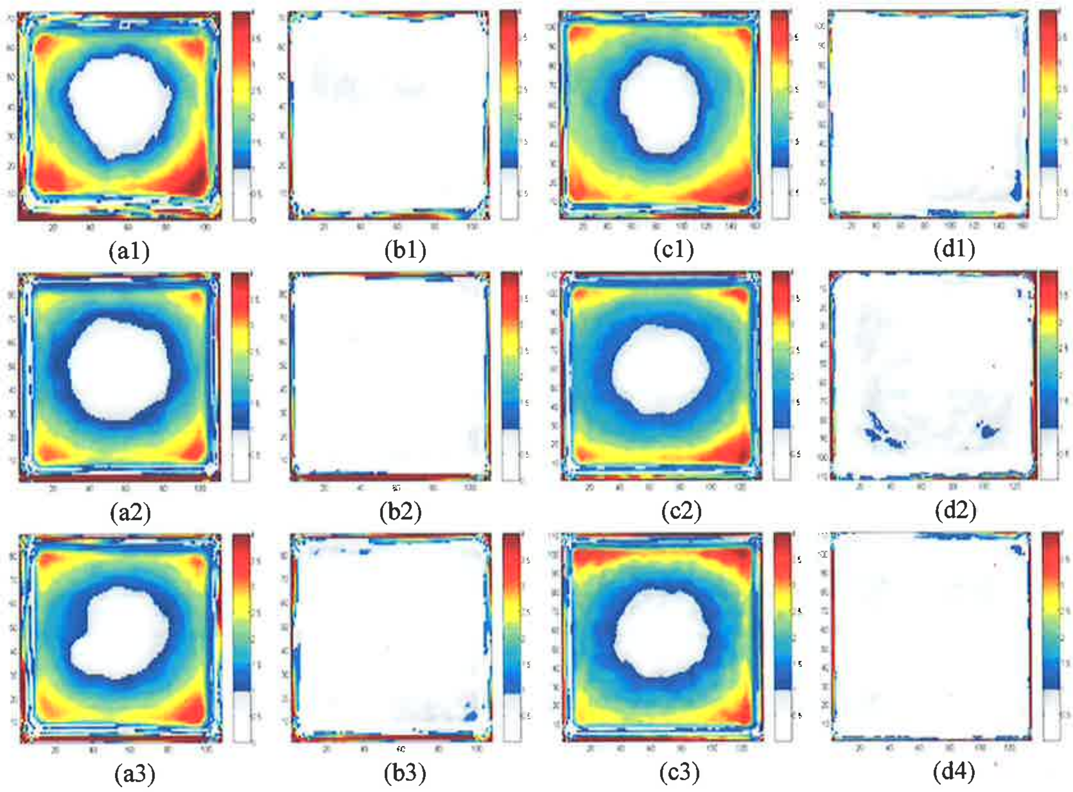

Figure 4.3. Gamma map comparisons of EDR2 film and EPID relative dose values before (a & c series) and after (b &d series) the application of CFM for: SSD = 130 cm (first raw) for 7.0×8.5 and 10.5×15.8 cm^2 field sizes, SSD = 140 cm (second raw) for 8×10 and 10 ×12 cm^2 field sizes, SSD = 160 cm (third raw) for 7.0×8.5 and 10 × 12 cm^2 field sizes. The gamma criteria were 1%/2.54 mm.

The percentage agreement before and after CFM application for open fields is shown in Table 4.1. The CFM increases the percentage agreement up to 90.9% and 97.6%, respectively, for the entire ROIs and 2.54 mm edge exclusion along the edges. No significant variation of the percentage agreement was observed as the SSD varied from 130 cm to 160 cm.

The CFMs obtained for the largest possible field sizes can be used to correct the EPID dose values measured at the same SEDs for smaller field sizes. An excellent agreement between EDR2 film and EPID dose values was observed with a dose tolerance of 1% and DTA = 2.54 mm. The possible reasons for the difference between the two measured dose maps are: (a) the different reconstruction procedure used for EDR2 film and EPID images; (b) artefacts occurred during the processing and scanning of EDR2 film; (c) the loss of EDR2 film pixel information during image resizing; (d) misalignment between two series of data sets; and (f) machine output fluctuation (within 1%).

Table 4.1. The percentage agreement between EDR2 film and EPI measurements using gamma function algorithm with 1%/2.54 mm for the whole ROI and 2.54 mm exclusion at the edges for open fields.

CFM	SSD (cm) & Field size(cm^2)	Agreement (%)		
		Before CFM	After CFM	After CFM & 2.5 mm edge excluded
CFM:130 (17.2×21)	130 (7.0×8.5)	25.7	87.8	97.2
	130 (10.5×15.8)	11.3	92.9	97.4
CFM:140 (16×19.6)	140 (8×10)	19.2	88.7	97.5
	140 (10×12)	14.1	93.1	98.5
CFM:160 (14×17)	160 (7×8.5)	16.0	89.3	97.0
	160 (10×12)	13.1	93.0	98.4

In conclusion, the results described in this section showed that SLIC-EPIDs can be used for relative dosimetry regarding open fields, either with the same size CFM or one that is smaller. This applies if the SLIC-EPI pixel values are corrected using an appropriate calibration method.

4.3. Verification of the calibration method for wedged fields

In section 4.1, it was shown that CFMs correct the EPID dose values in off-axis areas for open fields. This section of work attempts to find whether the dose maps measured using EPIDs are suitable for two-dimensional dosimetry in the presence of beam attenuators. To do this, the SLIC-EPID response has been investigated in the presence of physical wedges.

The EPIs, acquired for wedged conditions, were originally converted to the dose maps utilising the calibration procedure used for open fields. It was found that the CFMs, defined for open fields, do not suit wedged conditions. In order to define appropriate CFMs, several EPID and EDR2 film images were acquired under various wedged conditions. The details of the measurements are listed in Table 4.2. Due to different measurement conditions for open fields, a series of CFMs was defined using averaged CFMs obtained at various SSDs and physical wedges. The acquired EPIs were then corrected with the corresponding averaged CFM. The ROI of EPID and EDR2 film images were processed and compared using the same procedure as that described in section 3.4. In order to evaluate whether there is an agreement between EDR2 film and EPID dose values in the presence of physical wedges, gamma function of 2.54 mm and 1% were used for DTA and ΔD_{max} criteria, respectively.

The typical inplane profiles of the EPID, EDR2 film and corrected EPID relative dose values as well as the corresponding gamma values acquired in the presence of physical wedges W = 15° and W = 30° are shown in Figure 4.4. Consistency between EDR2 film and corrected EPID dose values was observed away from the edge of ROI. Differences, similar to those observed for open fields, were observed in the penumbra region.

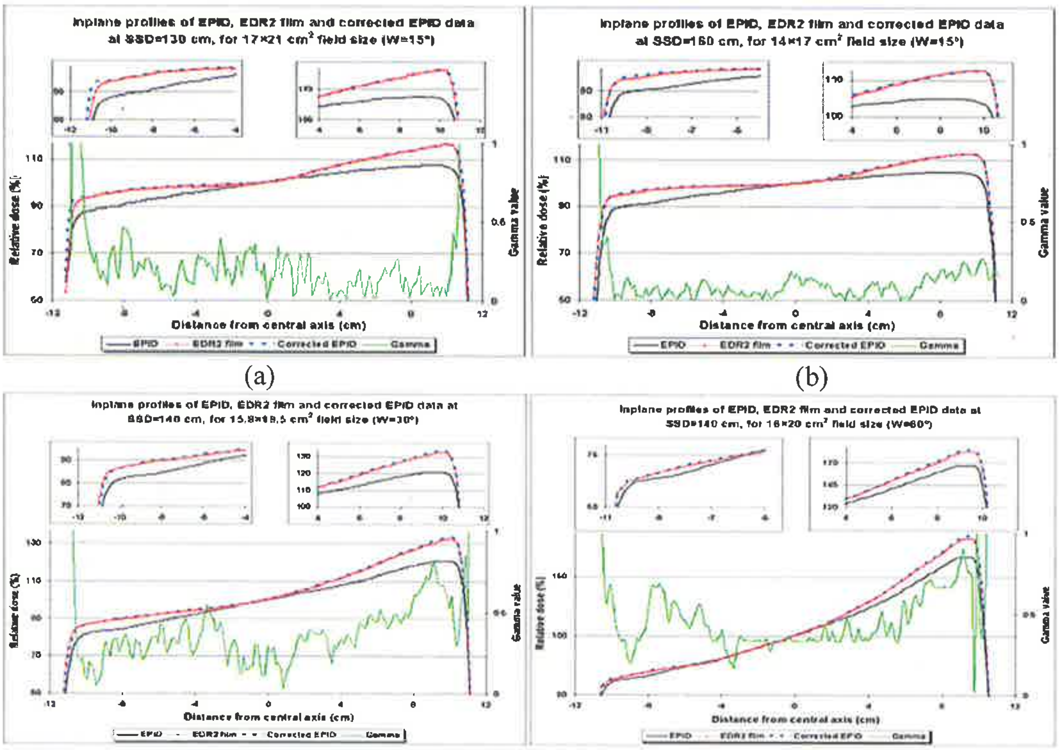

(a) (b)

(c) (d)

Figure 4.4. The inplane profiles of EDR2 film and EPID data (before and after the CFM application) and related gamma values acquired using: W = 15° (a) at SSD = 130 cm for a 17 × 21 cm^2 field size, (b) at SSD = 160 cm for a 14 × 17 cm^2 field size, (c) W = 30° at SSD = 140 cm for a 15.8 × 19.5 cm^2 field size, (d) W = 60° at SSD = 140 cm for a 16 × 20 cm^2 field size. DTA and ΔD_{max} criteria for gamma values were 1%/2.54 mm.

No systematic variation of gamma values were observed in the crossplane profiles with an increase in distance from the central axis towards the edge of the ROI. However, in several profiles in the wedged direction, the gamma values increased with distance from the central axis. The gamma values in the crossplane profiles were found to be lower than those in the inplane profiles. For instance, the average gamma values for crossplane and inplane profiles for the physical wedge = 15° were found to be 0.3, 0.3 and 0.2; and 0.5, 0.3 and 0.4 for SSD = 130, 140 and 160 cm, respectively. No significant variation was also observed in gamma values with a variation of SSD and radiation field size. Larger gamma values were observed for physical wedge = 60° compared to thinner wedges.

The crossplane and inplane profiles of the relative dose difference between EDR2 film and EPID data (before and after the application of the CFM) are shown in Figure 4.5. The differences between relative dose values were found to be less than 1% in the central part of the inplane and crossplane profiles.

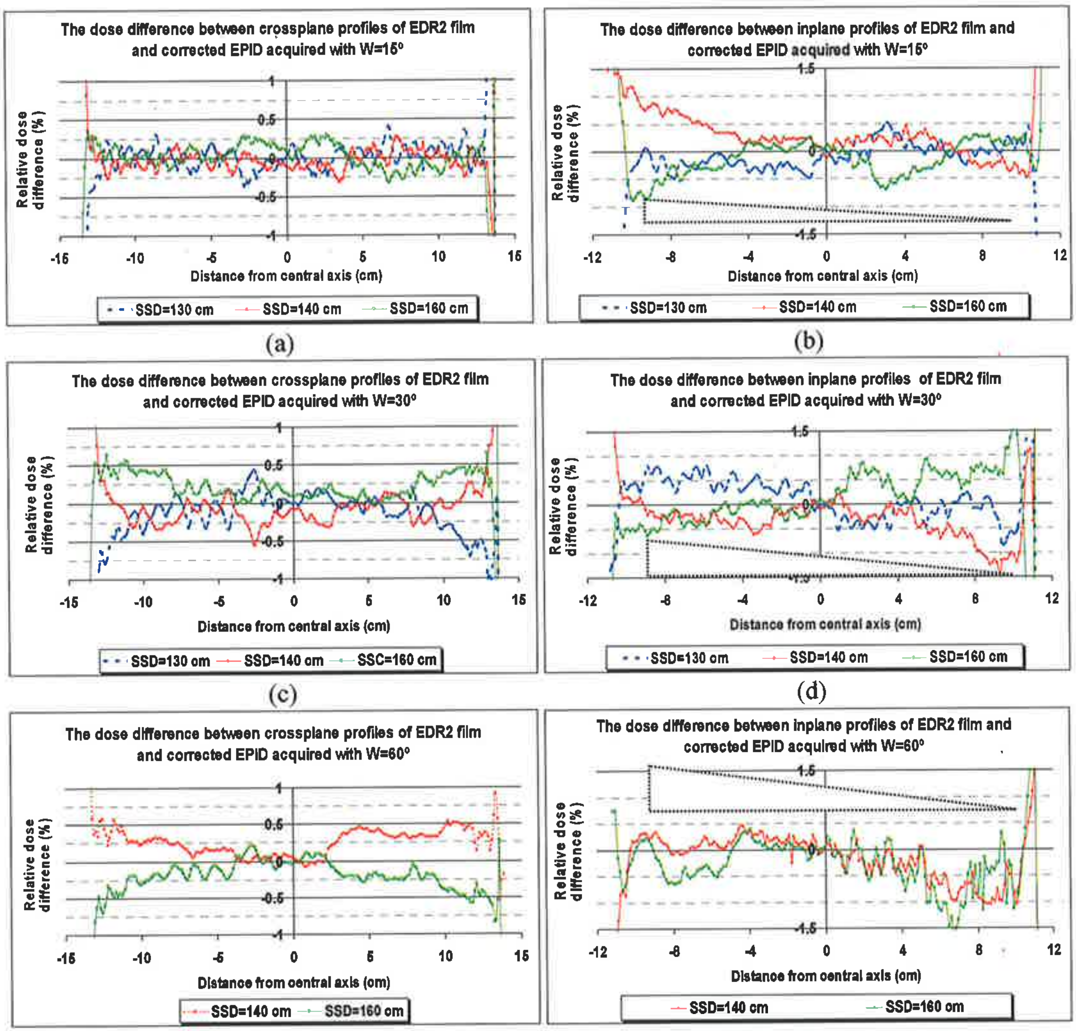

(a) (b) (c) (d) (e) (f)

Figure 4.5. The relative dose difference for EDR2 film and corrected EPID data for (a): crossplane and (b): inplane profiles at SSD = 130 cm for a 17 × 21 cm^2 field size, SSD = 140 cm for a 16 × 20 cm^2 field size, and SSD = 160 cm for a 14 × 17 cm^2 with W = 15° (c): crossplane and (d): inplane profiles at SSD = 130 cm for a 17 × 21 cm^2, SSD = 140 cm for a 16 × 20 cm^2 field size, and SSD = 160 cm for a 14 × 17 cm^2 with W = 30° (e): crossplane and (f): inplane profiles at , SSD = 140 cm for a 16 × 20 cm^2 field size, and SSD = 160 cm for a 14 × 17 cm^2 with W = 60°.

For inplane profiles, the relative dose differences increased towards the edge of the ROI. In contrast to crossplanes, no systematic variation in dose difference was observed with distance from the central axis. The physical wedge position is shown in the crossplane profiles.

The results of the gamma function are shown before and after the application of corresponding CFMs in Figures 4.6 and 4.7, respectively, for physical wedges 15° and 30°, and 60°. These results show that the CFMs, derived for wedges, increase the percentage of agreement between dose values measured using EPID and EDR2 film in the presence of physical wedges.

The percentage agreements between relative dose profiles measured using EDR2 film and EPID (before and after the application of CFM) are shown in Table 4.2 for a range of wedged fields. The maximum agreement before CFM application was found to be approximately 25% for W=60° cases. The average agreement before the application of CFM was found to be 6.5 %, 7.7 % and 22.7 % for EDR2 film and EPID data sets acquired at various SSDs for W=15°, W=30° and W=60°, respectively. The agreement increased to 93.4%, 93.7% and 95.4% using an average CFM for physical wedges 15°, 30° and 60°, respectively. Ignoring 2.5 mm of the edge of ROIs, the average of agreement increased by 4.2%, 4.3% and 3.5% for W=15°, W=30° and W=60°, respectively. No systematic variation was observed in the percentage of agreement with the angle of wedge filters for W=15° and W=30°.

CFMs can be used to correct EPID dose values in more complicated conditions than open fields. In this section, CFMs acquired for different SSDs and in the presence of the same physical wedge were averaged. The average CFM was then used to correct the EPID images for each SSD. The available data suggest that a gamma score greater than 95% can be routinely achieved with this calibration technique. However, for open fields, to obtain the desired agreement between EDR2 film and EPID (greater than 95%) the use of CFM depended on the SSD (see section 4.2). The results show that CFMs, acquired for different SSDs and for a particular physical wedge, can be used to correct the EPID data acquired in the presence of physical wedges.

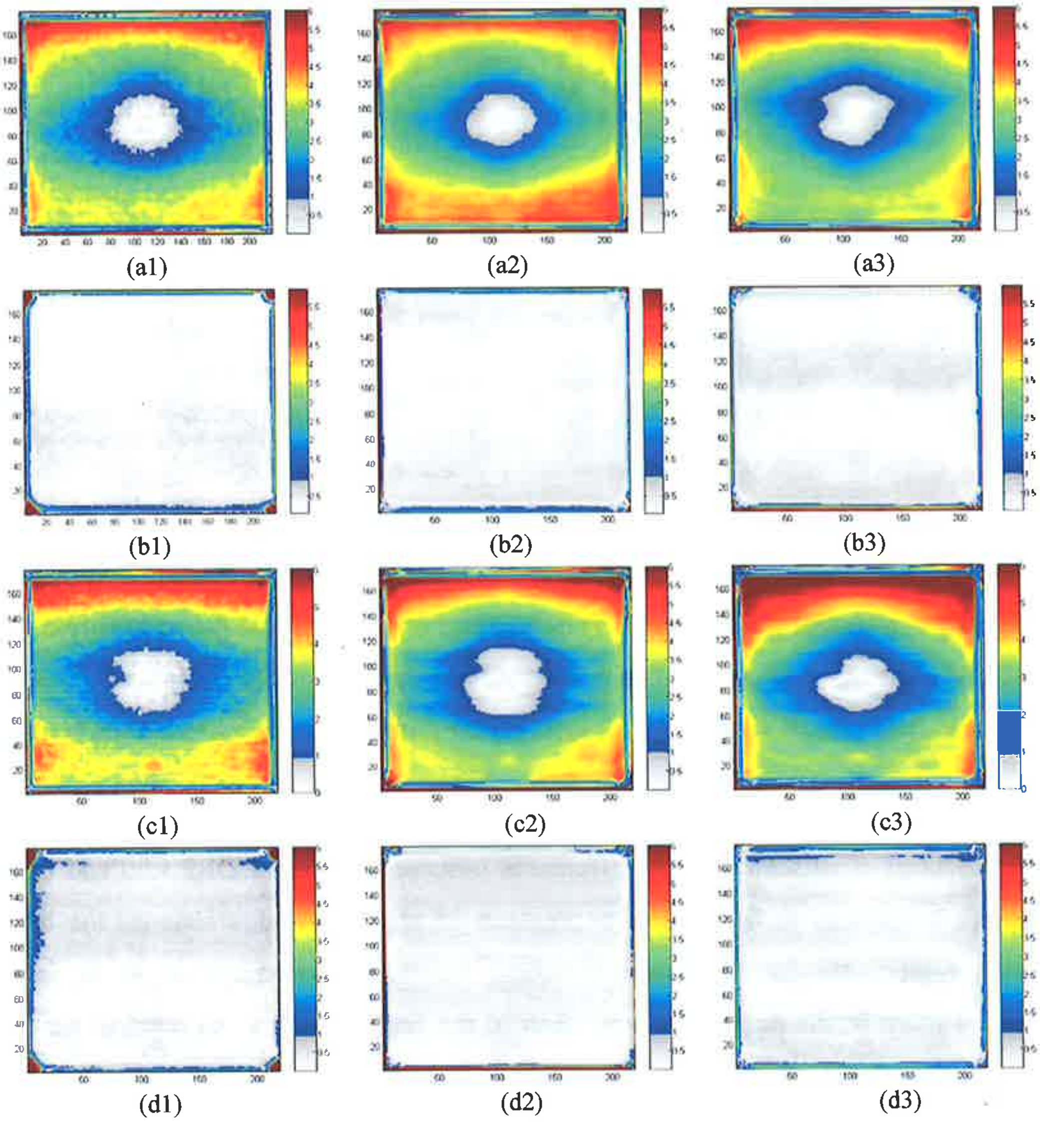

Figure 4.6. The gamma maps for the EDR2 and EPID data acquired using a W = 15° before (series a) and after the application of the CFM (series b) at SSD=130 cm for a 17×21 cm^2 field size, at SSD=140 cm for a 16×20 cm^2 field size and at SSD=160 cm for a 14×17 cm^2 field size, and using a W = 30° before (series c) and after the application of CFM (series d) at SSD=130 cm for a 17×21 cm^2 field size, at SSD=140 cm for a 16×20 cm^2 field size and at SSD=160 cm for a 14×17 cm^2 field size. The gamma criteria were 1%/2.54 mm.

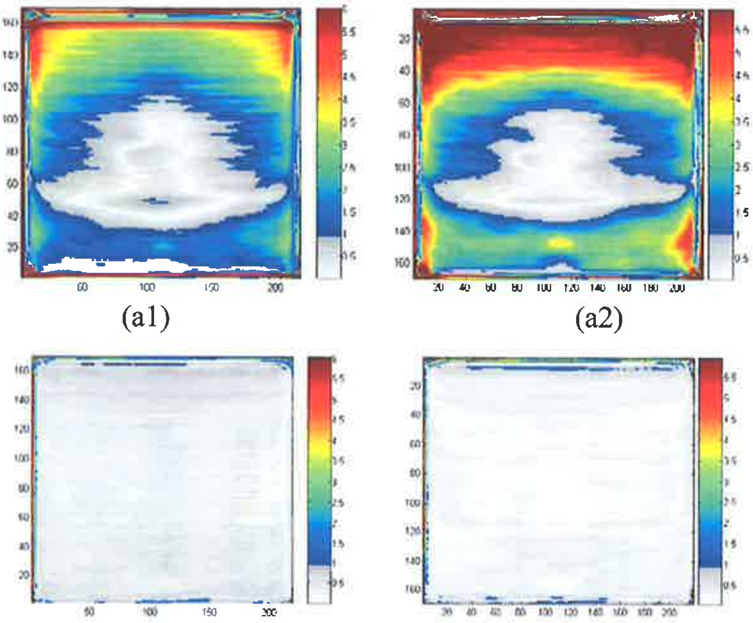

(a1) (a2)

(b1) (b2)

Figure 4.7. The gamma function results for the EDR2 and EPID data acquired using a 60° physical wedge (series a) before and (series b) after the application of the CFM at SSD = 140 cm for a 16 × 20 cm^2 field size and at SSD = 160 cm for a 14 × 17 cm^2 field size. DTA and ΔD_{max} criteria for gamma values were 2.54 mm and 1%, respectively.

Several factors contributing to the differences observed between EDR2 film and EPID images are listed in section 4.2. The presence of physical wedge changes the beam quality significantly. In the wedged direction, the physical wedge changes the beam spectrum more in the peripheral areas than in the regions around the central axis. In contrast, in un-wedged direction the energy spectrum of the radiation beam is more uniform compared to open fields. Crossplane profiles of relative dose difference show that the average dose difference in the crossplane profiles (i.e. unwedged direction) is less than 0.5%. Furthermore, the dose difference profiles in the presence of physical wedge 60° vary by a greater amount across the beam profile. The possible reasons are as follows. Firstly, in the presence of physical wedge in off-axis areas, the EPID response is more smooth compared to that achieved by EDR2 film, which measures beam "true" profiles (as measured in water tank). Due to the attenuation of the beam low energy photons for wedged fields, the discrepancy between EDR2 film and EPID dose response is lower than that for the open field.

Secondly, the beam energy depends significantly on the beam divergence. In the other words, for greater field sizes or shorter SSDs the beam energy spectrum is more spread out than those for smaller field sizes set up for longer SSDs. In the presence of physical wedge, the radiation beam is filtered significantly. The low energy photons are attenuated more than higher energy photons. As a result, the beam energy spectrum is hardened compared to that measured in open fields. This shows that the variation of photon energy with the angle or distance from central axis is less. As a result, CFM dependency on the SSD decreases compared to the open field CFMs.

Table 4.2. The agreement percentage between dose values measured using EDR2 film and EPIs by the gamma function algorithm with criteria of 1%/2.54 mm; before and after applying the corresponding average wedged CFM for the whole ROI and 2.54 mm exclusion in the edges.

CFM (SSD (cm) & W (°))	Agreement (%)		
	Before CFM	After CFM	After CFM & discarding 2.54 mm edge
CFM: Average 130W15, 140W15, 160W15			
130 W15	7.4	93.8	98.3
140 W15	5.8	93.3	97.2
160 W15	6.2	93.3	97.5
CFM: Average 130W30, 140W30, 160W30			
130 W30	8.2	94.2	98.1
140 W30	7.4	93.8	98.1
160 W30	7.5	93.1	97.7
CFM: Average 140W60, 160W60			
140 W60	23.0	95.4	98.8
160 W60	22.4	95.6	99.1

As the results show, the percentage agreement before and after the use of an appropriate CFM for data acquired using a physical wedge 60° is better than those observed for other conditions. As Figure 4.7 (series a) shows, in the central part of ROI, in the un-wedged direction, no correction is required for the EPID dose values. The agreed area is found to be larger compared to those measured using other wedges. The more attenuation of the beam produces more smoothed profiles for EDR2 films compare to those measured for open fields.

In this part of the current thesis, the EDR2 film and the SLIC-EPID two-dimensional dose measurements were compared using the gamma function algorithm. The DTA limit was set to two pixels corresponding to 2.54 mm, due to the pixel size of the SLIC-EPID (1.27 mm ×1.27 mm), and dose agreement was set to 1%. These conditions were stricter than those generally used for clinical treatment verification (DTA of 3-4 mm and the dose agreement within 3%). These conditions are important to ensure that the EPID is calibrated accurately and that it provides reliable dosimetric results; i.e. the calibration must be more accurate (within 1%) compared to the dose differences being measured (within 3%).

In conclusion, the SLIC-EPID has reliable dose responses in the presence of physical wedges provided an appropriate calibration procedure is used. Discarding the high gradient dose regions in the edge of ROIs, the dose difference between EDR2 film and EPID data, after applying an appropriate CFM, is less than 1%. This allows SLIC-EPID to be used as a reliable dosimeter in the open fields and wedged fields. For further investigation, the response of this empirical dosimetric method in the presence of homogeneous and inhomogeneous phantoms is investigated in the following sections.

4.4. Verification of the calibration method in the presence of homogeneous and inhomogeneous phantoms

The work, presented in this section, attempts to verify an empirical dosimetric calibration method developed using EDR2 film (see section 3.4) for SLIC-EPIDs in the presence of homogeneous and inhomogeneous phantoms. In order to do this, the transmitted dose maps, measured using a SLIC-EPID, were compared with those measured using EDR2 films as well as with those calculated by *Pinnacle*^{3} TPS for a range of homogeneous and inhomogeneous phantoms using the gamma function algorithm (Low *et al* 1998). Due to the importance of the correction for off-axis areas, the results are also shown before and after the application of CFM.

4.4.1. Homogenous phantoms

A range of 30 × 30 × 1 cm^3 RW3 slabs (ρ = 1045 g/cm^3, PTW Freiburg, Germany) were used as homogeneous phantoms. The thickness of the homogeneous phantoms used was 6 to 10, 16, and 20 cm.

A series of EPIs was acquired for homogeneous phantoms, using the isocentric technique for a 10 × 10 cm^2 nominal field size at SED = 140 cm with linac repetition rate of 300 MU/min. The acquired EPIs were converted into transmitted dose maps using the calibration procedure described in the section 3.4. EDR2 films were irradiated with 3 Gy and 5 Gy (588 and 980 MU) for 6 and 10, 16 and 20 cm phantom thicknesses, respectively, under the same conditions as described for the EPIs. The transmitted dose maps measured using EDR2 films were compared with those measured using SLIC-EPID. A CFM, derived for open fields at SSD =140 cm, was applied as a part of calibration procedure. Due to the different pixel size of scanned EDR2 films, the pixel size of EDR2 film images was rescaled to the EPI pixel sizes using bilinear interpolation. Both EPID and rescaled EDR2 film dose profiles were normalized relative to a 7 × 7 matrix at the calibration point. The agreement between EDR2 film and corrected EPID transmitted dose maps were then evaluated using the gamma function algorithm with DTA and ΔD_{max} criteria of 2.54 mm (2 pixels) and 1%, respectively. In addition, a 2.54 mm wide strip around the edge of the EPID and film images was excluded from gamma analysis. This was due to slight misalignment errors and slight rotation in the position of the film orientation relative to the EPID image.

Typical inplane and crossplane relative dose profiles for the EPID, EDR2 film, corrected EPID and the corresponding gamma profiles are shown in Figure 4.8 for phantom thicknesses of 6 and 20 cm. Similar to fluence maps (see section 4.1), discarding the penumbra region, a significant difference (maximum of 4.6%) between EDR2 film and EPI dose values before the CFM application was observed in off-axis areas.

After correcting the EPID transmitted dose measurements with the CFM, the gamma function results show that there is a close correlation (gamma score more than 90%) between EDR2 film dose and EPID dose values for the 1%/2.54 mm gamma function criteria. The corresponding relative dose difference between corrected EPID and EDR2 film was found to be less than 1% in the central part of the radiation field (see Figure

4.9). Excluding the penumbra region, no systematic variation in dose difference profiles was observed.

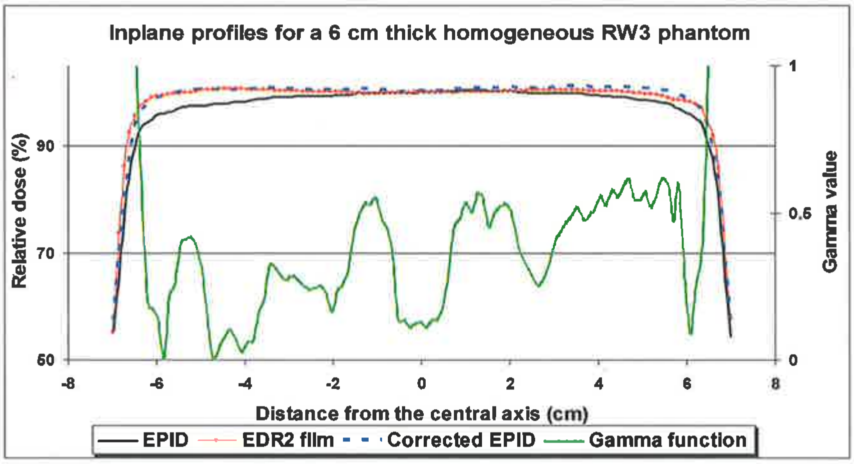

(a)

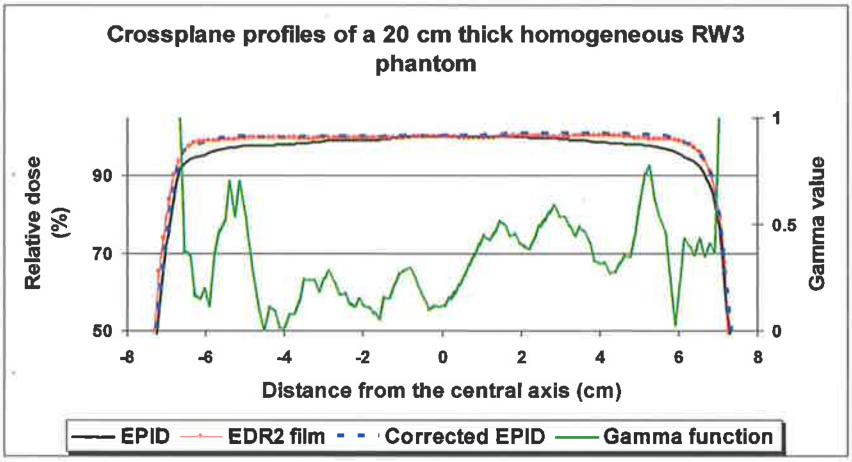

(b)

Figure 4.8. The inplane and crossplane relative dose profiles measured using EDR2 film, EPID (before and after CFM application), with corresponding gamma profiles using 1%/2.54 mm criteria, for homogeneous phantom thicknesses of (a) 6 cm and (b) 20 cm.

The agreement between relative transmitted doses for EDR2 film and corrected EPI, before and after the application of CFM, is shown in Figure 4.10. Prior to using a CFM, only the central regions of the gamma maps agreed. Applying the CFM significantly increases the area of agreement as indicated by the gamma maps. For more information, the agreement percentage between EDR2 film and corrected EPI is also shown in Table 4.3.

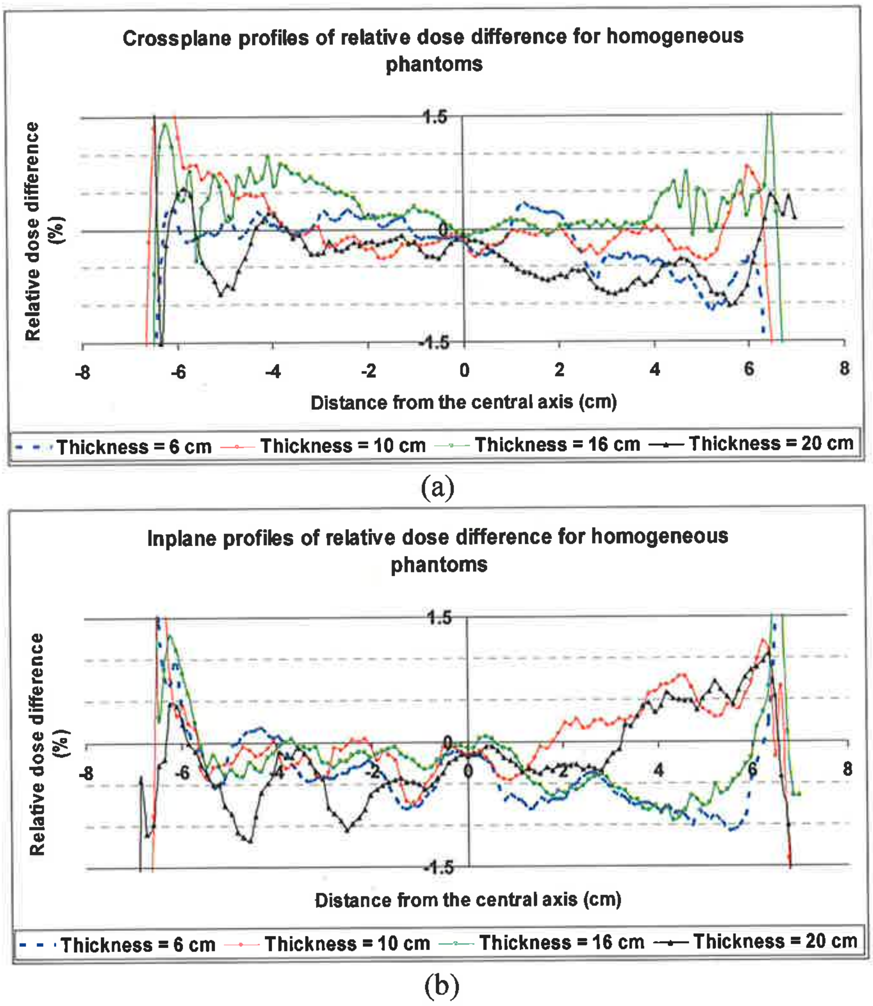

Figure 4.9. The (a) crossplane, and (b) inplane of relative dose difference between corrected EPI and EDR2 film for a 6, 10, 16, and 20 cm thick homogeneous phantom.

The use of CFM increases the percentage agreement between dose distributions measured using EDR2 film and EPID from 20-25% to approximately 90-95% for a range of homogeneous phantom thicknesses. Although several non-systematic differences were observed in the gamma maps, most of the disagreement occurred within 2.54 mm of the edge of the gamma maps and is most likely due to misalignment between the dose maps. The agreement between the two measured data sets, achieved using gamma function analysis, decreases with the increase of phantom thickness.

Table 4.3. The percentage agreement between transmitted dose values obtained from EDR2 film and SLIC-EPID, before and after the use of the CFM using the gamma function (1% / 2.54 mm) for a range of homogeneous phantom thicknesses.

Phantom thickness (cm)	Percentage of Agreement (%)		
	Before Correction	After correction	Excluding 2.5 mm edge
6	25.2	89.1	95.9
10	16.7	90.0	96.0
16	16.1	87.1	93.6
20	21.8	83.5	90.9

The results in this section show that the CFMs (measured in no-phantom condition) can be used to correct EPI dose values measured in the presence of homogeneous phantoms. Further investigation is required to assess the calibration method in the presence of inhomogeneities. More details will be discussed after the results concerning inhomogeneous phantoms.

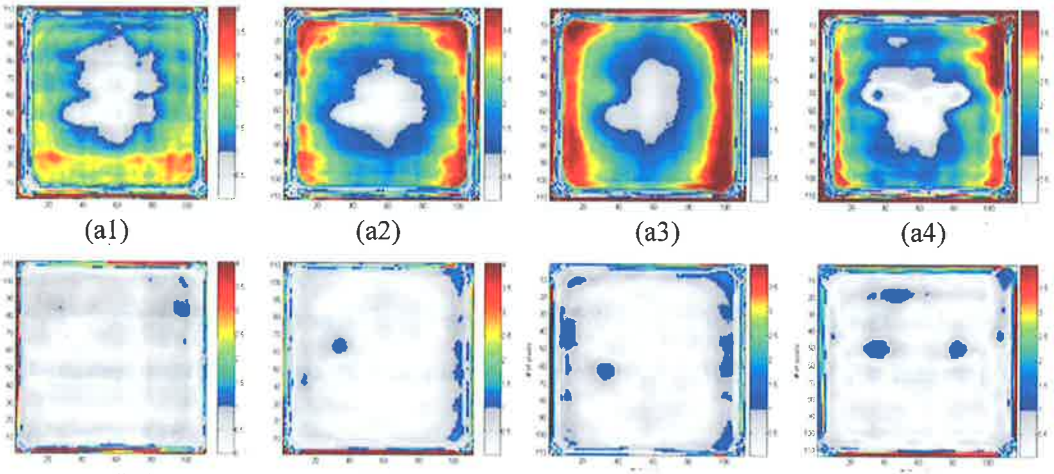
(a1) (a2) (a3) (a4)

(b1) (b2) (b3) (b4)

Figure 4.10. The agreement between EDR2 film and EPID dose values (series a) prior to correction (series b) after correction for 6, 10, 16 and 20 cm phantom thicknesses at SED = 140 cm for a 10×10 cm^2 field size. The gamma maps were calculated for 1%/2.54 mm criteria.

4.4.2. Inhomogeneous phantoms

In order to investigate the SLIC-EPID response after application of a dosimetric calibration procedure in the presence of large inhomogeneities, an inhomogeneous phantom was created by inserting two semi-conical objects of different density in a cylindrical phantom made of solid water. The original diameter and height of the cylindrical phantom were, respectively, 30 cm and 7 cm. In this work, a 6.8×12.8 cm^2 area of the cylindrical phantom was used as an inhomogeneous phantom including two semi-conical holes, as shown in Figure 4.11 below: the left insertion is made of lung equivalent material ($\rho = 0.0012$ g/cm^3); and the right insertion is made of bone (corticle) equivalent material ($\rho = 1.75$ g/cm^3).

The transmitted dose maps were measured using SLIC-EPID for an inhomogeneous phantom (see Figure 4.11). The thickness of the phantom was increased from 7 cm to 30 cm using additional RW3 layers placed on the top and bottom of the phantom. EDR2 films were also irradiated under the same condition with 588 and 980 MU for 7 cm, 17 cm and 20, 30 cm phantom thicknesses, respectively. In order to predict the transmitted dose distribution, the cylindrical phantom, a 4 cm thick RW3 slab, representing the modelled EPID, and a 38.5 cm air gap between centre of the phantom and the upper edge of the slab were scanned using a Philips AcQSim CT Imaging System (Philips Medical Systems, Cleveland, Inc.). The slice thickness used in this study was 5 mm in axial direction. A schematic sagittal view of the extended phantom, used in the current study, is shown in Figure 4.12. In the TPS, the thickness of the phantom was set at 17, 20, and 30 cm by converting the air density to the water equivalent material added to entrance and exit surface of the inhomogeneous cylindrical phantom CT data. The transmitted dose was calculated at d_{max} in the modelled EPID.

The EPI, EDR2 and TPS dose maps were aligned at the 50% isodose lines (see section 3.4). The EPID, EDR2 film and TPS dose values were compared using the gamma function algorithm. A DTA of 2.54 mm was used and ΔD_{max} was varied from 1%, to 2% for EDR2 film-EPID. For TPS-EPID comparison, due to the different properties of radiation modelling in the TPS compared to that used in measurement as well as the limitation of the algorithm used for TPS to calculate dose especially for air inhomogeneities (Battista and Sharpe 1992; Metcalfe *et al* 1997), the maximum dose difference criterion of 3 % was selected.

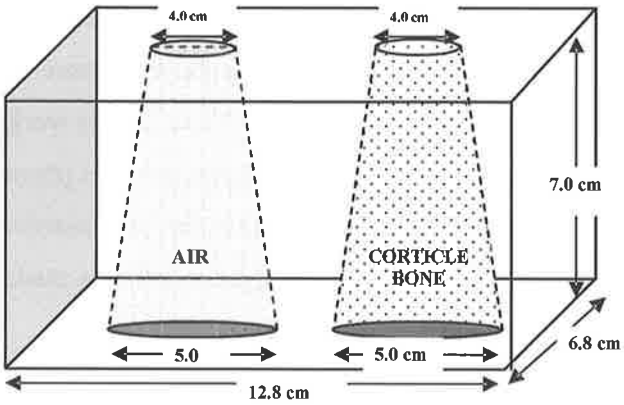

Figure 4.11. An inhomogeneous phantom, consisting of bone and air.

Typical crossplane, inplane and off-axis inplane profiles passing through the inhomogeneities and corresponding gamma values for EDR2 film-EPID and TPS-EPID comparisons are shown in Figure 4.13 for a 30 cm thick inhomogeneous phantom. The results show that the CFM, defined for in-air conditions, can be used with complex phantoms with reasonable accuracy. The gamma function assessment also shows that the majority of the corrected EPID dose values agree with those measured using EDR2 film. Several systematic discrepancies, however, were observed in the ROI edges, inhomogeneity boundaries and in the homogeneous regions. Towards the edges, an increase in disagreement was observed for all inplane profiles. No systematic variation in FILM-EPID gamma values was observed in crossplanes. When comparing TPS line profiles with corrected EPID and with EDR2 film, the greatest discrepancy was found in the TPS inplane profiles. This was not observed for other off-axis profiles passing through the inhomogeneous regions.

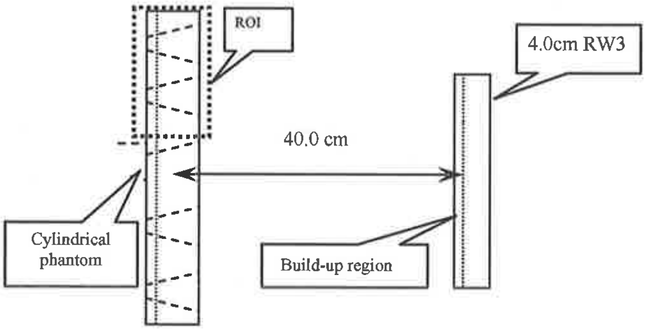

Figure 4.12. A sagittal view of scanned inhomogeneous phantom used in the TPS.

Due to the misalignment errors in the dose profiles causing by the rotational errors, significant differences were observed in high dose gradient regions, near the edge corresponding to the inhomogeneities. The relative dose differences for EDR2 film - EPID and TPS - EPID dose maps were found to be within 2% and 3%, respectively. When comparing the in/off axis inplanes of relative dose difference between TPS and EPID, the maximum and minimum relative dose difference was observed for air and bone inhomogeneities, respectively.

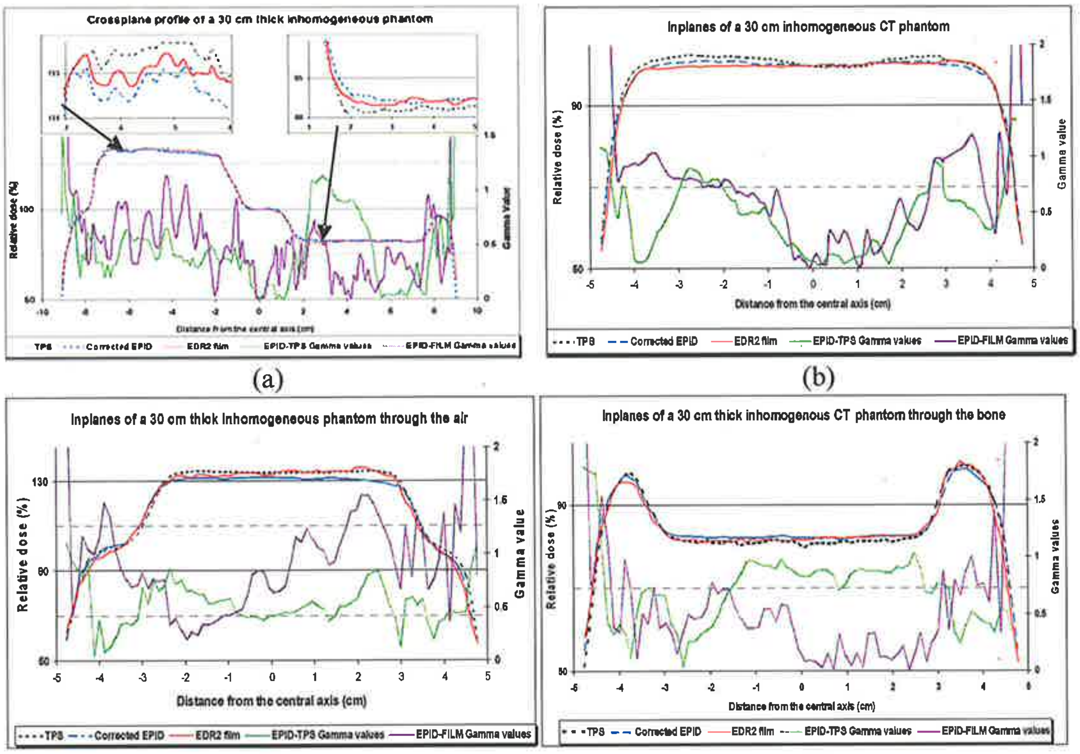

(a) (b)

(c) (d)

Figure 4.13. (a) Crossplane, (b) inplane, and off-axis inplane profiles for the radiation beam passing through (c) the air and (d) the bone inhomogeneities of the EDR2 film, TPS and the corrected EPI doses and the corresponding gamma values for 3%/2.5 mm for a 30-cm thick phantom.

Typical gamma maps for EDR2 film and TPS relative dose distributions are shown in Figure 4.14. As figures (a1-a4) & (c1-c4) show, the central part of the radiation field and the edge of inhomogeneities are in disagreement before application of the CFM. After correction of EPID dose maps, almost all whole radiation fields are in agreement, as shown in figures (b1-b4) & (d1-d4).

Although several non-systematic disagreements between dose distributions measured using EPID and EDR2 film were observed in the water-equivalent and air inhomogeneity regions, no significant discrepancies were observed in the bone inhomogeneity region. Regarding bone inhomogeneity, the only spot where the gamma function was larger than 1, was observed for the 7 cm phantom thickness.

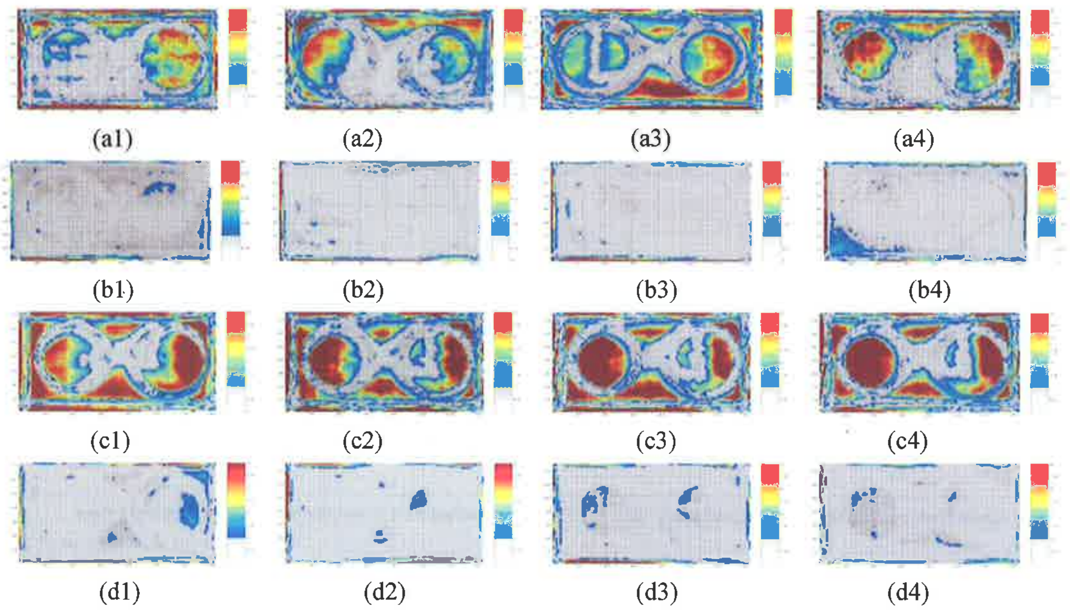
(a1) (a2) (a3) (a4)
(b1) (b2) (b3) (b4)
(c1) (c2) (c3) (c4)
(d1) (d2) (d3) (d4)

Figure 4.14. The gamma maps of EDR2 film-EPID (a1-a4) prior to correction (b1-b4) after correction with criteria 2%/2.54 mm. The gamma maps of TPS-EPID (c1-c4) prior to correction (d1-d4) after correction with criteria 3%/2.54 mm, for phantom thicknesses 7, 17, 20, and 30 cm, respectively. All images were acquired at SED = 140 cm for a 6.8 × 12.8 cm^2 field size.

The relative dose difference between EPID and TPS data sets were larger than those for the EDR2 film-EPID difference. The gamma values increased with the increasing phantom thickness. In the air inhomogeneity region, an increase in the gamma values, indicating more disagreement, was observed with the increase in phantom thickness. No significant increase in gamma values was observed for the bone inhomogeneity with increase in phantom thickness. Disregarding the edges of the radiation field, no significant difference was observed in the water equivalent region and in the bone inhomogeneity after application of the CFM. The average gamma value and related standard deviation for the water equivalent area, air and bone inhomogeneities are 0.6 ± 0.1, 0.5 ± 0.1 and 0.6 ± 0.2, respectively.

The percentage agreements for the film-EPID and TPS-EPID comparison, before and after the application of the CFM and discarding 2.54 mm edges for a dose difference criterion of 2% and 3%, are shown in Tables 4.4 and 4.5, respectively. It should be pointed out that the acceptable gamma values were obtained for TPS-EPID comparison only when dose difference criterion was defined as 2-2.5%. For the EDR2 film-EPID comparison, no systematic variation of gamma scores was found with the increase of phantom thickness before application of the CFM. However, after applying the CFM, generally a decrease in gamma scores was observed with increase in phantom thickness. A significant increase (44.9%) was observed in agreement between reference (EDR2 film) and evaluated (EPID dose measurements) transmitted dose maps for film-EPID data. Excluding 2.54 mm edges in the radiation field increased the agreement by approximately 7%. A close correlation (more than 94%) was observed using 3%/2.54 mm gamma criteria in all cases after discarding 2 pixels around the edges. In these cases the application of the CFM increases such agreement by 60%.

The measured transmitted doses for homogeneous and inhomogeneous phantoms are shown in Tables 4.3, 4.4 and 4.5. The increase in scattered radiation, due to increasing phantom thickness and decreasing primary radiation measured in the EPID detector layer for thicker phantoms, are the main reasons for the decline in agreement between reference and evaluated dose maps.

Table 4.4. The percentage agreement between EDR2 film and EPI dose maps using the gamma function algorithm for 2%/2.54 mm, before and after applying the corresponding CFM and discarding 2.54 mm field edges for a range of inhomogeneous phantom thicknesses.

Phantom thickness (cm)	Agreement (%) (DTA=2.54 mm & ΔD= 2%)		
	Before CFM	After CFM	Discarding 2.54 mm edges
7	46.2	91.7	97.2
17	47.5	89.4	96.4
20	35.3	89.5	96.1
30	46.7	84.7	92.2

The results show that the CFM, measured in no-phantom condition, can be used to correct EPI dose values measured in the presence of homogeneous and inhomogeneous phantoms. For the inhomogeneous phantoms, however, a 0.5% - 1.0% increase in ΔD_{max} criterion (for a fixed DTA) is required to reach the same results as the homogeneous phantoms. The main source of disagreement between EDR2 film and EPID arises from the misalignment between EDR2 films and EPID dose values, which are invariably present before and after the CFM is applied. In several cases, less than 1° rotation in the EDR2 film were observed for film positioning errors during irradiation and scanning. Due to the MATLAB software disability to rotate images for less than 1° for acquired images, this increases the disagreement between measurements in the edge of radiation fields. In addition, EDR2 films are not completely energy independent (Yeo *et al* 2004).

Table 4.5. The percentage agreement between TPS and EPI dose maps using the gamma function algorithm for 3%/2.54 mm, before and after applying the corresponding CFM and discarding 2.54 mm field edges for a range of inhomogeneous phantom thicknesses.

Phantom thickness (cm)	Agreement (%) (DTA=2.54 mm & ΔD= 3%)		
	Before CFM	After CFM	Discarding 2.54 mm edges
7	32.7	89.8	96.1
17	31.8	89.5	96.4
20	24.2	89.0	96.0
30	27.4	87.5	94.1

In empirical calibration methods, for example in Parsaei *et al*'s report (1998), although a flattening material placed in front of the radiation beam was sufficient enough to remove horn artefacts in the beam profiles, our results show that radiation profiles obtained using a 10 cm homogeneous phantom are not quite uniform. Furthermore, a significant decrease in agreement between EDR2 film-EPID measurements was observed in the off-axis areas (see Figure 4.10, a2 & b2). On the other hand, even with the use of flattening materials, a more accurate calibration method is required for dose profiles, measured using EPIDs, particularly in off-axis regions. On the other hand, the EPID dosimetric calibration method using flattening materials requires extra correction for off-axis areas to achieve accurate results.

Different gamma values were observed for inhomogeneous regions, compared to the same irradiation conditions for the homogenous phantoms. The main reason for the effectiveness of SLIC-EPID response in the inhomogeneous regions is the physical characteristics of the inhomogeneities. In this case, the physical characteristics of the bone are closer to those of soft tissue compared to the air, because the beam quality passing through the bone is higher than that of passing through the air. Moreover, the calibration procedure proposed here is performed using the radiation fluence map. Due to beam hardening, passing through phantoms the radiation spectrum especially in the off-axis area is changed. Because the average beam energy is greater than that on the central axis regions, the beam spectrum on the central axis is changed less as the radiation beam travels through a phantom. Therefore, the photon quality passing through the different materials produces different responses especially in the EDR2 films (As the field size increased to 24 × 24 cm^2, the deviation from ionization chamber measurements is approximately 5% for 6 MV photons) (Dogan *et al* 2002; Esthappan *et al* 2002).

The TPS, used in this study, overestimates the dose delivered to the ROI, where there are air inhomogeneities in the beam path (Battista and Sharpe 1992; Metcalfe *et al* 1997). The dose is calculated using the collapsed cone convolution superposition algorithm (Mackie *et al* 1985; Ahnesjo 1989). In this algorithm, the dose kernel is scaled based on the average density instead of the exact local density. This assumption leads to the overdose calculation in the air density areas (see Figure 4.14 series c). This phenomenon is clear in the transmitted dose maps before using the corresponding CFM. The use of CFM decreases the dose difference between TPS calculations and EPID measurements. In addition, the use of CFM, measured in air, overestimates the dose measurement when CFM is used for phantom/patient condition.

A significant difference was observed in the radiation field edges. Although the misalignment can be taken into account to some extent with the gamma function tool, the discrepancy in the edge area is large and cannot be corrected with conventional DTA values. We chose to exclude the disagreement in the peripheral ROI by excluding 2 pixels (2.54 mm) into the gamma function analysis. Due to the focus on the central part of radiation field, the radiation field edge is irrelevant for measurements. Therefore, this should not affect the results significantly.

4.5. Evaluation of maximum misalignment between evaluated dose maps

In order to find the maximum misalignment between dose maps obtained from the SLIC- EPID and TPS, the percentage agreement was investigated for a range of gamma function criteria. The DTA was varied from 1 to 4 pixels (1.27 mm to 5.08 mm) and the ΔD_{max} = 2.5 % was kept constant for all inhomogeneous phantoms. The results are shown in Figure 4.15. A significant increase in the agreement was observed with an increase in DTA from 1 pixel (1.27 mm) to 2 pixels (2.45 mm), while the agreement remains constant with the increase of DTA from 2 pixels to 3 or 4 pixels.

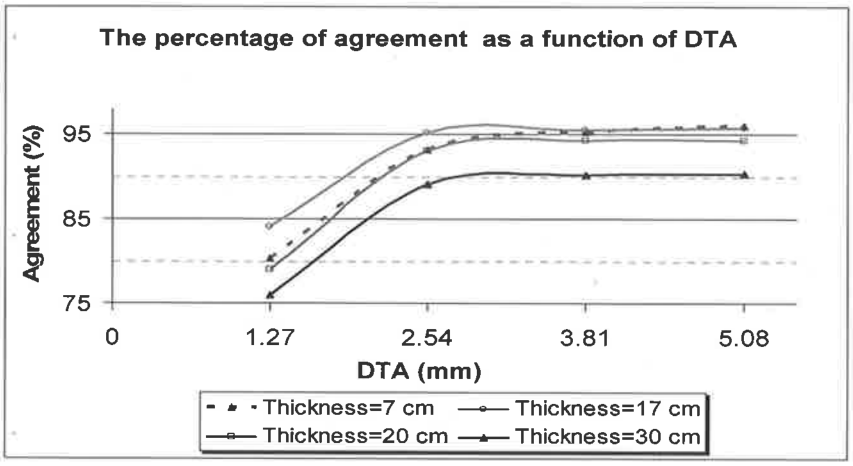

Figure 4.15. The variation of the percentage of agreement with DTA for EPID and TPS dose maps using gamma function algorithm for different thicknesses. ΔD_{max} was 2.5% in all cases.

Gamma function assessment is a suitable tool for comparing two-dimensional dose maps. As Figure 4.15 illustrates, it is also possible to identify the magnitude of the misalignment. In all cases, as presented in this chapter, the maximum misalignment was found to be 2 pixels because no significant variation of agreement was observed with the increase of DTA for more than 2 pixels. However, the gamma function is not able to discern between positive or negative dose differences as well as the direction of translational misalignments (see Appendix A).

4.6. Summary and Conclusion

In this chapter, the feasibility of relative transmitted dose determination using EPIs was investigated. In order to verify a comprehensive two-dimensional calibration method, several experiments were performed. Firstly, SLIC-EPID fluence maps for open field and wedged fields, for a range of field sizes, were compared with those measured using EDR2 films. Secondly, the transmitted dose distributions measured using EPID in the presence of homogeneous and inhomogeneous phantoms were compared to those measured using EDR2 film as well as to those calculated using TPS. Moreover, the determination of maximum misalignment using gamma function was also investigated.

Although the SLIC-EPIDs are routinely calibrated to generate uniform responses in a flood radiation field, they can also be used for two-dimensional dosimetry, provided that an appropriate dosimetric calibration is used. Application of an appropriate CFM accurately reconstructs the horns of radiation profiles removed during calibration for the portal imaging mode. The consistency between transmitted dose distributions measured using SLIC-EPID, EDR2 film and those calculated using TPS, showed that the SLIC-EPID can be used as a reliable two-dimensional dosimeter for pre-treatment assessments.

In order to enhance the agreement between measurement and calculation, Due to enhancement of dose calculation algorithms, the use of new versions of TPSs decreases the uncertainty of dose calculations (Williams and Metcalfe 2006). The empirical dosimetric calibration method can also be expanded for other EPID types and EPI acquisition settings. Due to the limitation in EPI acquisition time, further investigation is required to evaluate the response of SLIC-EPID for absolute dosimetry.

The dosimetric calibration method, proposed in the current work, can be applied in traditional radiation therapy, 3D CRT and sIMRT. Due to the limitation in EPI acquisition time and EPI pixel values dependency on the linac repetition mode, further investigation is required to use SLIC-EPID as a transmitted dosimeter for dynamic IMRT. In addition, the SLIC-EPID sensitivity when detecting either the phantom/patient shift or patient modification during treatment should also be taken into consideration.

Chapter 5. Evaluating the SLIC-EPID sensitivity for transmitted dosimetry purposes

5.1. Introduction

This chapter attempts to investigate the SLIC-EPID sensitivity as a two-dimensional transmitted dosimeter. The variation of the phantom/patient thickness and the variation in transmitted dose with the patient/phantom set-up uncertainties are studied. The minimum detectable variation of phantom thickness in different conditions and the minimum phantom/patient shifts that can be detected using the SLIC-EPID are determined.

5.2. The relationship between transmitted dose and phantom characteristics

The relationship between EPID pixel values and the attenuator thickness is evaluated and an exponential attenuation of the pixel values with increasing attenuation thickness on the central axis is reported (Roback and Gerbi 1995). Converting the EPID pixel values to dose values, the relationship between transmitted dose values, measured using

EPID, and phantom thickness is investigated on the central axis (Zhu *et al* 1995; Essers *et al* 1996). The relationship between ionization current, obtained from ion chamber measurements, and EPID pixel values is also investigated and the relationship between transmitted dose values and a range of phantoms with different thicknesses and materials is reported (Parsaei *et al* 1998). The maximum deviation of SLIC-EPID pixel values for two photon energies (6 and 10 MV) for Perspex, aluminium and lead were found to be 2%, 3% and 2.1% respectively. The dependence of EPID detector response as a function of patient thickness is investigated and a linear decrease in the corrected EPID response with the increase of absorber thickness was observed (He *et al* 1999). The variation of EPID pixel values with the increase of the thickness of the lead attenuator on the central axis of radiation field is also reported (Zhu *et al* 1995). Menon and Sloboda, in a study of compensator quality control procedures with an a-Si EPID showed that variation of the EPID response in the presence of attenuators in the beam path for a field size 20 × 20 cm^2 at SSDs of 105 cm and 140 cm, could be fitted with exponential curves (2003).

Although the correlation between transmitted dose, measured with different types of commercial EPIDs, and patient/phantoms thickness has been reported, the minimum detectable change of patient/phantom thickness, occurring as a result of organ motion or due to spatial shifts, has not been investigated.

In this work, experimental data was collected to investigate the dosimetric properties of EPIDs in the presence of homogeneous and inhomogeneous phantoms. Firstly, the variation of measured transmitted dose in the EPID with the increase of a homogeneous phantom thickness on the central axis was investigated. The relationship between transmitted dose and SLIC-EPID pixel values was investigated and the rate of transmitted dose variation with the change of phantom thickness was investigated for a range of phantom thicknesses. Several phantom thicknesses were selected as reference and the rate of dose variation per 1 centimetre of phantom thickness was investigated. Secondly, the effect of inhomogeneity position in the direction of radiation beam was also investigated.

In this part of the thesis, the relationship between the transmitted dose, measured using a SLIC-EPID, and phantom thickness for a range of homogenous phantoms, has been investigated. Firstly, the variation on the transmitted dose, measured using SLIC-EPID, with the increase of a homogeneous phantom thickness was investigated. The relationship between transmitted dose and SLIC-EPID pixel values was investigated and the rate of transmitted dose variation with the change of phantom thickness was investigated. Secondly, the variation in transmitted dose with a shift of a 2 cm inhomogeneity in the direction of radiation beam has been investigated.

5.2.1. The variation of transmitted dose values with the change of phantom thickness

Prior to the clinical use of EPIDs for two-dimensional dosimetric purposes clinically, the variation in the transmitted dose values with changes in phantom/patient thickness has to be investigated. In order to do this, several experiments were designed and performed to evaluate the SLIC-EPID dose response in the presence of various phantom thicknesses.

As Figure 5.1 illustrates, the thickness of a homogenous phantom varied from 0 cm to 28 cm using RW3 layers. In order to reach the electronic equilibrium in the EPID layer, 5 mm RW3 was used as additional build-up layer (see section 3.2.1). For each measurement, two consecutive EPIs were acquired and converted to the dose values using the developed calibration method (section 3.3) at the SED = 140 cm for a 10× 10 cm^2 field size, with a linac repetition rate of 300 MU/min. A 10 × 10 pixel matrix was selected as the Point Of Interest (POI) on the central axis. The area represented by this pixel array is 0.90 × 0.90 cm^2 at the isocentre and 1.27×1.27 cm^2 at the EPID sensitive layer. This array size was chosen to minimize statistical fluctuation in pixel response with enough spatial resolution.

The relationship between transmitted dose and the thickness of the homogeneous phantom was found. The variation in transmitted dose with the position of POI in the phantom was then investigated. The reliability of EPID response in the presence of a phantom was investigated and the relative error, defined as the ratio of the calculated standard deviation and the EPID mean dose value, was measured.

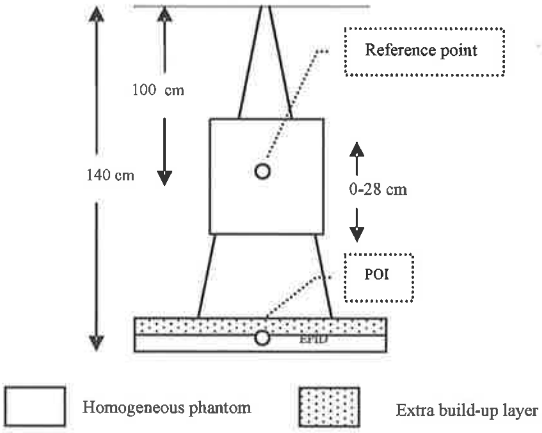

Figure 5.1. Schematic view of the measurement set-up used to evaluate the EPID response versus phantom thickness.

The variation in absolute transmitted dose values versus the phantom thickness is shown in Figure 5.2. The x and y axes represent the phantom thickness and the transmitted dose measured using SLIC-EPID, respectively. The transmitted dose decreases exponentially with the increase of the phantom thickness.

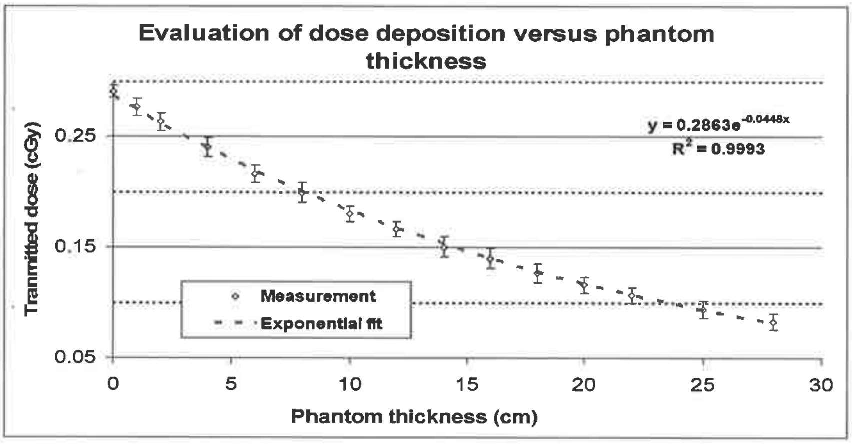

Figure 5.2. The variation of relative EPID dose with the position of the reference point.

As Figure 5.2. shows, the variation in transmitted dose measured in the EPID sensitive layer with phantom thickness is not linear. In order to describe this relationship in greater detail, this variation was investigated for various phantom thicknesses. Several phantoms with different thicknesses were selected as reference phantoms (6, 10, 16, 20 and 25 cm). Variation in relative transmitted dose with the change of phantom thickness, (±4 cm), was then investigated. The results are shown in Figure 5.3. The x and y axes represent, respectively, the variation in phantom thickness and the relative transmitted dose difference. To estimate the relative transmitted dose variation versus the change of phantom thickness, linear fits were added to the graphs. Although the linear function does not represent the most precise fit to the data, it can be used to estimate the relative dose difference for a given change of phantom thickness from the reference phantom. The results show that the maximum and minimum dose difference for 1 cm phantom thickness were found to be 5.4% and 3.9%, respectively, for a range of homogenous phantom thicknesses.

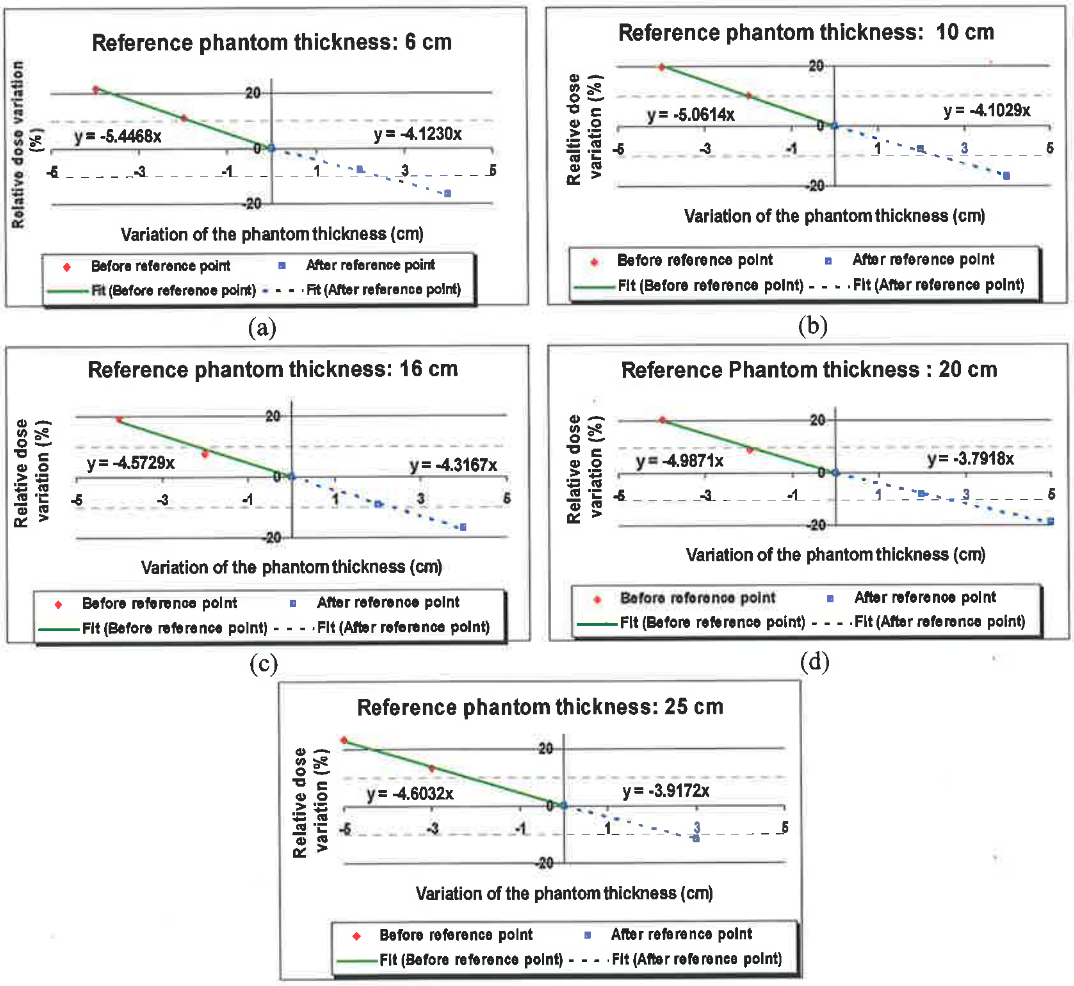

(a) (b) (c) (d) (e)

Figure 5.3. The variation in relative transmitted dose with the change of phantom thickness for several defined reference phantom thicknesses: (a) 6 cm, (b) 10 cm, (c) 16 cm (d) 20 cm, and (e) 25 cm.

Due to the noise level of SLIC-EPID response (see section 3.2.3), the reliability of response must be at least two times more than noise level. The minimum detectable thickness is based on the minimum variation of 2.2% of relative dose measured using SLIC-EPID. Using data shown in Figure 5.3, the minimum detectable phantom thickness change for a range of phantom thicknesses is indicated in Figure 5.4. An exponential increase in the minimum detectable thickness change was observed with the increase of the thickness of the homogenous phantom. The minimum and maximum values for the minimum detectable in the changing patient/phantom thickness were found to be 2.9 mm and 6.7 mm for the top and bottom 1 cm slabs, respectively for a 20 cm homogenous thick phantom. The SLIC-EPID's ability to detect the minimum detectable thickness decreases as phantom thickness increases. The main reason for this may be the decrease of exponential slope, shown in Figure 5.2, and consequently the decrease in relative dose variation as phantom thickness increases.

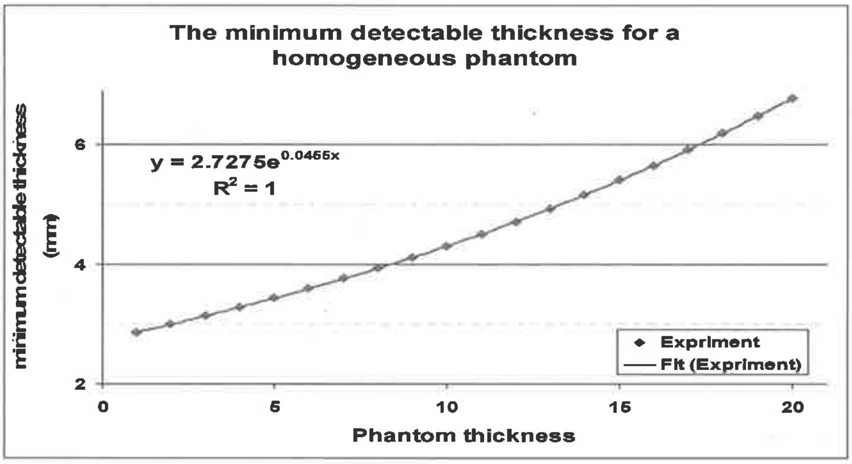

Figure 5.4. The minimum detectable thickness of a homogeneous phantom using SLIC-EPID response.

The relative error, defined as the ratio of the calculated standard deviation and the EPID average dose value for a 10×10 pixel matrix in the centre of radiation field, increases with the phantom thickness. The increase in the relative error of the transmitted dose with the increase of phantom thickness is shown in Figure 5.5. The x and y axes represent the phantom thickness and relative error of transmitted dose values, respectively. The relative error did not exceed 0.7%.

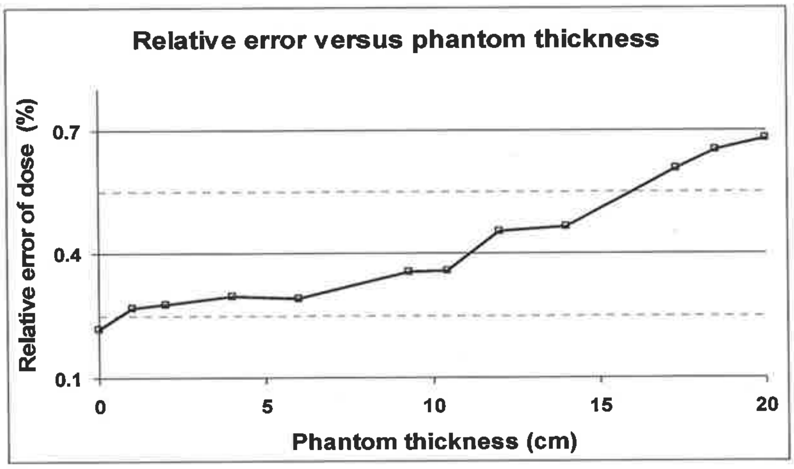

Figure 5.5. Variation in relative error of EPID dose values as phantom thickness increases.

The minimum detectable change of phantom thickness using transmitted dose measurements depends on: firstly, the accuracy of devices used for transmitted dose measurements; and secondly, beam energy. Due to the change in effective thickness of patient with the organ motion or patient set-up, this experiment determines the system's ability to detect the change of the patient/phantom movements, especially patient set-up and anatomical changes, during the course of treatment.

The EPID dose values measured on the central axis using a SLIC-EPID in the presence of homogeneous phantoms obey an exponential form (see Figure 5.2). This was found to be in agreement with curves and equations reported in the literature (Essers *et al* 1996; Menon and Sloboda 2003). The differences between exponential equation parameters introduced by Menon and Sloboda and this thesis can be due to different calibration procedures and different type of EPIDs. Due to the SLIC-EPI noise level in the current work, being approximately 1%, if the percentage of dose deposition per increase of phantom thickness by one centimetre is less than 2%, the SLIC-EPID is not able to detect this thickness change.

This part of the current work showed that a 4 mm and a 6 mm change in phantom thickness in the central layer and lower layers of a 20.0 cm thick homogeneous phantom can be detected using SLIC-EPID. The uncertainty of detection increases as phantom thickness increases, because the dose deposition depends exponentially on the phantom thickness. As discussed before, the variation in relative transmitted dose with the change of reference phantom thickness is not linear (see Figures 5.2 and 5.3). For instance, in a typical reference phantom, 6.0 cm thick, the rates of relative dose delivered to the phantom per centimetre before and beyond the reference point are 5.45% /cm and 4.12% /cm, respectively. With the increase of variation in the phantom thickness, the increase in beam quality with depth and exponential attenuation are the main reasons for the variation in the dose deposited at the EPID layer. In other words, the low energy photons are absorbed in upper layers of the phantom and lower layers interact with harder X-rays.

With an increase in phantom thickness, the probability of scattering processes taking place will increase. In addition, due to more absorption of photons passing through the phantom, the radiation fluence reaching the EPID surface decreases as phantom thickness increases. As a result, with an increase in scattering component, as well as with a decrease in photon intensity, uncertainty of the dose measurement will increase. As a result, the increase in the relative error of the EPID dose values increases with an increase in phantom thickness. The maximum relative error in this work was found to be 0.7 %. This is an improvement on other published data, for example 2% in one particular study (Parsaei *et al* 1998).

5.2.2. Dependence of the transmitted dose on the position of an inhomogeneity

To evaluate the effect of an air gap position on the transmitted EPID dose values, the variation in transmitted dose on the central axis with the change of an air gap position was investigated. A 2 cm thick foam layer was used to simulate the air gap, which was initially located on the top of an 18 cm thick homogeneous RW3 layers. The position of the air gap was then shifted through the phantom in 2 cm steps, moving the air gap inhomogeneity from the top to the bottom of the 18 cm RW3 layers (see Figure 5.6). The acquired EPIs were converted to the transmitted dose maps using the calibration method described in section 3.4. The ROI was selected in measured dose maps surrounded by the 50% isodose line image boundary using a MATLAB in-house code

(MATLAB 6.5 Mathworks Inc.). The radiation profiles were normalized to the value on the central axis for a 10 × 10 pixel matrix.

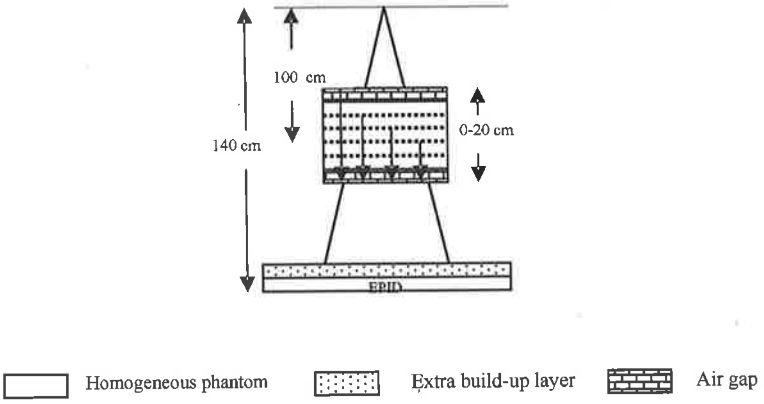

Figure 5.6. Schematic view of the measurement set-up used to evaluate the EPID response versus the inhomogeneity position in a phantom, in the direction of the radiation beam.

The EPIs, acquired for a RW3 phantom and incorporating an air gap in the different position along the central axis, were analysed to determine the average pixel value of an array of 8 × 8 pixels on the beam's central axis. The area represented by this pixel array is 0.7 × 0.7 cm² at the isocentre and 1 × 1 cm² at the EPID sensitive layer. The transmitted dose values measured for 10 various air gap positions were normalized relative to the first measurement. The results are shown in Figure 5.7. The x and y axes represent the distance of the centre of the air gap from an 18.0 cm thick homogeneous phantom surface and relative dose values, respectively. No significant variation was observed in the transmitted dose values with the change of air gap geometry inside of the phantom. The maximum and minimum fluctuations were found to be less than 0.5% of relative average transmitted dose value.

The relative transmitted dose inplane and crossplane profiles acquired for a range of air gap positions are shown in Figure 5.8. The x and y axes represent the distance from the central axis and relative transmitted dose, respectively. Although several discrepancies were observed in the left part of crossplanes, no systematic or significant variations occurred between inplane and crossplane profiles acquired for different positions of the 2 cm thick air gap.

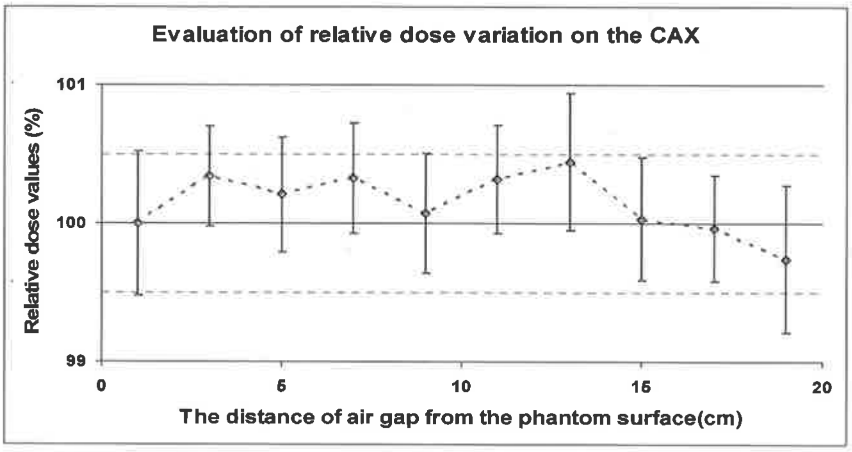

Figure 5.7. Variation of transmitted dose values on the central axis with the air gap position in an 18 cm thick homogeneous RW3 layers.

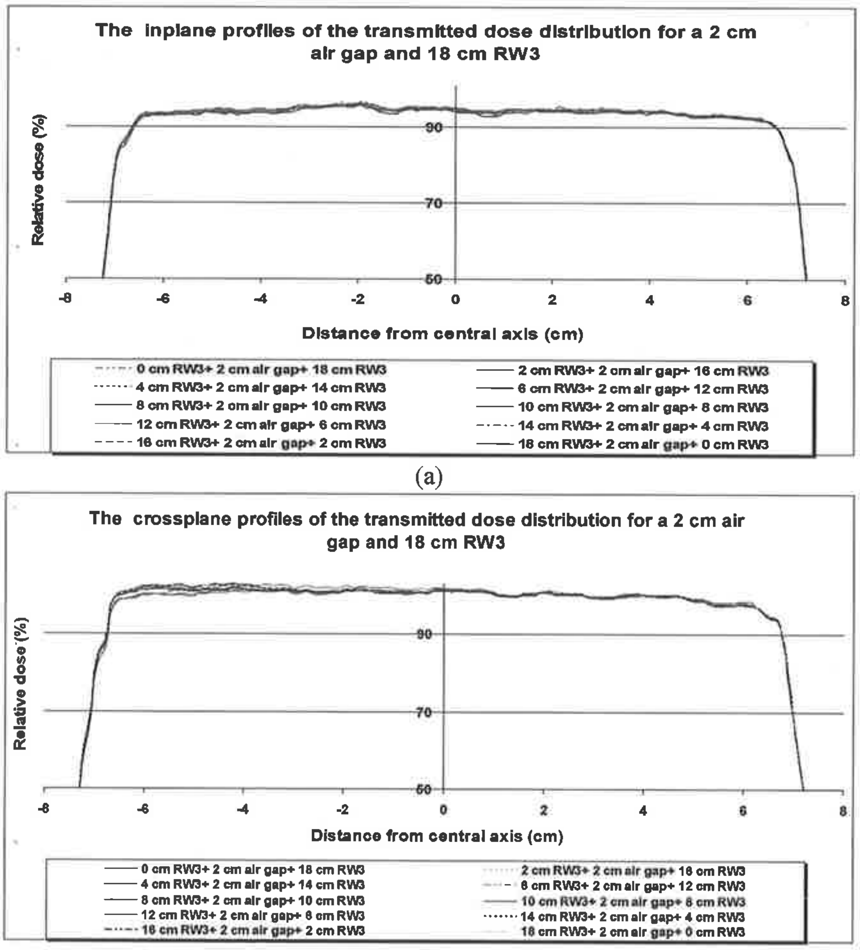

(a)

(b)

Figure 5.8. (a) Inplane and (b) Crossplane profiles of the relative transmitted dose maps measured using a SLIC-EPID for various positions of a 2 cm air gap within the 18 cm RW3 phantom.

As Figures 5.7 and 5.8 show, the position and shift along the central axis of inhomogeneity inside of the phantom cannot be detected using portal images. Although the X-ray beam spectrum varies for different positions of the inhomogeneity, the total effective path for the radiation beam is the same for all measurement conditions. The variation in beam quality with the inhomogeneity position leads to a variation in scattered photons. However, due to the large air gap situated between the phantom and portal imager, the difference arising from the different scattering component can be ignored.

The impact of magnification of inhomogeneity was eliminated by using a large inhomogeneity: as large as the homogenous layers, the edges of which were located out of the radiation field. However, phantom inhomogeneity interface can be used to find the inhomogeneity located in the direction of the radiation beam.

5.2.3. Summary

The minimum detectable variation of the phantom thickness as well as the impact of the shift of inhomogeneity inside a phantom are evaluated using transmitted dose measured by a SLIC-EPID. In order to find the rate of dose deposited, several reference phantom were defined and the variation of dose delivered to the phantom thicknesses in the vicinity of reference phantoms were investigated. Two cm thick foam layer, as air gap, was shifted in the beam direction to evaluate the variation of transmitted dose with the shift of inhomogeneity position inside of phantom. An exponential decrease of the transmitted dose values was observed with the increase of the thickness of attenuators. The maximum and minimum rate of dose deposited per unit of phantom thickness was found to be 5.4% /cm and 3.9% /cm, respectively. The minimum detectable variation in the phantom thickness depends on the phantom thickness significantly. Due to the reproducibility and noise level of SLIC-EPID, a 3 mm and 6.5 mm of the thickness variation can be detected with a good reliability for a 6 cm and 20 cm thick homogeneous phantoms, respectively. The relative error of EPID dose values increases with an increase of phantom thickness for both data sets. The relative error did not exceed 0.7%. No significant variation in transmitted dose inplane and crossplane profiles were found with the shift of inhomogeneity in the beam direction.

5.3. The impact of patient/phantom positioning uncertainties on the transmitted dose maps

The anatomy and position of a patient during the course of radiation therapy usually varies compared to those used during planning procedures. In addition, due to patient movement, inaccuracy in patient positioning and organ motion, the measured absorbed dose distribution varies from the planned absorbed dose distribution. The efficiency of modern radiation therapy, due to smaller margins, can be increased by monitoring the uncertainties of dose delivery. Limiting the sources of these uncertainties can be used to increase the accuracy of treatment. Although the variation in patient position and patient movement can be controlled reasonably with an accurate patient set-up procedures and immobilization devices, internal organ motions present a challenge in radiation therapy.

The geometrical uncertainties including set-up errors and internal organ motion, are derived from portal images acquired during the course of radiation therapy. Although films are generally used to assess the set-up uncertainties during a radiation therapy session, the long processing procedure is a significant drawback for them. In contrast, EPIDs, used in recent decades for radiation therapy verifications (Boyer *et al* 1992b), can be more helpful for high precision QA of patient set-up. Set-up errors can be minimised using off-line EPID images (Bel *et al* 1993; 1996), before the next course, and on-line, when the patient is placed on the treatment couch (Vigneault *et al* 1997; Van de Steene *et al* 1998; Stroom *et al* 2000; Brock *et al* 2002; Pouliot *et al* 2003; Vetterli *et al* 2004). EPIDs have also been used to detect organ movement during a radiation therapy course (Kroonwijk *et al* 1998; Stroom *et al* 2000; Kaatee *et al* 2002) and the minimum detectable patient displacement is reported to be larger than 5 mm.

Although EPIDs have been used for dosimetric purposes, the impact of patient/phantom positioning uncertainties on the transmitted dose maps measured using EPIDs are not clear. As a result, the minimum detectable shift of patient/phantom with a given detector is evaluated. Furthermore, the dosimeter capability for patient/phantom shift detection for regular/irregular field shapes, and the impact of phantom/patient shift on the transmitted dose distributions, measured using a SLIC-EPID, are also discussed.

Several MLC radiation fields including rectangular, circular and diamond shape were manually created using a commercial Varian's MLC shaper software. The radiation field sizes were selected for 10 × 10 cm^2, 5 cm radius and 10 cm diameter, for rectangular, circular and diamond shape fields, respectively. The conventional jaws were placed 1 cm behind of maximum retracted leaf in the radiation field for all cases. An inhomogeneous chest phantom was fixed on the couch to find the amount of the minimum detectable shift of patient during dose delivery. The couch was then shifted laterally from 1 mm to 5 mm for all radiation fields.

Two consecutive EPIs were acquired and averaged for each situation with a 300 MU/min repetition rate at SED = 140 cm. The SLIC-EPID pixel values were converted to transmitted dose maps (see section 3.4). The first transmitted dose maps for each field shape, were selected as reference dose maps. The relative dose difference and the corresponding gamma maps were then achieved. These will be described in the following sub-sections.

5.3.1. Evaluation of patient positioning uncertainties using relative dose difference map

Typical relative dose difference maps between the reference and shifted relative transmitted dose maps for 1 mm, 3 mm and 5 mm phantom shifts in the lateral direction are shown in Figure 5.9 for rectangular, circular and diamond shape radiation fields. Due to the noise level of SLIC-EPID, the relative dose difference values within 1% are shown in grey.

The average and maximum dose difference between two series of reference transmitted dose maps for all cases, evaluated in this experiment, were found to be approximately 0.5% and 22 % respectively in the irradiated part of transmitted dose maps. With a 1 mm, 3 mm and 5 mm lateral shift of the chest phantom, the maximum relative dose difference values were found to be 6.9%, 16.1%, 22.2%, respectively.

In order to describe this difference in greater detail, the crossplane profiles of relative dose difference maps, which are along the chest phantom shift, and a typical relative dose profile, are shown in Figure 5.10. With a 1 mm phantom lateral shift, a significant difference in the relative dose values was observed. However, a significant inconsistency between corresponding crossplanes, obtained from different field shapes, was observed. The maximum and minimum difference in relative dose values were found for circular and rectangular radiation fields, respectively. In contrast, for greater than 2 mm phantom shift, no significant differences were observed for crossplanes profiles obtained from different field shapes.

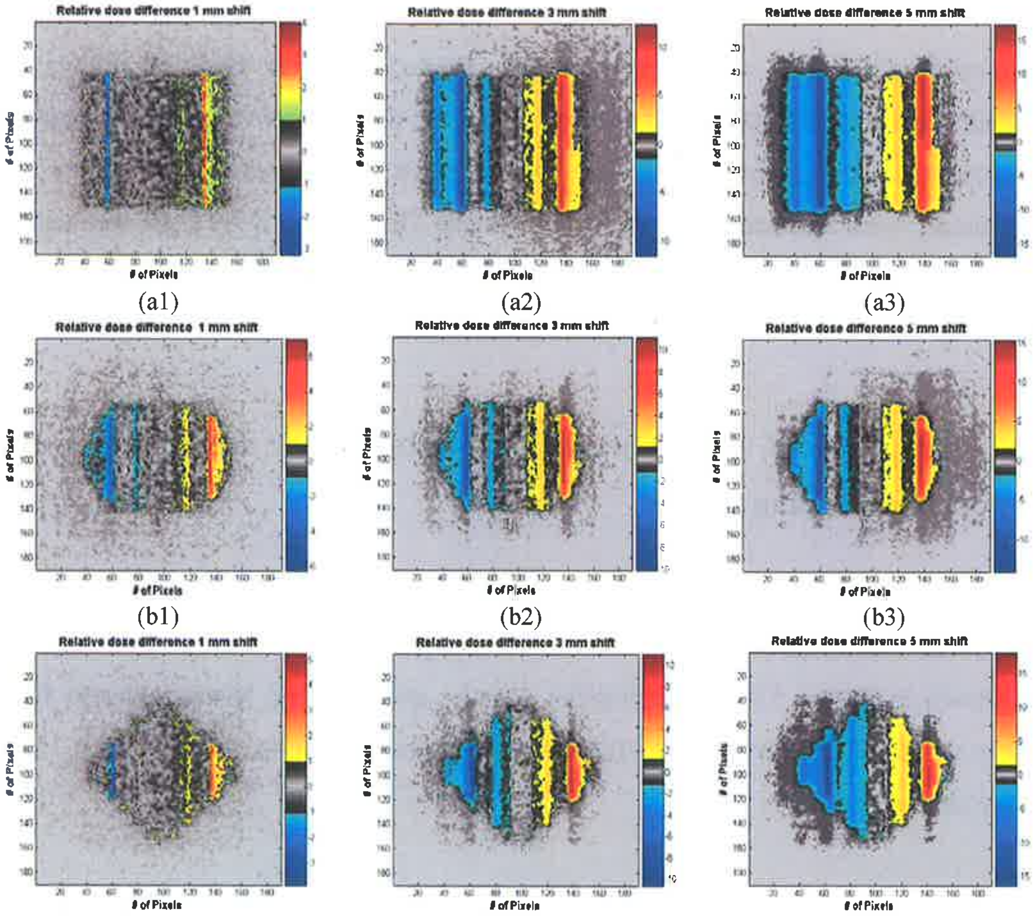

(a1) (a2) (a3)

(b1) (b2) (b3)

(c1) (c2) (c3)

Figure 5.9. Relative dose difference maps (series a) for a 10 × 10 cm² rectangular field (series b) for a 5 cm radius circular field (series c) for a 10 cm diameter diamond shape field with 1, 3, and 5 mm lateral shift of the chest phantom.

As Figures 5.9 shows, phantom shifts from 1 mm to 5 mm can be detected in all cases. The minimum possible shift (the accuracy of couch movement is 1 mm) produces approximately 6% change in relative dose difference in the inhomogeneous areas. The relative dose difference values depend on the inhomogeneities' conditions. This is significantly larger than the noise level of EPIs acquired using a SLIC-EPID (see section 3.2.3). Additionally, in Figure 5.10 crossplane profiles show that in high gradient regions a 1 mm shift of the phantom is detectable. Although several inconsistencies were observed with regard to the change in radiation field shape, with the increase of phantom shift greater than 2 mm the crossplane curves were found to be similar for all radiation field shapes.

5.3.2. Evaluation of patient positioning uncertainties using gamma function algorithm

The agreement between reference and shifted dose maps were also assessed using gamma function algorithm with DTA = 2.54 mm and $\Delta D_{max} = 3\%$, which are the routine criteria used for clinical purposes (Childress and Rosen 2003; Agazaryan *et al* 2003; Bucciolini *et al* 2004; Van Esch *et al* 2004; Sandilos *et al* 2004). Typical gamma maps for 1 mm, 3 mm, and 5 mm phantom shifts are shown for rectangular, circular and diamond shape radiation fields in Figure 5.11.

Two tools, relative dose difference map and gamma maps, have been used to detect patient positioning uncertainties. Due to the noise level in EPIs (approximately 1%, section 3.2.3), the dose difference map is found to be a sensitive tool for detecting an approximate 1 mm shift with reasonable accuracy. A variation in relative dose difference values with the change of radiation field shape was observed for 1 mm shift. In specific conditions, when dose map alignments are accurate, relative dose differences can detect 1 mm patient/phantom positioning uncertainties. However, during treatment sessions, due to the patient positioning misalignment, the applicability of this tool decreases.

More details about gamma scores are provided in Table 5.1. The average agreement between two series of reference EPIs acquired consecutively was found to be approximately 98% for all cases (no phantom shift). With 1 and 2 mm phantom shift no significant variation in gamma scores occurred. A significant variation in gamma scores was observed for 3 mm lateral shift. The increase in disagreement after gamma score correction for radiation field size is shown in Figure 5.12. After 3 mm shift, a 1 mm phantom shift causes approximately 5 % increase of disagreement between corresponding and reference EPIs.

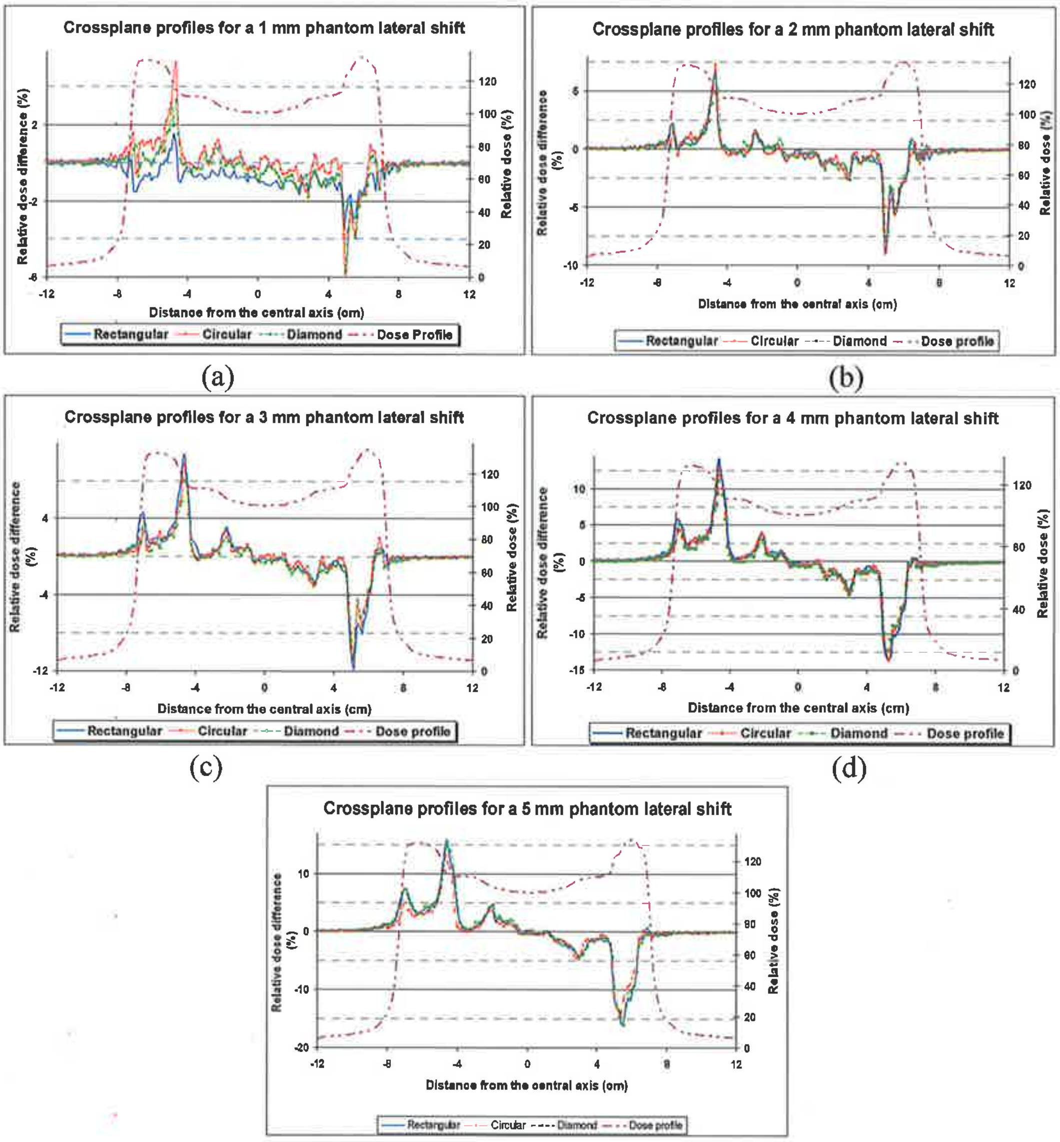

(a) (b)

(c) (d)

(e)

Figure 5.10. Crossplane profiles of relative dose difference between reference and 1 mm to 5 mm phantom-shifted dose maps (figures (a) to (e) respectively). The crossplane of the corresponding reference relative dose profile is also shown.

Gamma function is used extensively to evaluate the agreement between reference and evaluated two-dimensional dose maps. In the clinical context a misalignment criterion is defined as DTA and it is typically 3 mm. This criterion compares dose values of POI with other corresponding dose values located around 3 mm of reference POI. As a result, any misalignments with less than DTA values for dose values within the dose difference criterion are less than 1 (PASSED). This is the main limitation of gamma function when detecting positioning uncertainties within DTA. Defined as DTA = 0, the gamma function is changed to a specific dose difference map with passed/failed criterion for dose tolerance only.

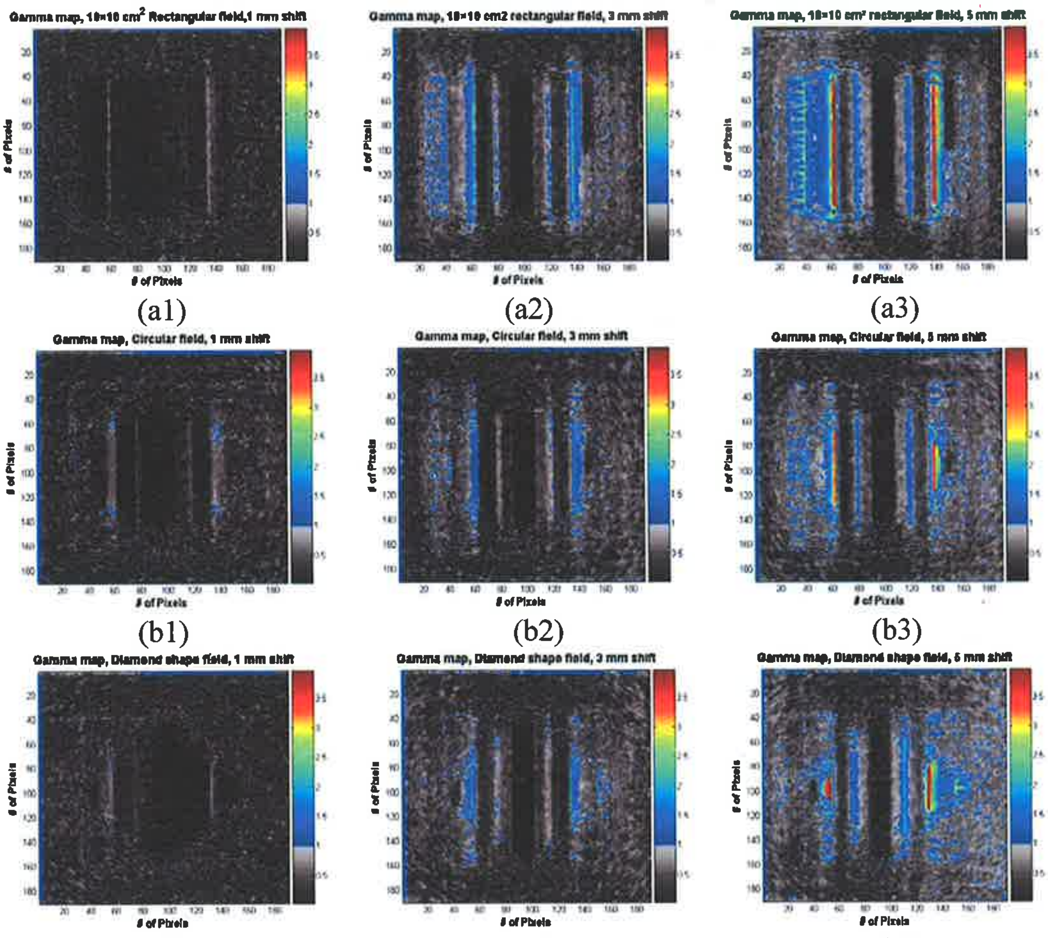

(a1) (a2) (a3)

(b1) (b2) (b3)

(c1) (c2) (c3)

Figure 5.11. Gamma maps of reference and phantom-shifted relative dose maps: (series a) for a 10×10 cm² rectangular; (series b) for a 5 cm radius circular field; (series c) 10 cm diameter of a diamond shape radiation field. Gamma function criteria were 3%/2.5mm.

In short, the relative dose difference map is a sensitive tool for intra-course assessment. The minimum phantom/patient shift detection using relative dose difference map is 1 mm. For inter-course and TPS data set evaluations, due to the unavoidable misalignment, the gamma function is the alternative tool. The minimum detectable phantom/patient shift using gamma function depends on the DTA criterion setting. In this case, with DTA= 2.54 mm (two pixels of SLIC-EPID), the minimum phantom/patient detectable shift is 3 mm.

The SLIC-EPID pixel size is 1.27 × 1.27 mm2 and 1 mm shift affects at least one row or column. However, when considering EPI magnification, a 1 mm shift is 1.4 mm at the EPID sensitive layer for SED = 140 cm used in this study. This involves at least two rows or columns of EPID ionization chambers for minimum phantom/patient displacements. The smaller pixel size of the imager or the increase in magnification factor, increases the resolution of positioning uncertainties.

Table 5.1. The agreement percentages obtained from gamma function evaluation between reference and phantom-shifted EPIs for a range of radiation field shapes.

Phantom shift (mm)	Agreement (%)		
	10×10 cm² rectangular	5 cm radius circular	10 cm diameter diamond
0	98.3	98.5	97.9
1	98.4	98.1	98.4
2	97.3	97.2	97.3
3	91.1	95.1	95.6
4	85.1	91.0	93.7
5	79.6	89.6	86.9

It should also be pointed out that the accuracy of treatment couch set-up is 1 mm. This increases the uncertainty for 1 mm phantom shift. The discrepancy between crossplane profiles observed in Figure 5.10 (a) may originate from this source of uncertainty. In addition, the specific radiation field shape changes the contribution of scattered photons measured using SLIC-EPID.

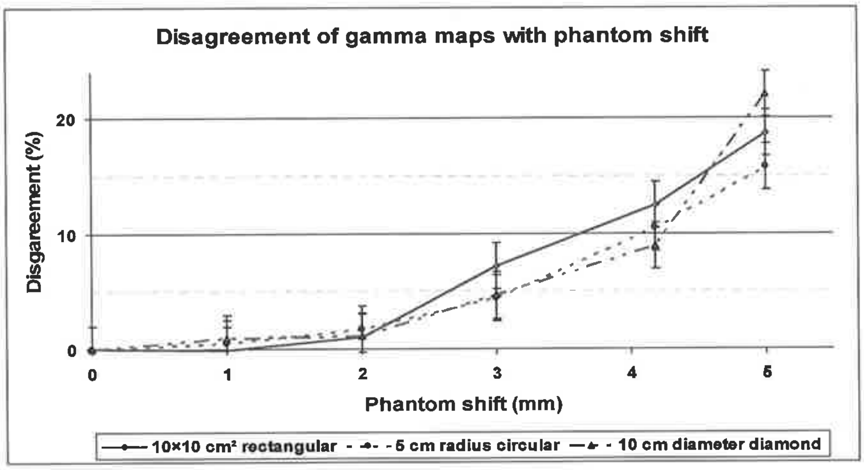

Figure 5.12. The increase in disagreement between reference and phantom-shifted dose maps for rectangular, circular and diamond shape radiation fields.

5.4. Summary and Conclusion

In assessing the EPID response for dosimetric purposes, the variation in EPID dose values with the change of phantom thickness was investigated. EPID dose values decrease exponentially when phantom thickness increases. A good exponential fit was obtained for dose values measured using an EPID as a function of phantom thickness. Several phantoms with different thicknesses were selected as reference phantoms (6, 10, 16, 20 and 25 cm). The results showed that a 3 mm and 6.5 mm change in thickness can be detected with a good reliability for a 6 cm and 20 cm thick homogeneous phantoms, respectively using a transmitted dose deposited on the sensitive layer of a SLIC-EPID. In addition, disregarding the magnification artefacts, no significant difference was observed regarding the shift of inhomogeneity in the beam direction.

The EPIs can be used to detect the phantom/patient shifts for intra/inter course of treatment. In the controlled misalignment of patient set-up, a 1 mm shift can be detected with high accuracy and reliability using relative dose difference maps. For two independent conditions, i.e. two individual treatment courses, the use of gamma function is unavoidable. The minimum detectable shift in this case depends significantly on the gamma function criteria settings (here the minimum detectable shift is 3 mm).

This indicates that SLIC-EPID is a sensitive tool for dosimetry and with 1-3 mm patient positioning uncertainties, leads to a significant difference in the dose distributions measured using a SLIC-EPID.

Chapter 6. Evaluation of dosimetric characteristics of multileaf collimator fields using a SLIC-EPID

6.1. Introduction

In order to achieve highly conformal dose delivery in Conformal Radiation Therapy (CRT) and Intensity Modulated Radiation Therapy (IMRT), irregular radiation fields are generally used. MLCs are excellent substitutes for lead and Cerrobend blocks due to the shorter set-up time (Brewster *et al* 1995; Helyer and Heisig 1995), convenience of use, cleaner environment and automated radiation field set-up (Boyer *et al* 1992b). As a result of the complexity of MLC performance, an adequate quality assurance procedure is required. Many dosimetric characteristics of the MLC fields such as depth dose, isodose curves, field sizes effects, penumbra regions, and leaf positioning properties have already been comprehensively studied (Boyer *et al* 1992b; Galvin *et al* 1993; Huq *et al* 1995; Klein *et al* 1995; Palta *et al* 1996; Boyer and Li 1997; Stasi *et al* 1999; Pasquino *et al* 2001; Huq *et al* 2002; Cheng *et al* 2003).

Before investigating the SLIC-EPID dosimetric response for IMRT fields, the MLC radiation field characteristics from the dosimetric point of view are discussed in this chapter. Several characteristics of MLC radiation fields including the comparison of dosimetric characteristics of MLC fields with conventional radiation fields, and the evaluation of MLC leaf positioning are presented.

6.2. Dosimetric characteristics of MLC and conventional fields

The radiation fields set up using MLCs have different properties compared to those set up using conventional jaws (Boyer *et al* 1992b; Brewster *et al* 1995; Palta *et al* 1996; Stasi *et al* 1999; Klein and Low 2001; Huq *et al* 2002; Killoran *et al* 2002; Kwok *et al* 2004; Chow *et al* 2005). This section concentrates on several dosimetric characteristics of the MLC radiation field including: characteristics of the radiation field size; and penumbra regions of the transmitted dose maps measured using a SLIC-EPID. The characteristics of the MLC radiation fields have been evaluated previously using ionization chamber and radiographic films (Boyer *et al* 1992b; Jordan and Williams 1994; Huq *et al* 1995; Klein *et al* 1995; Palta *et al* 1996; Stasi *et al* 1999; Pasquino *et al* 2001; Boyer *et al* 2001b; Huq *et al* 2002; Kwok *et al* 2004). The width of MLC field penumbra measured using a SLIC-EPID has been reported (Curtin-Savard and Podgorsak 1997). However, due to the limitation of the experiment in the above citation to a rectangular field, and due to the further development of the supporting software and electronics used in the latest versions of SLIC-EPIDs as used in the current work, further study is required to assess the suitability of EPID for QA of MLCs characteristics.

Research into the radiation field penumbra (transmission peunmbra), defined as the region limited by 80% - 20% isodose lines, is reported in several studies that used films (Boyer *et al* 1992b; Galvin *et al* 1993; Jordan and Williams 1994; Frazier *et al* 1995; Huq *et al* 1995; Klein *et al* 1995; Palta *et al* 1996; Boyer and Li 1997; Stasi *et al* 1999; Pasquino *et al* 2001; Childress *et al* 2002; Huq *et al* 2002; Killoran *et al* 2002; Butson *et al* 2003; Cheng *et al* 2003; Tangboonduangjit *et al* 2004; Chow *et al* 2005). It has been shown, for example, that the penumbra region of MLC radiation fields is slightly wider (by 1-3 mm) than those set up using conventional collimator jaws (Boyer *et al* 1992b; Cheng *et al* 2003). In several circular, square, and irregular fields for patients with cancer of the head and neck, lung and pelvis, the field penumbra width for all MLC fields was approximately 2 mm larger than those with conventional blocks (Frazier *et al*

1995). Although films are useful tools, a tool or procedure that would enable MLC field characteristics to be assessed quickly, is preferred.

This chapter discusses the SLIC-EPID's ability to assess the properties of radiation fields that utilize using MLC leaves and conventional jaws. In addition, in contrast to other similar studies, the two-dimensional transmitted dose values are used instead of raw EPI pixel values. Although this decreases the image quality because more processing is required in the primary data set, useful information can be obtained from the dosimetric point of view.

6.2.1. Comparison of radiation field size set up using conventional collimators and MLCs

All MLC fields were generated using the Varian commercial MLC shaper software. Several EPIs were acquired for nominal radiation field sizes ranging from 3 × 3 cm^2 to 15 × 15 cm^2 (on the central axis) using conventional collimators and MLCs. All EPIs were converted to relative dose maps using the dosimetric calibration as described in section 3.4. The radiation field was selected as an area surrounded by 50% of isodose line using an in-house code written in MATLAB. For MLC field measurements, in order to reduce extra-transmission through and between MLC leaves, the conventional collimators were placed 1.0 cm behind the retracted MLC leaves positions. The radiation field sizes were then compared.

To describe the relationship between radiation fields set up using conventional jaws and MLCs in greater detail, the size of radiation fields at the EPID sensitive layer (SED = 140 cm) were measured using multiplying the number of EPID pixels and the size of each pixel (1.27 mm × 1.27 mm). The theoretical field size was calculated to be the multiplication of the magnification factor and nominal radiation field size at the calibration point. The sizes of the calculated fields were then compared to those measured for radiation fields set up using the MLCs and conventional collimators.

A comparison of the crossplane and inplane profiles (across and along the direction of MLC movement, respectively), extracted for both radiation fields formed using conventional collimators and MLCs for a range of radiation field sizes, is shown in Figures 6.1(a) and 6.1(b), respectively. To reduce the effect of the inter-leaf leakage on data analysis, three relative dose off-axis crossplane profiles in the vicinity of the central crossplane profile, located approximately 4 mm above and below the central crossplane profiles (~ 5.5 mm on the EPID sensitive layer) were extracted and averaged. No significant difference was observed between the corresponding line profiles in the central part of ROIs. The length of crossplane and inplane profiles obtained from MLC fields were greater than those obtained for conventional collimators in all cases. The maximum and minimum inplane discrepancies were observed for 3 × 3 cm² and 12 × 12 cm² field sizes. The average difference between two similar line profiles was 4 pixels (approximately 5 mm).

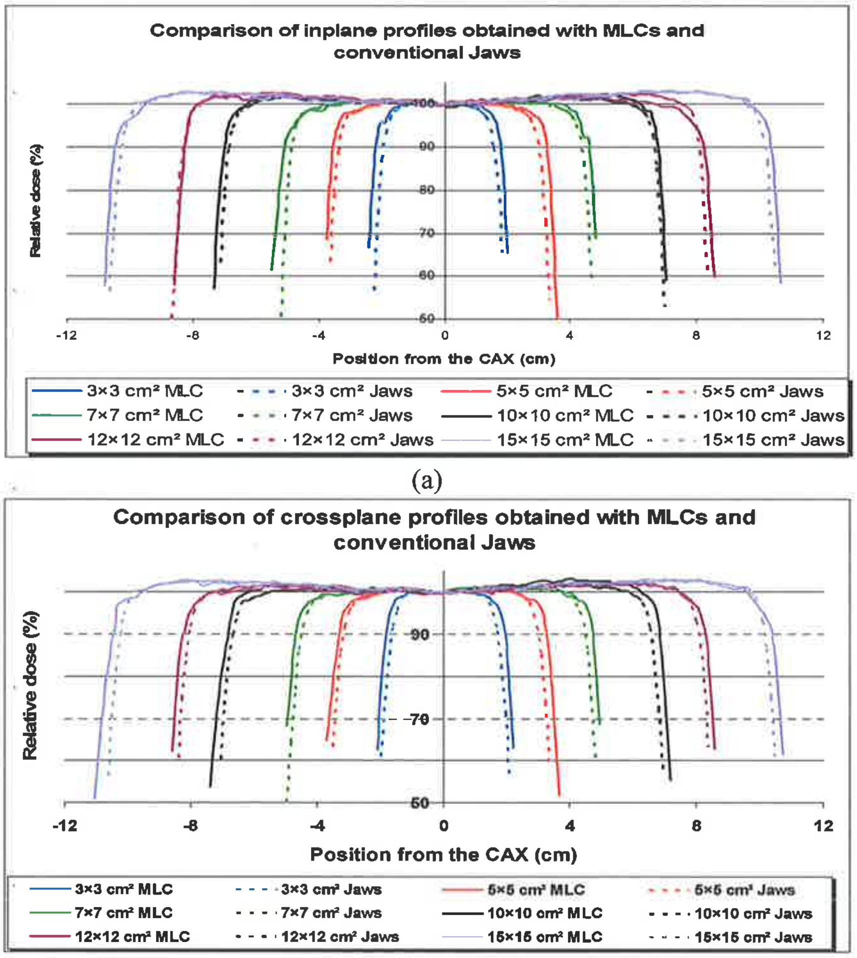

(a)

(b)

Figure 6.1. The (a) inplane and (b) crossplane profiles for a range of radiation field sizes from 3 × 3 to 15 × 15 cm², set up using MLCs and conventional collimators.

The radiation field sizes in the EPID sensitive layer, calculated and measured for radiation beams set up using conventional collimators and MLCs, were compared. The ratios of the calculations and measurements are shown in Figure 6.2. The differences between the calculated and measured radiation field sizes are also presented on the secondary axis. The difference between the magnitudes of field sizes measured using a MLC and conventional collimators indicated that the radiation field sizes set up using an MLC are greater than those set up with conventional collimators in all cases. As the radiation field size increased, an increase in the radiation field size difference (approximately 6% and 3%) between calculated and measured radiation field sizes set up using MLC and conventional collimators, respectively, was observed for a 15 × 15 cm² field size. Several fluctuations in the difference between calculated and measured radiation field sizes were observed for field sizes smaller than 5 × 5 cm².

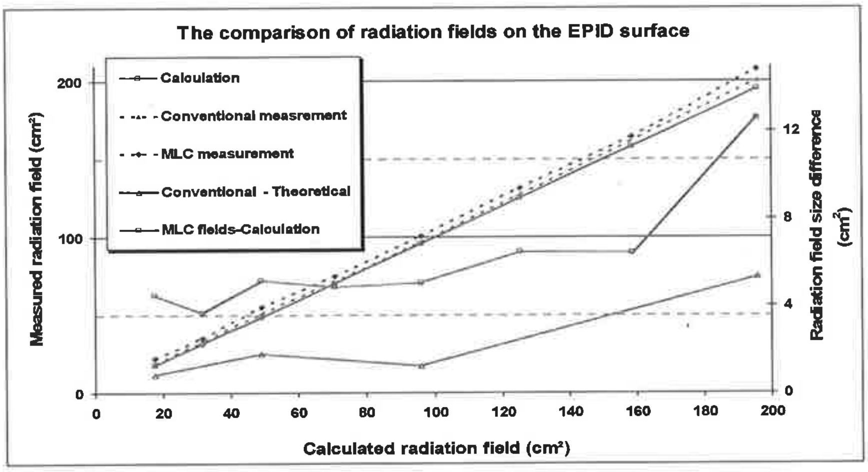

Figure 6.2. The comparison and difference between calculated and measured radiation field sizes set up using conventional collimators and MLCs.

As Figures 6.1 and 6.2 show, the differences between radiation fields set up by MLCs and conventional jaws can be detected using SLIC-EPID. It is known that the MLC rounded leaf end design in case of Varian MLCs is the main reason for increased radiation field sizes set up using MLCs. In addition, the uncertainty in collimators' positioning contributes to the discrepancy between radiation field sizes formed using collimators (for both conventional and MLC fields) and calculated (Jordan and Williams 1994; Boyer and Li 1997; Bayouth *et al* 2003).

Several factors such as pixilation of EPID decrease the accuracy of measurements. As a single value is attributed for each pixel, there is a loss of information for each pixel size. In other words, the resolution of an image strongly depends on its pixel size. The new generation of EPIDs, like a-Si EPIDs (Boyer *et al* 1992a), due to the smaller detector cells, are more accurate for this kind of measurements compared to the SLIC-EPID. It should also be pointed out that the data processing procedure decreases the measurement accuracy. For example, the accuracy of ROI identification using in-house code is ±1 pixel.

6.2.2. The penumbra width of radiation fields set up using MLCs and conventional jaws

Due to the different design used in MLCs and conventional jaws, major differences in radiation fields characteristics have been reported for penumbra regions (Boyer *et al* 1992b; Galvin *et al* 1993; Huq *et al* 1995; Palta *et al* 1996; Stasi *et al* 1999; Pasquino *et al* 2001; Huq *et al* 2002; Bayouth and Morrill 2003). In order to evaluate the dosimetric characteristics of the transmission penumbra using SLIC-EPID, several symmetrical square field sizes (5 × 5, 7 × 7, 10 × 10, 12 × 12 and 15 × 15 cm^2) were set up using MLCs and conventional collimators. A 20 cm homogeneous phantom was placed in the beam path and the isocentric technique was used to acquire EPIs. A 24 × 24 cm^2 area in the central part of EPI was selected as the ROI. The penumbra widths for both conventional jaws and MLCs were extracted from the relative transmitted dose maps, and were compared. The maximum penumbra width was determined for directions across and along the MLC leaf movement for both radiation fields created using MLCs and conventional collimators. The typical penumbra widths for radiation fields set up using conventional jaws and MLCs are shown in Figure 6.3.

Several fluctuations in the isodose curves were observed for the penumbra region of transmitted dose maps; these had been acquired using conventional collimators. Compared to the radiation fields set up using conventional collimators, a scalloping of the isodose curves was observed for the central region of edges in the direction of MLCs movement for radiation fields obtained using MLCs. An increase in isodose curve undulation was observed with the increase in radiation field size established using MLCs. In contrast, no significant variation in isodose curves was observed for conventional radiation fields. The maximum isodose curve undulation was observed for 70% of isodose lines for MLC fields.

The relative dose difference between radiation fields produced with MLCs and conventional collimators was also investigated. The penumbra region for the MLC radiation fields were found to be greater than those measured using conventional jaws. The same results were reported for the penumbra region created using MLCs measured using films (Boyer *et al* 1992b; Palta *et al* 1996; Stasi *et al* 1999; Huq *et al* 2002; Killoran *et al* 2002).The inplane and crossplane profiles of relative dose difference maps are shown in Figure 6.4 for a range of field sizes. The maximum relative dose difference was found to be 1.4% for all investigated field sizes. An increase in relative dose difference was observed with a corresponding increase in field size for outside the evaluated ROIs. Sharp and rounded peaks of relative dose difference were observed for inplane and crossplane profiles of relative dose difference maps, respectively, in all cases.

The evaluation of relative dose difference maps, where the corresponding inplane and crossplane profiles are displayed in Figure 6.4, showed that the dose delivered outside of the ROIs for MLC fields are greater than those delivered under the same conditions by conventional jaw set-ups. This increases as radiation field size increases. Due to the increase in scattered radiation contribution, and due to the variation in radiation beam spectrum as radiation field size increases, a systematic increase in the dose delivery was observed for outside the ROI regions of MLC fields. This analysis shows that SLIC-EPID is a sensitive tool that can be used to evaluate low dose regions.

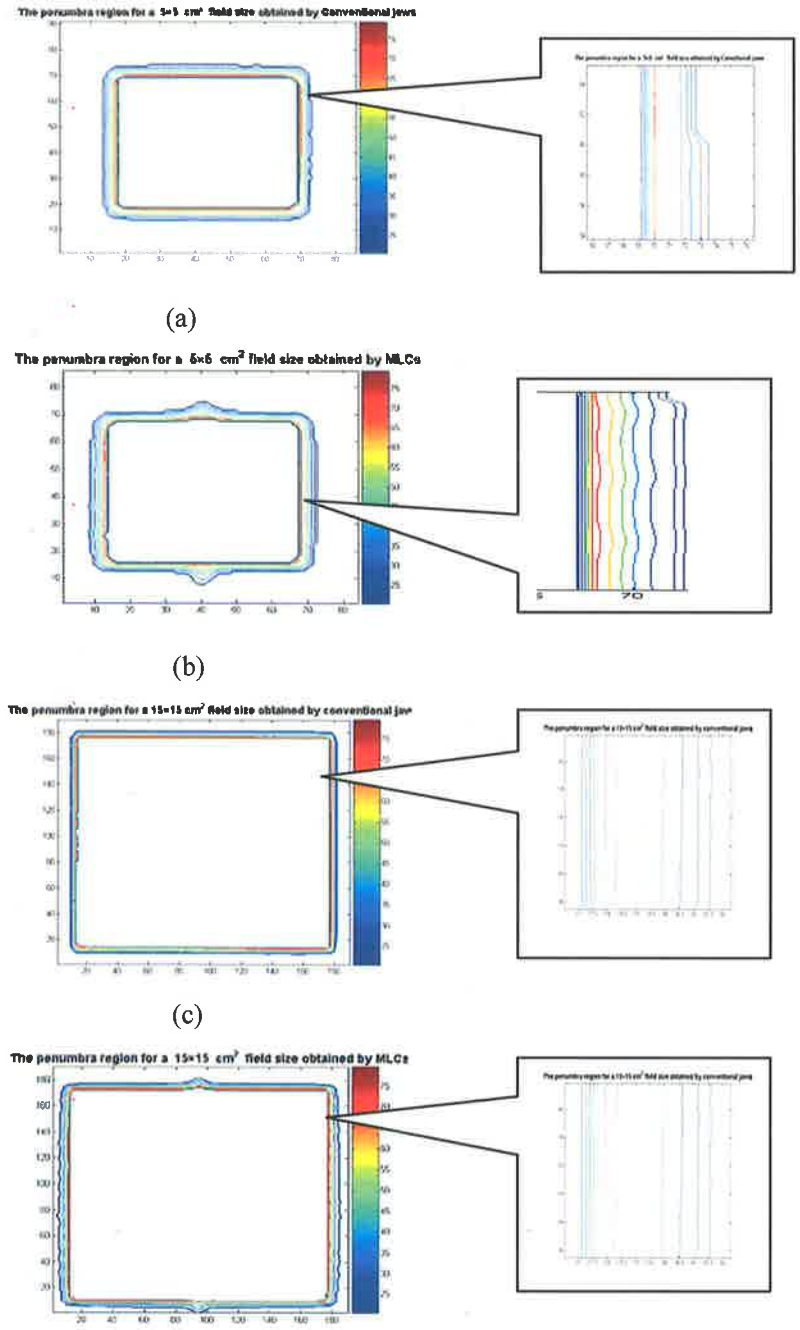

(a)

(b)

(c)

(d)

Figure 6.3. The penumbra width of the radiation field obtained for a 5 × 5 cm² rectangular field set up using (a) conventional jaws and (b) MLC. The penumbra width of the radiation field obtained for a 15 × 15 cm² rectangular field set up using (a) conventional jaws and (b) MLC. Indicated parts of penumbra regions are zoomed.

The conventional jaws positioning behind MLCs is one the most important ways to minimize intraleaf and interleaf leakages. However, in IMRT techniques, especially in dIMRT, the jaws must be left opened to a large field. Although due to MLC transmission, the additional dose to the protected area is not too large; an attention should be considered when sensitive organs are located in the vicinity of target volumes.

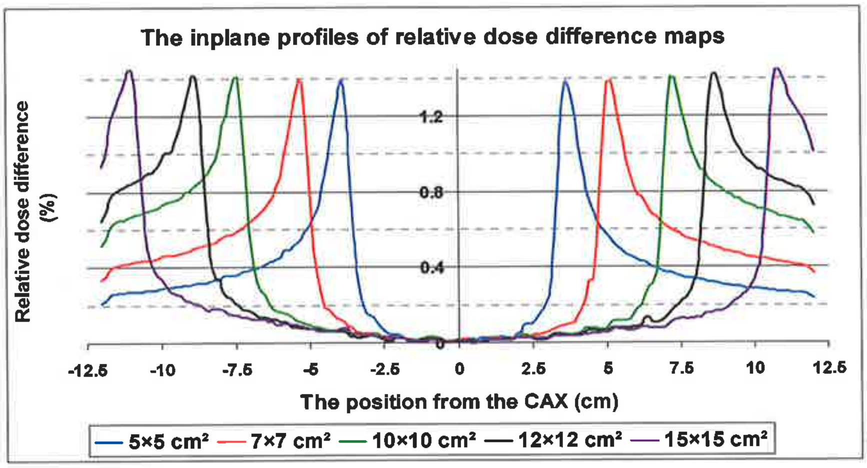

(a)

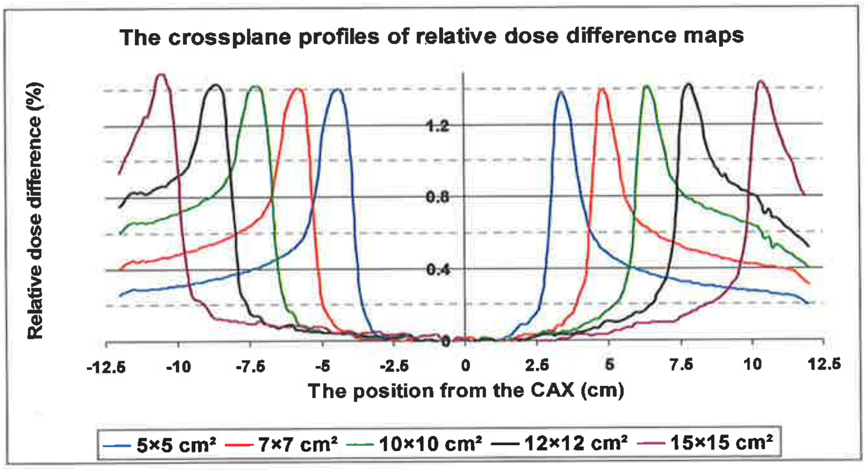

(b)

Figure 6.4. (a) The inplane and (b) the crossplane profiles of relative dose difference between radiation fields obtained by MLCs and conventional collimators for a range of field sizes.

SLIC-EPID can be used to study differences between the penumbra region of radiation fields created using MLCs and conventional collimators. The structure of the MLC used in the current study, including the rounded end of MLC leaf and transmission through the MLC leaves, are the main reasons for increased width of radiation field penumbra. The "tongue and groove" effect also increases the penumbra. The increase in field size increases the divergence of incident beam. Consequently, the transmission of a divergent beam differs from that of a direct beam. In addition, due the variation in intensity of incident photons, the radiation fluence varies. This increase the penumbra width and that of the radiation field size for the sides along MLC leaves movement. They are comparable to those located across MLC leaves movement.

6.2.3. The characteristics of the penumbra region for rectangular and rounded fields

In order to evaluate the dosimetric characteristics of the penumbra region further, a range of asymmetrical rectangular and semi-circular radiation fields were created. For both rectangular and circular fields, a bank of the MLC leaves were kept in the "closed" position and another was used to set up the fields (see figure 6.5). The asymmetrical rectangular fields with 3 × 10, 5 × 10, 7 × 10, and 10 × 10 cm² field sizes, were used. For rounded fields, a range of semi-circular radiation fields with radii of 4, 5, 7 and 10 cm were set up using MLCs. A 20 cm homogeneous phantom was placed in the beam path and the isocentric technique was used to acquire EPIs. The penumbra width and the isodose line undulation in the defined points for each field were then investigated.

Typical penumbra regions for asymmetrical rectangular and semi-circular fields are shown in Figure 6.6. An isodose undulation was observed in the penumbra region for all cases. The maximum undulation was observed for approximately 40% - 50% isodose curves in all cases. As the field size increased, an increase in the penumbra width and more scalloping in the isodose curves were observed for both rectangular and semi-circular fields. The isodose curve undulations for rectangular fields were found to be less compared to those for semi-circular fields.

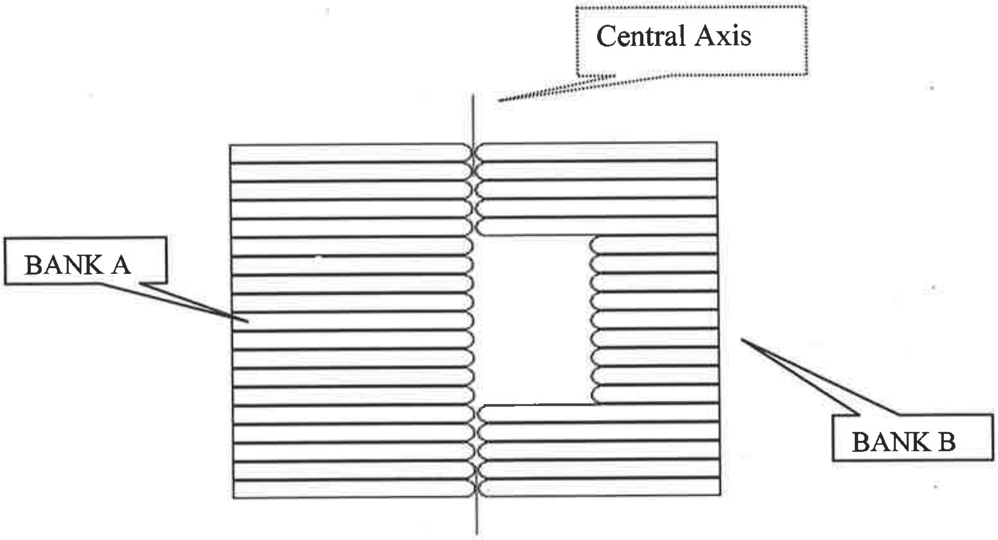

Figure 6.5. Schematic view of MLC leaves positioning for asymmetrical fields.

In order to give quantitative information about the penumbra width and isodose curve undulation, the number of pixels of the transmitted dose map being in the penumbra region was counted in several points selected in both the rectangular and semi-rounded penumbra regions. These are shown in Figure 6.6. Points A, B and C were defined as the points with the maximum penumbra width in the middle and in the peripheral part of MLC leaf Bank A, closed bank, for both rectangular and rounded fields. The points of E, D and F were defined as the penumbra width on the horizontal and vertical edges, respectively, for all cases. Points G and H were defined as the points located in the "staircase" positions of the semi-rounded fields. The magnitude of penumbra width for the defined points is shown in Table 6.1 (a & b), for rectangular and rounded radiation fields, respectively.

The minimum width of the penumbra region was found to be perpendicular to the MLC leaf movement direction (points D & E) for all cases. The maximum penumbra width was observed for the B and C points, which are defined in the area where the opposing leaves of banks A and B are closed where minimal gaps between two leaf banks can occur and the dose increased further due to transmission through the rounded leaf ends. For circular fields, the maximum width of the penumbra was also found in the rounded-straight line junction (points A & B). Due to the "staircase" shape of rounded region of semi-circular fields, compared to the rectangular fields, a significant difference in the penumbra region (approximately 1 cm) was observed between the minimum and maximum width of that penumbra. A small increase in the penumbra width was observed as field size increased.

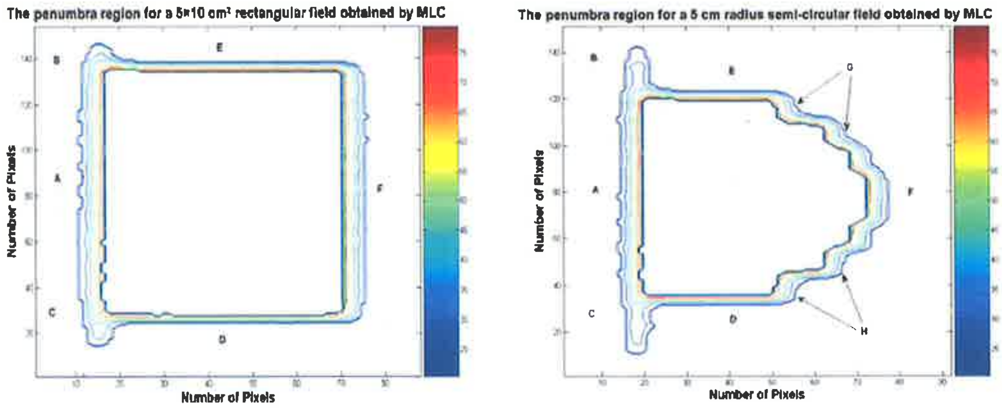

(a) (b)

Figure 6.6. The penumbra region for an asymmetrical (a) 5×10 cm² rectangular field and (b) a 5 cm radius semi-circular field.

Details of the penumbra width for all rectangular and semi-rounded fields investigated in this study are shown in Table 6.1. The penumbra width for points A & B in the semi-rectangular fields are significantly greater than those measured for rectangular fields. No significant difference of penumbra width was observed for points D & E, which are extracted generally from the line profiles perpendicular to MLC leaf direction of movement. In contrast, for points G & H for the rounded fields, due to the staircase shape of the field, a significant increase in the penumbra width was observed. The accuracy in measuring penumbra width, due to SLIC-EPID pixel size, is ±1.27 mm.

A variation in penumbra width was observed between the rounded fields and the rectangular fields set up using MLCs. The width of the penumbra in the rounded field depends on the stepping distance of the adjacent MLC leaves. The results obtained from the transmitted dose maps, using a SLIC-EPID, showed a good consistency with those measured using raw film data sets (Frazier *et al* 1995; Stasi *et al* 1999; Pasquino *et al* 2001; Huq *et al* 2002; Killoran *et al* 2002; Butson *et al* 2003; Greer and Popescu 2003).

Table 6.1. The penumbra width for several points of asymmetrical (a) rectangular and (b) semi-circular radiation fields.

(a)

Field size (cm²)	Point					
	A (mm)	B (mm)	C (mm)	D (mm)	E (mm)	F (mm)
3 × 10	7.6	17.8	17.8	3.8	3.8	6.4
5 × 10	7.6	17.8	16.5	5.1	5.1	7.6
7 × 10	7.6	19.1	17.8	5.1	5.1	7.6
10 × 10	8.9	19.1	17.8	5.1	6.4	7.6

(b)

Field size Radius (cm)	Point							
	A (mm)	B (mm)	C (mm)	D (mm)	E (mm)	F (mm)	G (mm)	H (mm)
4.0	6.3	27.9	27.9	5.1	5.1	6.4	16.5	14.0
5.0	7.6	27.9	27.9	5.1	5.1	8.9	14.0	15.2
7.0	8.9	29.2	27.9	6.4	6.4	8.9	16.5	15.2
10.0	8.9	29.2	29.2	6.4	6.4	10.2	16.5	16.5

6.2.4. Conclusion

In conclusion, SLIC-EPID is a sensitive device that can detect small variation in the penumbra regions. The detection is limited to the SLIC-EPID pixel size. The variation in radiation field sizes set up using MLCs and conventional collimators can be detected using SLIC-EPID. SLIC-EPIDs were found to be sensitive devices for evaluating the characteristics of radiation fields created using MLCs. SLIC-EPIDs can also be used to evaluate the characteristics of the penumbra region, including its width and the undulation of isodose curves.

6.3. Evaluation of MLC leaf positioning using a SLIC-EPID

The MLC design and the corresponding QA have extensively been reviewed by the AAPM Task Group 50 in the American Association of Physicists in Medicine (AAPM) report 72 (Boyer *et al* 2001b). It contains a test for MLC leaf calibration and determination of the MLC leaf relative position using radiographic films. Due to the difficulties associated with radiographic films, EPIDs can be used for QA of MLCs as a suitable alternative. Several studies investigated the use of EPIDs for regular MLC QA (James *et al* 2000; Samant *et al* 2002; Vieira *et al* 2002; Chang *et al* 2004; Yang and Xing 2004; Baker *et al* 2005; Williams and Metcalfe 2006). For example, the average and best MLC detection precisions were reported to be 1 and 0.1 mm, respectively, for both fluoroscopic and a-Si EPIDs (Vieira *et al* 2002; Yang and Xing 2004). For SLIC-EPID, with the use of *single* electronic portal image (EPI) and a one-dimensional Laplacian-of-Gaussian (LoG) operator, leaf positioning was determined to be approximately 0.1 mm (Eilertsen 1997). This operator is a zero-crossing algorithm used to find edges by looking for zero crossings after filtering. Although this method enables the detection of MLC leaf positioning accurately, its result is a binary data set. In addition, because several studies have used the geometric mode of EPID response (based on EPID raw pixel values), the relationship between MLC leaf displacement and variation in dose delivered to the patient has not been investigated.

The quantitative measurement of MLC displacement, using a two-dimensional transmitted dose by a SLIC-EPID, is analysed here. The relative dose difference maps, obtained from the subtraction of a reference and several evaluated dose maps with tiny shifts in MLC positioning, were used to find the minimum detectable MLC displacement. In addition, standard edge detection techniques were used to find the MLC leaf displacements. The results were also used to determine the accuracy as well as the reproducibility of the MLC leaf positioning.

6.3.1. The relationship between relative dose difference values and MLC leaf spatial displacement

An investigation was carried out on the relationship between portal dose, measured using a SLIC-EPID, and MLC leaf displacement. Several EPIs were acquired as reference dose maps for a range of MLC field sizes (5×5, 7×7, 10×10, 12×12 and 15×15 cm^2), formed using Shaper software, in the anterior-posterior direction. Due to the variation in SLIC-EPID response with gantry angle (Van Esch *et al* 2001; Chin *et al* 2004), in order to find the SLIC-EPID sensitivity the MLC leaf positioning was also assessed at a lateral and oblique directions for typical prostate and head and neck fields. The prostate and head and neck site of an anthropomorphic Rando phantom were used as ROI (see figure 6.11 (a1) & 6.11 (b1)). Typical irregular subfields, generally used for sIMRT, were selected. The MLC leaves used to form the corresponding radiation fields were then shifted along the direction of MLC leaf movement to reduce the gap between opposing leaves. The corresponding leaf shifts varied from 0.1 to 1.6 mm and 0.1 to 2.0 mm for regular and irregular radiation fields, respectively, using shaper MLC software manually and corresponding EPIs were acquired. In order to control intra/inter leaf leakages through MLC leaves, the conventional jaws were placed 1 cm behind the maximum retracted MLC leaves. In order to reduce statistical fluctuations, two consecutive EPIs were acquired and averaged for each situation. The EPIs acquired at non-zero degree of gantry angles were also corrected for bulging effect using a method developed by Van Esch et al (2001) (see also section 3.2.3). All acquired EPIs were then converted to dose maps using the calibration method described in section 3.4.

In order to create relative dose difference maps, the dose maps corresponding to the shifted MLC positions were subtracted from the reference dose maps. The effect of the inter-leaf leakage on data analysis was reduced using the average of three off-axis relative dose crossplane profiles in the vicinity of central crossplane profile, located approximately 3 mm above and below the central crossplane profiles on the isocentre (approximately 5 mm at the EPID sensitive layer). The relationship between average relative dose difference and MLC leaf spatial shift was investigated.

The typical crossplane profiles of relative dose difference maps for a range of MLC leaf displacements are shown in Figures 6.7 and 6.8 for a range of regular and irregular radiation fields, respectively. As Figure 6.7 (a & b) shows, the MLC leaf displacement can be detected using relative dose difference maps measured using a SLIC-EPID. No significant variation in relative dose difference was observed with the variation in MLC leaf shift for different field sizes.

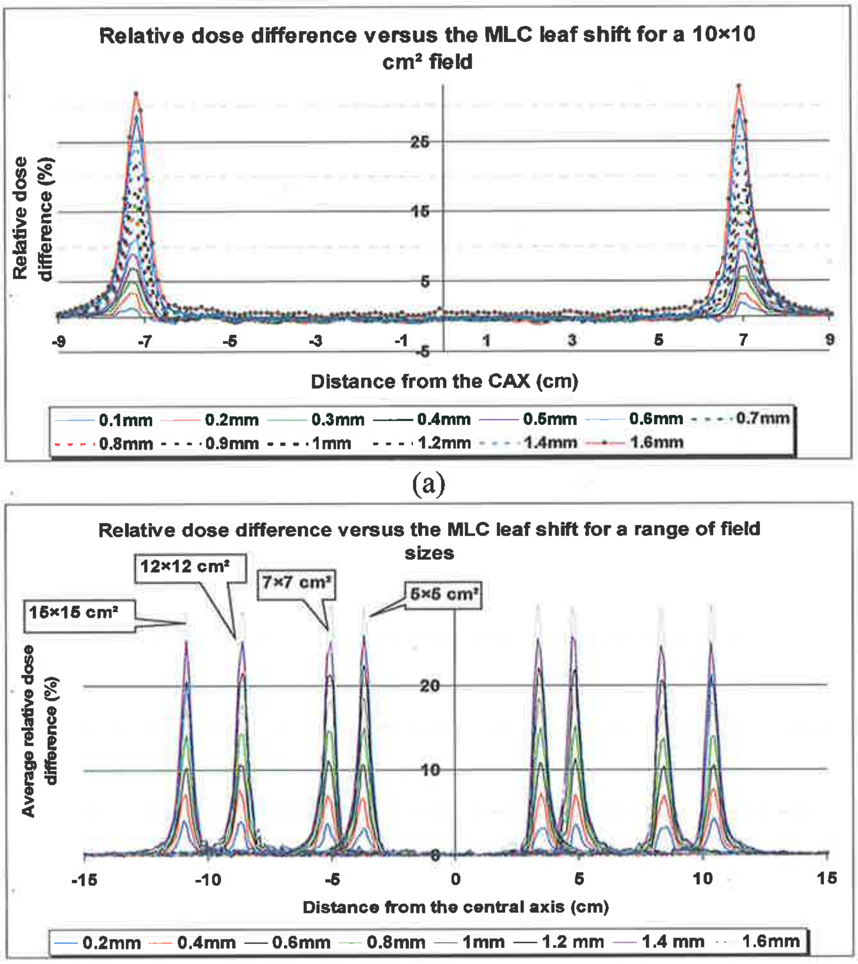

(a)

(b)

Figure 6.7. The crossplane profiles of relative transmitted dose difference for a range of MLC leaf shifts from 0.1 to 1.6 mm (a) for a 10×10 rectangular radiation field size, (b) for a range of radiation field sizes 0.2 to 1.6 mm (5×5, 7×7, 12×12, and 15×15 cm²).

The relationship between the relative dose difference values at the position of the MLC leaf shift and the spatial displacement of the MLC is shown in Figure 6.9 for regular and irregular fields. For each condition, a linear fit and the corresponding R-squared value are also displayed as $\Delta D = c\,\Delta X$, where ΔD and ΔX are relative dose difference (%) and MLC leaf shift (mm), respectively. The c is a coefficient and it depends on the transmitted dose map characteristics, such as the properties of normalization point and patient/phantom positioning at the position of MLC leaf shifts.

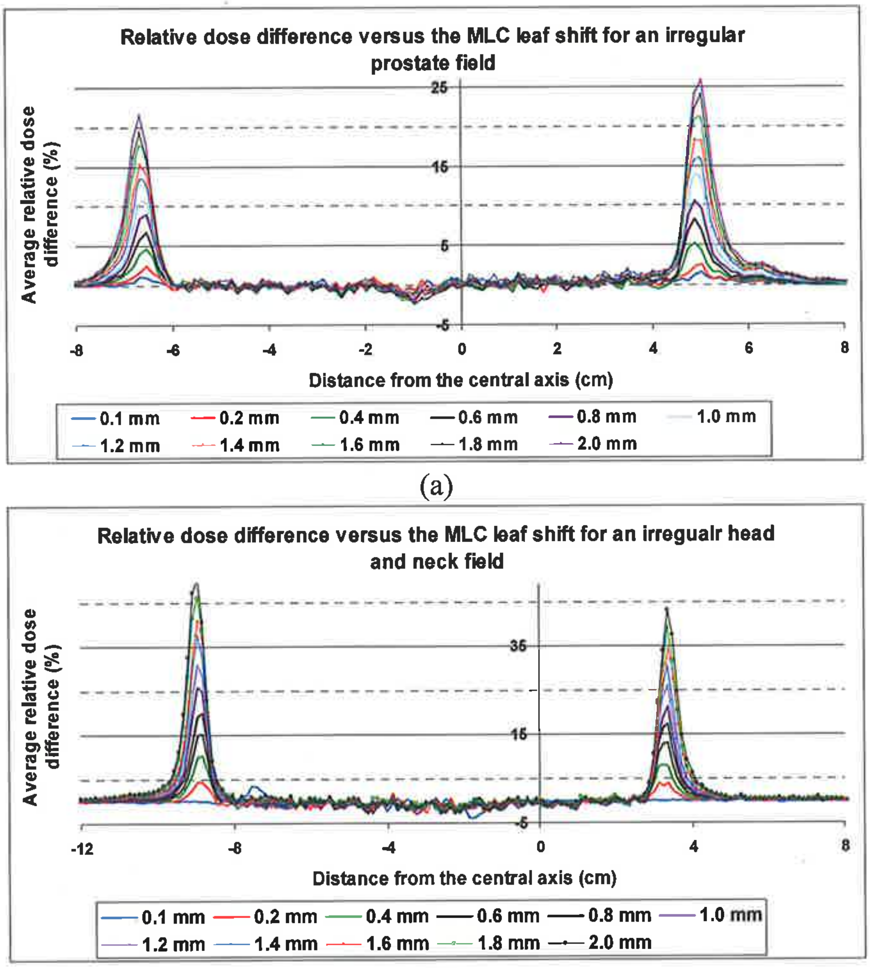

(a)

(b)

Figure 6.8. Typical crossplane profiles of relative transmitted dose difference maps for MLC leaf shift from 0.1 to 2.0 mm for (a) a prostate case at gantry angle of 90°, and (b) a head and neck case at gantry angle of 120°.

Due to the noise level in the raw SLIC-EPIs, (within 1 %) (van Herk 1991; Boyer *et al* 1992a), and in the corresponding derived transmitted dose maps (within 1.2%) (Essers *et al* 1995; Van Esch *et al* 2001), (see also section 3.2.1), the minimum detectable displacement of MLC leaf was found to be 0.2 mm using relative dose difference maps. This can be measured reliably for primary fluence maps as well as for transmitted dose maps measured in the presence of phantoms for non-zero gantry angles. A variation of 0.2 mm in leaf position leads to approximately 4.0% change in the primary fluence maps at the position of MLC leaf shift. For transmitted dose maps, the change of relative dose difference values depends significantly on the normalization point and the phantom/patient position (in this study 2.7% and 5.1% for prostate and head and neck cases, respectively).

The relationship between the relative dose difference and MLC leaf spatial displacement is well described by a linear fit, with R-squared values of more than 0.99. With this technique the relative transmitted dose maps can not only be used to detect the MLC leaf positioning errors; but the undesired dose variation in a given position can also be estimated. This is important for CRT and IMRT treatments where the main focus is to protect sensitive neighbouring organs using MLC blocking.

Although similar results for the minimum detectable MLC leaf displacement as found for SLIC-EPID, were reported for fluoroscopic (Vieira *et al* 2002) and amorphous silicon EPIDs (Yang and Xing 2004), the spatial resolution of these types of imagers should also be taken into consideration. The pixel size of fluoroscopic and amorphous silicon EPIDs are 0.25×0.25 mm^2 and 0.784×0.784 mm^2, respectively. In contrast, the SLIC-EPID pixel size is 1.27×1.27 mm^2. The large pixel size leads to a decrease in resolution and loss of information. Despite significant differences in pixel size and consequently in the spatial resolution of the acquired EPI, it can be concluded that the SLIC-EPID is a useful tool for MLC quality assurance with similar accuracy compared to a-Si EPID results (Yang and Xing 2004).

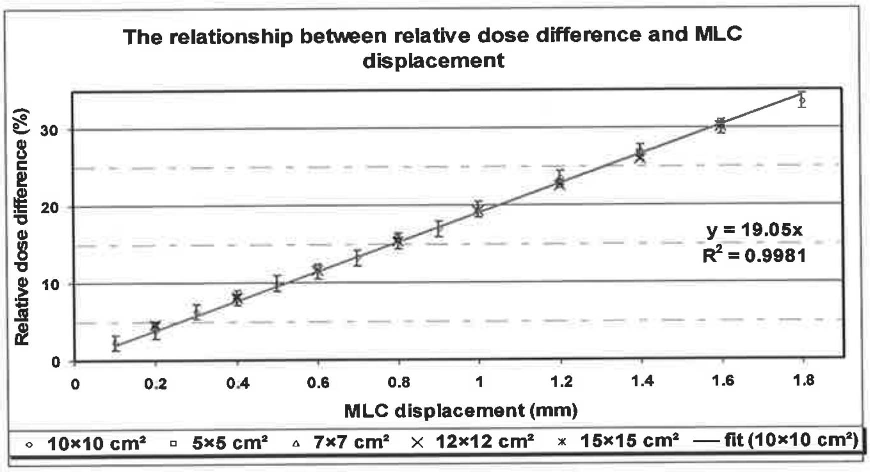

(a)

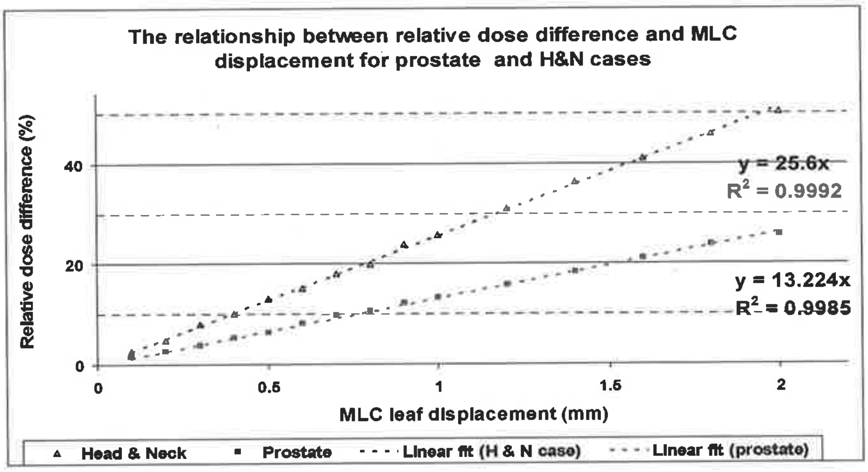

(b)

Figure 6.9. The relationship between relative dose difference and MLC leaf shift for (a) a range of radiation field sizes, and (b) irregular fields for prostate and head and neck cases.

6.3.2. Edge detection algorithms

In order to investigate the minimum detectable MLC leaf displacement, the relative dose difference maps were calculated by subtracting the shifted MLC fields from the corresponding reference relative dose maps (section 6.3.1). The relative dose difference maps were also evaluated using standard edge detection algorithms, including gradient-based algorithms: "Sobel", "Prewitt", "Roberts" and "Canny" and intensity-based algorithms: "Laplacian of Gaussian" and "morphological" (zero-cross). The details of these algorithms are discussed extensively in literature (Roberts 1965; Prewitt and Mendelsohn 1966; Davis 1975; Canny 1986; Huertas and Medioni 1986). The most suitable algorithm with a range of possible thresholds was investigated using MATLAB software (version 7, MathWorks Inc, Natick, MA).

The results of standard edge detection algorithms for 0.1 mm MLC shifts are shown in Figure 6.10 (a) for a 10×10 cm^2 rectangular field size. From the standard edge detection algorithms, the "Canny" algorithm was the best one for detecting the small MLC leaf displacements. The threshold values of 0.62 and 0.31 for evaluated primary fluence maps and transmitted dose maps, respectively, were found to be the optimum values for this assessment. However, the edge detection techniques can only find the position of variation in either intensities or gradients. In the other words, the outcome of this approach is a binary data set and there is no further information about the magnitude of MLC leaf positioning assessment.

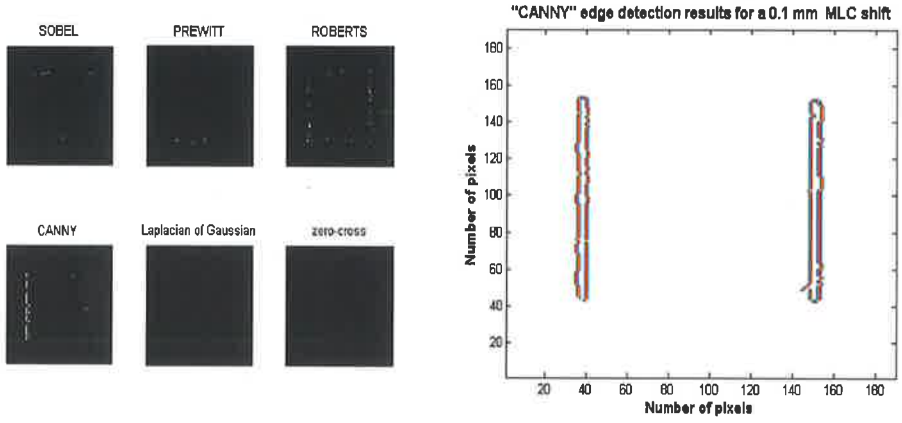

(a) (b)

Figure 6.10. (a): The response of the standard edge detection algorithms. (b): The result of the application of the "Canny" edge detection algorithm on the relative dose difference map to find the minimum detectable MLC leaf displacement (0.1 mm).

The results of the "Canny" edge detection technique are shown in Figures 6.10 (b), 6.11 (a2) and 6.11 (b2), respectively, for a 0.1 mm MLC leaf shift in the direction of MLC leaves. This refers to movement of the primary fluence map and transmitted dose maps for a prostate and head and neck case, respectively. The corresponding relative dose maps are also shown for prostate and head and neck fields in Figures 6.11 (a1) and 6.11 (b1), respectively. The minimum detectable MLC leaf displacement was 0.1 mm for all regular and irregular fields.

Although using a zero-cross edge detection operator has been reported as able to detect the MLC position, using the possible direction assessment (horizontal and vertical) and threshold values, the intensity-based edge detection algorithms (LoG and zero-cross) can not detect the sharp peaks (see Figures 6.10 (a). In the other words, the LoG operator is a reliable tool for detecting physical radiation field edges (like 50% isodose lines) (Eilertsen 1997). In addition, in the cited study due to the use of a *single* EPI, the intensity-based algorithms are not good options for detecting the MLC leaf displacements. Therefore, these are not suitable for assessing the accuracy of re-positioning and shifts. Moreover, because of the raw EPI evaluation, an extra build-up layer was not used (Eilertsen 1997; Samant *et al* 2002). In contrast, the use of this additional build-up layer, placed on the EPID cover surface, is necessary for dosimetric purposes (Boellaard *et al* 1996; Essers *et al* 1996; Parsaei *et al* 1998; Van Esch *et al* 2001). The additional build-up layer and the presence of phantom/patient reduce the contrast of EPIs due to increased contribution of scattered photons through the additional build-up layer (Boellaard *et al* 1996). More scattering increases the "fog phenomenon" in EPIs, and this decreases the sensitivity of edge detection algorithms because image sharpness decreases. In contrast, gradient base algorithms responses, especially "Roberts" and "Canny", responses are very good. Compared to other edge detection algorithms, the "Canny" method uses two thresholds to detect strong and weak edges. This method appears to be the best option for finding weak edges (Canny 1986).

Due to the smaller pixel size in amorphous silicon and fluoroscopic EPIDs as well as lower noise level (Munro and Bouius 1998; Vieira *et al* 2002), it is believed that with the application of the proposed method with other EPID types the results would improve significantly.

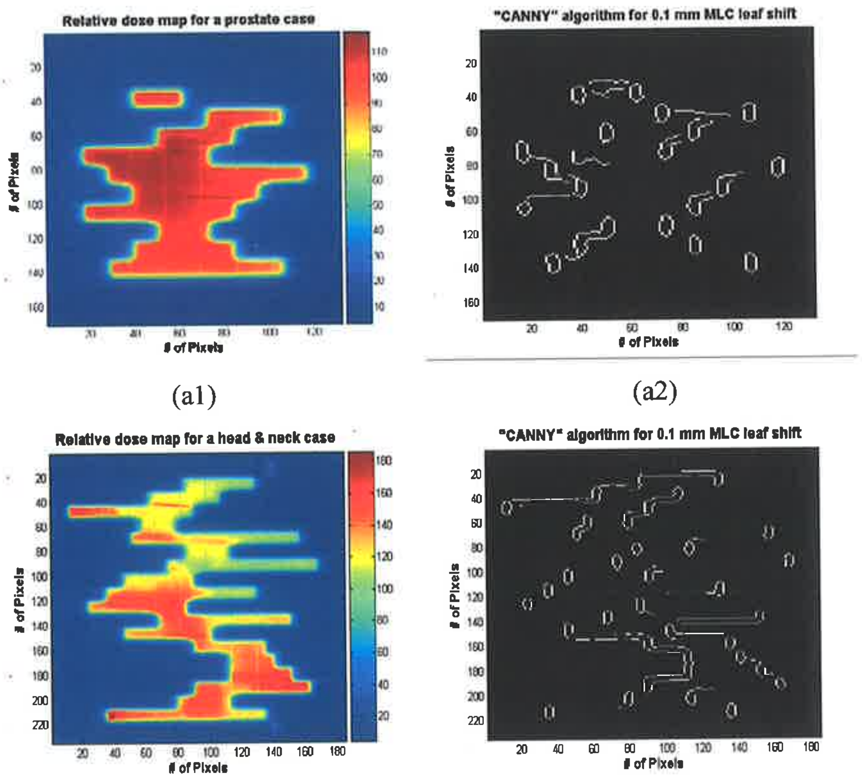

(a1) (a2)

(b1) (b2)

Figure 6.11. Typical relative transmitted dose maps for (a1) prostate and (b1) head and neck fields measured using a SLIC-EPID. The result of the relative dose difference map evaluated using "Canny" edge detection algorithm to detect 0.1 mm for (a2) a prostate MLC field (b2) a head and neck MLC field.

6.3.3. Reproducibility of MLC leaf positioning

The reproducibility of MLC leaf positioning has been investigated in several studies (Jordan and Williams 1994; Samant *et al* 2002; Bayouth *et al* 2003; Kwok *et al* 2004; Sastre-Padro *et al* 2004; Baker *et al* 2005). This is also studied in the current work using the methods described in sections 6.3.1 and 6.3.2. Several rectangular field sizes (5 × 5, 10 × 10 and 15 × 15 cm²) were set up using MLCs for the same conditions as mentioned above. Following the image acquisition, the MLC leaves were set up for closed field. The radiation field was then opened again for the afore-mentioned field sizes. This action was repeated 10 times for each field size and the corresponding EPIs were acquired. The EPIs were then converted to dose maps, as described in section 3.4. The first series of the relative dose maps for each field size was selected as a reference and the subsequent dose maps were then subtracted from the reference transmitted dose map to create relative dose difference maps for each field size. The relationship between average relative dose difference values versus the MLC leaf shift was used to evaluate the reproducibility of MLC leaf positioning.

From 30 EPIs acquired to evaluate the short-term reproducibility of MLC positioning, possible positioning discrepancies were found in two of the EPIs. Two typical relative dose difference maps are shown in Figure 6.12. In Figure 6.12 (a), the displacement of a single leaf is shown. The position of other leaves is consistent with those in the reference dose map. The deviation from the expected MLC position was found to be 0.3 mm using the linear equation derived from the variation in relative dose values with a variation in MLC displacement. In another case, the displacement of the whole bank of MLC leaves was observed. In this case the average displacement of MLC leaves was estimated to be around 0.15 mm. The range of noise level of SLIC-EPID dose values is shown in grey for both cases.

The reason for MLC displacement, as shown in Figure 6.12 (a1 & b1), may arise from a performance tolerance of an individual MLC motor. However, the MLC displacement of the whole leaf shown in Figure 6.12 (a2 & b2) can be caused by the integrated supporting electronics or software. The maximum uncertainty of a short-term reproducibility observed in this study was around 0.3 mm. This can be detected using a SLIC-EPID. Using the relationship between dose and MLC leaf shift in this work, this magnitude of MLC displacement leads to a variation in the delivered dose of approximately 6% in the penumbra regions of a given radiation field. Compared to the literature, the results were found to be in agreement with those measured using radiographic films (Jordan and Williams 1994; Bayouth and Morrill 2003) and EPIDs (Samant *et al* 2002; Baker *et al* 2005).

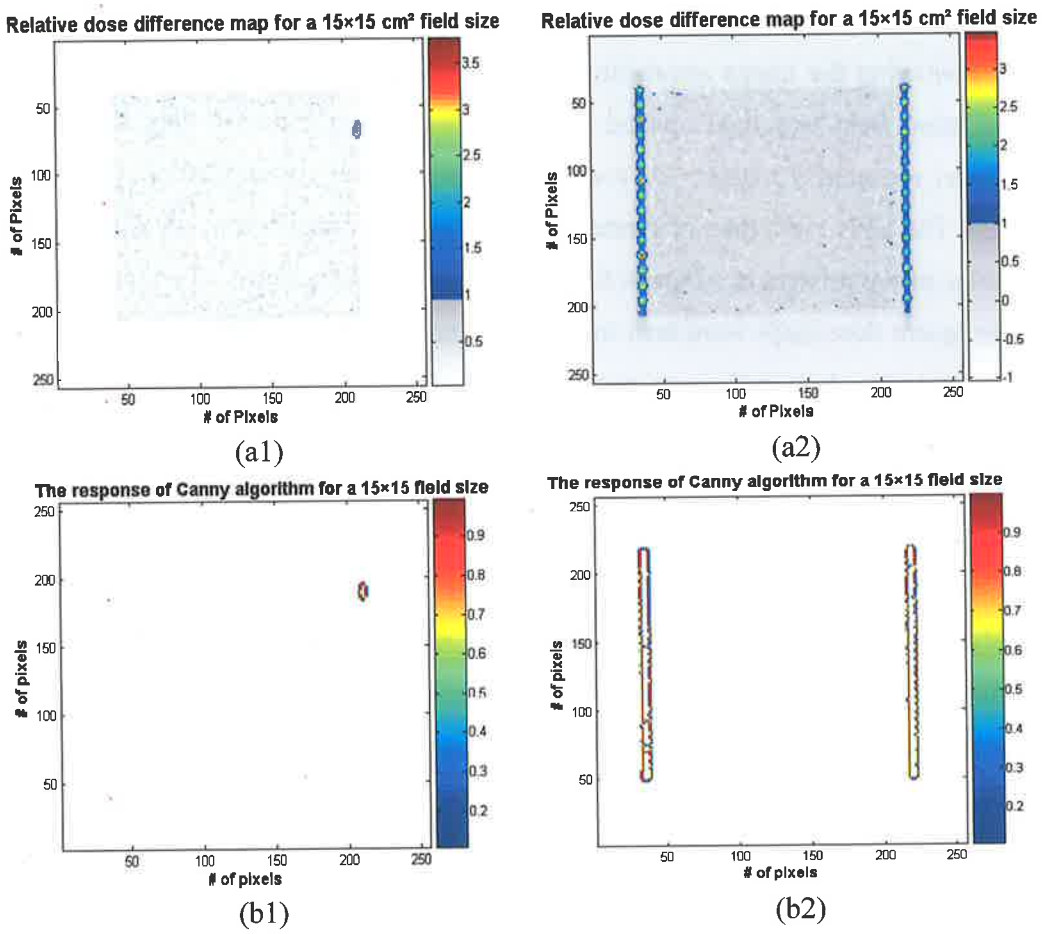

(a1) (a2)

(b1) (b2)

Figure 6.12. Identification of the MLC displacement during the short-term reproducibility evaluation for MLC leaf positioning using (series a) relative dose difference maps and (series b) "Canny" edge detection algorithm.

6.3.4. Summary and Conclusion

This part of the thesis concentrates on the quantitative measurement of MLC positioning using a SLIC-EPID. It shows that the SLIC-EPID is quite sensitive to measuring the small MLC displacements similar to other types of EPIDs. The use of dose maps, instead of EPID raw pixel values, not only enables the detection of slight MLC shifts, but also shows the amount of variation in the delivered dose to the affected tissues. It is concluded that it is possible to use a standard edge detection technique to find the MLC leaf positioning within 0.1 mm. SLIC-EPID can also be used to detect 0.2 mm of MLC shifts with further information about delivered dose. The simplicity, accuracy, and efficiency of delivered dose are the advantages of this technique and it can also provide additional dose information. In short, it can be concluded that the SLIC-EPID can be used for fast and relative quality assurance.

The fast processing time of the proposed method may enable EPID images to be assessed in real time and in conjunction with the current EPI acquisition software. In addition, the use of a proposed method for higher resolution EPIDs leads to improved results. Due to the variation in SLIC-EPID output with the linac repetition rate (see section 3.2.1) and motion artefact for SLIC-EPIDs output (Ploeger *et al* 2001), further investigation is required to extend the proposed method for dynamic MLC fields.

6.4. Summary

In order to investigate the dosimetric characteristics of radiation fields, measured using SLIC-EPID, for more complex radiation therapy modalities such as CRT and IMRT, several experiments were performed. In the first stage, the radiation field sizes, set up using conventional jaws and MLCs for the same conditions, were compared. The radiation field characteristics, including penumbra region width and undulation of isodose curves for a range of field sizes set up using conventional collimators and MLCs were also investigated. In the second stage, the accuracy of SLIC-EPID in detecting the MLC displacement was assessed. Finally, the SLIC-EPID response was investigated to determine the minimum detectable phantom/patient uncertainties using transmitted dose maps measured by EPIs.

SLIC-EPID is a sensitive device that can evaluate the dosimetric characteristics of the radiation fields. It detects the variation in radiation field sizes set up using MLCs and conventional collimators. It can also be used to evaluate the dosimetric characteristics of penumbra region, including the penumbra width and the undulation of isodose curves. In addition this device can be used to evaluate the MLC leaf positioning QA and related tests. Due to the SLIC-EPID ability to evaluate MLC fields, the use of SLIC-EPID for IMRT fields is recommended for further study. This is a theme that is discussed in the next chapter.

Chapter 7

Verification of dose delivery for sIMRT treatment cases using a SLIC-EPID

7.1. Introduction

Although several studies have investigated either Conformal Radiotherapy (CRT) or IMRT dose verification using EPIDs (Chang *et al* 2000; Fielding *et al* 2002; Vieira *et al* 2002; Vieira *et al* 2003; Zeidan *et al* 2004), all of the studies have only been performed for either primary radiation fluence or homogeneous attenuators in Anterior-Posterior (A-P) directions. This is not the true case for CRT and IMRT treatments where multiple gantry angles (other than zero) are generally used. CRT and IMRT treatments typically involve more complex set-up parameters. The author of this work could not identify any previously published work that performed complete dosimetry using EPID for sIMRT using all gantry angles and realistic anthropomorphic phantom. These observations motivated us to investigate transmitted dose distributions, measured using a SLIC-EPID for a typical step-and-shoot prostate and head and neck IMRT treatment applied to an anthropomorphic phantom for the A-P, lateral and oblique beam directions. Details and results of this work are outlined in the following sections.

7.2. Dose delivery verification for a prostate sIMRT treatment

7.2.1. Transmitted dose measurement using SLIC-EPID

MLC fields typical for prostate treatment were applied. The prostate treatment used in this study includes 5 fields with gantry angles of 0, 60, 120, 240 and 300°. Each field consists of several subfields (around 9-12 subfields). A Varian 600CD linac equipped with a standard 80-leaf MLC, and a SLIC-EPID was used. An anthropomorphic Rando phantom, containing real bony anatomy inside a solid water material was used to measure and to calculate the dose transmitted passing through the phantom. 5.022 g/cm^2 of white water, RW3 material, was placed on the surface of EPID cover as an additional build-up layer to achieve the electronic equilibrium at the EPID detector layer (see section 3.2.1). In order to reduce statistical fluctuations of EPI pixel values, each EPI used in the current study was obtained as the average of three independent and consecutively acquired EPIs with a pixel value standard deviation of less than 1% on the central part of radiation field. A series of EPIs were acquired using an anthropomorphic phantom and each of the sIMRT sub-field applied for prostate radiotherapy. The acquired EPIs were then converted into dose maps using the dosimetric calibration method (as described in section 3.4). Due to the bulging effect observed for SLIC-EPID response with varying gantry angle, the method developed by Van Esch *et al* (2001) was used to remove this effect from the measured EPIs (see also section 3.2.3).

7.2.2. Calculation of predicted portal dose images

7.2.2.1. Treatment planning set-up for transmitted dosimetry

The anthropomorphic phantom was initially scanned using a CT simulator (AcQSim CT, Philips Medical System, Cleveland, OH) with a 3 mm slice thickness and a matrix size of 512 × 512 pixels. In order to model the EPID at 140 cm from the radiation source, the images were then extended to 1024 × 1024 pixels by adding rows of pixels with pixel values corresponding to air CT numbers around the acquired CT image (see Figure 7.1(a)). The planning couch was removed by converting the corresponding CT data into CT numbers of the air. For non-zero gantry angles, in order to extract the calculated transmitted dose distributions easily through the calculated dose grid matrix, the original CT images were rotated in the opposite direction to the gantry rotation (see Figure 7.1(b)). The modified images were then transferred via DICOM to the TPS. The commercial TPS *Pinnacle*[3], version 6-2b, was used to calculate the transmitted dose delivered to the modelled EPID sensitive layer. The EPID was modelled as a $4\times30\times30$ cm^3 thin slab with uniform density ($1.0\ g/cm^3$), so that the upper edge of the modelled slab is positioned at a distance of 38.5 cm from the isocentre. The conventional jaws were positioned 1 cm behind the maximum retracted MLC leaf, for each subfield, matching the measurements conditions. A corresponding fraction of 2 Gy total dose was prescribed for each MLC subfield to the isocentre point located inside the anthropomorphic phantom. A three-dimensional dose grid consisting of voxels of $0.175 \times 0.175 \times 0.175\ mm^3$ was defined to calculate the dose distributions.

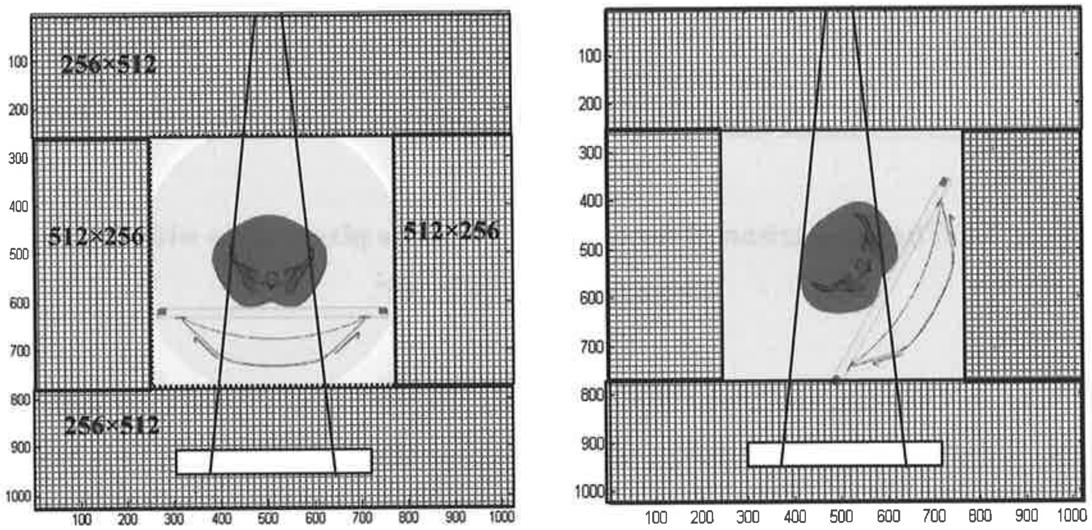

Figure 7.1. Typical extended CT image (a) in A-P direction and (b) at 60° gantry angle position. The position of modelled EPID is shown in both cases.

7.2.2.2. Evaluation of CT image quality during image rotation

Image processing procedure causes some undesired variation in the CT image pixel values during the rotation of original CT images around the isocentre. The impact of possible image processing tools, available in MATLAB software, on the CT image degradation was investigated. The typical line profiles of the original CT image pixel values before and after a 45° rotation are shown in Figure 7.2. From algorithms available in the MATLAB software used for data interpolation in image rotation commands, the *bilinear* interpolation algorithm emerged as the best option for processing the image information during rotation. This algorithm caused the smallest variation between the corresponding pixel values before and after the image rotation. The maximum and average percentage of difference in pixel values for a 45° rotation was 11.6% and 0.19%, respectively.

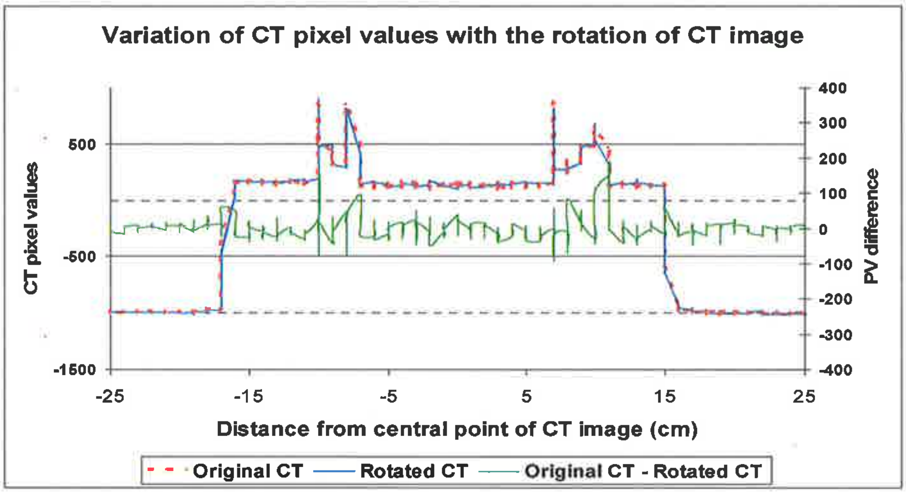

Figure 7.2. The comparison of the original CT image pixel values with those after the image rotation by 45°.

In order to calculate the transmitted dose for non-zero gantry positions, two basic methods can be used. Firstly, the patient/phantom positioning is the same as it has been during CT image acquisition and therefore, the EPID should be modelled in a position perpendicular to the central axis of the radiation beam (McNutt *et al* 1997). Using this method, the quality of the CT images is preserved, however due to the oblique position of the modelled EPID, the extraction of a corresponding transmitted dose distribution is more complicated because it is present in many dose grid slices. In addition, the dose accuracy in ROI decreases due to the undulation (stair-case shape) of isodose curves, which arises from pixelation of the dose matrix. Furthermore, for oblique EPID positions, a large dose grid matrix is required. Because TPS memory is limited, this leads to a larger voxel size in the dose grid matrix and consequently to decreasing resolution of ROI. In the second approach, the patient/phantom positioning, obtained during CT image acquisitions, is rotated in the opposite direction to the gantry rotation. Consequently, the EPID can be modelled in a position such that the extraction of ROI is easier and more accurate than in the former method, as the corresponding dose map is contained in one slice only. As Figure 7.2 shows, although a difference between rotated and original CT image pixel values can be observed, only for three out of 512 pixels of a line profile of CT slice (less than 0.5% in the whole matrix) the corresponding differences were found to be greater than 3%. This shows that the image degradation during rotation can be neglected and the rotation of CT images does not affect the accuracy of dose calculation.

7.2.2.3. Electronic equilibrium in the modelled EPID layers

Since the quality of the radiation beam depends on the patient thickness, the position of the dose distribution in the modelled EPID to reach the electronic equilibrium should be considered for each subfield individually. The results of a typical investigation of the layer, in which the electronic equilibrium was achieved, is shown in Figure 7.3. The x and y axes represent the CT slice number and the dose delivered to a central POI in the slices, respectively. The electronic equilibrium corresponds to the layer in which the maximum dose has been delivered in the modelled EPID. Although the dose delivered to the POI differs for subfields due to the dose fraction and subfield positioning, the investigation showed that the depth of maximum dose in the EPID is the same for all subfields.

As the EPID dose measurements were performed in electronic equilibrium, the dose calculation using TPS should also be performed under the same conditions. Identification of the layer, in which electronic equilibrium is achieved for either the EPID or modelled EPID is necessary (see section 3.2.1). A lack of electronic equilibrium leads to increase in inaccuracy of dose measurements, especially for high dose gradient regions and absolute dose measurements. The electronic equilibrium depends strongly on the beam quality and consequently, the quality of radiation beam depends on the SED, beam energy, beam divergence, density and thickness of phantom/patient. Due to variation in the beam characteristics in off-axis areas, an evaluation of electronic equilibrium in off-axis areas should also be taken into account. In addition, using large voxel size in the dose grid matrix, defined to calculate the dose distribution, decreases the accuracy of electronic equilibrium positioning.

The results in the current work show that the impact of the variation of phantom thickness and MLC leaf positioning has not been enough to vary the depth of the layer of electronic equilibrium.

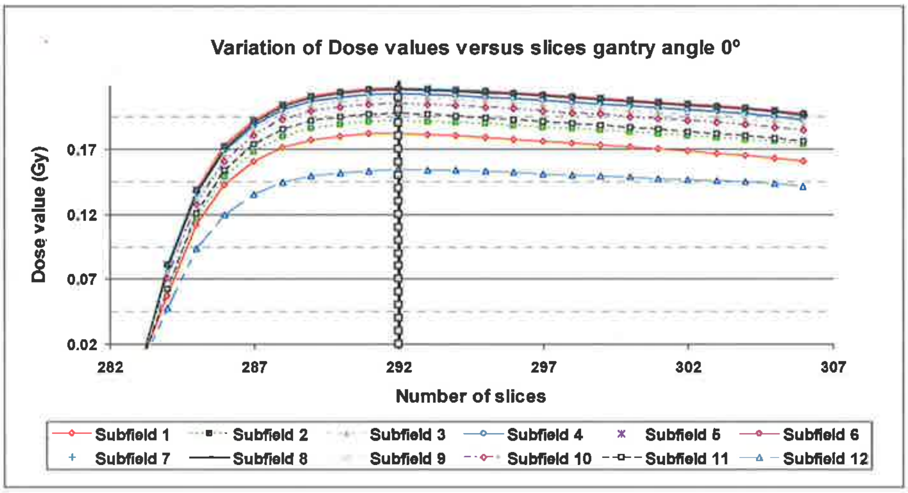

Figure 7.3. The variation of transmitted dose in the modelled EPID layers calculated using a TPS for an A-P direction field.

7.2.2.4. Evaluation of offset values for MLC positioning

Due to the discrepancy between the rounded leafs end of MLCs, incorporated in Varian linacs, and the straight leafs end simulated in the available version of the *Pinnacle*^{3} TPS, a difference between measured and calculated dose maps has been reported (Cadman *et al* 2002). This difference can be accounted for by introducing MLC offset values in a TPS. To determine this offset value, the MLC radiation fields, measured using SLIC-EPID, were compared with those calculated using the TPS. A part of a typical crossplane relative radiation fluence profiles measured with the SLIC-EPID and those calculated using the *Pinnacle*^{3} TPS for several MLC offset values (with corresponding increases of radiation field sizes by 0.6 mm and 1.5 mm), and the corresponding relative dose difference are shown in Figure 7.4. The decrease in relative dose difference between corresponding measured and calculated crossplane profiles with the application of a 0.6 mm offset shows the best possible agreement between the two dose maps. Good correlation between measured and calculated transmitted dose maps is achieved when an offset value of 0.6 mm is used in *Pinnacle³* TPS.

Due to the use of rounded leaf end MLCs in Varian linacs, the radiation MLC fields measured using SLIC-EPID were found to be larger than those calculated using *Pinnacle³*. Although the majority of discrepancies between planned and measured dose maps were observed in the penumbra region, due to the use of several subfields in sIMRT, these discrepancies perturb the total dose map significantly. Findings in the current work confirm the offset values reported by Cadman *et al* (2002). The use of new version of TPSs, that the rounded end leaf are accounted for, can be used to increase the accuracy of the MLC field calculations (Williams and Metcalfe 2006).

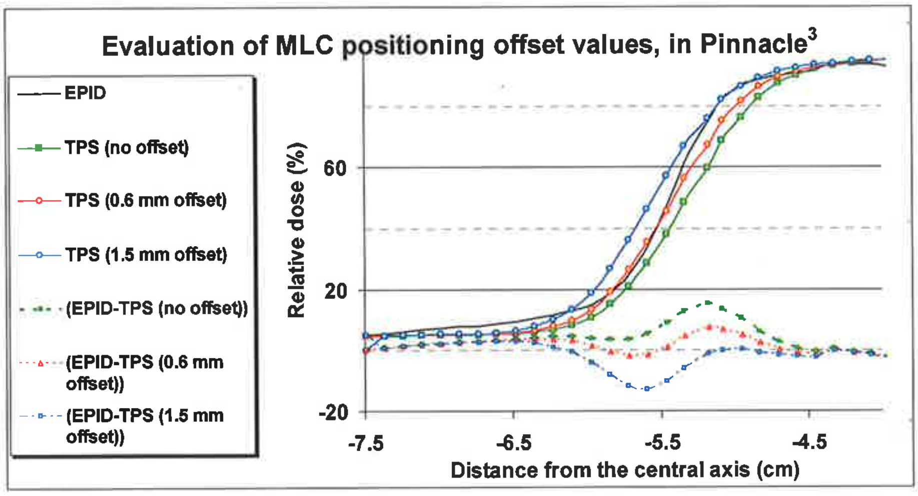

Figure 7.4. The crossplane profiles of transmitted dose measured using SLIC-EPID and calculated by *Pinnacle³* TPS to identify the MLC offset values used in *Pinnacle³*.

7.2.3. Comparison of measured and calculated transmitted dose maps

The transmitted dose maps measured using the SLIC-EPID, and calculated using TPS were compared. The maximum dose deposited in the modelled EPID was found for each subfield and a two-dimensional dose distribution was then extracted at the depth of maximum dose in the modelled EPID layer. The calculated transmitted dose maps were rescaled to pixel size corresponding to the transmitted dose maps measured with SLIC-EPID using *bilinear* interpolation. All image processing and dose distribution comparison procedures were performed using in-house codes written in MATLAB 7. The agreement between the calculated and measured transmitted dose maps was assessed for each subfield and the total field, based on the gamma function algorithm developed by Low *et al* (1998) with the DTA and ΔD_{max} criteria of 2.54 mm and 3%, respectively.

A typical series of the measured and calculated transmitted dose maps, and the corresponding relative dose difference and gamma maps for subfields acquired in the A-P direction are shown in Figure 7.5. The x and y axes represent the number of pixels for all cases. The dose tolerances within 3% are shown in grey scale on the relative dose difference maps. For gamma maps, the gamma indices smaller than or equal to 1, indicating that the point of evaluation in the "evaluated dose map" is in agreement with the corresponding point in the "reference dose map" within the defined criteria (Low and Dempsey 2003). These points are also shown in grey scale.

The inplane and crossplane profiles of the compared transmitted dose distributions, as well as the corresponding relative dose differences and the gamma profiles for all total fields are shown in Figure 7.6. For inplane profiles, the gamma values never exceed 1 (i.e. the two dose maps are in agreement within the specified criteria) in the central portion of radiation fields assessed in the AP direction. In contrast, for non-zero gantry angles, several significant discrepancies were observed between the measured and calculated transmitted dose map crossplane profiles.

The relative two-dimensional transmitted dose distributions measured using EPID and those calculated by a *Pinnacle*^{3} TPS as well as the corresponding gamma maps for accumulated fields are shown in Figure 7.7. DTA and ΔD_{max} criteria of 2.54 mm and 3% of dose on the CAX, respectively, were generally used for all cases. The gamma score of 96% or more was obtained for dose profiles for AP direction. In other fields, some disagreements between measured and calculated transmitted dose maps were observed due to the presence of the treatment couch edge, causing more attenuation in the profiles measured by EPID.

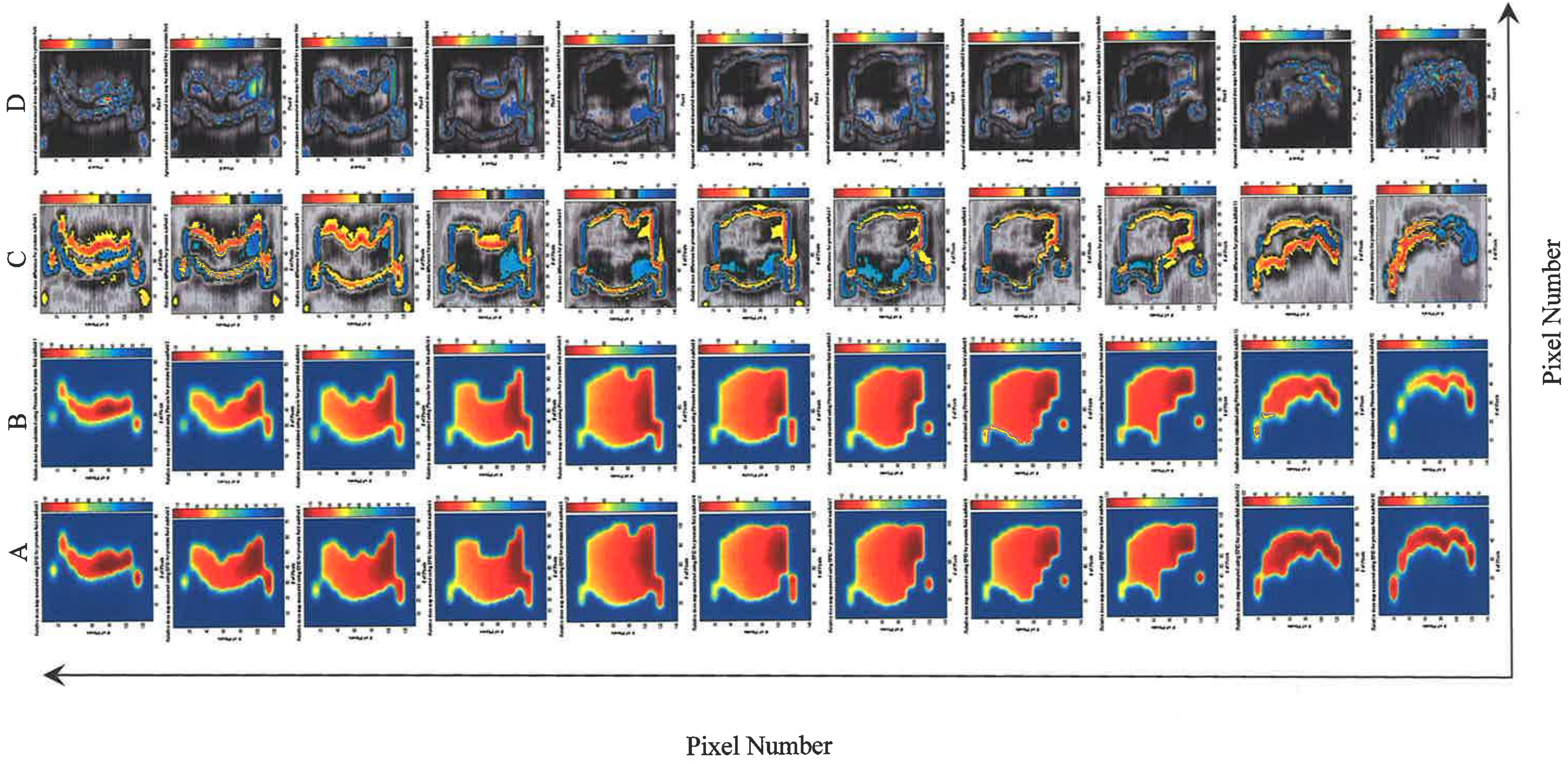

Figure 7.5 (A & B series) Transmitted dose maps measured using SLIC-EPID and the corresponding maps calculated using *Pinnacle*^{3} TPS, respectively, (C series) the corresponding relative dose difference and (D series) gamma maps for subfields acquired in AP direction. The gamma function criteria were 3%/2.54 mm for all cases. The area within 3% for relative dose difference and passed area for gamma function (within 2.54 mm) are shown in grey scale.

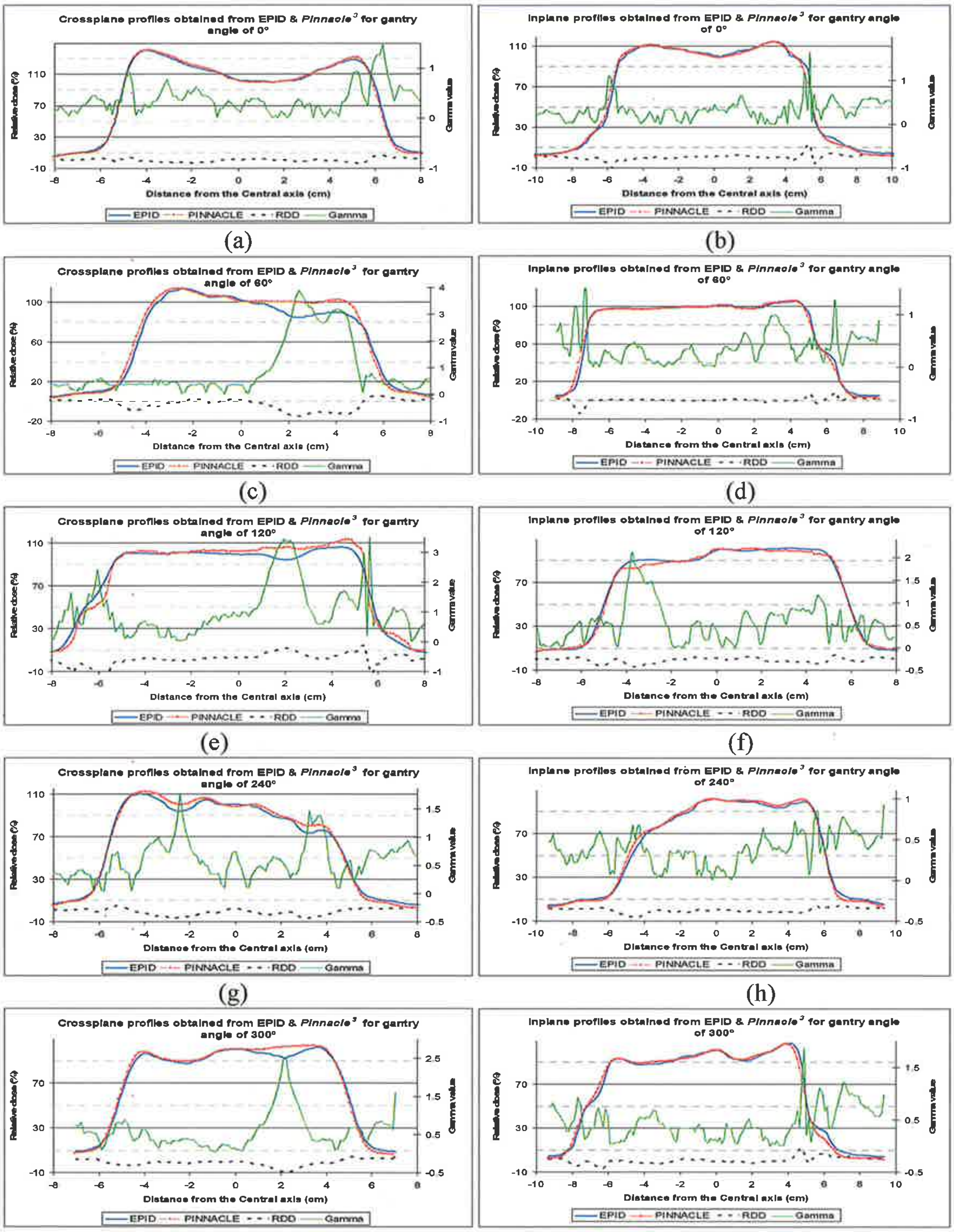

(a) (b)

(c) (d)

(e) (f)

(g) (h)

(i) (j)

Figure 7.6. Crossplane and inplane profiles of relative measured and calculated transmitted dose maps, the corresponding gamma value and Relative Dose Difference (RDD) maps of a prostate field (a & b) for AP direction and gantry angles of (c & d) 60°, (e & f) 120 °, (g & h) 240 ° and (I &j) 300°. DTA and ΔD_{max} criteria of 2.54 mm and 3%, respectively, have been used.

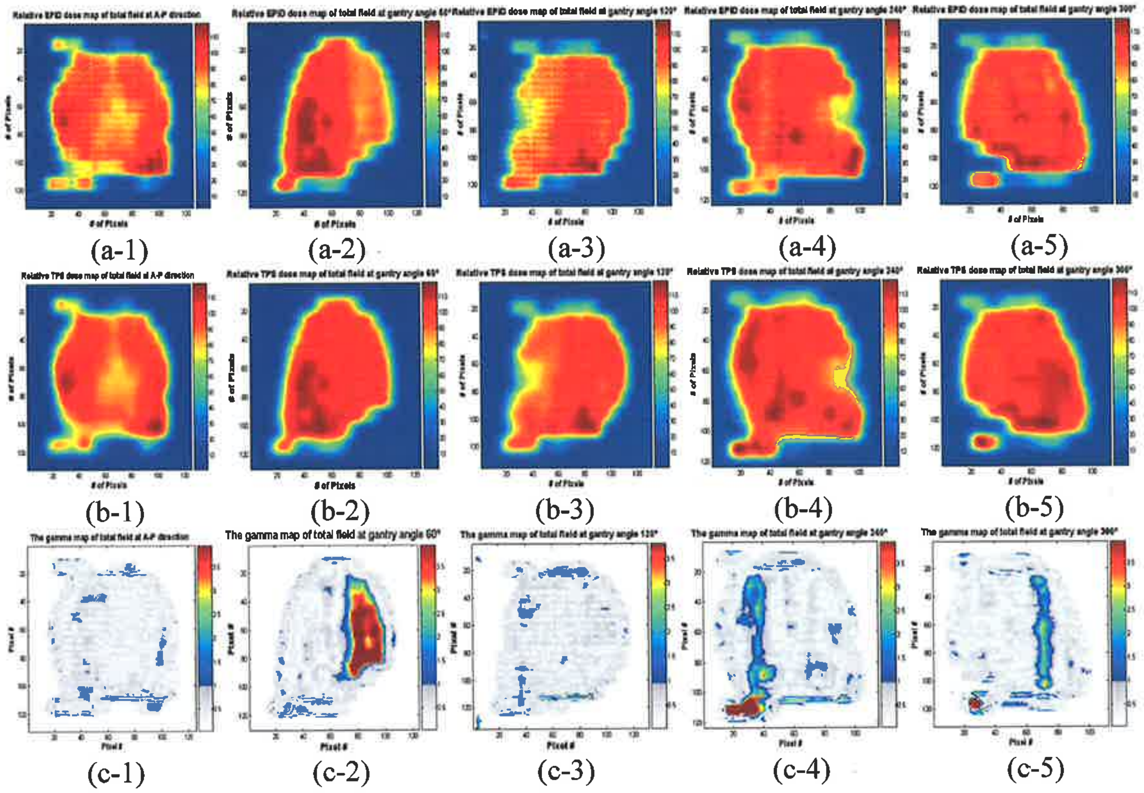

(a-1) (a-2) (a-3) (a-4) (a-5)

(b-1) (b-2) (b-3) (b-4) (b-5)

(c-1) (c-2) (c-3) (c-4) (c-5)

Figure 7.7. The relative transmitted dose maps (a series), (b series) calculated using Pinnacle^3 TPS and (c series) the corresponding gamma maps for a prostate IMRT field for 0, 60,120, 240, and 300°. The DTA and ΔD_{max} were selected 2.54 mm and 3% of the dose at CAX.

The details of agreement between measured and calculated transmitted dose distributions for each subfield and total field are shown in Table 7.1. Although some blurring in EPIs was observed for subfields positioned in the off-axis areas, excellent agreement was still observed. The maximum, minimum and average gamma scores for all subfields were found to be 96.3%, 70.8% and 87.4%, respectively. Generally, the minimum gamma scores related to the peripheral subfields.

The results of the current work show that the calibrated SLIC-EPID can be used to verify dose delivery for sIMRT. However, several modifications to the usual Pinnacle procedure, as mentioned above, must be taken into consideration. The simulation of the exact shape of the MLCs in TPSs would makes the TPS calculations more accurate (Williams and Metcalfe 2006). However, this is not implemented in the current version of *Pinnacle*^{3} software.

Table 7.1. The agreement percentages between relative transmitted dose maps measured using a SLIC-EPID and those calculated using a *Pinnacle^3* TPS. The DTA and ΔD were 2.54 and 3%, respectively.

The agreement percentage between subfields and total field of sIMRT fields													
Field	Subfield												Total field
	1	2	3	4	5	6	7	8	9	10	11	12	
A-P	83.3	93.8	95.9	93.3	90.3	91.1	95.4	94.9	95.0	93.9	93.4	81.7	96.3
60.0°	87.2	91.0	92.5	88.2	87.7	85.8	86.9	86.6	75.0	--	--	--	74.5
120.0°	88.4	87.2	87.3	85.5	87.0	87.4	94.7	95.3	95.7	86.6	--	--	80.4
240.0°	86.1	92.7	90.5	89.7	89.1	89.1	87.8	89.1	94.9	94.9	87.7	--	82.0
300.0°	87.5	94.8	88.6	87.1	87.7	89.1	89.9	89.7	86.3	85.1	--	--	87.3

Due to the limitation of routine TPSs in calculating transmitted dose distributions because of the size of CT images, a modification is required to increase the dose calculation volume behind the patients. This may cause several difficulties. Due to the inclusion of the modelled EPID, patient data set and the air gap between patient and modelled EPID, a large dose grid matrix is required. Due to the limitation of the TPS machine's memory, calculating the dose for large dose grid matrix leads to increased size of the voxels in the dose grid matrix. Consequently, the resolution of the calculated dose maps decreases. This is one of the main factors that affects the accuracy of the transmitted dose calculation when using TPSs.

The treatment couch presence in the beam path is one of the main contributing factors to the discrepancy observed between the measured and calculated transmitted dose maps, due to the exit dose perturbation before reaching the dosimeter. The crossplane profiles of two fluence maps measured with and without the treatment couch in the radiation beam are shown in Figure 7.8. The dose difference between the beam profiles for a total field measured with and without treatment couch was found to be up to 15%. This agrees with the couch attenuation measured using a fluoroscopic EPID (Vieira *et al* 2003). Although this effect can be corrected using appropriate correction techniques (Fielding *et al* 2002), the presence of different materials such as carbon fibre and aluminium supporting rods and particularly their position in respect to the EPID position, evaluating dose attenuation and its subsequent reconstruction require more study. In addition, the use of additional corrections decreases the accuracy of measurements. This perturbation in dose distribution not only reduces the applicability of portal dosimetry (see Figure 7.7), but also more considerations are required for exit dose or mid-plane dose measurements using back-projection techniques (Huyskens *et al* 1994; Boellaard *et al* 1998).

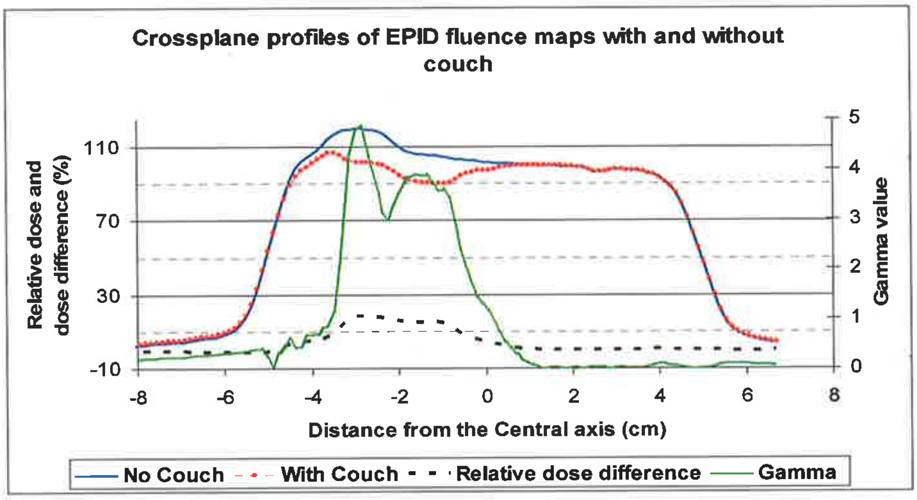

Figure 7.8. The crossplane profiles of transmitted fluence maps with and without treatment couch.

7.2.4. Summary

Although IMRT is an increasingly popular radiotherapy technique, due to the complexity of treatment more attention should be paid to verify the dose delivery procedure. In this part of current work, the transmitted dose maps were measured using a SLIC-EPID for a typical step-and-shoot prostate IMRT treatment applied to an anthropomorphic phantom in the A-P, and several non-zero gantry angles. Typical five-field prostate sIMRT MLC files were used to form radiation fields. EPIs, acquired for each subfield, were converted to the transmitted dose maps using an appropriate calibration method described comprehensively in chapter 3. The total field transmitted dose maps were then created by multiplying the contribution for each subfield with the corresponding relative weighing factor. Due to the limitation of commercially available TPS (*Pinnacle*^{3} version 6.2b) for calculation of transmitted dose behind the patient, phantom CT image matrices were extended and were then imported to the TPS. To account for the straight leaf end simulated in *Pinnacle*^{3}, the MLC offset value was found to be 0.6 mm and was applied for all calculations. The EPID was modelled as a thin water equivalent slab behind the patient, at the same distance as that at which the SLIC-EPID was positioned. For oblique beams, in order to extract the transmitted dose distributions calculated at the d_{max} of the modelled EPID, the patient CT data was rotated at the opposite direction of gantry angle and the EPID was modelled as was positioned for A-P direction. The dose distributions measured using the SLIC-EPID were then compared with those calculated in the modelled EPID for each subfield and consequently for the corresponding total fields using the gamma function algorithm with a DTA and ΔD_{max} criteria of 2.54 mm and 3%, respectively.

The agreement between measured and calculated transmitted dose maps with the gamma function criteria, used in this thesis, proves that SLIC-EPID after an appropriate dosimetric calibration can be used to verify the dose delivery for either segment or total dose assessment. The average agreements between calculated and measured transmitted dose maps were found to be approximately 95%. The presence of treatment couch in the radiation beam path, before reaching the EPID detectors, decreases the agreement by 15%. However, precautions must be taken to calibrate the EPID for dosimetric purposes. The achieved agreement between calculated and measured transmitted dose maps, presented in the current work, indicates that patient/phantom shifts in respect with that defined during the planning procedure can be determined with EPID transmitted dosimetry. In addition, the significant variation of patient anatomy in the ROI compared with that recorded during planning can also be identified. Further investigation is required to extend this dose delivery verification technique for real patients.

In conclusion, SLIC-EPIDs can be used to verify the dose delivered to the patient for prostate sIMRT when appropriate corrections are applied. However, the radiation beam attenuation of the treatment couch should be viewed as the main limitation of dose verification for oblique beam deliveries.

7.3. Dose delivery verification for a head and neck sIMRT treatment

In order to investigate the SLIC-EPID response in a treatment scenario for more inhomogeneous regions compared to the prostate case, a typical MLC file for a sIMRT designed for a head and neck treatment and an anthropomorphic Rando phantom were used. The head and neck sIMRT treatment includes 5 fields for gantry angles of 0, 20, 230, 270 and 300°. The minimum and maximum subfields were 10 and 18 for gantry angles of 300° and 230°, respectively. In order to control the undesired beam attenuation effects on the transmitted dose maps, caused by the treatment couch (see section 7.2.3), the treatment couch was removed from under the head and neck area of the phantom. A sagittal view of treatment couch, water equivalent modelled EPID, Rando phantom and the defined dose grid matrix, is shown in Figure 7.9.

7.3.1. Transmitted dose maps measured using SLIC-EPID

The EPI acquisition was similar to the procedure described in the section 7.2.1. However, the EPI acquisition software was updated after the prostate sIMRT study. To reach the same raw pixel values as achieved in the prostate case, all EPI pixel values were deducted from a constant (2^{16}). The SLIC-EPID dosimetric calibration procedures, especially the relationship between dose rate and dose with EPI pixel values, were remeasured and confirmed. To prevent possible fluctuation in EPI pixel values, three consecutive EPIs were acquired for each subfield and averaged. Other procedures were the same as described previously for sIMRT prostate case.

7.3.2. Transmitted dose maps calculated using Pinnacle^3 TPS

In order to calculate the predicted transmitted dose maps using the available TPS, like for prostate case, the patient CT data was firstly extended from 512 × 512 pixels to 1024 × 1024 pixels. The EPID was then modelled as a 5 × 30 × 30 cm^3 slab behind the phantom. The distance between d_{max} of a thin slab of water equivalent material representing EPID and the isocentre was set up to be 40 cm (SED = 140 cm). A corresponding fraction of 2 Gy total dose was prescribed for each subfield to the isocentre point located inside the anthropomorphic phantom. A three-dimensional dose grid with the voxel sizes of 0.175 × 0.175 × 0.175 mm^3 was defined to calculate the dose distributions. Due to the limited amount of available computer memory in the TPS computer, the dose grid voxel sizes were defined as 0.25 × 0.25 × 0.25 mm^3 for a gantry angle of 270°. MLC leaf offset with a value of 0.6 mm was applied manually to the TPS

MLC leaf settings for all subfields (see section 7.2.2.4). The build-up layer in the modelled EPID was found for all subfields and the transmitted dose distributions were extracted (see section 7.2.2.3).

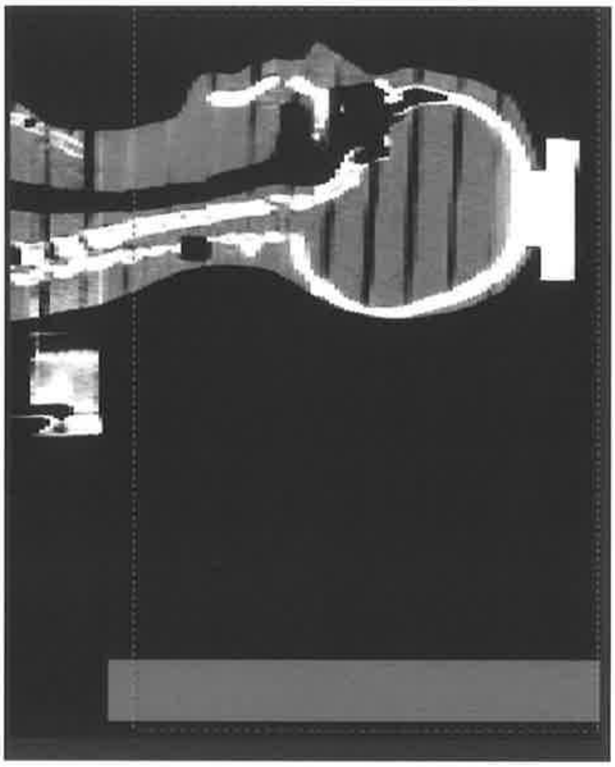

Figure 7.9. A sagittal view of a Rando phantom and the modelled EPID. The position of treatment couch removed is also shown outside the dose grid region.

The routinely available syntax command for image rotation in MATLAB software rotates the image around the central point of this image. In the prostate case, this command was used to rotate patient CT images for oblique beams. In contrast, for the head and neck case, due to the non-central position of the tumour site, the extended image was rotated around the centre of ROI.

The position of the central point of a CT image and the centre of a ROI is shown in Figure 7.10 (a). In addition, the difference in the CT numbers between a CT image rotated to 60° around central point of the CT image and around POI is illustrated in Figure 7.10 (b). The area affected by possible fluctuation of CT number, due to the use of image processing for image rotation, (approximately ± 50) (see section 6.2.2.2), is shown in grey scale. A significant variation in CT numbers was observed in the high CT number gradient regions. A maximum difference of ± 500 in CT numbers was observed in the edge of inhomogeneities.

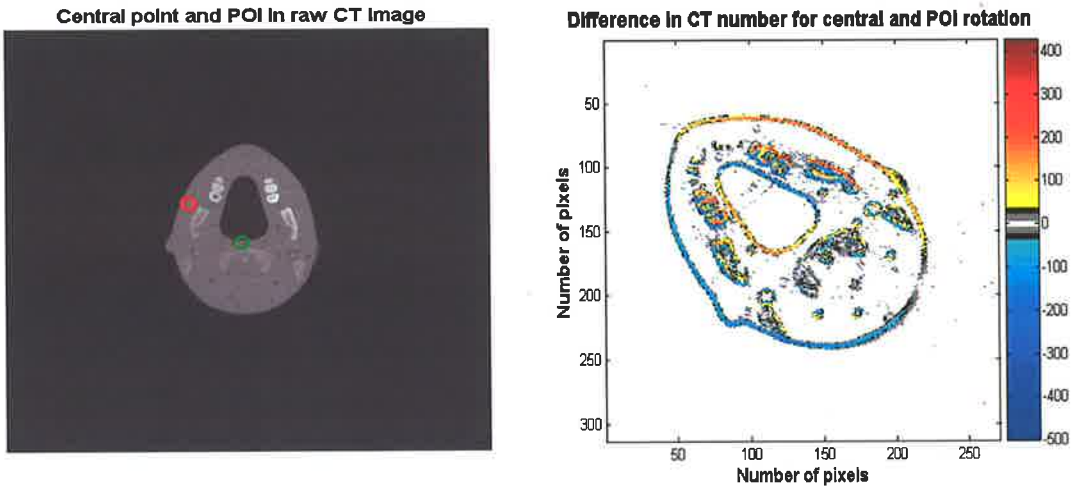

(a) (b)

Figure 7.10. (a) Raw CT image for head and neck region of a Rando phantom at AP direction. The central point of the CT image and the central point of ROI are shown in green and red, respectively; (b) The CT number difference for a CT image rotated around the central point of the image and around the central point of the ROI.

Crossplane and inplane profiles of the image rotated around the central point of image and around the central point of POI are shown in Figure 7.11. The corresponding CT number difference is also shown as a secondary axis. These line profiles show that in the boundaries of inhomogeneities, a significant variation of CT numbers was observed.

In case of transmitted dose calculation for prostate case, because of the ROI positioning in the central part of a patient (consequently in the central region of the images), the conventional image rotation does not affect the results significantly (see section 7.2.2.2). Additionally, the prostate and surrounding regions are more homogenous than the head and neck sites. In contrast, for ROIs located outside the central region of the body, the rotation around the image centre will cause artefacts. Therefore, the patient CT images must be rotated around the central point of the target volume.

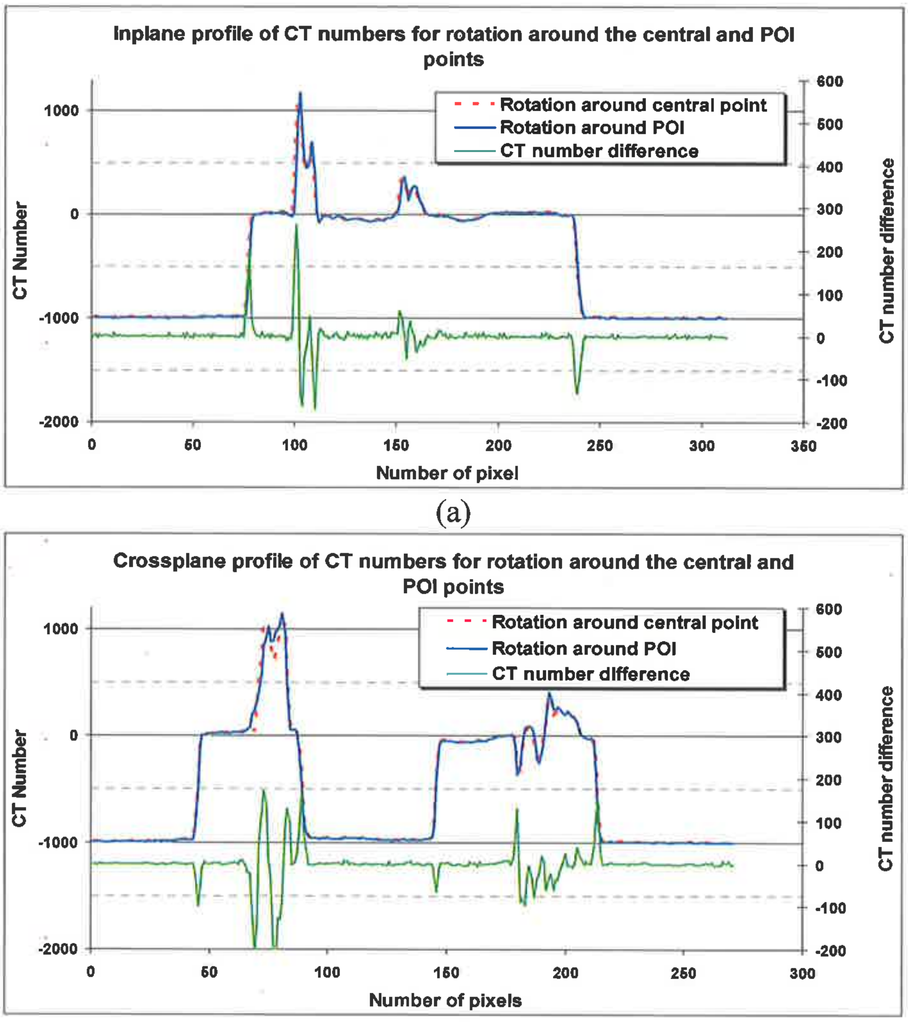

(a)

(b)

Figure 7.11. (a) Crossplane and (b) inplane profiles of two CT images rotated to 60° gantry angle around the central point of the image, around the POI and the corresponding CT number difference.

7.3.3. The comparison of the measured and calculated transmitted dose distributions for head and neck case

The measured and calculated transmitted dose maps measured using a SLIC-EPID and a *Pinnacle*^{3} TPS, respectively, were normalized to a typical point located in a large homogenous area of the irradiated field. In cases where the normalization point is positioned near significant inhomogeneities, the uncertainty in the normalization factor is greater. Both sets of transmitted dose maps were then compared using the gamma function algorithm for each subfield and the corresponding accumulated fields with the ΔD_{max} and DTA criteria of 3%/2.5 mm.

For a typical series of relative transmitted dose maps, the corresponding relative dose difference and gamma maps are shown in Figure 7.12. It refers to several radiation subfields achieved at an oblique beam (gantry angle of 230°). The x and y axes of all images represent the number of image pixels. The relative dose differences and the corresponding gamma maps show that a good agreement was observed inside the radiation fields for most MLC subfields. Several disagreeing regions were observed in the penumbral areas and more significant discrepancies were also observed for several small subfields (two of 18 subfields) used to boost the dose delivered to the central part of the tumour site. The total size of subfields with significant inconsistencies was approximately smaller than 8 cm^2. The differences will be discussed in the following sections.

After evaluating individual subfields, the corresponding total field transmitted dose maps were then created by multiplying the relative weighting factor contribution with the dose for each subfield. The corresponding calculated transmitted dose maps for total field were also prepared by adding up all of the subfields. The measured and calculated total transmitted dose maps were normalized to a point located in an approximately homogeneous area located inside the MLC field. The total relative measured and calculated transmitted dose maps, the relative dose difference and the corresponding gamma maps are shown in Figure 7.13 for all five gantry positions used in this part of the thesis. Although inaccuracy in the positioning of the normalization points and the possible misalignment of the corresponding subfields decreases the correlation between measured and calculated dose distributions, consistency was observed inside the ROIs for all gantry positions.

In some subfields and consequently in the accumulated total fields, several significant differences were observed between measured and calculated transmitted dose maps inside the MLC fields and outside the patient anatomy. The relative dose differences in these regions were found to be greater than 6% for all subfields observed for two series of data sets acquired at A-P direction and at the gantry angle of 300°. The calculated dose values were found to be greater than those measured using SLIC-EPID in all these cases.

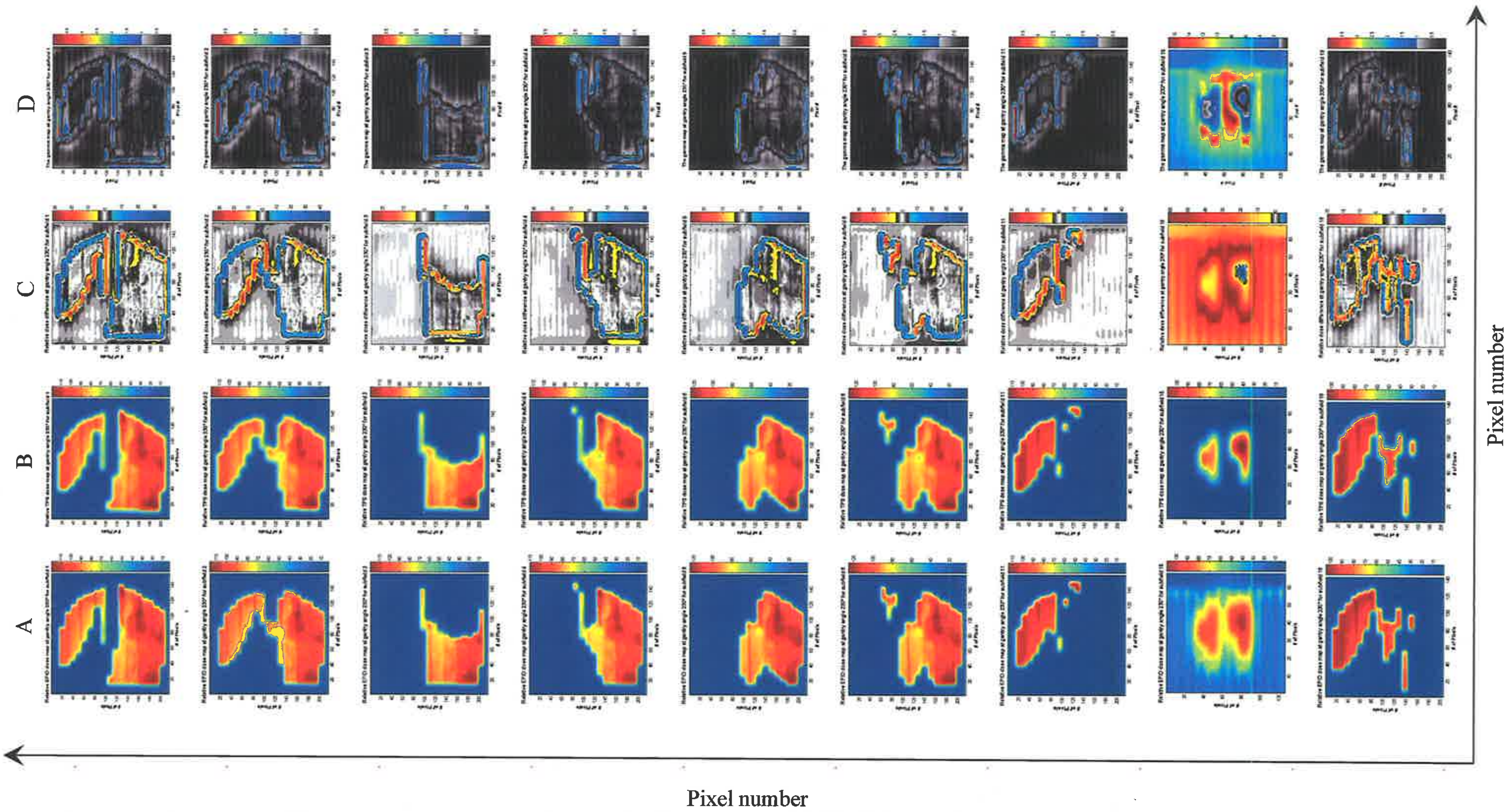

Figure 7.12. Transmitted dose maps measured and calculated using SLIC-EPID and Pinnacle^3 TPS (A &B series respectively), the corresponding relative dose difference (C series) and gamma maps (D series) for subfields acquired for the gantry angle of 230°. The gamma function criteria are 3%/2.54 mm for all cases. The area within 3% for relative dose difference and agreed area for gamma function (3%/2.54 mm) are shown in grey scale.

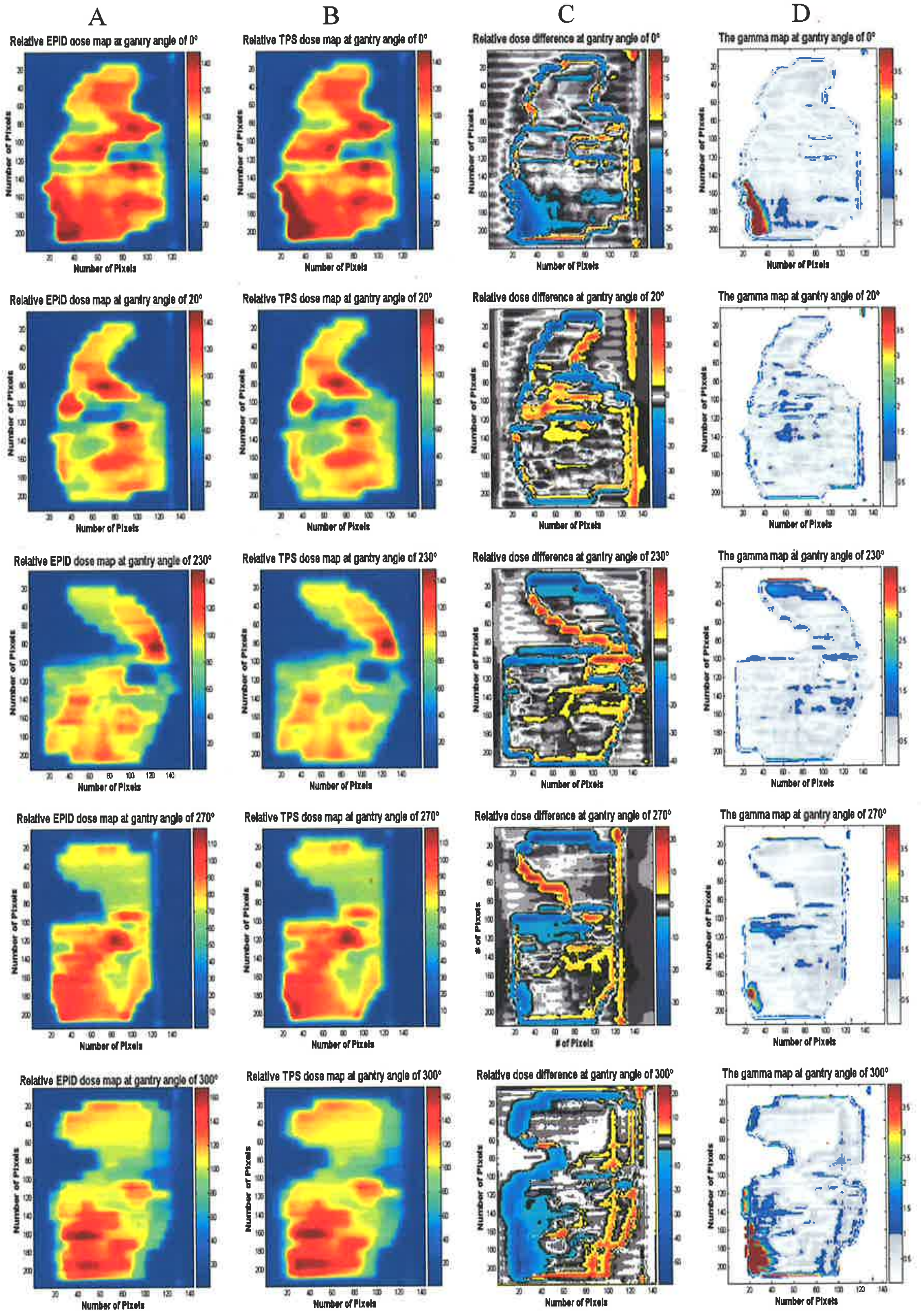

Figure 7.13. (A series) Total field transmitted dose maps, (B series) calculated transmitted dose maps, (C series) relative dose differences, and (D series) the corresponding gamma maps with criteria of 3%/2.54 mm at gantry angles of 0, 20, 230, 270, and 300 degrees.

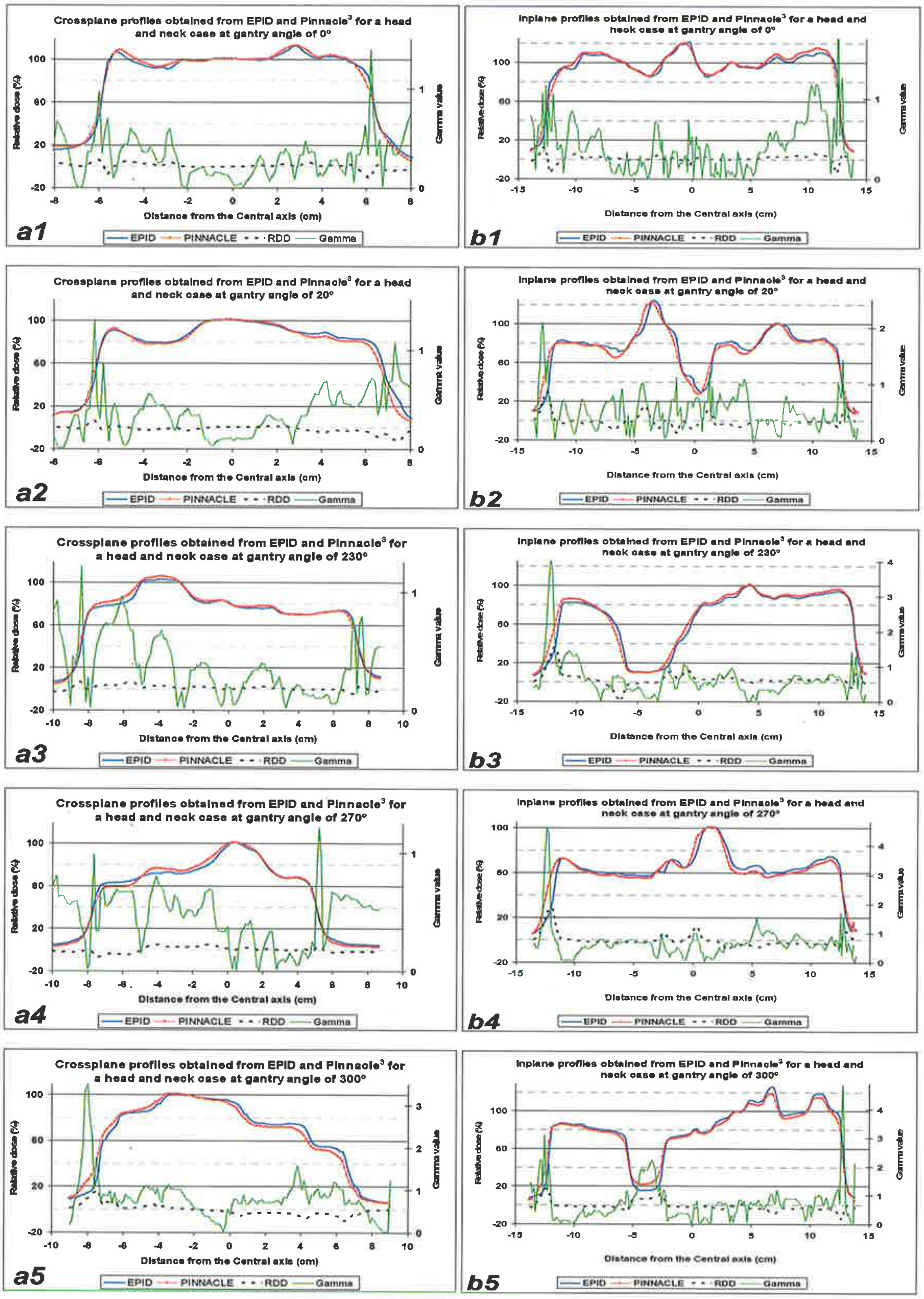

a1 Crossplane profiles obtained from EPID and Pinnacle^3 for a head and neck case at gantry angle of 0°

b1 Inplane profiles obtained from EPID and Pinnacle^3 for a head and neck case at gantry angle of 0°

a2 Crossplane profiles obtained from EPID and Pinnacle^3 for a head and neck case at gantry angle of 20°

b2 Inplane profiles obtained from EPID and Pinnacle^3 for a head and neck case at gantry angle of 20°

a3 Crossplane profiles obtained from EPID and Pinnacle^3 for a head and neck case at gantry angle of 230°

b3 Inplane profiles obtained from EPID and Pinnacle^3 for a head and neck case at gantry angle of 230°

a4 Crossplane profiles obtained from EPID and Pinnacle^3 for a head and neck case at gantry angle of 270°

b4 Inplane profiles obtained from EPID and Pinnacle^3 for a head and neck case at gantry angle of 270°

a5 Crossplane profiles obtained from EPID and Pinnacle^3 for a head and neck case at gantry angle of 300°

b5 Inplane profiles obtained from EPID and Pinnacle^3 for a head and neck case at gantry angle of 300°

Figure 7.14. The (a series) inplane and (b series) crossplane profiles of total field measured and calculated transmitted dose maps, Relative Dose Differences (RDDs), and the corresponding gamma indices with 3%/2.54 mm for gantry angle of 0, 20, 230, 270, and 300 degrees.

Crossplane and inplane profiles for total fields are shown in Figure 7.14 for transmitted dose maps measured and calculated using EPID and *Pinnacle*^{3} TPS, respectively. The x and y axes represent the distance from the central axis and relative dose values, respectively. The gamma index is also shown as the secondary axis. In the high dose gradient regions, several discrepancies were observed. The corresponding relative dose difference and the gamma indices are also shown in Figure 7.14. Gamma scores generally were smaller than 1, which shows the PASSED regions within the defined criteria inside the radiation field.

In order to show more information on the agreement between measured and calculated transmitted dose distributions for each subfield and for the corresponding total field, the gamma scores for all evaluated subfields and total fields are shown in Table 7.2. Due to the blurring of the EPIs, for subfields approximately smaller than 8 cm^2 used to boost the radiation in the tumour active regions, several significant inconsistencies were observed. The average agreement for these subfields was found to be less than 39.5%. The result for a typical small MLC field is shown in Figure 7.12 (see subfield 15). The relative dose difference values for regions outside the MLC fields was found to be greater than 3% of the dose delivered to the central part of MLC field, defined as the dose difference criterion for gamma assessment. Discarding the results for small fields, the maximum, minimum and average gamma score for all subfields were found to be 98.3%, 72.1% and 92.6%, respectively. As a result (the agreement between two series of consecutive EPIs the agreement is approximately 99%) it can be said that for most fields there is an excellent agreement between TPS and EPID transmitted dose distributions.

The reasons for the differences between the calculated and measured transmitted dose maps were investigated. The first group of inconsistencies were for small fields (smaller than 8 cm^2 at the isocentre). EPI blurring was found to be the main source of the uncertainty. The second group of inconsistencies referred to several subfields for which not all parts of the radiation beam were incident on the phantom, but were passing through air. Although this type of discrepancy is irrelevant to transmitted dose passing through the patient, the gamma score, for the MLC fields affected by this problem, decreases significantly. These two important issues are discussed in the following sections.

Table 7.2. The agreement percentages between relative transmitted and the corresponding calculated dose maps. The gamma criteria were 3%/2.54 mm.

Subfield	The agreement percentage between subfields and total field of sIMRT fields (%)				
	Field 1 (0°)	**Field 2 (20°)**	**Field 3 (230°)**	**Field 4 (270°)**	**Field 5 (300°)**
1	95.7	95.7	91.0	94.3	92.6
2	95.1	92.9	91.7	95.00	93.6
3	94.2	94.7	93.3	95.2	91.7
4	94.5	95.0	94.4	96.2	91.3
5	94.1	93.6	96.7	96.0	84.3
6	95.4	94.0	94.4	96.6	46.8
7	97.6	93.9	94.5	97.3	22.6
8	87.0	50.4	92.7	97.4	29.4
9	88.3	2.1	95.9	36.9	72.1
10	89.0	93.4	96.5	5.2	89.4
11	2.6	92.7	96.3	96.4	--
12	2.2	93.5	0.7	--	--
13	21.8	95.1	94.2	--	--
14	52.8	95.5	2.3	--	--
15	90.5	95.7	6.2	--	--
16	92.5	--	98.3	--	--
17	--	--	97.7	--	--
18	--	--	95.9	--	--
Total field	**86.7**	**90.2**	**89.8**	**88.6**	**82.3**

7.3.3.1. SLIC-EPID response for small radiation fields

Throughout this thesis, a blurring of SLIC-EPIs was observed for small radiation field sizes (see sections 3.2.2 and 7.2.3 for off-axis narrow fields). This blurring is evaluated in the current section for regular and irregular radiation fields. The effect of the additional build-up layer and the positioning of the conventional jaws for MLC fields are discussed.

The additional build-up layer increases the free electrons reaching the EPID sensitive layer and the contribution of scattered photons (Boellaard *et al* 1996). More scattering increases the "fog phenomenon" in EPIs, and this decreases the sharpness of EPI. In this section, the impact of additional build-up layer on the EPI quality, used for dosimetric calibration, is analysed.

In order to do this, several EPIs were acquired for rectangular radiation field sizes from 1 × 1 to 5 × 5 cm² with and without additional build-up layer used (5 mm RW3 layer). To prevent the impact of statistical fluctuations on EPIs, for each set-up three consecutive EPIs were acquired, averaged and converted to the radiation fluence map using calibration dosimetric calibration method developed in the current work (see section 3.4). Two series of EPIs acquired with/without an additional build-up layer were compared and the absolute dose difference between EPIs was obtained.

Typical radiation fluence maps for field sizes from 1 × 1 cm² to 4 × 4 cm² are shown in Figure 7.15. The x and y axes represent the number of pixels for all cases. A significant blurring of EPIs was observed for 1 × 1 cm² radiation field size acquired both with and without the build-up layer. The absolute dose difference map between two averaged EPIs shows that the additional build-up layer increases uniformly the EPI pixel values in the blurred area as is expected. As a result, due to the consistency between dose maps and the corresponding dose difference maps shown in Figure 7.15, the additional build-up layer has no significant effect on the blurring of small field images.

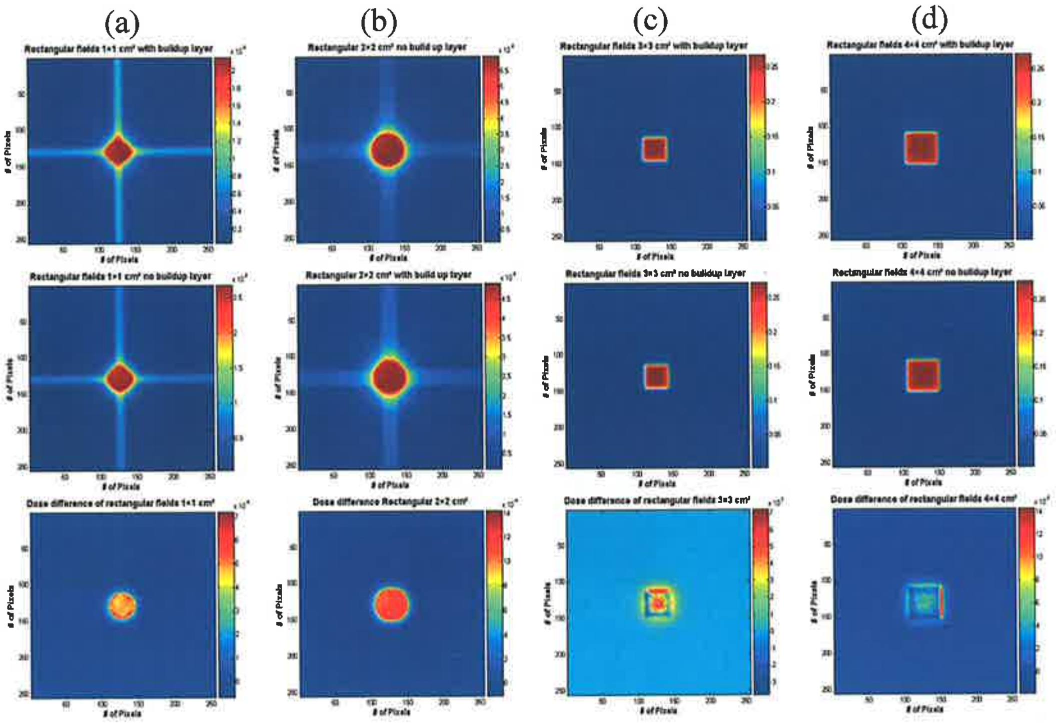

Figure 7.15. The primary fluence maps (a series) without build-up layer, (b series) with the use of build-up layer, and (c series) the corresponding dose difference maps for rectangular radiation field sizes for 1 ×1, 2 × 2 and 4 ×4 cm².

Two horizontal and vertical strip bands, exactly the width of defined radiation field size, were observed for radiation field sizes smaller than 9 cm^2. The width of strip bands was found to be the same size as the radiation field size. This shows that the scanning of the row and column processing in the SLIC-EPID affects the pixel values.

The impact of conventional jaws positioning on the blurring of EPIs acquired for small MLC fields was also explored. Setting up the conventional jaws in various positions, the impact of intra/inter leaf leakage on the EPI blurring was investigated. This was done for two groups of MLC fields: firstly, small fields and secondly, the small fields in the presence of larger fields. Typical results are shown in Figure 7.16. In the first row of the figure, a small MLC field with three separated areas is shown. The conventional jaws were positioned far from MLC leaf positioning (14 × 20 cm^2) and also close to the opened MLC leaf positions (0.5 cm behind). The corresponding absolute dose difference is also displayed. Due to the blurring observed in the EPIs, three small fields can not be distinguished. The absolute dose difference map shows that the impact of jaw positioning does not either remove or reduce the blurring effect.

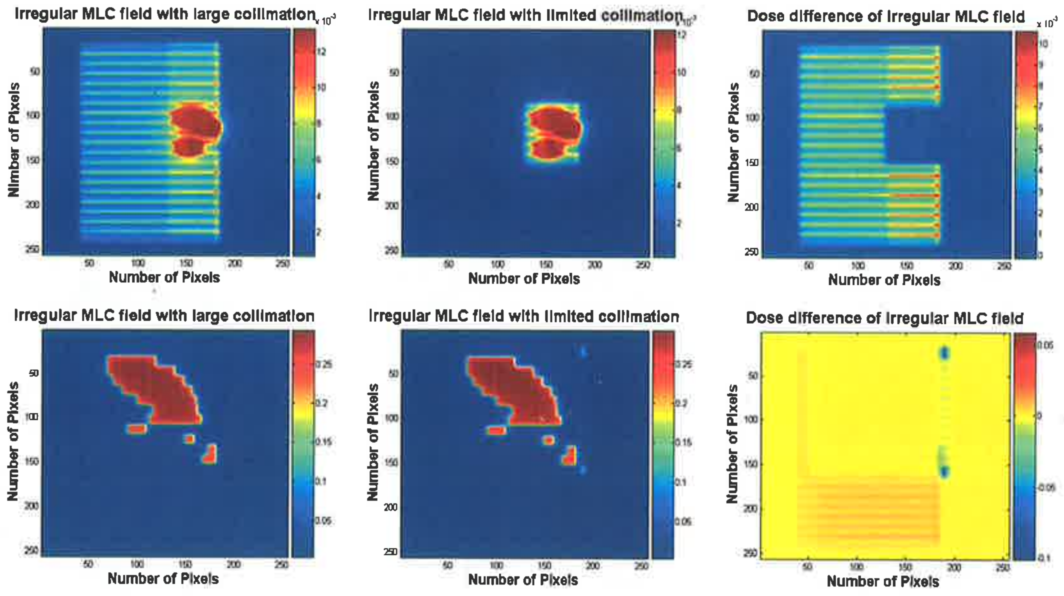

Figure 7.16. Absolute transmitted dose maps of MLC fields with the jaws positioned away and close to the MLC field and the corresponding absolute dose difference map for (first row) several small MLC fields, (second row) several small fields in the vicinity of a large irradiated area.

Although the blurring effect is observed in EPIs acquired using SLIC-EPID for small radiation fields, in the presence of large irradiated areas, the small irradiated areas can be detected clearly. As the second row in figure 7.16 shows, no blurring was observed for small MLC fields (less than 9 cm^2) when there is a large irradiated area in the vicinity of small fields. In this case, no significant difference was observed for retracted and closed jaw positioning.

SLIC-EPIDs, like other EPIDs, are generally developed to acquire an EPI for large open fields to verify patient positioning. It can be assumed therefore, that the row and column scanning procedure as well as the supporting software do not process correctly the EPIs acquired for small radiation fields. No significant effect of the additional build- up layer and conventional jaws positioning was found on the blurred EPIs. The main reason for this is not exactly clear. The vertical and horizontal strips show that the supporting SLIC-EPID image construction including hardware and software could be responsible for EPI blurring because there is no radiation deposition in the off-axis areas.

7.3.3.2. SLIC-EPID response for high dose gradient regions

Several discrepancies between EPID measurements and TPS calculation were observed in the peripheral part of the MLC radiation fields. Typical gamma maps obtained from EPID and TPS comparisons for subfields of field 1 (AP direction), field 4 (gantry angle 270°) and field 5 (gantry angle of 300°) are shown in Figure 7.17. All of the significant disagreements were found to be located in the areas where beams were passing through air (outside the patient). As all gamma maps show (series a), there is a good agreement for gamma maps in regions where the radiation beam passed through the patient/phantom. On the other hand, significant discrepancies exist for radiation field sites where the beam is passing through the air. The corresponding relative dose difference maps (series b) show that the TPS relative dose values are greater than those measured using SLIC-EPID for disagreeing areas.

In order to find the reason for this discrepancy in the special part of the gamma maps, two possibilities were investigated. Firstly, there was a concern about the calibration method used in this work; particularly for the off-axis correction performed using EDR2 films (see section 3.4). The second concern was about how EPID or TPS responded at the interface between inhomogeneities. For the first hypothesis, in order to check the calibration method in the specific site of radiation dose maps, where consistently disagreement were observed, the agreement between EPID and TPS dose values was investigated for a large radiation field (17.0 ×17.0 cm^2). 10 cm RW3 layers were used as a homogeneous attenuator. The acquired EPIs were averaged and converted to dose using calibration procedure developed here (see section 3.4). The same condition was set up and calculated using Pinnacle^3 TPS. The relative transmitted dose map and the corresponding PDI were compared using a gamma function algorithm with 3%/2.54 mm criteria.

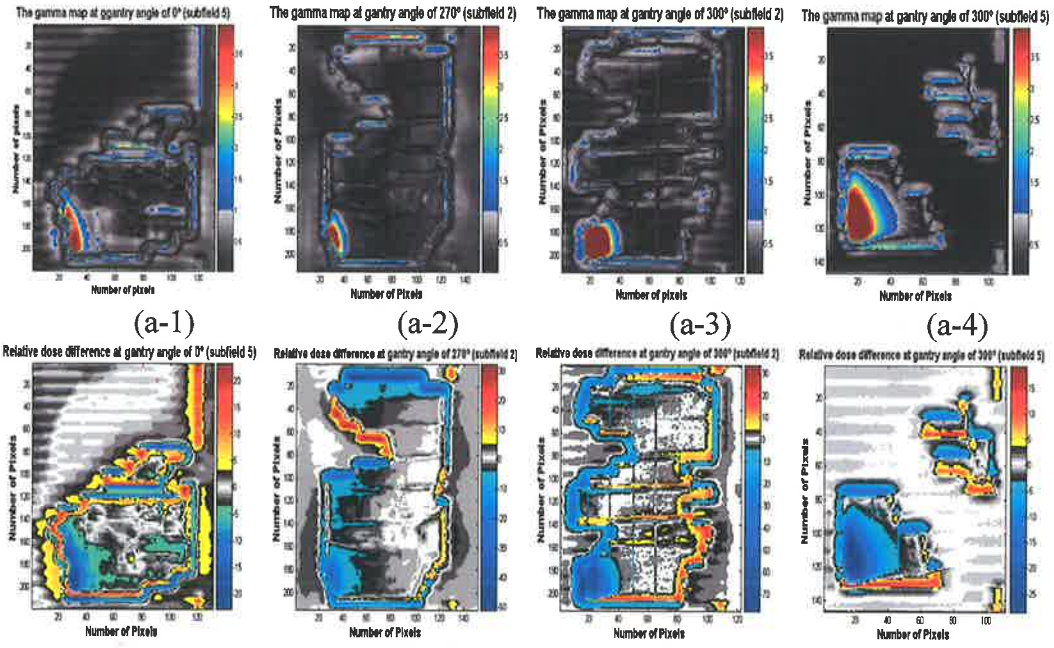

(a-1) (a-2) (a-3) (a-4)

(b-1) (b-2) (b-3) (b-4)

Figure 7.17. (a series): The gamma and (b series) the relative dose difference maps for typical radiation subfields at AP direction, at gantry angle of 270° and 300°. The PASSED area for gamma criteria 3%/2.54 mm and dose difference within 3% for relative dose difference maps are shown in grey scale.

The EPID and TPS relative dose maps, the corresponding relative dose difference and gamma maps are shown in Figure 7.18. As the relative dose difference and the corresponding gamma maps show, there is no special area revealing any disagreement between TPS calculation and EPID measurements. This proves that the calibration method used in this study imposes enough accuracy when using the EPID dosimetry.

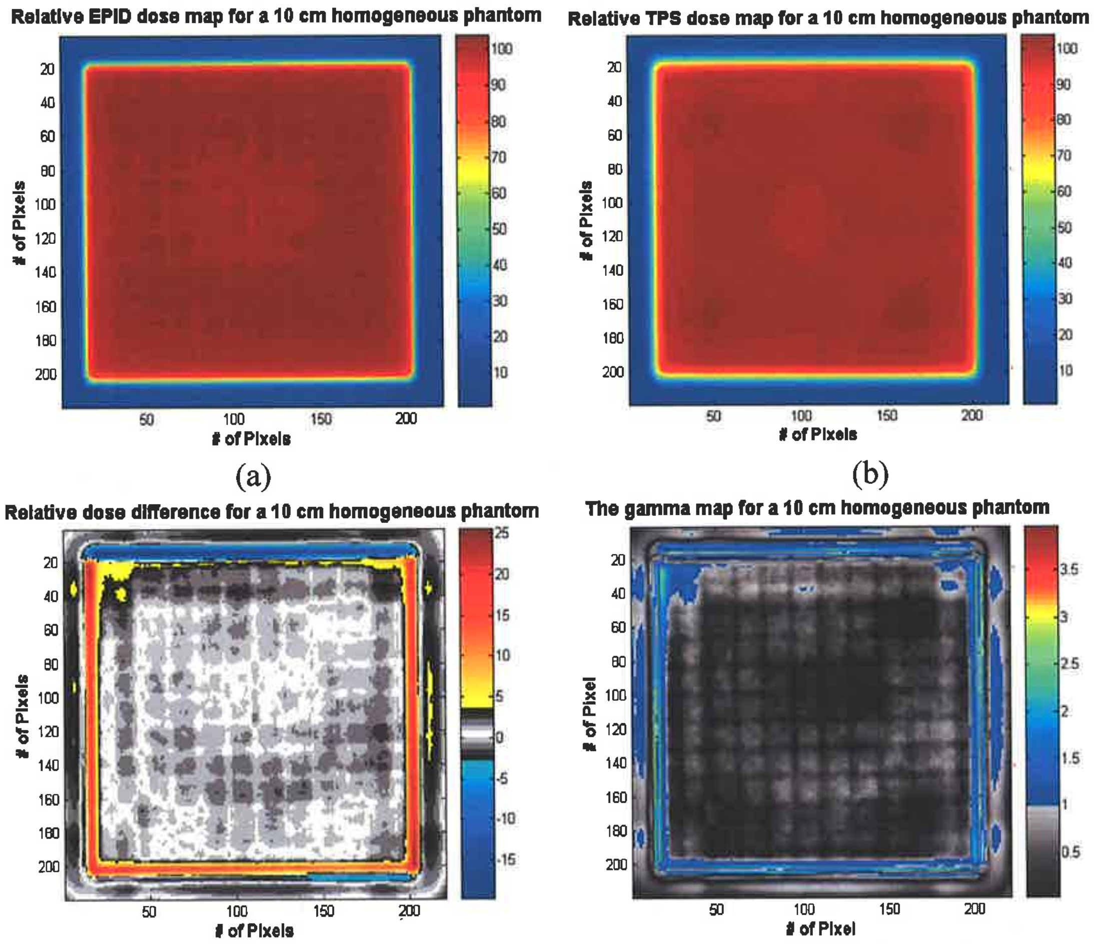

(a)

(b)

(c)

(d)

Figure 7.18. (a & b) Relative measured and calculated transmitted dose maps for a 17 × 17 cm² in the presence of a 10 cm homogenous attenuator; (c & d) the relative dose difference and gamma maps with 3%/2.54 mm criteria.

In order to investigate the TPS and SLIC-EPID response in the interface between air and phantom, the homogenous phantom, used to verify the proposed calibration procedure, was shifted by 2 cm in the direction of the x and y axes. The homogenous phantom was positioned so that a part of the radiation beam passed through the air. The measured and calculated transmitted dose maps, corresponding relative dose difference and, gamma maps are indicated in Figure 7.19. The corresponding line profiles are shown in figure 7.20. The results showed that after normalization to the central point located in the homogeneous phantom region, a significant discrepancy was observed between the measured and calculated transmitted dose maps in the area corresponding to the air region. In addition, the relative dose difference map showed that at all points that the beam passed through the air, the dose calculated using TPS is greater than those measured using SLIC-EPID. Moreover, the area irradiated through the air for EPID measurements was found to be wider than those calculated using TPS.

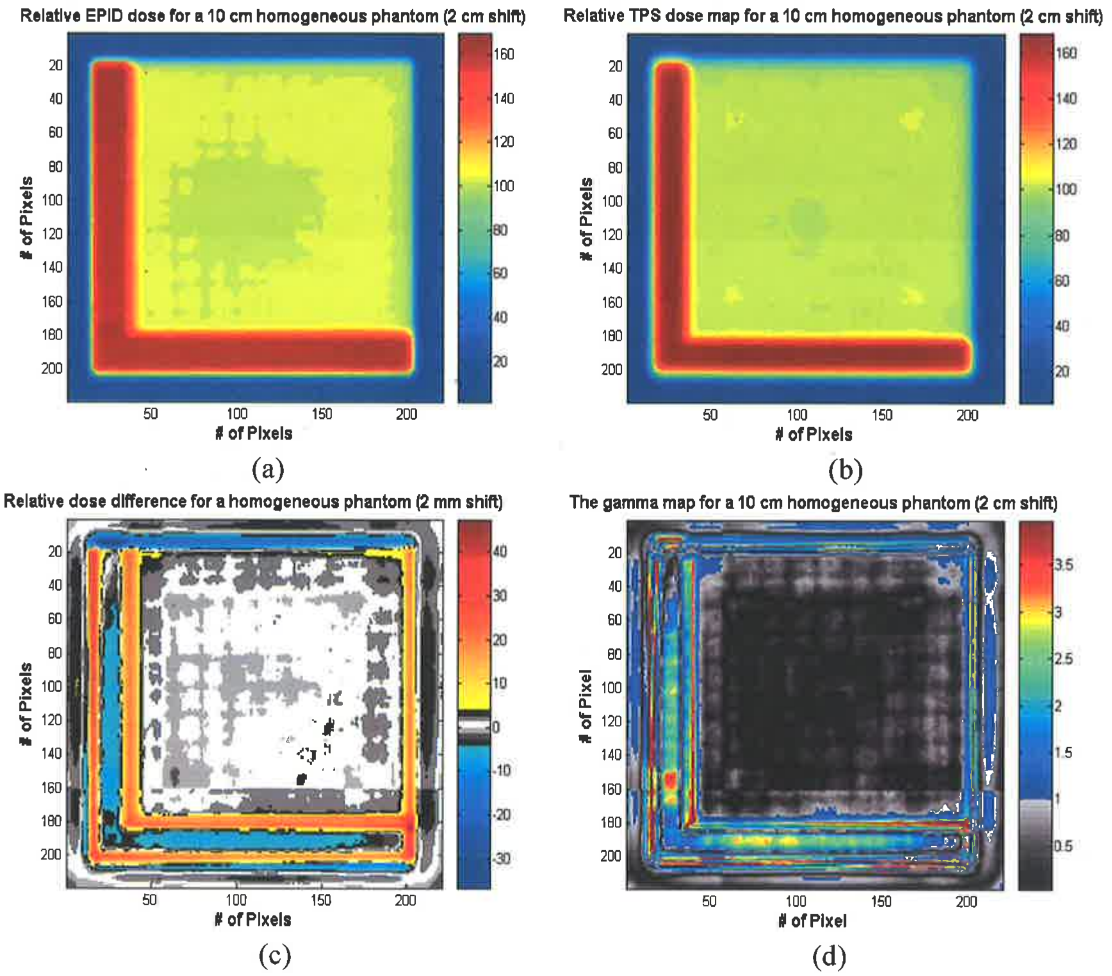

(a) (b)

(c) (d)

Figure 7.19. (a & b) Relative measured and calculated dose for a 17× 17 cm^2 for a 2 cm shifted 10 cm homogenous attenuator in x and y axes directions; (c & d) the corresponding relative dose difference and gamma maps with criteria of 3%/2.54mm.

Discrepancies between TPS and EPID dose profiles in the air areas can arise due to EPI construction. Two factors, SLIC-EPID hardware and data processing software, allow the EPID output to change. By using a 1 mm liquid film (Iso-octane, spectro-scopical pure, Merck) as an ionization medium (van Herk and Meertens 1988), the SLIC-EPID ionization chambers are not quite independent and each pixel value can be affected by the neighbouring pixels located in the surrounding region. The impact of software used to construct the EPI should also be taken into consideration.

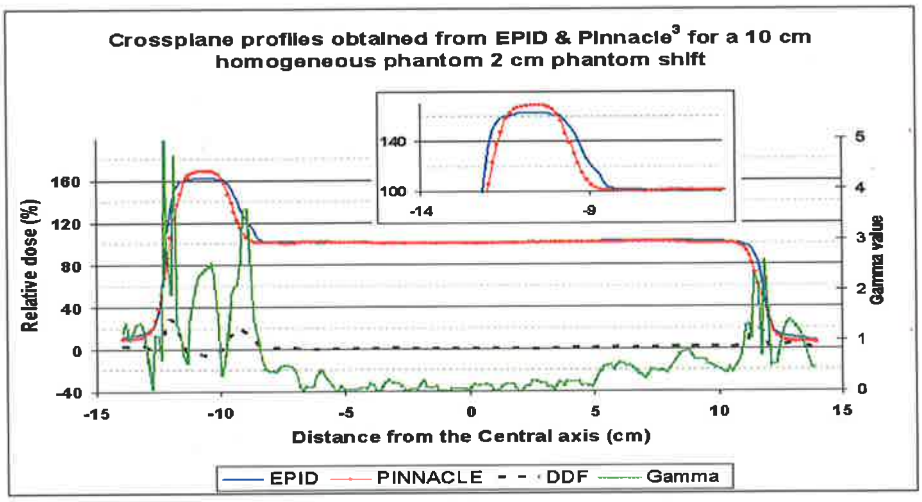

(a)

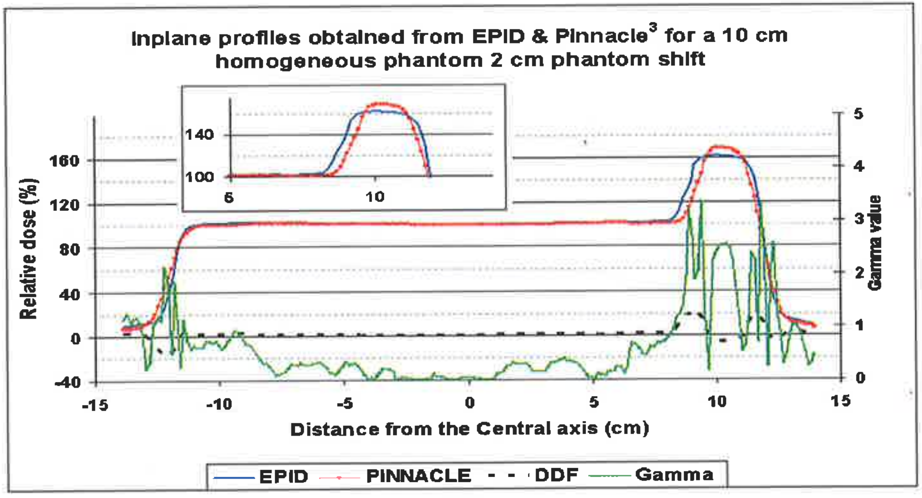

(b)

Figure 7.20. (a) Crossplane and (b) inplane profiles of the measured and calculated relative dose maps, the corresponding relative dose difference and gamma map with 3%/2.54 mm criteria for a 17× 17 cm² field size for a 2 cm shifted 10 cm homogenous attenuator in x and y axes.

Several modifications including offset, dark field and flood field corrections are defined in the image acquisition software (PortalVision LC250, Varian Medical System Inc, Switzerland) have been used to construct EPI. Moreover, several additional corrections such as filtering, linear correction and linear fix correction algorithms can be applied following the image acquisition (Varian-medical-system 2000). These corrections control the undesired noise and to smooth EPI pixel values. Through these procedures it is expected that the EPID response to be lower and wider than that calculated using TPS for the same conditions.

The output of the TPS on the interface between air and phantom should also be taken into account. The available TPS, Pinnacle^3 (version 6.2) calculates the dose with the collapsed cone convolution superposition algorithm (Mackie *et al* 1985; Ahnesjo 1989). This algorithm is based on average density scaling method rather than a local density scaling. The scaling leads to the overdose/lowerdose calculations compared to the measurements and Monte Carlo simulations (Battista and Sharpe 1992; Metcalfe *et al* 1997).

In conclusion, several issues like EPI blurring and difference observed between calculated and measured transmitted dose maps decrease the accuracy of transmitted dose measurements. However, due to the small size of these radiation fields and their contribution, the impact of blurred EPIs on the total field evaluation is negligible. Moreover, significant inconsistencies occurring between measured and calculated dose maps, due to their location (in the air), they are irrelevant to the patient dose delivered and do not compromise the accuracy of dose delivery verification.

7.3.4. Summary

The dose delivery verification for a head and neck sIMRT case using SLIC-EPID was investigated. In order to control the attenuation of a beam passing through the treatment couch, the phantom was set up at the end of the treatment couch. The transmitted dose measurement using EPIs, acquired using SLIC-EPID, was the same as described for the prostate sIMRT case. For transmitted dose calculations, although the patient CT data was extended in much the same way as the prostate case, for oblique dose deliveries in contrast to prostate case the CT images were rotated around the tumour centre. For large MLC fields, an excellent agreement was observed between transmitted dose measured using SLIC-EPID and calculated by TPS (gamma score approximately 95%). For several small subfields, however, due to EPI blurring a significant disagreement was found in the gamma results. Additionally, a significant disagreement between EPID and TPS dose maps was found in several parts of the radiation subfields, when the radiation beam passed through the air.

The transmitted dose distributions measured using portal imagers such as SLIC-EPID can be used to verify the dose delivery to the patient. However, several issues such as accurate calibration procedure and imager response under different conditions should be taken into the consideration. For instance, the SLIC-EPID image construction procedure reduces the quality of EPIs acquired for small fields. In addition, SLIC-EPID response differs from TPS response when a large inhomogeneity, for example a large air pocket, is positioned in the radiation beam path.

7.4. Summary and Conclusion

Transmitted dose distributions can be used to verify dose delivery. In addition, they can be useful to reconstruct the dose delivered to the patient using back-projection algorithms. In this chapter the response of SLIC-EPID as a comprehensive two-dimensional dosimeter for typical sIMRT cases was discussed in detail. The transmitted dose measured in the EPID sensitive layer was compared with those calculated using TPS. Comparison of transmitted dose map distributions indicates that several precautions must be taken into account to calibrate the EPID for dosimetric purposes. For instance, the main limitation of this study is that the treatment couch position during treatment affects dose distributions. The blurring of EPIs acquired for small radiation field sizes should also be noted.

Although IMRT is an increasingly popular radiotherapy technique, due to the complexity of treatment more attention should be paid to verify the dose delivery procedure. The agreement between measured and calculated transmitted dose maps with the proposed criteria for gamma function evaluation verifies that SLIC-EPID after an appropriate dosimetric calibration can confirm the dose delivery for either segment or total dose assessment.

Section 7.2 shows that SLIC-EPID can be used for dose delivery verification for step-and-shoot prostate IMRT treatment. However, the prostate region of the pelvis is close to being homogeneous and for more complex regions like head and neck positions further investigation was required. Section 7.3 shows that the SLIC-EPID can also be used in more complex conditions compared to the prostate case.

SLIC-EPID is reliable for dose delivery verification for sIMRT treatment cases. However, due to the variation of nominal linac repetition rate for dynamic treatments, and SLIC-EPID response dependency on the linac repetition rate (see section 3.2.1), as well as due to the use of small and narrow radiation fields in dIMRT, further investigations are recommended to show SLIC-EPID behaviour in dynamic IMRT treatments.

Chapter 8. Conclusions and possible future researches

8.1. Summary of findings and conclusions

The evaluation of Scanning Liquid Ionization Chamber Electronic Portal Imaging Device's (SLIC-EPID) response as a two-dimensional comprehensive dosimeter for step-and-shoot Intensity Modulated Radiation Therapy (sIMRT) was the main objective of this work. In order to do this, due to the EPID's primary function to verify patient set up, the SLIC-EPID must be calibrated for dosimetric purposes. The validity of the calibration procedure must also be evaluated for a range of conditions such as conventional radiotherapy and IMRT.

Due to the SLIC-EPID main role for patient set up verification, in order to use the EPID for dosimetric tasks, a dosimetric calibration is required. In addition, prior to the dosimetric calibration procedure, several properties such as reproducibility and noise level of Electronic Portal Images (EPIs) must be assessed. In chapter 3 it has been shown that SLIC-EPID has good short-term and medium-term reproducibilities and the noise level is around 1%. In addition, a comprehensive dosimetric calibration procedure has been developed. The application of dosimetric calibration method for primary radiation fluence maps, and for homogeneous and inhomogeneous phantoms has been investigated in chapter 4. The results showed that the primary fluence maps measured using SLIC-EPID are in agreement with those measured using Extended Dose Range (EDR2) films using gamma function algorithm with Distance To Agreement (DTA) and Dose difference (ΔD_{max}) criteria of 2.54 mm and 1%, respectively. The transmitted dose maps measured for homogeneous and inhomogeneous phantoms were found to be in agreement with EDR2 film measurements and Treatment Planning System (TPS) calculations with 2%/2.5 mm and 3%/2.5 mm criteria, respectively.

In order to investigate the SLIC-EPID sensitivity for dosimetric purposes, two experiments were also performed to evaluate its capability to detect variations in phantom/patient thickness as well as it sensitivity to find the set-up uncertainties in the transmitted dose maps. These are described in chapter 5. In other words, experiments were performed to evaluate the SLIC-EPID capability to detect patient anatomy variation, either due to the set up errors or any physiological changes during a treatment course.

Before using the SLIC-EPID for complex modalities such as sIMRT, its capability to evaluate dosimetric properties of radiation fields formed by Multileaf Collimators (MLCs) was investigated. In chapter 6, it was found that the SLIC-EPID can detect the difference in radiation field size formed by conventional jaws and MLCs. The dosimetric characteristics of penumbral regions, the isodose curves undulation and scalloping for radiation fields set up using MLCs can also be measured using SLIC-EPID. The MLC leaf positioning was also investigated and it was found that SLIC-EPID detects 0.1 mm MLC leaf displacement using standard edge detection algorithms. The impact of the patient set-up uncertainties on the transmitted dose maps was also studied and the corresponding results have shown that the both relative dose difference and the gamma maps can be used as useful tools for intra-course and inter-course evaluations.

In chapter 7, the SLIC-EPID response as a two-dimensional comprehensive dosimeter at Anterior-Posterior (AP), lateral directions as well as for oblique beam deliveries was investigated for two typical prostate and head and neck step-and-shoot IMRT cases. The measured transmitted dose maps were then compared with those calculated using

Pinnacle^3 TPS using gamma function algorithm with 3%/2.5 mm criteria. If the attenuation of treatment couch is controlled, an excellent agreement (gamma score >95%) could be observed for the measured and calculated transmitted dose maps for large radiation fields. In contrast, several blurring in EPIs were observed for small radiation fields (approximately less than 8 cm^2). The radiation beam attenuation by treatment couch increases the differences between measured and calculated dose distributions. This can be considered as the main limitation of portal dosimetry, especially for oblique beam dose deliveries.

Several other limitations were observed during this study. Although the EPI acquisition time is one of the main obstacles to measure the absolute transmitted dose, the acquisition time is long enough to achieve reliable response (van Herk 1991) for relative dosimetry. This limitation can be resolved with the use of either integrated acquisition mode or accumulation of consecutive EPIs during irradiation. However, the dead time between two consecutive EPIs can decrease the accuracy of absolute dosimetry (Greer and Popescu 2003).

The SLIC-EPI burring for small radiation fields is another limitation if SLIC-EPID is used for dosimetry. This phenomenon occurs for radiation fields approximately smaller than 8 cm^2 on the isocentre as well as for very narrow beams positioned in off-axis areas. Although most radiation fields for conventional and conformal radiotherapy are larger than 8 cm^2, small radiation fields could be used to boost radiation dose to the tumour critical sites. In addition, in both static and dynamic IMRT the narrow fields are mostly used to deliver the radiation dose to the patient. As a result, because of the blurring of entire dose maps for a given segment, the relative dosimetry for segment will be affected.

In conclusion, it is believed that SLIC-EPID can be used as a two-dimensional comprehensive dosimeter, provided a dosimetric calibration is applied. This idea can also be extended for other EPID types. However, for dosimetric calibration special characteristics of each EPID type should be taken into account.

8.2. Possible future researches

This thesis shows that SLIC-EPID can be used to verify dose delivery verification for static radiation fields including conventional, conformal and step-and-shoot (segmented) IMRT modalities if a suitable dosimetric calibration is used. The relative transmitted doses measured using EPID can be verified either with those measured using other reliable two-dimensional dosimeters like EDR2 film or with those calculated using a TPS. Due to the limitation of the access to the real patient in our department, further investigation is required to evaluate the SLIC-EPID for real patients.

Due to the dependency of EPI pixel values on linac repetition rate (see section 3.3), the summation of EPIs (like sIMRT or other static fields) cannot be used for dynamic fields. However, EPIs as DICOM images include a header and EPI acquisition and linac setting information are embedded in image header. If all consecutive EPIs are processed individually regarding particular information in image header, it is believed that they can also be used to evaluate dynamic fields used in dIMRT and radiation fields set up using Enhanced Dynamic Wedge (EDW).

The EPID response has been reported in a few works for compensator design (Yin *et al* 1994; Evans *et al* 1995; Roback and Gerbi 1995; Curtin-Savard and Podgorsak 1997; Pasma *et al* 1999; Menon and Sloboda 2003) and dose delivery verification for electron beams with the use of bremsstrahlung photos in an electron beam to obtain portal images of electron beam treatments (Jarry and Verhaegen 2005). Further investigation might be directed to investigate the SLIC-EPID response either to design compensator or to verify the transmitted dose verification for electron beam.

Mohammadi, M., Bezak, E., and Reich, P., (2006) Comparison of two-dimensional transmitted dose maps: evaluation of existing algorithms.
Australasian Physical and Engineering Sciences in Medicine, v. 29 (2), pp. 179-187.

Appendix B

The programs developed to process the data measured used Scanning Liquid Ionization Chamber Electronic Portal Imaging Device (SLIC-EPID) and Kodak Extended Dose Range (EDR2) film and were calculated using Pinnacle^3 Treatment Planning System (TPS) using MATLAB software (MATLAB 7, MathWorks Inc, Natick, MA, USA). The codes embedded here are the only major programs developed.

B.1. The Region Of Interest (ROI) finder

This program enables to find the effective radiation field surrounded by 50% isodose lines. It can be modified for other isodose lines. This program includes the opening of DICOM images, averaging of two images and converting the average image raw pixel values to the dose. The dose values are corrected by the Correction Factor Matrix (CFM) data set, measured as the relative dose values of the EDR2 film and EPID primary fluence maps. After finding the exact ROI, the radiation field is normalized to the central point.

```
function ROIfinder (A)
% Y=ROIfinder(A)
% This function enables to find the radiation field surrounded by the A% isodose line.

aa= A/100;
% ----------------------------------------- EPID IMAGE ----------------------------------------------
% ------------------------------------- FIRST EPID IMAGE -----------------------------------------
FilePath = ('C:\Documents and Settings\rahuser\My Documents\matlab exersices\*.dcm');
[dFILENAME, dPATHNAME] = uigetfile(FilePath, 'File Open');
filename = [dPATHNAME dFILENAME];
info = dicominfo(filename);
E1=dicomread(info);
 FilePath = ('C:\Documents and Settings\rahuser\My Documents\matlab exersices\*.dcm');
[dFILENAME, dPATHNAME] = uigetfile(FilePath, 'File Open');
filename = [dPATHNAME dFILENAME];
info = dicominfo(filename);
E2=dicomread(info);
 % ---------------------------- CHANGING THE SIGN OF EPIDs ----------------------------------
IE1=abs(double(E1));
IE2=abs(double(E2));
% --------------------------- AVERAGING TWO EPID IMAGES ---------------------------------
 IE=(IE1+IE2)/2;
% -----CHANGING OF THE IMAGE PIXEL VALUES INTO THE DOSE VALUES------
```

```
 a=0.0000001;
 b=1.7908;
 ED=a*(double(IE)).^b;

 % ------------CORRECTION OF THE EPID DOSE VALUES USING CFM -----------------
% --------------(The CFM data set is converted into the XLS sheet previously)-----------------

CF=xlsread ('C:\Documents and Settings\rahuser\My Documents\current affairs\data
file2\OPEN FIELDS\140\CFM140SQ.xls');
 % -- Due to the limitation of the EDR2 film, peripheral part of EPID images is discarded --
EPID1=IE(33:222,33:222);
EPID=medfilt2(EPID1);
 CFM1=CF(1:190,1:190);
CFM=medfilt2(CFM1);
 CEPID=CFM.*EPID;
 % ------------------------------------------RROI OF EPID ----------------------------------------
% -----------------------to define the boundaries of roughly ROI (RROI) -----------------------
RROIE=CEPID;
SZRROI=size(RROIE);
% --------------------------------------- ROI OF EPID ----------------------------------------------
SZE=size(RROIE);
IP_E=RROIE(round(SZE(1)/2),:);
XP_E=RROIE(:,round(SZE(2)/2));
% ----using find command it is possible to separate the position of ROI as new matrix -----
SZIPE=size(IP_E);
hd=5;
MIPE=mean2(IP_E(1,round(SZIPE(2)/2)-hd:round(SZIPE(2)/2)+hd));
LIMIT1E=aa*MIPE;
[x11,y11]=find(IP_E>=LIMIT1E);
SZXPE=size(XP_E);
MXPE=mean2(XP_E(round(SZXPE(1)/2)-hd:round(SZXPE(1)/2)+hd,1));
LIMIT2E=aa*MXPE;
[x22,y22]=find(XP_E>LIMIT2E);
% ------------------------- and then it is possible to define the exact ROI------------------------
CPFSZ=size(y11);
IPFSZ=size(x22);
B1=x22(IPFSZ(1));
B2=x22(IPFSZ(2));
B3=y11(CPFSZ(2));
B4=y11(CPFSZ(1));
ROI_E=RROIE(B2:B1,B4:B3);
SZROIE=size(ROI_E);
%--------------------- PLOTTING XP&IP PLANES IN THE ROI EPID -----------------------
% --------------------------------- NORMALAIZATION -----------------------------------------
m=2;
CPVE=mean2(ROI_E((round(SZROIE(1)/2)-
m):(round(SZROIE(1)/2)+m),(round(SZROIE(2)/2)-m):(round(SZROIE(2)/2)+m)));
NFE=100/CPVE;
NROIE=double(ROI_E)*NFE;
 % ---------------------------------------------- PLOT ---------------------------------------------------------
figure; imagesc(NROIE)
```

B.2. Comparison of two-dimensional dose maps

Based on the concept of two-dimensional dose map comparison proposed by Van Dyk et al (1993), Composite analysis (Harms *et al* 1998) and gamma function (Low *et al* 1998) are often used to assess the correlation between a reference and an evaluated two-dimensional dose maps.

B.2.1. Evaluation of two dose maps based on the Composite Algorithm

This program allows to compare two radiation dose maps based on the Composite algorithm proposed by Harms et al (1998). The result of this algorithm is a binary map.

```
function Y=compositeharms(M,C)

% Y=compositeharms (M,C)
% ----------This function compares two dose maps based on the Composite algorithm
% ---------- proposed by Harms.
% Example:
% C=rand(10,12)
% M=rand(10,12)
% Y=compositeharms(M,C)

DTA=2;                  % It is selected two pixels (2.54 mm)
DD=0.03;                % For clinical purposes the this criterion is 3%
msize=size(M);
Gtemp=0;
mdist=2;
 TEMP_DTA=zeros(2*mdist+1);
mdiff1=0;
mdiff2=0;

for i=1:msize(1)
  for j=1:msize(2)
    ltemp1=i-mdist;
    ktemp1=j-mdist;
    ltemp2=i+mdist;
    ktemp2=j+mdist;
    if (ltemp1 <=0), ltemp1=1;end
    if (ltemp2 >msize(1)), ltemp2=msize(1);end
    if (ktemp1 <=0), ktemp1=1;end
    if (ktemp2 >msize(2)), ktemp2=msize(2);end

    for k=ktemp1:ktemp2
      for l=ltemp1:ltemp2
        TEMP_DTA(k,l)=(((i-k)^2+(j-l)^2)/DTA^2);
        DD=((M(i,j)-C(l,k))/(((DD^2)*M(i,j))))^2;
```

```
          if TEMP_DTA(k,l)<1,
            mdiff1=1;
          elseif DD<1
             mdiff2=1;
             Gtemp=mdiff1*mdiff2;
             if Gtemp<=1, break,end
           else
             mdiff1=0;
             mdiff2=0;
             Gtemp=10000;
           end
         end
         if Gtemp<=1, break,
end

     end
  G(i,j)=Gtemp;
  end
end
G1=G;
G(find(G1<=1))=1;
G(find(G1>1))=0;
G;

% -----------------------------------------------PLOT---------------------------------------------------------
figure; colormap(bone), pcolor(G), title('Gamma function result on two film and EPID images')

 % --------------------------------------- PERCENT OF THE AGREED PIXELS ----------------------
-------------------------------------------------------------------------------------------------------------------
--------

SZG=size(G);
A=sum(sum(G));
ACC_PCG_TOTAL=((A/(SZG(1)*SZG(2)))*100)
```

B.2.2. Evaluation of two dose maps based on the gamma function Algorithm

Two-dimensional dose maps can also be compared using the gamma function algorithm, proposed by Low et al (1998). In contrast to the Composite algorithm, the gamma function algorithm contains more information.

```
function  Y = gammalow(M,C)
% Y = gammalow(M,C)
% ----------This function compares two dose maps based on the gamma function algorithm
% ---------- proposed by Low(1998).
% M = measured data (evaluated dose map)
% C = calculated data (reference dose map)
 % Example:
% C = rand(10,12)
% M = rand(10,12)
% Y = gammalow(M,C)
```

```
SZD=size(M);
m=3;
CPVE1=mean2(A((round(SZD(1)/2)-m):(round(SZD(1)/2)+m),(round(SZD(2)/2)-
m):(round(SZD(2)/2)+m)));
CPVE2=mean2(B((round(SZD(1)/2)-m):(round(SZD(1)/2)+m),(round(SZD(2)/2)-
m):(round(SZD(2)/2)+m)));
% ------------Normalization to the central point of ROI for both M &C dose maps ------------
NFE1=100/CPVE1;
NFE2=100/CPVE2;
M=double(M)*NFE1;
C=double(C)*NFE2;

SZ=size(M);
Field=2;
FRT=zeros(SZ(1),SZ(2));
DTAA=2;
DDA=0.03;
 for i=1:SZ(1)
    for j=1:SZ(2)
        k1=i-Field;
        k2=i+Field;
        l1=j-Field;
        l2=j+Field;
        if k1<=0, k1=i; end
        if k2>SZ(1); k2=SZ(1); end
        if l1<=0, l1=j; end
        if l2>SZ(2); l2=SZ(2); end
          M1=M(k1:k2,l1:l2);

          c=k2-k1+1;
          d=l2-l1+1;
           G=zeros(c,d);
            for k=1:c
            for l=1:d
                C1=C(i,j);
                v=i-(k-3);
                w=j-(l-3);
              DTA(k,l)=((((i-v)^2)+((j-w)^2))/(DTAA^2));
              DD(k,l)=((((double(C1)-double(M1(k,l)))/(double(M1(k,l))*DDA))^2);
              G(k,l)=sqrt(DTA(k,l)+DD(k,l));
          end
          end
       G;
       FRT(i,j)=min(min(G));
   end

 end
 FRT;
 gamma_map=FRT;

 figure;colormap(gray); pcolor(gamma_map)

 SZG=size(gamma_map);
 G= gamma_map;
```

```
A=sum(sum(G));
ACC_PCG_TOTAL=((A/(SZG(1)*SZG(2)))*100)
```

B.2.3. Evaluation of the percentage agreement inside the irregular radiation fields

In order to evaluate the gamma agreement inside the irregular fields, the radiation fields and penumbra region (80% - 20% isodose lines) the irregular fields set up using MLCs were found using the following code.

```
% -------FEEDING THE TRANSMITTED DOSE MAP MEASURED USING EPID------------
EPID=medfilt2(TOTAL_EPID, [3 3 ]);

% -------------------------FEEDING THE TRANSMITTED DOSE MAP ---------------------------
------------------------------------- CALCULATED USING PINNACLE3 TPS -----------------------
-------
PINNACLE=TOTAL_PINNACLE_F5;
PINNACLE=medfilt2(PINNACLE1,[3 3],'symmetric');
%-----------------------------------------RESCALING THE TPS DATA ------------------------------
----------------------------- SET TO BE THE SAME SIZE OF EPID DOSE MAP ------------------
m=1.75/1.27;
SZE=size(EPID);
SZP=size(PINNACLE);
RPINNACLE=imresize(PINNACLE,[m*SZP(1) m*SZP(2)],'bilinear');
figure, imagesc(EPID), title('EPID')
% ----------------------------BACKGROUND CONTROL FOR EPID & TPS------------------------
-------------------------------------------------------------------------------------------------------
--------
NEP=imcrop;
NE_FAC=mean2(NEP);
NFE=1/NE_FAC;
NEPID=double(EPID)*NFE;

imagesc(RPINNACLE), title('PINNACLE')
NP=imcrop;
NP_FAC=mean2(NP);
NFP=1/NP_FAC;
NPINNACLE=double(RPINNACLE)*NFP;
imagesc(NPINNACLE), title('Normalized Pinnacle')
% FINDING THE RECTANGULAR ROI FOR EPID

imagesc(NPINNACLE), title('Normalized Pinnacle')
imagesc(NEPID), title('Normalized EPID')
% -------------------FINDING THE EXACT ROI , DEFIND FOR EPID----------------------------
-------------------------------- DOSE MAPS FOR PINNACLE DOSE MAPS-------------------------
---------
E1=imcrop;-
```

```
P1=autoposition1(NPINNACLE,E1);
SZ=size(E1);

E1=NEPID;
P1=NPINNACLE;
SZ=size(E1);
P1=imresize(NPINNACLE,[SZ(1) SZ(2)]);
% ----------------NORMALIZATION TO A PONIT FOR EPID AND TPS DOSE MAPS---------
tt=4;
imagesc(E1), title('put the cursor for PON')
[mm1,nn1]=ginput(1);
NCFE2=mean2(E1(round(nn1)-tt:round(nn1)+tt,round(mm1)-tt:round(mm1)+tt));
NF2=100/NCFE2;
FINAL_EPID3=double(E1)*NF2;

NCFP2=mean2(P1(round(nn1)-tt:round(nn1)+tt,round(mm1)-tt:round(mm1)+tt));
NF1=100/NCFP2;
FINAL_PINNACLE=double(P1)*NF1;
SZP=size(FINAL_PINNACLE);

NFE2=100/NCFE2;
FINAL_EPID3=double(E1)*NFE2;

NCFP2=mean2(P1(round(nn1)-tt:round(nn1)+tt,round(mm1)-tt:round(mm1)+tt));
NFP2=100/NCFP2;
% --------------------CONTROL THE FIELD SIZE FOR EPID & TPS DOSE MAPS-------------
----
FINAL_EPID=imresize(FINAL_EPID3, [SZP(1) SZP(2)]);
FINAL_PINNACLE=FINAL_PINNACLE;

% ---------------------------------RELATIVE DOSE DIFFERENCE MAP- --------------------------

DDF=FINAL_EPID-FINAL_PINNACLE;
imagesc(DDF), title ('Relative dose difference °'), xlabel ('# of Pixels'), ylabel('# of Pixels')
figure, imagesc(FINAL_EPID), title('Relative EPID dose map '), xlabel ('# of Pixels'), ylabel('#
of Pixels')
figure, imagesc(FINAL_PINNACLE), title('Relative TPS dose map '), xlabel ('# of Pixels'),
ylabel('# of Pixels')


mm=round(mm1);
nn=round(nn1);

%------------------------------------------------------------------------------------------------------------
%------------------------------------------------------------------------------------------------------------
%------------------------------------------------------------------------------------------------------------
%---------------GAMMA EVALUATION WITH PIXELATION CONTROL------------------------
%------------------------------------------------------------------------------------------------------------
%------------------------------------------------------------------------------------------------------------
%------------------------------------------------------------------------------------------------------------


M=FINAL_EPID;
C=FINAL_PINNACLE;
FRT= gammalow(M,C)
```

```
colormap(jet), imagesc(FRT), title('The gamma map '),xlabel('Pixel #'), ylabel('Pixel #')

gamma_function=FRT;
gamma_function(find(gamma_function<=1))=1;
gamma_function(find(gamma_function>1))=0;

% --------------------------------agreement percentage for the regular field -----------------------------
%------------------------------------------------------------------------------------------------------------
AGP=gamma_function;
SZAGP=size(AGP);
A=sum(sum(AGP));
PERCENTAGE_OF_AGREEMENT_ROI=(((A/(SZAGP(1)*SZAGP(2))))*100)

 %----------------------------------------------line profiles------------------------------------------------
%------------------------------------------------------------------------------------------------------------

XPE=(FINAL_EPID(nn,:)');
XPP=(FINAL_PINNACLE(nn,:)');
XPG=(FRT(nn,:)');
XPDDF=(DDF(nn,:)');

IPE=(FINAL_EPID(:,mm));
IPP=(FINAL_PINNACLE(:,mm));
IPG=(FRT(:,mm));
IPDDF=(DDF(:,mm));

TT=size(FINAL_EPID);
X=(TT(1)*1.27)/20;
XS=[-X:0.01:X];
SZIP=size(IPE);
XX1=imresize(XS,[SZIP(2),SZIP(1)]);
XX=XX1';

Y=(TT(2)*1.27)/20;
YS=[-Y:0.01:Y];
YS1=YS';
SZXP=size(XPE);
YY=imresize(YS1,[SZXP(1),SZXP(2)]);

 IPS=[XX,IPE,IPP,IPDDF,IPG];
XPS=[YY,XPE,XPP,XPDDF,XPG];

 xlswrite(XPS)
 xlswrite(IPS)

 % -----------------------------agreement percentage for the irregular field -----------------------------
%------------------------------------------------------------------------------------------------------------

TT=FINAL_EPID;
SZTT=size(TT);
ZZT=ones(SZTT(1),SZTT(2));

for i=1:SZTT(1)
   for j=1:SZTT(2)
```

```
        if TT(i,j)<30
           ZZT(i,j)=0;
        else
        end
     end
end
ZZT;

ZZT1=1.001*ZZT;
 FINAL_GAMMA=FRT.*ZZT1;
 colormap(jet), imagesc(FINAL_GAMMA), title('The gamma map for a head and neck' )
,xlabel('Pixel #'), ylabel('Pixel #')


 FINAL_GAMMA1=FINAL_GAMMA;
  PRCT=zeros(SZTT(1),SZTT(2));

 for i=1:SZTT(1)
    for j=1:SZTT(2)
       if FINAL_GAMMA1(i,j)>0.0001 & FINAL_GAMMA1(i,j)<=1
          FINAL_GAMMA1(i,j)=1;
       else FINAL_GAMMA(i,j)>1;
          FINAL_GAMMA1(i,j)=0;
       end
    end
 end

 FINAL_GAMMA1;

 TOTAL=sum(sum(ZZT));
 GAMMA1=sum(sum(FINAL_GAMMA1));
 GAMMA_SCORE=(GAMMA1/TOTAL)*100
```

B.3. The rotated and extended CT image

For oblique beam dose delivery planning, the patient CT data is rotated at the opposite direction of gantry angle and the EPID was modelled as was positioned for A-P direction. (This code originally developed by Paul Reich for A-P direction and it was then modified for gantry rotations)

```
clear all
close all
clc;
%----------------------------------------- OPENING THE CT IMAGES ------------------------------
----------------------------------------------------------------------------------------------

FilePath = ('C:\Documents and Settings\MMohamma\My Documents\current affairs\H&N
IMRT\CT IMAGES\NEW CT IMAGES\ORIGINAL CT IMAGES\*.img');
```

```
[dFILENAME, dPATHNAME] = uigetfile(FilePath, 'File Open','MultiSelect', 'on');

%------------------------- EXTENSION  AND ROTATION OF THE CT IMAGES -------------------
----------------------------------------------------------------------------------------

sz = size(dFILENAME);
A=-1000*ones(444,1400);
B=-1000*ones(512,444);
T=300;        % <<FOR AP DIRECTION, ANGLE T IS 0>>

for i = 1:sz(2);
    S{i} = [dPATHNAME dFILENAME{i}];
      info(i) = dicominfo(S{i});
        X{i} = dicomread(S{i});
        XX{i} = (X{i});
        figure, imagesc(XX{i})
        EXT_CT{i}=[A;B,XX{i},B;A];
        figure; imshow(EXT_CT{i},[]), title('EXTENDED CT{i}')
        ROT_CT{i}=imrotate(EXT_CT{i},T,'bilinear');
        SZ=size(EXT_CT{i});
        SZ=size(ROT_CT{i});
        LX=round(SZ(1)/2); LY=round(SZ(2)/2);
%          CENT_EXT_ROT_CT{i}=EXT_CT{i}(LX-511:LX+512,LY-511:LY+512);
        CENT_EXT_ROT_CT{i}=ROT_CT{i}(LX-511:LX+512,LY-511:LY+512);
        figure, imshow(CENT_EXT_ROT_CT{i},[]),title('CENTRAL ROTATAD IMAGE')
        SZ=size(CENT_EXT_ROT_CT{i});
        ZZ{i}=-1000*ones(SZ(1),SZ(2));
        CENT_EXT_ROT_CT{i}=ZZ{i};

       DIR_1{i} = ['C:\Head and neck images_expand\h&n phantom\' dFILENAME{i}];
  dicomwrite(CENT_EXT_ROT_CT{i},DIR_1{i},info(i),'ObjectType','CT Image Storage')
end
%----------- SAVING THE EXTENDED & ROTATED CT IMAGE AS DICOM IMAGE ------
----------------------------------------------------------------------------------------

FilePath = ('C:\Head and neck images_expand\h&n no phantom\*.dcm');
[dFILENAME, dPATHNAME] = uigetfile(FilePath, 'File Open');
filename = [dPATHNAME dFILENAME]
info = dicominfo(filename)
X = dicomread(info);
figure; imshow(X,[])
```

B.4. Evaluation of EPIs to find the minimum MLC displacement

The standard edge detection algorithms and relative dose differences are used to find the minimum MLC leaf displacement.

```
% ------------------------------------------ EPID IMAGE ---------------------------------------------
% ------------------------------------ FIRST EPID IMAGE ------------------------------------------
```

```
FilePath = ('C:\Documents and Settings\MMohamma\My Documents\current affairs\MLC
study\edge detection\Prostate and Head neck cases\IRREGULAR\HEAD AND
NECK\IMAGES\*.dcm');
[dFILENAME, dPATHNAME] = uigetfile(FilePath, 'File Open');
filename = [dPATHNAME dFILENAME];
% info = dicominfo(filename);
E1=dicomread(filename);
IE1=(double(E1));
IE11=IE1-2^15;

% ------------------------------------------2nd EPID image -------------------------------------------
FilePath = ('C:\Documents and Settings\MMohamma\My Documents\current affairs\MLC
study\edge detection\Prostate and Head neck cases\IRREGULAR\HEAD AND
NECK\IMAGES\*.dcm');
[dFILENAME, dPATHNAME] = uigetfile(FilePath, 'File Open');
filename = [dPATHNAME dFILENAME];
% info = dicominfo(filename);
E2=dicomread(filename);
IE2=(double(E2));
IE22=IE2-2^15;

% ------------------------------------------3rd EPID image ------------------------------------------
FilePath = ('C:\Documents and Settings\MMohamma\My Documents\current affairs\MLC
study\edge detection\Prostate and Head neck cases\IRREGULAR\HEAD AND
NECK\IMAGES\*.dcm');
[dFILENAME, dPATHNAME] = uigetfile(FilePath, 'File Open');
filename = [dPATHNAME dFILENAME];
% info = dicominfo(filename);
E3=dicomread(filename);
IE3=(double(E3));
IE33=IE3-2^15;

% ------------------------------------------4th EPID image -------------------------------------------
FilePath = ('C:\Documents and Settings\MMohamma\My Documents\current affairs\MLC
study\edge detection\Prostate and Head neck cases\IRREGULAR\HEAD AND
NECK\IMAGES\*.dcm');
[dFILENAME, dPATHNAME] = uigetfile(FilePath, 'File Open');
filename = [dPATHNAME dFILENAME];
% info = dicominfo(filename);
E4=dicomread(filename);
IE4=(double(E4));
IE44=IE4-2^15;

 % -------------------------------------AVERAGING THE EPIs ------------------------------------------

IEE1=((IE11+IE22)/2);
IE1=abs(IEE1);
 IEE2=((IE33+IE44)/2);
IE2=abs(IEE2);

 % -----------------------------CONVERTING TO DOSE MAP --------------------------------------

ED1=0.00000005*IE1.^1.839;
ED2=0.00000005*IE2.^1.839;
```

```
 % ----------------------------------------------NORMALIZING ----------------------------------------

m=4;
SZCEPID=size(ED1);
CPVE1=mean2(ED1((round(SZCEPID(1)/2)-
m):(round(SZCEPID(1)/2)+m),(round(SZCEPID(2)/2)-m):(round(SZCEPID(2)/2)+m)));
NFE1=100/CPVE1;
NIE1=double(ED1)*NFE1;

 SZCEPID=size(ED2);
 CPVE2=mean2(ED2((round(SZCEPID(1)/2)-
m):(round(SZCEPID(1)/2)+m),(round(SZCEPID(2)/2)-m):(round(SZCEPID(2)/2)+m)));
NFE2=100/CPVE2;
NIE2=double(ED2)*NFE2;

% --------------------------CORRECTION FOR BULGING EFFECT ------------------------------

 AAA=xlsread('C:\Documents and Settings\MMohamma\My Documents\current affairs\Gantry
rotation angle\23 by 23\AAA.xls');
BBB=xlsread('C:\Documents and Settings\MMohamma\My Documents\current affairs\Gantry
rotation angle\23 by 23\BBB.xls');
CC=input('please enter the gantry angle');
GG=(sin((CC*pi)/180));
GRCF=(AAA+(GG*(BBB)));

GRNIE1=(NIE1.*GRCF);
GRNIE2=(NIE2.*GRCF);

 % -----------------------------------DOSE DIFFERENCE MAP ---------------------------------------
-
DF=NIE2-NIE1;
figure, imagesc(NIEE2)
figure, imagesc(DF), title('Relative dose difference')
DDF=imcrop;
figure, imagesc(DDF)

m=0.21;                            % Threshold of edge detection algorithm

BW1=edge(DDF,'sobel',m,'horizontal');
BW2=edge(DDF,'prewitt',m,'horizontal');
BW3=edge(DDF,'roberts',m,'horizontal');
BW4=edge(DDF,'canny',m,'horizontal');
BW5=edge(DDF,'log',m,'horizontal');
BW6=edge(DDF,'zerocross',m,'horizontal');

figure;
subplot(2,3,1),imshow(BW1,[]),title('SOBEL')
subplot(2,3,2),imshow(BW2,[]),title('PREWITT')
subplot(2,3,3),imshow(BW3,[]),title('ROBERTS')
subplot(2,3,4),imshow(BW4,[]),title('CANNY')
subplot(2,3,5),imshow(BW5,[]),title('Laplacian of Gaussian')
subplot(2,3,6),imshow(BW6,[]),title('zero-cross')

SZDF=size(DDF);
MDDF=zeros(SZDF(1),SZDF(2));
```

```
for i=1:SZDF(1)
   for j=1:SZDF(2)
      if DDF(i,j)<2,
         MDDF(i,j)=0;
      else MDDF(i,j)=DDF(i,j);
      end
   end
end
MDDF;


BW44=double (BW4);

 % -----------------------------------------------------PLOT -------------------------------------------------------
------------------------------------------------------------------------------------------------------------------------------
---------

figure, imagesc(BW44);
  figure, imagesc(DDF),  title('Relative EPID dose map ',
'fontsize',14,'fontweight','bold'),xlabel('# of Pixels', 'fontsize', 12,'fontweight','bold'),ylabel('# of
Pixels','fontsize', 12,'fontweight','bold')
figure, imagesc(BW4);  title('CANNY algorithm for 0.1 mmMLC laf shift ',
'fontsize',14,'fontweight','bold'),xlabel('# of Pixels', 'fontsize', 12,'fontweight','bold'),ylabel('# of
Pixels','fontsize', 12,'fontweight','bold')

DDF1=fliplr(DDF);
lprofx(DDF1)
```

References

Agazaryan N, Solberg T and Demarco J (2003) "Patient specific quality assurance for the delivery of intensity modulated radiotherapy" *J Appl Clin Med Phys* **4** 40-50.

Ahnesjo A (1989) "Collapsed cone convolution of radiant energy for photon dose calculation in heterogeneous media" *Med Phys* **16** 577-92.

Alaei P, Higgins P, Weaver R and Nguyen N (2004) "Comparison of dynamic and step-and-shoot intensity-modulated radiation therapy planning and delivery" *Med Dosim* **29** 1-6.

Antonuk L (2002) "Electronic portal imaging devices: a review and historical perspective of contemporary thechnologies and research" *Phys Med Biol* **47** R31-R56.

Antonuk L E, Boudry J, Huang W, Mcshan D L, Morton E J, *et al* (1992) "Demonstration of megavoltage and diagnostic x-ray imaging with hydrogenated amorphous silicon arrays" *Med Phys* **19** 1455-66.

Arnfield M, Otto K, Aroumoungame V and Alkins R (2005) "The use of film dosimetry of the penumbra region to improve the accuracy of intensity modulated radiotherapy" *Med Phys* **32** 12-18.

Baily N, Horn R and Kampp T (1980) "Fluoroscopic visualization of megavoltage therapeutic x ray beams" *Int J Radiat Oncol Biol Phys* **6** 935-9.

Bakai A, Alber M and Nusslin F (2003) "A revision of the gamma-evaluation concept for the comparison of dose distributions" *Phys Med Biol* **48** 3543-53.

Baker S J, Budgell G J and Mackay R I (2005) "Use of an amorphous silicon electronic portal imaging device for multileaf collimator quality control and calibration" *Phys Med Biol* **50** 1377-92. Epub 2005 Mar 16.

Balter J M, Lam K L, Sandler H M, Littles J F, Bree R L, *et al* (1995) "Automated localizationof the prostate at the time of treatment using implanted radiopaque markers: Technical feasibility" *Int J Radiat Oncol Biol Phys* **33** 1281-86.

Battista J J and Sharpe M B (1992) "True three-dimensional dose computations for megavoltage x-ray therapy: a role for the superposition principle" *Australas Phys Eng Sci Med* **15** 159-78.

Bayouth J E and Morrill S M (2003) "MLC dosimetric characteristics for small field and IMRT applications" *Med Phys* **30** 2545-52.

Bayouth J E, Wendt D and Morrill S M (2003) "MLC quality assurance techniques for IMRT applications" *Med Phys* **30** 743-50.

Bel A, Van Herk M, Bartelink H and Lebesque J (1993) "A verification procedure to improve patient set-up accuracy using portal images" *Radiother Oncol* **29** 253-60.

Bel A, Vos P, Rodrigus P, Creutzberg C, Visser A, *et al* (1996) "High-precision prostate cancer irradiation by clinical application of an offline patient setup verification procedure, using portal imaging" *Int J Radiat Oncol Biol Phys* **35** 321-32.

Bharanidharan G, Manigandan D, Devan K, Subramani V, Gopishankar N, *et al* (2005) "Characterization of responses and comparison of calibration factor for commercial MOSFET detectors" *Med Dosim* **30** 213-8.

Bijhold J, Lebesque J V, Hart a A and Vijlbrief R E (1992) "Maximizing setup accuracy using portal images as applied to a conformal boost technique for prostatic cancer" *Radiother Oncol* **24** 261-71.

Bissonnette J and Munro P (1996) "Evaluation of a high-density sciltillationg glass for portal imaging" *Med Phys* **23** 401-6.

Boellaard R, Essers M, Van Herk M and Mijnheer B J (1998) "New Method to obtain the midplane dose using in vivo dosimetry" *Int J Radiat Oncol Biol Phys* **41** 465-74.

Boellaard R, Van Herk M and Mijnheer B J (1996) "The dose response relationship of a liquid-filled electronic imaging device" *Med Phys* **23** 1601-11.

Boellaard R, Van Herk M and Mijnheer B J (1997a) "A convolution model to convert transmission dose images to exit dose distributions" *Med Phys* **24** 189-99.

Boellaard R, Van Herk M, Uiterwaal H and Mijnheer B (1997b) "Two-dimensional exit dosimetry using a liquid-filled electronic portal imaging device and a convolution model" *Radiother Oncol* **44** 149-57.

Boellaard R, Van Herk M, Uiterwaal H and Mijnheer B (1998b) "First clinical tests using a liquid-filled electronic portal imaging device and a convolution model for the verification of the midplane dose" *Radiother Oncol* **47** 303-12.

Bogaerts R, Huyskens D, Weltens C and Dutreix A (2000) "Variation of relative transit dose profiles with patient-detector distance" *Radiother Oncol* **54** 29-37.

Bogaerts R, Van Esch A, Reyman R and Huyskens D (2000) "A method to estimate the transit dose on the beam axis for verification of dose delivery with portal images" *Radiother Oncol* **54** 39-46.

Bos L, Danciu C, Cheng C, Brugmans M, Van Der Horst A, *et al* (2002) "Interinstitutional variations of sensitometric curves of radiographic dosimetric films" *Med Phys* **29** 1772-80.

Boyer A, Biggs P, Galvin J, Klein E, Losasso T, *et al* (2001b). Basic Application of Multileaf Collimators. Madison, Task Group 50, AAPM.

Boyer A, Butler E, Dipetrillo T, Engler M, Fraass B, *et al* (2001a) "Intensity-modulated radiotherapy: current status and issues of interest" *Int J Radiat Oncol Biol Phys* **51** 880-914.

Boyer A and Li S (1997) "Geometric analysis of light-field position of a multileaf collimator with curved ends

" *Med Phys* **24** 757-62.

Boyer A, Ochran T, Nyerick C, Waldron T and Huntzinger C (1992b) "Clinical dosimetry for implementation of a multileaf collimator" *Med Phys* **19** 1255-61.

Boyer a L, Antonuk L, Fenster A, Van Herk M, Meertens H, *et al* (1992a) "A review of electronic portal imaging devices (EPIDs)" *Med Phys* **19** 1-16.

Brahme A (1984) "Dosimetric precision requirements in radiation therapy" *Acta Radiol Oncol* **23** 379-91.

Brahme A, Roos J E and Lax I (1982) "Solution of an integral equation encountered in rotation therapy" *Phys Med Biol* **27** 1221-9.

Brewster L, Mohan R, Mageras G, Burman C, Leibel S, *et al* (1995) "Three dimensional conformal treatment planning with multileaf collimators" *Int J Radiat Oncol Biol Phys* **33** 1081-9.

Brock K, Mcshan D and Balter J (2002) "A comparison of computer-controlled versus manual on-line patient setup adjustment" *J Appl Clin Med Phys* **3** 241-7.

Broggi S, Fiorino C and Calandrino R (2002) "In vivo estimation of midline dose maps by transit dosimetry in head and neck radiotherapy" *Br J Radiol* **75** 974-81.

Bucciolini M, Buonamici F and Casati M (2004) "Verification of IMRT fields by film dosimetry" *Med Phys* **31** 161-68.

Bucciolini M, Buonamici F B, Mazzocchi S, De Angelis C, Onori S, *et al* (2003) "Diamond detector versus silicon diode and ion chamber in photon beams of different energy and field size" *Med Phys* **30** 2149-54.

Burch S, Kearfott K, Trueblood J, Sheils W, Yoe J, *et al* (1997) "A new approach to film dosimetry for high energy photon beams: lateral scatter filtering" *Med Phys* **24** 775-83.

Butson M, Yu P and Cheung T (2003) "Rounded end multi-leaf penumbral measurements with radiochromic film" *Phys Med Biol* **48** N247-52.

Cadman P, Bassalow R, Sidhu N P S, Ibbott G and Nelson A (2002) "Dosimetric considerations for validation of a sequential IMRT process with a commercial treatment planning system" *Phys Med Biol* **47** 3001-10.

Canny J (1986) "A computational approach to edge detection" *IEEE Trans Pattern Anal Mach Intell* **8** 679-98.

Chang J, Mageras G S, Chui C S, Ling C C and Lutz W (2000) "Relative profile and dose verification of intensity-modulated radiation therapy" *Int J Radiat Oncol Biol Phys* **47** 231-40.

Chang J, Mageras G S and Ling C C (2003) "Evaluation of rapid dose map acquisition of a scanning liquid-filled ionization chamber electronic portal imaging device." *Int J Radiat Oncol Biol Phys* **55** 1432-45.

Chang J, Mageras G S, Ling C C and Lutz W (2001) "An iterative EPID calibration procedure for dosimetric verification that considers the EPID scattering factor" *Med Phys* **28** 2247-57.

Chang J, Obcemea C H, Sillanpaa J, Mechalakos J and Burman C (2004) "Use of EPID for leaf position accuracy QA of dynamic multi-leaf collimator (DMLC) treatment" *Med Phys* **31** 2091-6.

Cheng C, Wong J, Ndlovu A, Das I, Schiff P, *et al* (2003) "Dosimetric evaluation and clinical application of virtual mini-multileaf collimator" *Am J Clin Oncol* **26** e37-44.

Childress N and Rosen I (2003) "The design and testing of novel clinical parameters for dose comparison" *Int J Radiat Oncol Biol Phys* **56** 1464-79.

Childress N and Rosen I (2004) "Effect of processing time delay on the dose response of Kodak EDR2 film" *Med Phys* **31** 2284-8.

Childress N L, Dong L and Rosen I I (2002) "Rapid radiographic film calibration for IMRT verification using automated MLC fields" *Med Phys* **29** 2384-90.

Chin P, Lewis D and Spezi E (2004) "Correction for dose-response variations in a scanning liquid ion chamber EPID as a function of linear gantry angle" *Phys Med Biol* **40** N93-N103.

Chin P W, Spezi E and Lewis D G (2003) "Monte Carlo simulation of portal dosimetry on a rectilinear voxel geometry: a variable gantry angle solution" *Phys Med Biol* **48** N231-8.

Chiu-Tsao S, Ho Y, Shankar R, Wang L and Harrison L (2005) "Energy dependence of response of new high sensitivity radiochromic films for megavoltage and kilovoltage radiation energies" *Med Phys* **32** 3350-4.

Chow L, Seguin M and Alexander A (2005) "Dosimetric effect of collimating jaws for small multileaf collimated fields" *Med Phys* **32** 759-65.

Chui S, Spirou S and Losasso T (1996) "Testing of dynamic multileaf collimation" *Med Phys* **23** 635-41.

Cozzi L, Fogliata A and Nicolini G (2004) "Pre-treatment verification of intensity modulated photon beams with films and electronic portal imaging--two years of clinical experience" *Z Med Phys* **14** 239-50.

Curtin-Savard A and Podgorsak E B (1997) "An electronic portal imaging device as a physics tool." *Med Dosim* **22** 101-5.

Curtin-Savard a J and Podgorsak E B (1999) "verification of segmented beam delivery using a commercial electronic portal imaging device (EPID)" *Med Phys* **26** 737-42.

Danciu C, Proimos B, Rosenwald J and Mijnheer B (2001) "Variation of sensitometric curves of radiographic films in high energy photons" *Med Phys* **28** 966-74.

Daniels F and Rieman W (1956) "Thermoluminescence dosimeter. Final Rept, Project 4-12-80-178" *Chemical Procurement Agency.*

Davis L (1975) "A survey of edge detection techniques" *CGIP* **4** 248-70.

Day M and Stein G (1950) "Chemical effects of ionizing radiation in some gel" *Nature* **166** 146-7.

De Boer J, Heijmen B, Pasma K and Visser A (2000) "Characterization of a high-elbow, fluoroscopic electronic portal imaging device for portal dosimetry" *Phys Med Biol* **45** 197-216.

Depuydt T, Van Esch A and Huyskens D (2002) "A quantitative evaluation of IMRT dose distribution: refienment and clinical assessment of the gamma evaluation" *Radiother Oncol* **62** 309-19.

Dogan N and Glasgow G (2003) "Surface and build-up region dosimetry for obliquely incident intensity modulated radiotherapy 6 MV x rays" *Med Phys* **30** 3091-6.

Dogan N, Leybovich L B and Sethi A (2002) "Comparative evaluation of Kodak EDR2 and XV2 films for verification of intensity modulated radiation therapy" *Phys Med Biol* **47** 4121-30.

Dunscombe P, Humphreys S and Leszczynski K (1999) "A test tool for the visual verification of light and radiation fields using film or an electronic portal imaging device" *Med Phys* **26** 239-43.

Dutreix A (1984) "When and how can we improve precision in radiotherapy" *Radiother Oncol* **2** 275-92.

Eilertsen K (1997) "Automatic detection of single MLC leaf positions with corrections for penumbral effects and portal imager dose rate characteristics" *Phys Med Biol* **42** 313-34.

El-Mohri L, Antonuk L, Yorkston J, Jee K, Maolinbay M, *et al* (1999) "Relative dosimetry using active matrix flat panel imager (AMFPI) technology" *Med Phys* **26** 1530-41.

Essers M, Boellaard R, Van Herk M, Lanson H and Mijnheer B J (1996) "Transmission dosimetry with a liquid- filled electronic portal imaging device" *Int J Radiat Oncol Biol Phys* **34** 931-41.

Essers M, Hoogervorst B R, Van Herk M, Lanson H and Mijnheer B J (1995) "Dosimetric characteristics of a liquid-filled electronic portal imaging device" *Int J Radiat Oncol Biol Phys* **33** 1265-72.

Esthappan J, Mutic S, Harms W B, Dempsey J F and Low D A (2002) "Dosimetry of therapeutic photon beams using an extended dose range film" *Med Phys* **29** 2438-45.

Evans P M, Gildersleve J Q, Morton E J, Swindell W, Coles R, *et al* (1992) "Image comparison techniques for use with megavoltage imaging systems" *Br J Radiol* **65** 701-09.

Evans P M, Hansen V N, Mayles W P, Swindell W, Torr M, *et al* (1995) "Design of compensators for breast radiotherapy using electronic portal imaging" *Radiother Oncol* **37** 43-54.

Fielding A, Evans P and Clarck C (2002) "The use of electronic portal imaging to verify patient position during intensity-modulated radiotherapy delivered by the dynamic MLC technique" *Int J Radiat Oncol Biol Phys* **54** 1225-34.

Fielding a L, Evans P M and Clark C H (2004) "Verification of patient position and delivery of IMRT by electronic portal imaging" *Radiother Oncol* **73** 339-47.

Fiorino C, Del Vecchio A, Cattaneo G, Fusca M, Longobardi B, *et al* (1993) "Exit dose measurements by portal film dosimetry" *radiother Oncol* **29** 336-40.

Fraass B, Doppke K, Hunt M, Kutcher G, Starkschall G, *et al* (1998) "American Association of Physicists in Medicine Radiation Therapy Committee Task Group 53: quality assurance for clinical radiotherapy treatment planning" *Med Phys* **25** 1773-829.

Franken E M, De Boer J C, Barnhoorn J C and Heijmen B J (2004) "Characteristics relevant to portal dosimetry of a cooled CCD camera-based EPID" *Med Phys* **31** 2549-51.

Frazier A, Du M, Wong J, Vicini F, Taylor R, *et al* (1995) "Dosimetric evaluation of the conformation of the multileaf collimator to irregularly shaped fields" *Int J Radiat Oncol Biol Phys* **33** 1229-38.

Gager L D, Wright a E and Almond P R (1977) "Silicon diode detectors used in radiological physics measurements. Part I: Development of an energy compensating shield" *Med Phys* **4** 494-8.

Galvin J M, Smith a R and Lally B (1993) "Characterization of a multi-leaf collimator system" *Int J Radiat Oncol Biol Phys* **25** 181-92.

Goitein M (1983) "Nonstandard deviations" *Med Phys* **10** 709-11.

Greer P B (1996) "Image timing and detector performance of a matrix ion-chamber electronic portal imaging device" *Australas Phys Eng Sci Med* **19** 264-9.

Greer P B and Popescu C C (2003) "Dosimetric properties of an amorphous silicon electronic portal imaging device for verification of dynamic intensity modulated radiation therapy" *Med Phys* **30** 1618-27.

Grein E E, Lee R and Luchka K (2002) "An investigation of a new amorphous silicon electronic portal imaging device for transit dosimetry" *Med Phys* **29** 2262-8.

Guy a W, Chou C K and Mcdougall J A (1999) "A quarter century of in vitro research: a new look at exposure methods" *Bioelectromagnetics* **Suppl** 21-39.

Halvorsen P H (2005) "Dosimetric evaluation of a new design MOSFET in vivo dosimeter" *Med Phys* **32** 110-7.

Hanley J, Lumley M A, Mageras G S, Sun J, Zelefsky M J, *et al* (1997) "Measurement of patient positioning errors in three-dimensional conformal radiotherapy of the prostate" *Int J Radiat Oncol Biol Phys* **37** 435-44.

Hansen V N, Evans P M and Swindell W (1996) "The application of transit dosimetry to precision radiotherapy" *Med Phys* **23** 713-21.

Hansen V N, Swindell W and Evans P M (1997) "Extraction of primary signal from EPIDs using only forward convolution" *Med Phys* **24** 1477-84.

Harms W B, Low D A, Wong J W and Purdy J A (1998) "A software tool for the quantitative evaluation of 3D dose calculation algorithms" *Med Phys* **25** 1830-6.

Haus A, Strubler K and Marks J (1972) "A film technique for determining the absorbed dose at exit from the patient during radiation exposure" *Radiology* **104** 197-200.

Haus a G and Marks J E (1976) "Film techniques in radiotherapy for treatment verification, determination of of patient exit dose, and detection of localization error" *J appl Photogr Eng* **2** 11-16.

He X, Van Esch A, Reymen R and Huyskens D (1999) "Evaluation of an electronic portal imaging device for transit dosimetry" *Acta Oncol* **38** 591-6.

Heijmen B J, Pasma K L, Kroonwijk M, Althof V G, De Boer J C, *et al* (1995) "Portal dose measurement in radiotherapy using an electronic portal imaging device (EPID)" *Phys Med Biol* **40** 1943-55.

Helyer S and Heisig S (1995) "Multileaf collimation versus conventional shielding blocks: a time and motion study of beam shaping in radiotherapy" *Radiother Oncol* **37** 61-4.

Huertas A and Medioni G (1986) "Detection of intensity changes with sub pixel accuracy using Laplacian-Gaussian masks" *IEEE Trans Pattern Anal Mach Intell* **8** 651-64.

Huq M S, Das I J, Steinberg T and Galvin J M (2002) "A dosimetric comparison of various multileaf collimators" *Phys Med Biol* **47** N159-70.

Huq M S, Yu Y, Chen Z P and Suntharalingam N (1995) "Dosimetric characteristics of a commercial multileaf collimator" *Med Phys* **22** 241-7.

Hurkmans C W, Remeijer P, Lebesque J V and Mijnheer B J (2001) "Set-up verification using portal imaging; review of current clinical practice" *Radiother Oncol* **58** 105-20.

Huyskens D, Van Dam J and Dutreix A (1994) "Midplane dose determination using in vivo dose measurements in combination with portal imaging" *Phys Med Biol* **39** 1089-101.

Icru (1976). Determination of absorbed dose in a patient irradiated by means of x or gamma rays in radiotherapy procedures. Washington, DC, International Commission on Radiation Units and measurements.

Jaffray D A, Battista J J, Fenster A and Munro P (1994) "X-ray scatter in megavoltage transmission radiography: physical characteristics and influence on image quality" *Med Phys* **21** 45-60.

Jaffray D A, Battista J J, Fenster A and Munro P (1995) "Monte Carlo studies of x-ray energy absorption and quantum noise in megavoltage transmission radiography" *Med Phys* **22** 1077-88.

James H V, Atherton S, Budgell G J, Kirby M C and Williams P C (2000) "Verification of dynamic multileaf collimation using an electronic portal imaging device" *Phys Med Biol* **45** 495-509.

James H V, Scrase C D and Poynter a J (2004) "Practical experience with intensity-modulated radiotherapy" *Br J Radiol* **77** 3-14.

Jarry G and Verhaegen F (2005) "Electron beam treatment verification using measured and Monte Carlo predicted portal images" *Phys Med Biol* **50** 4977-94. Epub 2005 Oct 12.

Johns H E and Cunningham J R (1983). The Physics of Radiology. Ilinois, Charles Thomas.

Johnson J and Khan F (1994) "Dosimetric effects of abutting extended source to surface distance electron fields with photon fields in the treatment of head and neck cancers" *Int J Radiat Oncol Biol Phys* **28** 741-7.

Jordan T and Williams P (1994) "The design and performance characteristics of a multileaf collimator" *Phys Med Biol* **39** 231-51.

Jornet N, Ribas M and Eudaldo T (2000) "In vivo dosimetry: intercomparison between p-type based and n-type based diodes for the 16-25 MV energy range" *Med Phys* **27** 1287-93.

Ju S, Ahn Y, Huh S and Yoe I (2002) "Film dosimetry for intensity modulated radiation therapy: Dosimetric evaluation" *Med Phys* **29** 351-5.

Kaatee R S, Olofsen M J, Verstraate M B, Quint S and Heijmen B J (2002) "Detection of organ movement in cervix cancer patients using a fluoroscopic electronic portal imaging device and radiopaque markers" *Int J Radiat Oncol Biol Phys* **54** 576-83.

Kausch C, Schreiber B, Kreuder F, Schmidt R and Dossel O (1999) "Monte Carlo simulations of the imaging performance of metal plate/phosphor screens used in radiotherapy" *Med Phys* **26** 2113-24.

Keller H, Fix M and Ruegsegger P (1998) "Calibration of a portal imaging device for high-precision dosimetry: a Monte Carlo study" *Med Phys* **25** 1891-902.

Khan F M (1993). The physics of radiation therapy. Philadelphia, Lippincott Williams & Wilkins.

Killoran J, Giraud J and Chin L (2002) "A dosimetric comparison of two multileaf collimator designs" *Med Phys* **29** 1752-8.

Kirby M (1995) "A multipurpose phantom for used with electronic portal imaging devices" *Phys Med Biol* **40** 323-34.

Kirby M C and Williams P C (1993) "Measurement possibilities using an electronic portal imaging device" *Radiother Oncol* **29** 237-43.

Kirby M C and Williams P C (1995) "The use of an electronic portal imaging device for exit dosimetry and quality control measurements" *Int J Radiat Oncol Biol Phys* **31** 593-603.

Klassen N, Van Der Zwan L and Cygler J (1997) "GafChromic MD-55: investigated as a precision dosimeter" *Med Phys* **24** 1924-34.

Klein E, Harms W, Low D, Willcut V and Purdy J (1995) "Clinical implementation of a commercial multileaf collimator: dosimetry, networking, simulation, and quality assurance" *Int J Radiat Oncol Biol Phys* **33** 1195-208.

Klein E and Low D (2001) "Interleaf leakage for 5 and 10 mm dynamic multileaf collimation systems incorporating patient motion" *Med Phys* **28** 1703-10.

Kron T (1994) "Thermoluminescence dosimetry and its applications in medicine--Part 1: Physics, materials and equipment" *Australas Phys Eng Sci Med* **17** 175-99.

Kron T (1995) "Thermoluminescence dosimetry and its applications in medicine--Part 2: History and applications" *Australas Phys Eng Sci Med* **18** 1-25.

Kroonwijk M, Pasma K L, Quint S, Koper P C, Visser a G, *et al* (1998) "In vivo dosimetry for prostate cancer patients using an electronic portal imaging device (EPID); demonstration of internal organ motion" *Radiother Oncol* **49** 125-32.

Kwok C, Lam G and El-Sayed S (2004) "Suitability of using multileaf collimator (MLC) for photon field matching" *Med Dosim* **29** 184-95.

Langmack K A (2001) "Portal imaging" *Br J Radiol* **74** 789-804.

Leong J (1986) "Use of digital fluoroscopy as an on-line verification device in radiation therapy" *Phys Med Biol* **31** 985-92.

Liu G, Van Doorn T and Bezak E (2000) "Evaluation of the mechanical alignment of a linear accelerator with an electronic portal imaging device (EPID)" *Australas Phys Eng Sci Med* **23** 74-80.

Liu G, Van Doorn T and Bezak E (2002) "Assessment of flatness and symmetry of megavoltage x-ray beam with an electronic portal imaging device (EPID)" *Australas Phys Eng Sci Med* **25** 58-66.

Liu G, Van Doorn T and Bezak E (2004) "The linear accelerator mechanical and radiation isocentre assessment with an electronic portal imaging device (EPID)" *Australas Phys Eng Sci Med* **27** 111-7.

Losasso T, Chui C and Ling C (1998) "Physical and dosimetric aspects of a multileaf collimation system used in the dynamic mode for implementing intensity modulated radiotherapy" *Med Phys* **25** 1919-27.

Losasso T, Chui C and Ling C (2001) "Comprehensive quality assurance for the delivery of intensity modulated radiotherapy with a multileaf collimator used in the dynamic mode" *Med Phys* **28** 2209-19.

Louwe R, Tielenburg R, Van Ingen K, Mijnheer B and Van Herk M (2004) "The stability of liquid-filled matrix ionization chamber electronic portal imaging devices for dosimetry purposes" *Med Phys* **31** 819-27.

Low D and Dempsey J (2003) "Evaluation of the gamma dose distribution comparison method" *Med Phys* **30** 2455-64.

Low D A, Harms W B, Mutic S and Prudy J A (1998) "A technique for the quantitative evaluation of dose distribution" *Med Phys* **25** 656-61.

Luchka K, Chen D, Shalev S, Gluhchev G and Rajapakshe R (1996) "Assessing eadiation and light field congruence witha video based electronic portal imaging device" *Med Phys* **23** 1245-52.

Ma L, Geis P and Boyer A (1997) "Quality assurance for dynamic multileaf collimator modulated fields using a fast beam imaging system" *Med Phys* **24** 1213-20.

Mackie T R, Scrimger J W and Battista J J (1985) "A convolution method of calculating dose for 15-MV x rays" *Med Phys* **12** 188-96.

Mccurdy B M, Luchka K and Pistorius S (2001) "Dosimetric investigation and portal dose image prediction using an amorphous silicon electronic portal imaging device" *Med Phys* **28** 911-24.

Mccurdy B M and Pistorius S (2000) "A two-step algorithm for predicting portal dose images in arbitrary detectors" *Med Phys* **27** 2109-16.

Mcdermott L N, Louwe R J, Sonke J J, Van Herk M B and Mijnheer B J (2004) "Dose-response and ghosting effects of an amorphous silicon electronic portal imaging device" *Med Phys* **31** 285-95.

Mcnutt T R, Mackie T R and Paliwal B R (1997) "Analysis and convergence of the iterative convolution/superposition dose reconstruction technique for multiple treatment beams and tomotherapy" *Med Phys* **24** 1465-76.

Mcnutt T R, Mackie T R, Reckwerdt P and Paliwal B R (1996b) "Modeling dose distributions from portal dose images using the convolution/superposition method" *Med Phys* **23** 1381-92.

Mcnutt T R, Mackie T R, Reckwerdt P and Papanikolaou N (1996a) "Calculation of portal dose using the convolution/superposition method" *Med Phys* **12** 527-35.

Melian E, Mageras G S, Fuks Z, Leibel S A, Niehaus A, *et al* (1997) "Variation in prostate position quantitation and implications for three-dimensional conformal treatment planning." *Int J Radiat Oncol Biol Phys* **38** 73-81.

Menon G V and Sloboda R S (2003) "Compensator quality control with an amorphous silicon EPID" *Med Phys* **30** 1816-24.

Metcalfe P, Kron T and Hoban P (1997). The physics of radiotherapy x-rays from linear accelerators. Madison, Medical Physics Publishing.

Mijnheer B, Battermann J and Wambersie A (1987) "What degree of accuracy is required and can be achieved in photon and neutron therapy?" *Radiother Oncol* **8** 237-52.

Morton E J, Swindell W, Lewis D G and Evans P M (1991) "A linear array, scintillation crystal-photodiode detector for megavoltage imaging" *Med Phys* **18** 681-91.

Mosleh-Shirazi M, Evans P, Swindell W, Symonds-Tayler J, Webb S, *et al* (1998) "Rapid portal imaging with a high-efficiency, large field-of-view detector" *Med Phys* **25** 2333-46.

Munro P and Bouius D C (1998) "X-ray quantum limited portal imaging using amorphous silicon flat-panel arrays" *Med Phys* **25** 689-702.

Nijsten S, Minken A, Lambin P and Bruinvis I (2004) "Verification of treatment parameter transfer by means of electronic portal dosimetry" *Med Phys* **31** 341-7.

Nilsson B, Ruden B and Sorcini B (1988) "Characteristics of silicon diodes as patient dosemeters in external radiation therapy" *Radiother Oncol* **11** 279-88.

Niroomand Rad A, Blackwell C, Coursey B, Gall K, Galvin J, *et al* (1998) "Radiochromic film dosimetry: recommendations of AAPM Radiation Therapy Committee Task Group 55. American Association of Physicists in Medicine" *Med Phys* **25** 2093-115.

Noel A, Aletti P, Bey P and Malissard L (1995) "Detection of errors in individual patients in radiotherapy by systematic in vivo dosimetry" *Radiother Oncol* **34** 144-51.

Nutting C, Dearnaley D P and Webb S (2000) "Intensity modulated radiation therapy: a clinical review" *Br J Radiol* **73** 459-69.

Olch A (2002) "Dosimetric performance of an enhanced dose range radiographic film for intensity-modulated radiation therapy quality assurance" *Med Phys* **29** 2159-68.

Olsson L E, Arndt J, Fransson A and Nordell B (1992) "Three-dimensional dose mapping from gamma knife treatment using a dosimeter gel and MR-imaging" *Radiother Oncol* **24** 82-6.

Palta J, Yeung D and Frouhar V (1996) "Dosimetric consideration for a multileaf collimator system" *Med Phys* **23** 1219-24.

Parsaei H, El-Khatib E and Rajapakshe R (1998) "The use of an electronic portal imaging system to measure portal dose and portal dose profiles" *Med Phys* **25** 1903-9.

Partridge M (2000) "Reconstruction of megavoltage photon spectra from electronic portal imager derived transmission measurements" *Phys Med Biol* **45** N115-31.

Partridge M, Ebert M and Hesse B M (2002) "IMRT verification by three-dimensional dose reconstruction from portal beam measurements" *Med Phys* **29** 1847-58.

Partridge M, Evans P M, Van Herk M, Ploeger L, Budgell G, *et al* (2000) "Leaf position verification during dynamic beam delivery: A comparison of three applications using electronic portal imaging" *Med Phys* **27** 1601-09.

Pasma K, Kroonwijk M, Van Dieren E, Visser A and Heijmen B (1999) "Verification of compensator thicknesses using a fluoroscopic electronic portal imaging device" *Med Phys* **26** 1524-9.

Pasma K L, Dirkx M L, Kroonwijk M, Visser a G and Heijmen B J (1999) "Dosimetric verification of intensity modulated beams produced with dynamic multileaf collimation using an electronic portal imaging device" *Med Phys* **26** 2373-8.

Pasma K L, Heijmen B J, Kroonwijk M and Visser a G (1998) "Portal dose image (PDI) prediction for dosimetric treatment verification in radiotherapy. I. An algorithm for open beams" *Med Phys* **25** 830-40.

Pasma K L, Kroonwijk M, De Boer J C, Visser a G and Heijmen B J (1998) "Accurate portal dose measurement with a fluoroscopic electronic portal imaging device (EPID) for open and wedged beams and dynamic multileaf collimation" *Phys Med Biol* **43** 2047-60.

Pasma K L, Vieira S C and Heijmen B J (2002) "Portal dose image prediction for dosimetric treatment verification in radiotherapy. II. An algorithm for wedged beams" *Med Phys* **29** 925-31.

Pasquino M, Casanova Borca V and Tofani S (2001) "Physical-dosimetric characterization of a multi-leaf collimator system for clinical implementation in conformational radiotherapy" *Radiol Med (Torino)* **101** 187-92.

Planskoy B (1980) "Evluation of diamond radiation dosemeters" *Phys Med Biol* **25** 519-32.

Ploeger L, Smitsmans M, Gilhuijs K and Van Herk M (2001) "Accurate measurement of the dynamic response of a scanning electronic portal imaging device" *Med Phys* **28** 310-6.

Pouliot J, Aubin M, Langen K, Liu Y, Pickett B, *et al* (2003) "(Non)-migration of radiopaque markers used for on-line localization of the prostate with an electronic portal imaging device" *Int J Radiat Oncol Biol Phys* **56** 862-6.

Pouliot J and Lirette A (1996) "Verification and correction of setup deviations in tangential breast irradiation using EPID: gain versus workload" *Med Phys* **23** 1393-8.

Prewitt J and Mendelsohn M (1966) "The analysis of cell images" *Ann NY Acad Sci* **128** 1035-53.

Prisciandaro J, Herman M and Kruse J (2003) "Utilizing an electronic portal imaging device to monitor light and radiation field congruence" *J Appl Clin Med Phys* **4** 315-20.

Proimos B S (1960) "Synchronous field shaping in rotational megavoltage therapy" *Radiology* **74** 735-57.

Reich P, Bezak E, Mohammadi M and Fog L (2006) "The prediction of transmitted dose distributions using a 3D treatment planning system" *Australas Phys Eng Sci Med* **29** 18-29.

Roback D and Gerbi B (1995) "Evaluation of electronic portal imaging device for missing tissue compensator design and verification" *Med Phys* **22** 2029-34.

Robar J and Clark B (1999) "The use of radiographic film for linear accelerator stereotactic radiosurgical dosimetry" *Med Phys* **26** 2144-50.

Roberts L (1965). Machine perception of three-dimensional solids", *Optical and Electro-Optical information processing*. Cambridge, MIT, pp.159-197.

Rowlands J A, Hunter D M and Araj N (1991) "X-ray imaging using amorphous selenium: a photoinduced discharge readout method for digital mammography" *Med Phys* **18** 421-31.

Ruchala K J, Olivera G H, Schloesser E A and Mackie T R (1999) "Megavoltage CT on a tomotherapy system" *Phys Med Biol* **44** 2597-621.

Ruden B (1976) "Evaluation of the clinical use of TLD" *Acta Radiol Ther Phys Biol* **15** 447-64.

Samant S, Zheng W, Parra N, Chandler J, Gopal A, *et al* (2002) "Verification of multileaf collimator leaf positions using an electronic portal imaging device" *Med Phys* **29** 2900-12.

Sandilos P, Angelopoulos A, Baras P, Dardoufas K, Karaiskos P, *et al* (2004) "Dose verification in clinical IMRT prostate incidents" *Int J Radiat Oncol Biol Phys* **59** 1540-7.

Sankaran A, Gokarn R S and Gangadharan P (1981) "Portable transfer digital dosemeter for beam output measurements with X and gamma rays, electrons and neutrons" *Br J Radiol* **54** 328-34.

Sastre-Padro M, Van Der Heide U and Welleweerd H (2004) "An accurate calibration method of the multileaf collimator valid for conformal and intensity modulated radiation treatments" *Phys Med Biol* **49** 2631-43.

Siebers J V, Kim J O, Ko L, Keall P J and Mohan R (2004) "Monte Carlo computation of dosimetric amorphous silicon electronic portal images" *Med Phys* **31** 2135-46.

Spezi E and Lewis D G (2002) "Full forward Monte Carlo calculation of portal dose from MLC collimated treatment beams" *Phys Med Biol* **47** 377-90.

Stasi M, Baiotto B, Palamara F, Gabriele P and Scielzo G (1999) "Dosimetric characterization of a multileaf collimator" *Radiol Med (Torino)* **97** 382-8.

Steciw S, Warkentin B, Rathee S and Fallone B G (2005) "Three-dimensional IMRT verification with a flat-panel EPID" *Med Phys* **32** 600-12.

Stroom J, Kroonwijk M, Pasma K, Koper P, Van Dieren E, *et al* (2000) "Detection of internal organ movement in prostate cancer patients using portal images" *Med Phys* **27** 452-61.

Stroom J, Olofsen-Van Acht M, Quint S, Seven M, De Hoog M, *et al* (2000) "On-line set-up corrections during radiotherapy of patients with gynecologic tumors " *Int J Radiat Oncol Biol Phys* **46** 499-506.

Suchowerska N, Hoban P, Butson M, Davison A and Metcalfe P (2001) "Directional dependence in film dosimetry: radiographic and radiochromic film" *Phys Med Biol* **46** 1391-7.

Suchowerska N, Hoban P, Davison A and Metcalfe P (1999) "Perturbation of radiotherapy beams by radiographic film: measurements and Monte Carlo simulations" *Phys Med Biol* **44** 1755-65.

Swindell W and Evans P M (1996) "Scattered radiation in portal images: A Monte Carlo simulation and a simple physical model" *Med Phys* **23** 63-73.

Sykes J, James H and Williams P (1999) "How much does film sensitivity increases at depth for larger field sizes?" *Med Phys* **26** 329-30.

Symonds-Tayler J R N, Partridge M and Evans P M (1997) "An electronic portal imaging device for transit dosimetry" *Phys Med Biol* **42** 2273-83.

Taborsky S, Lam W, Sterner R and Skarda G (1982) "Digital imaging for radiation therapy verification" *Opt Eng* **21** 888-93.

Takahashi S (1965) "Conformation Radiotherapy: Rotation techniques as applied to radiogarghy and radiotherapy of cancer" *Acta Radiol Suppl* **242** 1-42.

Tangboonduangjit P, Metcalfe P, Butson M, Quach K and Rosenfeld A (2004) "Matchline dosimetry in step and shoot IMRT fields: a film study" *Phys Med Biol* **49** N287-92.

Tate T, Brace H, Morgan H and Skegg D (1986) "Conformation therapy: A method for improving the tumor's volume ratio" *Clin Radiol* **37** 267-71.

Teh B S, Mai W Y, Grant W H, 3rd, Chiu J K, Lu H H, *et al* (2002) "Intensity modulated radiotherapy (IMRT) decreases treatment-related morbidity and potentially enhances tumor control" *Cancer Invest* **20** 437-51.

Troccaz J, Menguy Y, Bolla M, Cinquin P, Vassal P, *et al* (1993) "Conformal external radiotherapy of prostatic carcinoma: requirements and experimental results" *Radiother Oncol* **29** 176-83.

Tsai J, Wazer D E, Ling M N, Wu J K, Fagundes M, *et al* (1998) "Dosimetric verification of the dynamic intensity-modulated radiation therapy of 92 patients." *Int J Radiat Oncol Biol Phys* **40** 1213-30.

Van De Steene J, Van Den Heuvel F, Bel A, Verellen D, De Mey J, *et al* (1998) "Electronic portal imaging with on-line correction of setup error in thoracic irradiation: clinical evaluation" *Int J Radiat Oncol Biol Phys* **40** 967-76.

Van Den Heuvel F, De Neve W, Verellen D, Coghe M, Coen V, *et al* (1995) "Clinical implementation of an objective computer-aided protocol for intervention in intra-treatment correction using electronic portal imaging" *Radiother Oncol* **35** 232-9.

Van Dyk J, Barnett R B, Cyglar J E and Shragge P C (1993) "Commissioning and quality assurance of treatment planning computers" *Int J Radiat Oncol Biol Phys* **26** 261-73.

Van Elmpt W J, Nijsten S M, Mijnheer B J and Minken a W (2005) "Experimental verification of a portal dose prediction model" *Med Phys* **32** 2805-18.

Van Esch A, Depuydt T and Huyskens D P (2004) "The use of an aSi-based EPID for routine absolute dosimetric pre-treatment verification of dynamic IMRT fields." *Radiother Oncol* **71** 223-34.

Van Esch A, Vanstraelen B, Verstraete J, Kutcher G and Huyskens D (2001) "Pre-treatment dosimetric verification by means of a liquid-filled electronic portal imaging device during dynamic delivery of intensity modulated treatment fields" *Radiother Oncol* **60** 181-90.

Van Herk M (1991) "Physical aspects of a liquid filled ionization chamber with pulsed polarizing voltage" *Med Phys* **18** 692-702.

Van Herk M and Meertens H (1988) "A Matrix ionization chamber imaging device for on-line patient setup verification during radiotherapy" *Radiother Oncol* **11** 369-78.

Varian-Medical-System (2000). Portal Vision LC250 MKII. Palo Alto CA.

Vetterli D, Riem H, Aebersold D, Greiner R, Manser P, *et al* (2004) "Introduction of a novel dose saving acquisition mode for the PortalVision aS500 EPID to facilitate on-line patient setup verification" *Med Phys* **31** 828-31.

Vieira S C, Dirkx M L, Pasma K L and Heijmen B J (2002) "Fast and accurate leaf verification for dynamic multileaf collimation using an electronic portal imaging device" *Med Phys* **29** 2034-40.

Vieira S C, Dirkx M L, Pasma K L and Heijmen B J (2003) "Dosimetric verification of x-ray fields with steep dose gradients using an electronic portal imaging device" *Phys Med Biol* **48** 157-66.

Vieira S C, Kaatee R S, Dirkx M L and Heijmen B J (2003) "Two-dimensional measurement of photon beam attenuation by the treatment couch and immobilization devices using an electronic portal imaging device" *Med Phys* **30** 2981-7.

Vigneault E, Pouliot J, Laverdiere J, Roy J and Dorion M (1997) "Electronic portal imaging device detection of radioopaque markers for the evaluation of prostate position during megavoltage irradiation: a clinical study" *Int J Radiat Oncol Biol Phys* **37** 205-15.

Visser A, Huizenga H, Althof V and Swanenburg B (1990) "Performance of a prototype fluoroscopic radiotherapy imaging system" *Int J Radiat Oncol Biol Phys* **18** 43-50.

Warkentin B, Steciw S, Rathee S and Fallone B G (2003) "Dosimetric IMRT verification with a flat-panel EPID" *Med Phys* **30** 3143-55.

Webb S (2003) "The Physical basis of IMRT and inverse planning" *Br J Radiol* **76** 678-89.

Weltens C, Huyskens D, Dutreix A and Van Der Schueren E (1998) "Assessment of dose inhomogeneities in clinical practice by film dosimetry" *Radiother Oncol* **49** 287-94.

Wendling M, Louwe R J, Mcdermott L N, Sonke J J, Van Herk M, *et al* (2006) "Accurate two-dimensional IMRT verification using a back-projection EPID dosimetry method" *Med Phys* **33** 259-73.

Williams M J and Metcalfe P (2006) "Verification of a rounded leaf-end MLC model used in a radiotherapy treatment planning system" *Phys Med Biol* **51** N65-78. Epub 2006 Feb 1.

Williams P (2003) "IMRT: delivery techniques and quality assurance" *Br J Radiol* **76** 766-76.

Williamson J, Khan F and Sharma S (1981) "Film dosimetry of megavoltage photon beams: a practical method of isodensity-to-isodose curve conversion" *Med Phys* **8** 94-8.

Winkler P, Hefner A and Georg D (2005) "Dose-response characteristics of an amorphous silicon EPID" *Med Phys* **32** 3095-105.

Wong J W, Slessinger E D, Hermes R E, Offutt C J, Roy T, *et al* (1990) "Portal dose images. I: Quantitative treatment plan verification" *Int J Radiat Oncol Biol Phys* **18** 1455-63.

Wright a E and Gager L D (1977) "Silicon diode detectors used in radiological physics measurements. Part II: Measurement of dosimetry data high-energy photons" *Med Phys* **4** 499-502.

Wright K A, Proimos B S and Trump J G (1959) "Field shaping and selective protection in megavoltage therapy" *Radiology* **72** 101.

Xing L, Curran B, Hill R, Holmes T, Ma L, *et al* (1999) "Dosimetric verification of a commercial inverse treatment planning system." *Phys Med Biol* **44** 463-78.

Yang Y and Xing L (2004) "Quantitative measurement of MLC leaf displacements using an electronic portal image device " *Phys Med Biol* **49** 1521-33.

Yeo I J, Beiki-Ardakani A, Cho Y B, Heydarian M, Zhang T, *et al* (2004) "EDR2 film dosimetry for IMRT verification using low-energy photon filters" *Med Phys* **31** 1960-3.

Yin F, Schell M and Rubin P (1994) "Input/output characteristics of a matrix ion-chamber electronic portal imaging device" *Med Phys* **21** 1447-54.

Yin F F, Schell M C and Rubin P (1994) "A technique of automating compensator design for lung inhomogeneity correction using an electron portal imaging device" *Med Phys* **21** 1729-32.

Ying X G, Geer L Y and Wong J W (1990) "Portal dose images. II: Patient dose estimation" *Int J Radiat Oncol Biol Phys* **18** 1465-75.

Yudelev M, Alyyousef K, Brandon J, Perevertailo V, Lerch M, *et al* (2004) "Application of semiconductors for dosimtery of fast neutron therapy beam" *radiat Prot dosimetry* **110** 573-8.

Zeidan O A, Li J G, Ranade M, Stell a M and Dempsey J F (2004) "Verification of step-and-shoot IMRT delivery using a fast video-based electronic portal imaging device " *Med Phys* **31** 463-76.

Zhu Y, Jiang X and Van Dyk J (1995) "Portal dosimetry using a liquid ion chamber matrix: Dose response studies" *Med Phys* **22** 1101-06.

Zietman a L, Desilvio M L, Slater J D, Rossi C J, Jr., Miller D W, *et al* (2005) "Comparison of conventional-dose vs high-dose conformal radiation therapy in clinically localized adenocarcinoma of the prostate: a randomized controlled trial" *JAMA* **294** 1233-9.